A Dynamic Computational Model of Pulsatile Brain Blood Flow

Kajal Saroay

Supervisor: Prof. Kevin Murphy

School of Physics and Astronomy
Cardiff University

This thesis is submitted for the degree of
Doctor of Philosophy

December 2023

Abstract

Declining vessel health in the brain is associated with the development and progression of cerebrovascular disease. As arteries become less compliant with age, their ability to dampen pulsatile energy decreases. A model of blood flow across the cerebrovascular network was developed in this thesis to understand how cardiac pulsatile energy is dissipated in the brain. Existing models are limited in their ability to model local changes in flow following changes in blood volume in compliant vessels. A computational model was developed to simulate dynamic flow in a branched network of cerebral vessels, with the aim of modelling pulsatile flow across the network.

An overview of cerebral anatomy and haemodynamics is presented in Chapter 1. In Chapter 2, methods for measuring blood flow are outlined and compared. Existing models are evaluated in Chapter 3. The development of the computational model is described in Chapter 3. An existing model was replicated and extended to incorporate dynamic changes in a network of compliant vessels following changes in pressure across time. The results from steady state simulations, which were carried out as a first step validation are presented in Chapter 5. The development of the Plausible Vessel Network is described in Chapter 6. Results from dynamic simulations, assessing shape changes in flow across the Plausible Vessel Network are presented in Chapter 7. A proof of concept to estimate vessel compliance using MRI data in the model is outlined in Chapter 8.

Results presented in this thesis suggest that many parameters need to be set to realistically model blood flow in cerebral vessels including compliance and pulse wave velocity across the network. Further research into setting these parameters will help increase the accuracy, and thus the utility of the model to gain an improved understanding of the deterioration of cerebrovascular health with age and disease.

Table of contents

List of figures

List of tables

Nomenclature

Acronyms / Abbreviations

ABP Arterial Blood Pressure

ACA Anterior Cerebral Artery

ACoA Anterior Communicating Artery

AD Alzheimer's Disease

ASL Arterial Spin Labelling

BA Basilar Artery

BBB Blood-Brain Barrier

BOLD Blood Oxygenation Level Dependent

CBF Cerebral Blood Flow

CBFV Cerebral Blood Flow Velocity

CBV Cerebral Blood Volume

CSF Cerebrospinal Fluid

CTTH Capillary Transit Time Heterogeneity

CVR Cerebrovascular Reactivity

DIMAC Dynamic Inflow Magnitude Contrast

fMRI Functional Magnetic Resonance Imaging

FPI Flow Pulsatility Index

GRAPPA GeneRalized Autocalibrating Partially Parallel Acquisitions

GRE Gradient Recalled Echo

ICA Internal Carotid Artery

ICP Intracranial Pressure

MCA Middle Cerebral Artery

MCI Mild Cognitive Impairment

MRA Magnetic Resonance Angiography

MRI Magnetic Resonance Imaging

PCoA Posterior Communicating Artery

PI Pulsatility Index

PVN Plausible Vessel Network

PWV Pulse Wave Velocity

RF Radiofrequency

SE Spin Echo

SVD Small Vessel Disease

TCD Transcranial Doppler Ultrasound

TE Echo Time

TR Repetition Time

VAN Vascular Anatomical Network

VA Vertebral Artery

Chapter 1

Blood Vessels and Blood Flow

Chapter Overview

Blood vessel health deteriorates with ageing and disease as arteries stiffen. This has a detrimental effect on the dampening of pulsatile energy across the vascular network. In this chapter, an overview of the structure and function of the vascular tree will be presented, along with the mechanisms that control the supply of blood to the brain. The effect of pulsatility on vessel anatomy, blood flow and the development and progression of cerebrovascular disease will be discussed.

1.1 Introduction

Blood vessels play a vital role in the supply of oxygenated blood from the heart to the brain. A sufficient supply of blood to the brain is fundamental to ensuring an adequate amount of oxygen and nutrients are delivered to maintain normal functioning (Cipolla, 2009). Furthermore, the brain requires approximately 15-20% of total cardiac output, making it a highly perfused organ (Xing et al., 2017) and hence blood flow is regulated by several mechanisms to achieve a constant supply. Blood vessels form the circulatory system along with the heart, allowing oxygenated blood to travel from the heart to the peripheral organs and deoxygenated blood to return to the heart before re-oxygenation in the lungs. Changes in blood flow can occur as vessel health deteriorates and, since it is so sensitive to blood supply, this is particularly detrimental to the brain. Declining vessel health in the brain, primarily as a result of ageing, has been associated with the development and progression of cerebrovascular diseases such as cerebral Small Vessel Disease (SVD) (Poels et al., 2012) as well as cognitive impairment and dementia (Iulita et al., 2018). Arterial stiffness is an indicator of increased risk of cardiovascular disease (Cecelja and Chowienczyk, 2012) and has also been associated with cerebrovascular changes relating to cerebrovascular disease (Badji et al., 2019). Blood flow is pulsatile as it travels from the heart and becomes steady once it reaches the microvessels. However as vessels become stiffer

with age, their ability to dampen the pulsatile energy decreases, leading to the deterioration of vessel health (O'Rourke and Hashimoto, 2007). In this chapter, an overview of the structure and function of the vascular tree will be presented, along with key concepts relating to cerebral haemodynamics and the regulation of blood flow to the brain.

1.2 The Vascular System

Blood vessels are categorised into five groups: arteries, arterioles, capillaries, venules and veins, with the arterioles, capillaries and venules forming the microvasculature. Fully oxygenated blood returning from the lungs is pumped by the heart towards the aorta, the largest artery in the body. The aorta branches into arteries which have smaller diameters. This branching continues across the arterial network, eventually reaching the arterioles. As the arterioles become smaller they branch into the capillaries, the smallest vessels in the vascular system and this is where the majority of perfusion occurs. Perfusion involves the exchange of oxygen and nutrients to the tissue. In the brain, the blood loses roughly 40% of its bound oxygen in this process (Buxton, 2009). This deoxygenated blood is then transported through the converging venules and veins until it reaches the heart. Blood vessels consist of three layers: the tunica intima, tunica media and tunica adventia. The structure of each layer is dependent on the function of the vessel and differs for each type of vessel (Cipolla, 2009).

1.2.1 Vessel Structure and Function

Arteries are either elastic or muscular in nature, depending on their function and position along the vascular tree (Fig. 1.1). Due to their proximity to the heart, large arteries consist mainly of elastic tissue, allowing them to withstand the large pressure waves emanating from the heart. In contrast, muscular arteries are surrounded by smooth muscle which enables them to contract and distend following changes in pressure (Shirwany and Zou, 2010). As arteries decrease in diameter along the vascular tree, resistance to flow increases and blood velocity decreases. The medial layer of the arterioles mainly consist of smooth muscle cells which are important for altering vascular tone. Due to their small diameter and smooth muscle content, arterioles are also known as resistance vessels and play a key role in controlling blood flow to the capillaries (Martinez-Lemus, 2012).

Capillaries are thin-walled vessels consisting of a single endothelial cell layer to allow for exchange of oxygen and nutrients to the tissue. Blood flow is steady once it reaches the capillaries. Blood travels from the capillaries, firstly draining into the venules and then the larger diameter veins. Veins are less elastic compared to arteries and have thinner walls and bigger lumen diameters. This is due to the lower pressures experienced on the venous side of the vascular tree. Valves are a unique feature to the veins which ensure that blood flows in the correct direction towards the heart at low pressure (Cipolla, 2009).

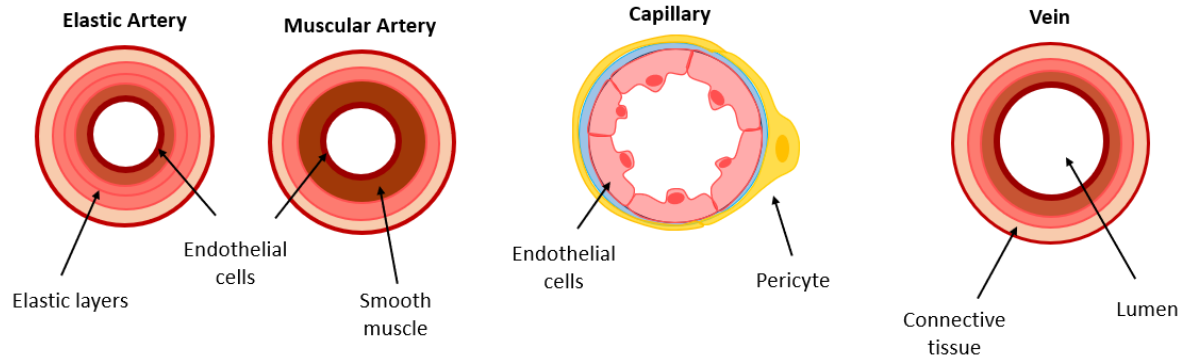

Fig. 1.1 Cross-sectional diagram of the artery, capillary and vein. All vessels are lined with endothelial cells. Elastic arteries consist mainly of concentric layers of elastic tissue whereas muscular arteries are mainly made up of smooth muscle. Pericytes surround the endothelial cells in the capillaries. Veins have thinner walls compared to arteries and venous lumens are larger in diameter to allow blood to flow back to the heart with less resistance.

1.2.2 Cerebrovascular Anatomy

Blood is supplied to the brain via pairs of internal carotid and vertebral arteries, which join with other large arteries to form the Circle of Willis, a ring-shaped arterial structure located at the base of the brain (Cipolla, 2009) (See Fig.1.2). The vertebral arteries (VA) join together to form the basilar artery (BA), which is connected to the internal carotid artery (ICA), anterior cerebral artery (ACA), middle cerebral artery (MCA) and anterior (ACoA) and posterior communicating arteries (PCoA) (Payne, 2016). The main function of the Circle of Willis is to provide collateral paths of blood flow to ensure sufficient oxygen supply to the cerebral tissue, even in the event of vessel occlusion (Jones et al., 2021). Variability exists in Circle of Willis across individuals, and it is not always fully intact. Variability in the Circle of Willis is clinically important as variations may reduce the collateral ability of the structure. Incomplete structures are associated with cerebrovascular disease (Hindenes et al., 2020).

Arteries in the Circle of Willis continue to branch into smaller vessels. Pial vessels on the surface of the brain eventually branch into arteries and arterioles which penetrate the surface of the cerebral cortex. Capillaries stem from the penetrating arterioles, forming the capillary bed where the exchange of oxygen and nutrients with the surrounding tissue occurs. Following this, the vessels converge to form branches of venules and veins. Cerebral blood is drained through the superficial cortical veins and the deep veins. Blood travelling through the deep veins is emptied into the superior sagittal sinus (Cipolla, 2009).

1.2.3 The Blood-Brain Barrier

The blood-brain barrier (BBB) is a border that separates the blood flowing through the capillaries from brain tissue (Fig. 1.3). The exchange of compounds between the vessels and tissue is strictly controlled to ensure that oxygen and nutrients are able to pass through to the tissue whilst

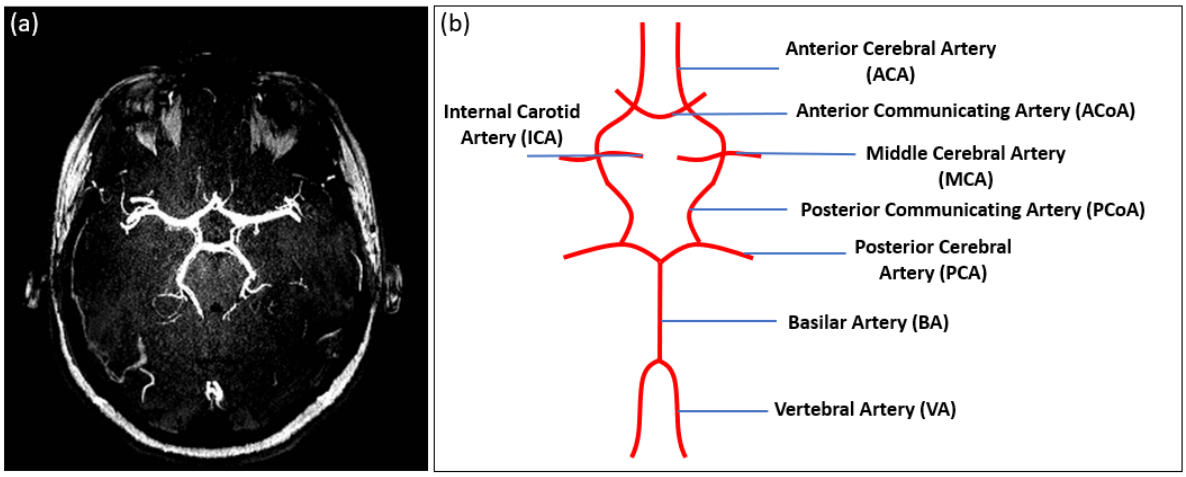

Fig. 1.2 (a) Maximum intensity projection time-of-flight image showing the Circle of Willis. (b) Diagram of the arteries in and connected to the Circle of Willis.

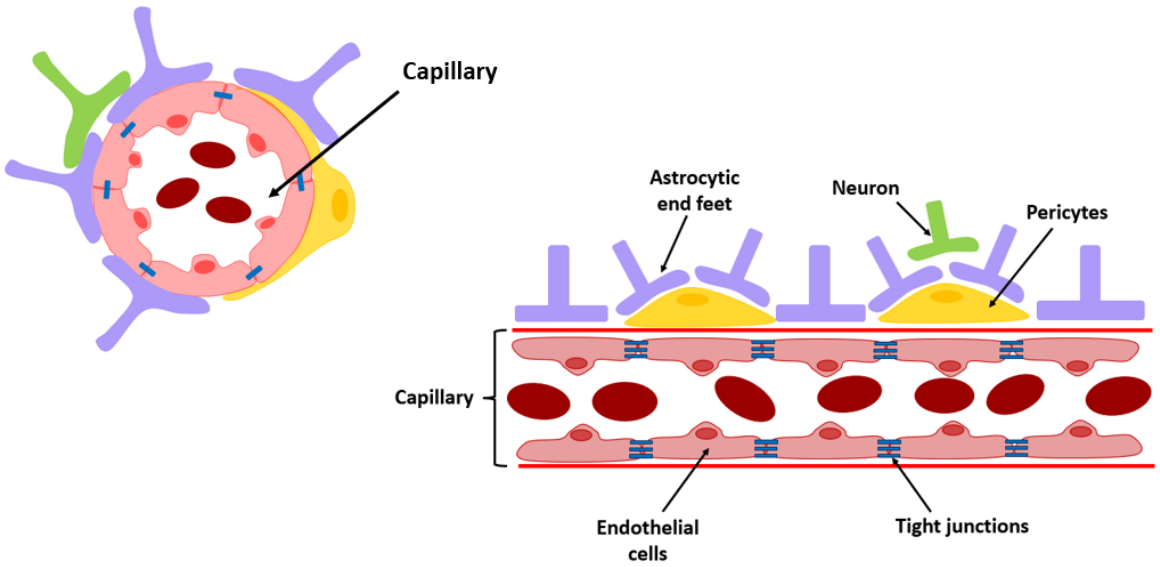

Fig. 1.3 Diagram of the Blood-Brain Barrier. A single layer of endothelial cells line the vessel wall. Pericytes border the endothelial cells. Astrocytic end-feet surround the vessel walls.

keeping out toxins. The blood-brain barrier consists of endothelial cells which line the capillaries and are organised to form tight junctions. Astrocytic end-feet surround the vessel walls and play a key role in the formation of tight junctions (Ballabh et al., 2004). Aquaporin channels in the vessel wall allow oxygen-carrying water to move from the blood in the vessel to the surrounding tissue (Verkman, 2002). Pericytes border the endothelial cells in the capillaries and contribute to the maintenance of the blood-brain barrier (Attwell et al., 2016). A functioning blood-brain barrier is important for maintaining brain homeostasis (Weiss et al., 2009).

1.3 Blood Pressure, the Cardiac Cycle and Pulsatility

Blood pressure is the term used to describe the pressure exerted by blood on the walls of the vessels. Blood pressure is typically recorded as two values, the systolic pressure and diastolic pressure. Systolic blood pressure is the pressure due to the ejection of blood during ventricular constriction and diastolic blood pressure is the pressure during ventricular relaxation. Pulse pressure is the difference between the systolic and diastolic pressures (Malone and Reddan, 2010).

The cardiac cycle describes the phases of blood entering the heart and being pumped to the body, starting from the beginning of a heartbeat and ending at the start of the next. The relaxation period, known as the diastolic phase, is when the heart receives blood from the veins. In atrial diastole, blood travelling from the pulmonary veins fills the chambers of the heart. The systolic phase describes the contraction of the heart where blood is ejected from the chambers of the heart to the peripheral organs through the arteries (John K-j Li, 2004). A diagram of a typical blood pressure wave across the cardiac cycle is shown in Fig. 1.4. As the pressure wave travels from the aorta to the peripheral arteries it encounters sites of mismatched resistance, typically at branching points, resulting in two components of the pressure wave. The first component is the transmitted pressure wave which travels forward in the same direction as the propagated pressure wave along the arterial system. The second component is the reflected pressure wave which travels in the opposite direction of blood flow towards the heart. The timing of this reflected pressure wave is important. In healthy arteries, the reflected pressure wave returns to the aorta during diastole, augmenting the diastolic pressure (Shirwany and Zou, 2010).

Pulsatility refers to the changes in blood pressure and blood flow across the cardiac cycle (Wagshul et al., 2011). Healthy blood flow is pulsatile as it travels through the large arteries, gradually becoming steady as it reaches the capillaries. Variations in flow as a result of the periodic changes in blood pressure are most prominent in the arteries where flow is highly pulsatile (Ku, 1997). The dampening of the pulsatility is due to the elastic nature of the aorta and other large arteries and is key in ensuring that the smaller, delicate capillaries are not exposed to pulsatile energy (O'Rourke, 2007).

Pressure propagates through the vasculature at a speed equal to the pulse wave velocity (PWV). Pulse wave velocity is defined in Eq.1.1 where Δx is the distance between two points in

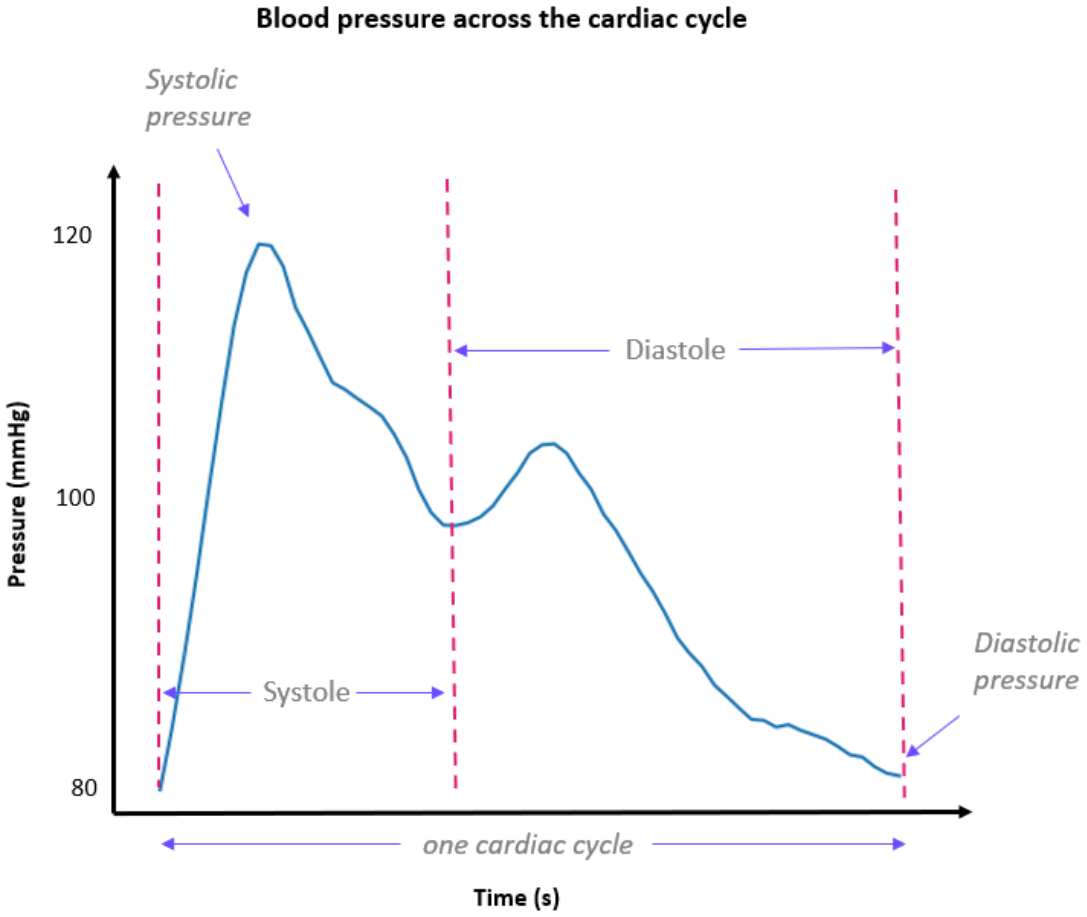

Fig. 1.4 Example of a typical blood pressure waveform across one cardiac cycle. Systolic pressure is the maximum pressure and diastolic pressure is the minimum pressure. Normal values of blood pressure in the cardiac cycle fall between 80 and 120 mmHg. The second peak is a result of the reflected pressure wave.

the arterial tree and Δt is the time taken for the pulse wave to travel from one site to the other (Bramwell and Hill, 1997).

$$PWV = \Delta x / \Delta t \tag{1.1}$$

Intracranial pressure (ICP) refers to the pressure exerted within the skull and is dependent on blood, cerebrospinal fluid (CSF) and brain tissue (Czosnyka, 2004). The Monro-Kellie hypothesis states that the total volume of these three components should stay constant. As the skull is a rigid structure with a fixed volume, an increase in volume of one of these components contained within the skull without a decrease in another causes an increase in ICP (Oswal and Toma, 2023).

1.4 Assessing Vessel Health

1.4.1 Blood Flow Regulation

Vessel Compliance

The ability of a vessel to respond to changes in pressure, P, through changes in volume, V, is known as compliance, C, and is defined in Eq. 1.2. A vessel that is more elastic is more compliant (Kelly and Chowienczyk, 2002).

$$C = \Delta V / \Delta P \tag{1.2}$$

Distensibility, D is the change in volume of a vessel as a proportion of its baseline volume following a change in pressure and is related to the elasticity of the vessel wall (Kelly and Chowienczyk, 2002). Distensibility is defined in Eq. 1.3. This differs to compliance as it also takes into account the diameter of the vessel.

$$D = \left| \frac{\Delta V / V}{\Delta P} \right| \tag{1.3}$$

Changes in blood vessel diameter following pressure changes are essential for achieving steady flow in the capillaries. As the cardiac cycle enters the systolic phase, arteries increase in volume following the increased pressure with blood flow and this is known as the Windkessel effect (Westerhof et al., 2009). Arterial compliance ensures the rise in systolic pressure is limited, whilst also maintaining diastolic pressure. Compliance plays an important role in the dynamics of blood flow across the vascular tree as it determines pulse wave velocity (Marchais et al., 1993). Veins are compliant to accommodate large volumes of blood flowing from the microvessels back towards the heart (Zamboni et al., 2018).

Cerebral Autoregulation

Cerebral Autoregulation (CA) refers to the regulation of blood flow with changes in arterial blood pressure (Payne, 2016). Blood flow is primarily controlled by vascular tone, defined as the size of a constricted vessel compared to its maximum dilated state. Therefore, vascular tone is altered through changes in vessel diameter (Payne, 2016). Regulation of blood flow changes due to blood pressure changes is controlled through different mechanisms which are dependent on the location and structure of the vessels across the network.

Vessel diameter passively changes with blood pressure due to the compliance of the vessel wall. This follows a linear relationship where the vessel diameter decreases as blood pressure decreases. In order to maintain a constant flow of blood to the brain following a drop in blood pressure, the passive response needs to be overcome to increase vessel diameter and therefore flow (Payne, 2016). The myogenic response is an active response involving the relaxation and constriction of smooth muscle cells in the arteries and arterioles. Arteriolar tone is mainly controlled through this method (Cipolla, 2009).

Blood flow through the capillaries is also regulated. Changes in capillary diameter are thought to be a result of passive changes following changes in arteriolar tone as well as active control due to the relaxation of pericyte cells causing vasodilation (Payne, 2016).

Local control of blood flow is related to the metabolic response associated with neural activity. Neurovascular coupling describes the relationship between neural activity and changes in cerebral blood flow in a localised area. Blood flow is increased through vasodilation resulting from the release of metabolites when there is a decrease in tissue oxygenation (Payne, 2016).

Cerebrovascular Reactivity

Flow is also influenced by vasoactive stimuli such as carbon dioxide. Cerebrovascular reactivity (CVR) is a metric which assesses the cerebral blood flow (CBF) response to a change in CO_2 levels through changes in vessel diameter (Duffin et al., 2018). Therefore, measurements of CVR can be used in the assessment of cerebrovascular health and disease (Sleight et al., 2021).

1.4.2 Arterial Stiffness and Cerebrovascular Disease

Arterial stiffness refers to the loss of elasticity in the arteries and is inversely proportional to compliance. Stiffness is associated with ageing as the loss of elasticity occurs over time due to the continuous stretching and relaxation of the arterial walls to accommodate changes in blood volume (O'Rourke, 2007). Arterial stiffness is a risk factor for cardiovascular disease (Shirwany and Zou, 2010) and has also been associated with cerebrovascular diseases including cerebral Small Vessel Disease (Poels et al., 2012; Rabkin, 2012) and stroke (Laurent et al., 2003; Mattace-Raso et al., 2006). Stiffness across the arteries has also been linked to cognitive decline and Alzheimer's Disease (AD) (Hughes et al., 2014; Tsao et al., 2013).

Arterial stiffness occurs due to changes in structure of the vessel wall (Lee and Oh, 2010). Changes in structure include the fragmentation of elastin fibres and the increase in collagen production, altering the proportion of the two proteins in the arterial wall (Shirwany and Zou, 2010). As a consequence of the structural changes resulting from vascular ageing, the normal functioning of arteries is hindered, with the reduced cushioning of the pulsations having a detrimental effect on the microvessels of the brain (O'Rourke, 2007). In addition, arterial stiffness has also been related to lower cerebral blood flow (Jefferson et al., 2018).

Arterial stiffness is detrimental to health for a number of reasons. Firstly, stiffness of the aorta affects the reflections of the pulse wave. As the pressure wave travels across the vascular tree, it encounters sites where reflections occur. This is typically at the branching points, following changes in resistance due to the differences in vessel diameter. In healthy vessels, the difference in resistance between a compliant aorta and the muscular arteries allows a fraction of the pulsatile energy in the forward travelling wave to be reflected, reducing the pulsatility travelling across the vascular tree. When the aorta stiffens, this difference between the resistances at the two sites is reduced which means that less of the pulsatile energy is reflected (Mitchell et al., 2011). A study by Zarrinkoob et al. (2016) found reduced dampening of the pulsatile flow across the cerebral arterial tree in elderly subjects compared to young subjects as a result of aortic stiffness due to ageing.

Furthermore, an increase in arterial stiffness reduces the time taken for the reflected wave to return to the heart, leading to the pressure wave arriving too early in the cardiac cycle. Reflected arterial waves arrive in the systolic phase instead of the diastolic phase which causes an increase in systolic pressure and a decrease in diastolic pressure (Nichols, 2005). As a consequence of the augmented pressure, pulse pressure is increased. Left ventricular workload is also increased (Nichols et al., 2008). An increase in pulse pressure can be found in central and peripheral arteries following arterial stiffness (Safar, 2018). This can cause increased wall thickness, as well as stenosis and plaques which in return causes local changes in compliance (Bianciardi et al., 2016). Vascular remodelling has also been associated with changes in pulse pressure to overcome changes in wall stress (Payne et al., 2010).

Arterial stiffness is particularly harmful to the brain as the loss of elasticity in the arteries results in less efficient buffering of the pulsatile energy. Without the dampening by compliant arteries, pulsatile energy propagates further down the vascular tree, eventually reaching the microvessels (O'Rourke and Hashimoto, 2007). This has been implicated in microvascular remodelling which adversely affects the reactivity of these vessels (Mitchell et al., 2005). Capillaries are particularly susceptible to the effects of pulsatile pressure and flow due to their lack of elastic tissue to provide a cushioning effect (O'Rourke, 2007). Excessive pulsatile energy propagating across the cerebral vasculature causes breakdown of the blood-brain barrier (Levin et al., 2020). Endothelial dysfunction affects blood flow through reduced production and release of nitric oxide which is important for vessel dilation (Quick et al., 2021). Blood-brain barrier dysfunction results in less control of the substances moving from blood to tissue (Hussain

et al., 2021). Breakdown of the blood-brain barrier has been associated with neurodegenerative diseases, and has been suggested as a potential biomarker for Alzheimer's Disease (Sweeney et al., 2018).

Pulse wave velocity is used as a non-invasive indirect measure of arterial stiffness, with higher PWV signifying stiffer arteries (Sun, 2015). PWV can be calculated using the Moens-Korteweg equation (Eq. 1.4) where E is the Young's modulus of the vessel wall, h is the thickness of the vessel wall, r is the radius and ρ is the density of blood. PWV can also be calculated using vessel distensibility, D, as shown in the Bramwell-Hill equation (Eq.1.5).

$$PWV = \sqrt{\frac{Eh}{2r\rho}} \tag{1.4}$$

$$PWV = \sqrt{\frac{1}{\rho D}} \tag{1.5}$$

Pulse wave velocity is typically calculated between the carotid and femoral arteries, as the gold-standard measure of systemic arterial stiffness (Vlachopoulos et al., 2012). Using the distance between the two arteries and the time delay between the two pulse waves at the two arterial sites (Fig. 1.5), PWV can be calculated using Eq. 1.1.

Arterial stiffness is associated with mild cognitive impairment. A study by Rabkin (2012) found that arterial stiffness increased across groups from normal cognitive function, mild cognitive impairment, Alzheimer's Disease and vascular dementia and that a higher PWV was a significant predictor of cognitive decline. Furthermore, Hughes et al. (2014) found that arterial stiffness was an independent indicator of amyloid beta progression, a marker of Alzheimer's Disease, in non-demented individuals.

Arterial stiffness has also been associated with cerebral SVD. A study by Poels et al. (2012) suggests that there is an association between increased arterial stiffness and volume of white matter lesions which is a diagnostic marker of SVD in MRI. Understanding the cause of SVD is of growing importance as it has been found to cause vascular dementia as well as contribute to the pathogenesis of Alzheimer's Disease and increase the risk of stroke (Quick et al., 2021).

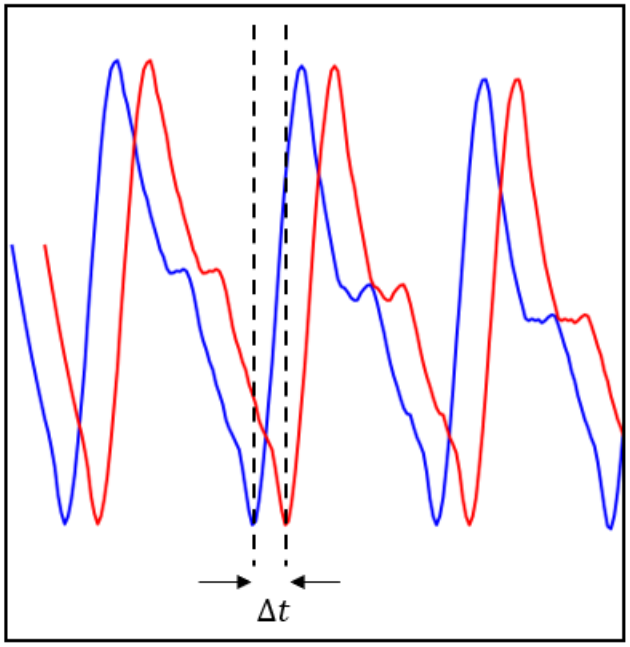

Fig. 1.5 Pulse waves measured simultaneously at two different arterial sites are shown in blue and red. The delay time, Δt, is the delay in arrival time of the foot of a pressure wave (red) compared to the other (blue). The foot of the pulse wave is found at the end of diastole, before the steep increase in pressure. To calculate PWV, the distance between the two arterial sites, Δx, is divided by Δt.

1.5 Modelling Cerebral Blood Flow

1.5.1 Haemodynamics

The relationship between blood pressure, P, flow, F, and resistance, R, is shown in Eq. 1.6. Blood travels from regions of high pressure to low pressure, with the change in pressure, ΔP, between two sites driving the flow. Assuming blood through a single vessel can be modelled as a Newtonian fluid and the flow is steady and laminar, resistance in a vessel can be calculated using the Poiseuille equation (Eq. 1.7). Here, R is the resistance to flow, η is the viscosity of blood, l is the length of the blood vessel and d is the diameter of the blood vessel (Washburn, 1921).

$$\Delta P = F \times R \tag{1.6}$$

$$R = \frac{128\eta l}{\pi d^4} \tag{1.7}$$

From the Poiseuille equation (Eq. 1.7), it is clear that resistance is highly influenced by vessel diameter as the resistance to flow in a vessel is inversely proportional to the fourth power of its diameter. Therefore a small change in vessel diameter can have a large effect on the resistance which impacts blood flow. Furthermore, the length of the blood vessel and the viscosity of blood typically only vary across long time periods where adaptation of the vessel network occurs, hence are generally considered constant across time. This means that blood flow is primarily controlled through changes in vessel diameter (Payne, 2016). Cerebral autoregulation is a physiological process in which vessel diameters are modified to change the amount of resistance to flow, regulating the amount of flow to the brain (Duffin et al., 2018). Arterioles are commonly referred to as resistance vessels as a result of their small diameters and thus play a key role in the control of blood to the capillaries.

A common method of approximating haemodynamic behaviour is to treat blood vessel networks analogously to electrical circuits as the relationship between pressure, flow and resistance is comparable to that of voltage, current and resistance (Payne, 2016). Total resistance across sections of the network can be calculated either in series or parallel, depending on the structure of the chosen vessels (Secomb, 2016). A diagram representing an example of a vascular tree reduced to a lumped parameter representation is shown in Fig. 1.6. In Fig. 1.7 two vessels are used to represent the capillaries in a) series and b) parallel. Eqs. 1.8 and 1.9 are used to calculate total resistance in two vessels in series and parallel respectively, where R_1 and R_2 are the values of resistance for two different vessels.

$$R_{series} = R_1 + R_2 \tag{1.8}$$

$$R_{parallel} = \frac{R_1 R_2}{R_1 + R_2} \tag{1.9}$$

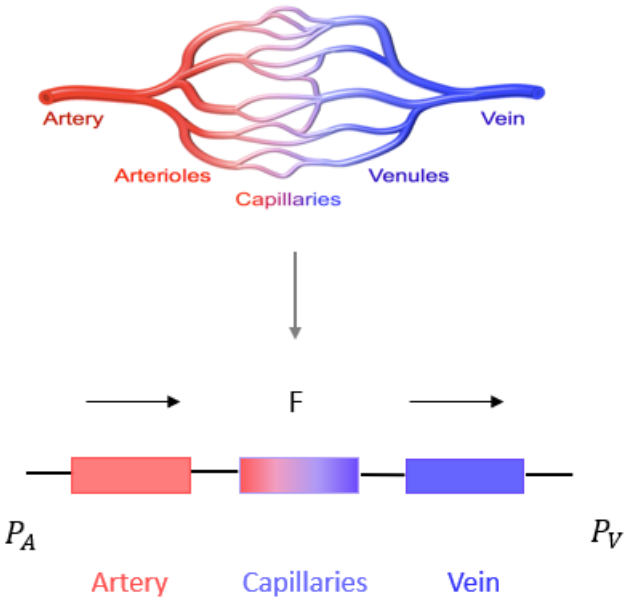

Fig. 1.6 Example of a vascular network reduced to a lumped parameter model. Vessels in sections of the network are combined into compartments to simplify the haemodynamic equations, treating the network analogously to an electric circuit. Flow across a compartment can be calculated using the corresponding pressure gradient and resistance for that compartment.

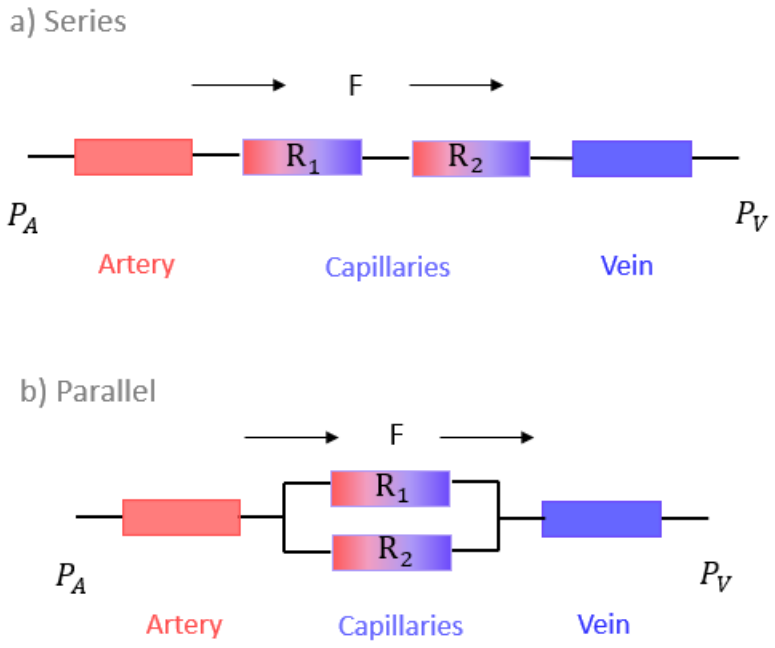

Fig. 1.7 Example of a vascular network with vessels in (a) series and (b) parallel. Here the vascular network consists of one compartment representing the arterial vessels, one for the venous vessels and two for the capillaries. Total resistance in the capillary compartment (R1 and R2) is either calculated in series using Eq. 1.8 or parallel using Eq. 1.9.

1.6 Summary

Cerebral blood flow is tightly regulated to ensure the brain receives a sufficient amount of oxygen and glucose to meet metabolic demands and this is achieved through a number of mechanisms. As blood travels from the heart to the capillaries in the brain, the pulsatile energy is dampened across the arteries and arterioles, resulting in a steady flow in the capillaries. Stiffening of the arteries leads to the pulsatility propagating further into the vascular tree which is detrimental to brain health for many reasons. This highlights the importance of studying the effects of arterial compliance on flow across the vascular tree. To better understand how pulsatile cardiac energy is dissipated in the brain, a dynamic model of flow across the cerebrovascular network is required. In this thesis, a dynamic vascular network model is developed to explore pressure-driven flow changes in compliant cerebral blood vessels.

Chapter 2

Measuring Arterial Stiffness and Pulsatility in the Brain

Chapter Overview

Arterial stiffness is typically measured using transcranial Doppler ultrasound (TCD), however there are some limitations to the method. Whilst arterial stiffness can be measured in a relatively cost-effective way using this method, blood flow is measured indirectly through cerebral blood flow velocity, and this assumes that vessel diameter is constant over time. Furthermore, arterial stiffness can only be measured by TCD in select arteries, which is unsuitable for studying the effect of increased pulsatility along the brain's vasculature. For this reason, MRI provides a much more versatile method for measuring arterial stiffness and pulsatility, leading to a more comprehensive understanding of how pulsatility travels across vessels in the brain. In this chapter an overview of TCD and the MRI methods used to measure blood flow will be presented and compared. The Dynamic Inflow Magnitude Contrast (DIMAC) method will be introduced.

2.1 Introduction

Arterial compliance diminishes with age which leads to reduced dampening of the pulsatile flow waveform (O'Rourke and Hashimoto, 2007). Excessive pulsatile energy reaching the cerebral microvessels causes microvascular damage which has a detrimental effect on brain function and is linked to the development and progression of cerebrovascular disease (Mitchell et al., 2011). Flow pulsatility has been investigated using methods such as transcranial Doppler ultrasound (TCD) and Magnetic Resonance Imaging (MRI). Despite TCD being a cost-effective and widely available method, it is limited to measuring cerebral blood flow velocity (CBFV) in the major cerebral arteries. As a consequence, this method is not appropriate for assessing pulsatility along the brain's vascular tree. Various MRI techniques have been developed to measure pulsatile flow across the cerebral vasculature which are either based on the inflow contrast or phase

contrast methods. In this chapter, an overview of the key methods will be provided, along with an evaluation of their advantages and disadvantages.

2.2 Transcranial Doppler Imaging

Transcranial Doppler ultrasound is a non-invasive and relatively inexpensive method which utilises the flow-related frequency shift of the reflected ultrasound waves that have been transmitted to the blood vessels. TCD provides a measure of blood flow velocity, from which values relating to pulsatility and cerebral compliance can be estimated (Afkhami et al., 2021). The arteries that can be assessed using TCD include the middle cerebral artery (MCA), posterior cerebral artery (PCA), anterior cerebral artery (ACA), vertebral artery (VA) and basilar artery (BA), if a suitable acoustic window exists for an individual (Harris et al., 2018).

2.2.1 Principles of TCD

Ultrasound waves with a frequency of approximately 2 MHz are transmitted by a transducer through the skull to the artery of interest. The waves are reflected by the red blood cells moving through the vessel. As a result of the Doppler effect, there is a shift in frequency between the emitted and reflected waves and this is proportional to blood flow velocity in the insonated vessel (Magee, 2020). The relationship between flow velocity and frequency shift is described in Eq. (2.1) where ϑ is the angle of insonation (Purkayastha and Sorond, 2012). As blood flow is laminar within a vessel, TCD obtains a distribution of frequency shifts which relate to different blood flow velocities. Values for peak systolic velocity and end diastolic velocity can then be extracted from this distribution and clinically relevant parameters such as mean flow velocity and pulsatility index can be calculated (Naqvi et al., 2013).

Insonation of a blood vessel requires a suitable acoustic window where ultrasound can travel through the skull. There are four windows for the cerebral arteries (Bathala et al., 2013). A major limitation of TCD is that not every subject possesses a suitable acoustic window (Marinoni et al., 1997). Furthermore, insonation may not be as effective in elderly individuals due to potential changes in thickness of the cranial bones with age (Roher et al., 2011).

$$Reflector speed = \frac{Doppler shift \times Propogation speed}{2 \times Incident\ frequency \times cos(\theta)} \tag{2.1}$$

The pulsatility index (PI) is calculated from blood flow velocity using Eq. 2.2 (Gosling and King, 1974). This index is commonly used to evaluate downstream resistance to blood flow (Pan et al., 2022).

$$Pulsatility Index = \frac{Peak Systolic Velocity - End Diastolic Velocity}{Mean Flow Velocity} \tag{2.2}$$

2.2.2 Assessing Cerebrovascular Health using TCD

Studies have been carried out to investigate the effectiveness of using TCD as a diagnostic tool for cerebrovascular disease. A study by Roher et al. (2011) used TCD to measure blood flow velocity and pulsatility index in 16 arterial segments and compared values for patients with Alzheimer's Disease (AD), Mild Cognitive Impairment (MCI) and healthy controls. The authors found a decreased mean arterial flow and increased PI in the AD group and believe that TCD can be used as an effective method for predicting whether a patient will develop AD. TCD has also been investigated for assessing cerebral autoregulation due to its ability to monitor flow velocity with a high temporal resolution. However, for flow to be proportional to flow velocity it is assumed that there are no dynamic changes in vessel diameter which limits the accuracy of the method (Panerai, 2009).

2.2.3 Advantages and Disadvantages of TCD

Transcranial Doppler ultrasound has been used to assess cerebrovascular health in many studies as it is a non-invasive and relatively inexpensive method in comparison to other imaging techniques which lends itself to continuous monitoring of blood flow, making it an effective method for checking the progression of disease (D'Andrea et al., 2016). TCD has a high temporal resolution which is one of the main reasons why it is particularly suited to measuring dynamic changes in blood flow, for example when assessing cerebral autoregulation (Markus, 2000).

However there are some limitations to the method. Firstly, TCD cannot be used universally as subjects may lack a suitable acoustic window for insonation, such that the ultrasound beam is unable to pass through the skull. An increased thickness of the temporal bone results in the ultrasound waves to be absorbed and scattered. A study by Itoh et al. (1993) found the rate of successful recording of blood flow velocity in the MCA using TCD decreased with increasing age and this was particularly prevalent in females. TCD is also dependent on the operator's ability to locate the required arteries in the brain and to achieve an accurate angle of insonation. Another key disadvantage of TCD is that it cannot measure pulse wave velocity which is the gold-standard method for measuring arterial stiffness. Cerebral blood flow is indirectly measured by TCD through blood flow velocity. However, the volume of a blood vessel is assumed to stay constant which does not account for dynamic physiological changes in vessel diameter. TCD is also restricted to assessing blood flow in the major cerebral arteries, hence the propagation of pulsatile energy in downstream vessels cannot be investigated. A measure of pulsatility in smaller cerebral vessels would provide a more comprehensive understanding of the deterioration of cerebrovascular health as a result of arterial stiffness.

In summary, TCD provides a method for assessing changes in blood flow velocity which can be indicative of cerebrovascular disease. However to obtain a complete assessment, blood flow should be measured in multiple arteries which is time consuming and heavily dependent on the operator's expertise to obtain accurate measurements of flow velocity.

2.3 Magnetic Resonance Imaging

MRI is a versatile technique which has led to many methods being developed for the purposes of imaging blood flow. A key advantage of MR methods is the ability to obtain whole-brain measures, unlike TCD which is restricted to measuring blood flow velocity in the large arteries. MRI methods for measuring blood flow in vessels can be separated into two categories: inflow methods and phase contrast methods.

2.3.1 Introduction to MRI

The following subsections outline key concepts relating to how MRI works that are relevant to measuring blood flow.

Spin, Magnetic Fields and Resonance

Hydrogen protons are abundant in the human body. Protons possess an intrinsic quantum property called spin angular momentum. Spin, along with electric charge results in the proton having a magnetic moment. In the presence of an external magnetic field, B_0, protons precess around the field. The frequency of precession, ω_0 is known as the Larmor frequency and can be calculated using the Larmor equation (Eq. 2.3) where γ is the gyromagnetic ratio and B_0 is the strength of the magnetic field (Jezzard et al., 2003). Spins either align parallel or anti-parallel to the direction of the B_0 field.

$$\omega_0 = \gamma B_0 \tag{2.3}$$

In quantum mechanical terms, protons exist in one of two energy states in the presence of B_0. The ratio of spins in the low and high energy states can be calculated using the Boltzmann distribution (Eq. 2.4). Here, N_+ and N_- are the low and high energy states respectively, k is the Boltzmann constant, T is the absolute temperature and ΔE is the difference in energy between the two spin states. A magnetic field strength of 1.5 T results in 10 more spins in every 1000000 aligned in the direction of the field and therefore contributing to the MR signal (Jezzard et al., 2003).

$$\frac{N_+}{N_-} = e^{\frac{-\Delta E}{kT}} \tag{2.4}$$

The number of spins aligning parallel to the field is slightly greater than anti-parallel, resulting net magnetization vector, **M**, in the direction of B_0 (Fig. 2.2). This is referred to as the longitudinal, or z-direction. At equilibrium **M** has a longitudinal component, M_z, which is equal to M_0 (Buxton, 2009).

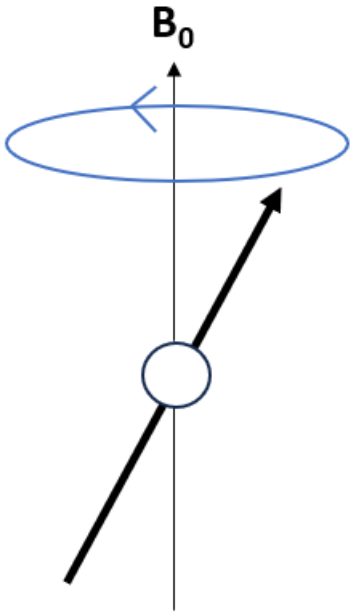

Fig. 2.1 Proton in the presence of an external magnetic (B_0) field. The proton is shown to be precessing around the field due to its spin angular momentum.

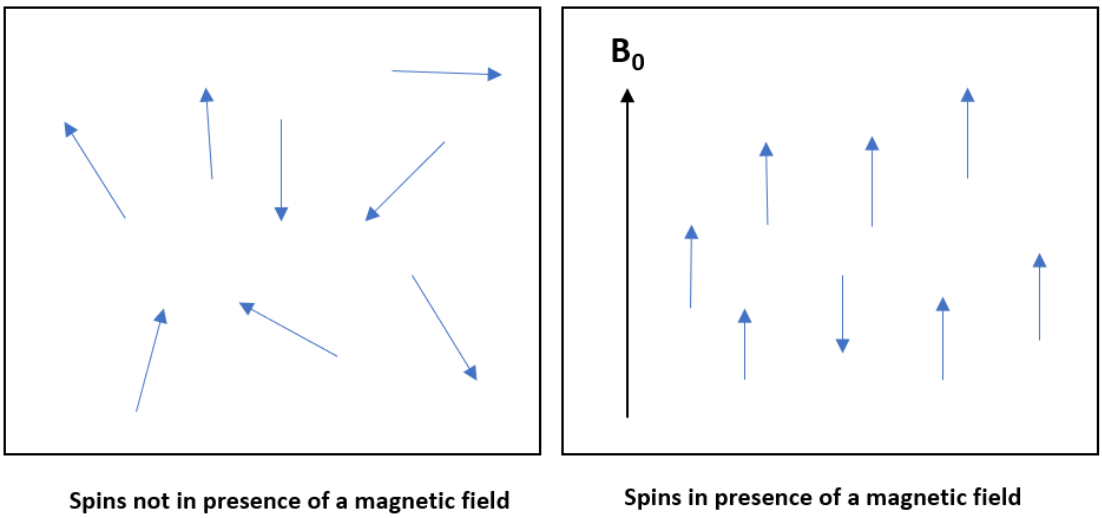

Fig. 2.2 Spins not in the presence of a magnetic field vs. spins in the presence of a magnetic (B_0) field. The proportion of spins aligning parallel to the B_0 field is slightly greater than anti-parallel.

T1 and T2 Relaxation

The net magnetization is tipped out of alignment with B_0 by applying a radiofrequency (RF) pulse which matches the Larmor (resonant) frequency. This is also referred to as the B_1 field. The excitation causes the net magnetization to be tipped into the transverse plane and hence has a transverse component, M_{xy}. When the RF pulse is applied, the net magnetization is rotated towards the transverse plane at an angle known as the flip angle. Therefore using a flip angle of 90°causes **M** to be tipped entirely into the transverse plane. Once the B_1 field is switched off, **M** continues to precess around the magnetic field relaxing back to equilibrium (Currie et al., 2013).Following excitation, **M** has both longitudinal (M_z) and transverse (M_{xy}) components. Precession causes a rotating magnetization in the transverse plane, thus a signal can be detected by the receiver coil.

Longitudinal relaxation, also referred to as T_1 relaxation, describes the recovery of the longitudinal (M_z) component of the net magnetization. Spins release energy to the surrounding lattice. Longitudinal relaxation is an exponential process and is characterised by T_1 which is the time taken for M_z to recover to 63% of its equilibrium value (Eq. 2.5) (Plewes and Kucharczyk, 2012). Recovery of the longitudinal magnetization across time is shown in Fig. 2.3.

$$M_z(t) = M_0(1 - e^{-t/T_1}) \tag{2.5}$$

T_1 can be measured using several methods including an inversion recovery or saturation recovery sequence. In an inversion recovery sequence, a 180° RF pulse is applied to flip the initial longitudinal magnetization in the opposite direction to the B_0 field in all tissues. After some time, known at the inversion time (TI), a 90° readout pulse is applied. As different tissues have different intrinsic T_1 relaxation times, the degree to which the longitudinal magnetization has recovered in different tissues varies at the time when the 90° pulse is applied, introducing a contrast. Varying the inversion time manipulates the image contrast and can be used to null the signal, for example in fat or fluids, by applying the readout pulse at the time when M_z for that tissue or fluid is equal to zero (Bydder and Young, 1985). After repeating the sequence multiple times with different inversion times, T_1 can be estimated by plotting the signal and fitting an exponential curve.

In a saturation recovery sequence, a 90° saturation RF pulse is applied to tip the magnetization into the transverse plane. The longitudinal magnetization starts to recover, and the degree to which this recovers in different tissues depends on the T_1 values for the tissues. After some time known as the repetition time (TR), a second 90° pulse is applied and the signal is acquired. Similarly to inversion recovery sequences, the sequence can be repeated using different TR times and T_1 can be estimated by plotting the signal for different TR values and fitting a curve using Eq. 2.5.

Transverse relaxation, or T_2 relaxation, refers to the decay of M_{xy} over time. Once the RF pulse has been applied, spins which are in phase with each other precess in the transverse plane

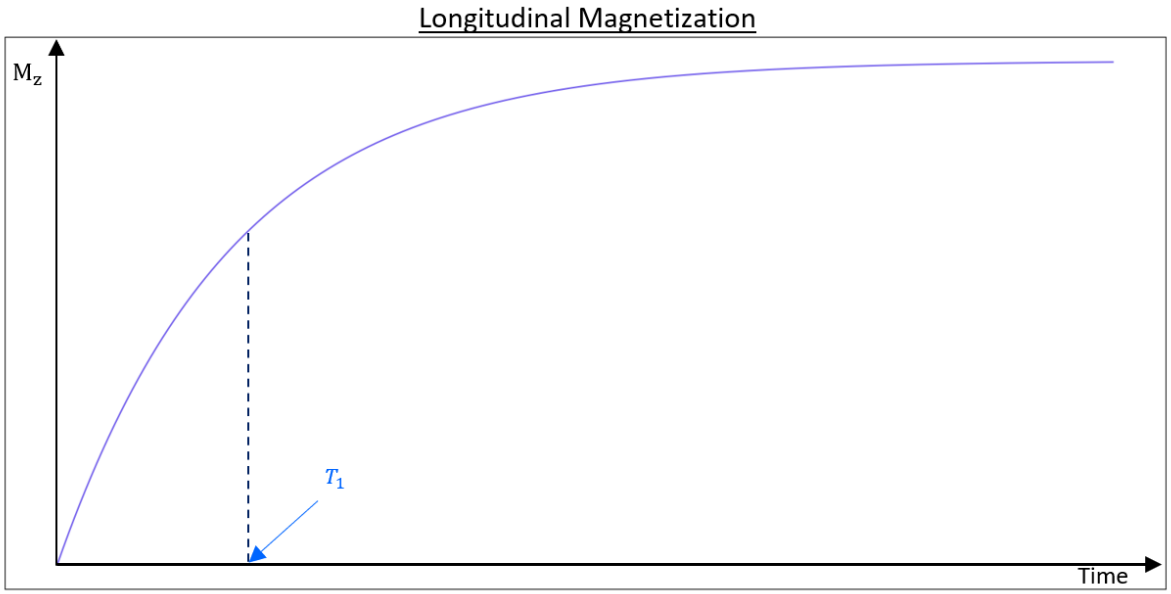

Fig. 2.3 Longitudinal magnetization (M_z) over time.

around the z-axis and the MR signal is generated. Over time, there is a loss in phase coherence which is caused by interactions between the spins leading to spins varying in their precessional frequencies (Plewes and Kucharczyk, 2012). Transverse relaxation is characterised by T_2 which is the time taken for the transverse component of the magnetization to decay to 37% of its value (Eq. 2.6). Decay of the transverse magnetization is shown in Fig. 2.4.

$$M_{xy}(t) = M_0 e^{-t/T_2} \tag{2.6}$$

As well as local fluctuations in the field due to spin-spin interactions, dephasing of spins can occur due to inhomogeneities within the magnetic field, causing spins to experience a different local magnetic field. This is described by T_2^* relaxation (Chavhan et al., 2009). T_2^* is less than or equal to T_2. The relationship between T_2^*, T_2 and T_2' (which represents the relaxation effects solely due to magnetic field inhomogeneities), is defined in Eq. 2.7.

T_2 can be measured using a spin-echo sequence. A 90° pulse is applied to excite the spins, tipping the magnetization into the transverse plane. A 180° refocusing pulse is applied and the signal is acquired at the echo time (TE). T_2 can be measured by acquiring the signal at multiple TE values (Jung and Weigel, 2013). The signal is plotted for different TE values and exponential curve is fitted using Eq. 2.6. Similarly, T_2^* can be measured using a gradient-echo sequence. Again, a 90° pulse is applied to excite the spins and gradients are used to rephase the spins (Tang et al., 2014). The signal is acquired at multiple TEs and a curve is fitted to estimate T_2^*.

Free Induction Decay is the term for the signal generated after a single RF pulse, typically with a flip angle of 90°, is applied. Fig. 2.5 shows the amplitude of the signal decreasing as spins precess out of phase with each other over time.

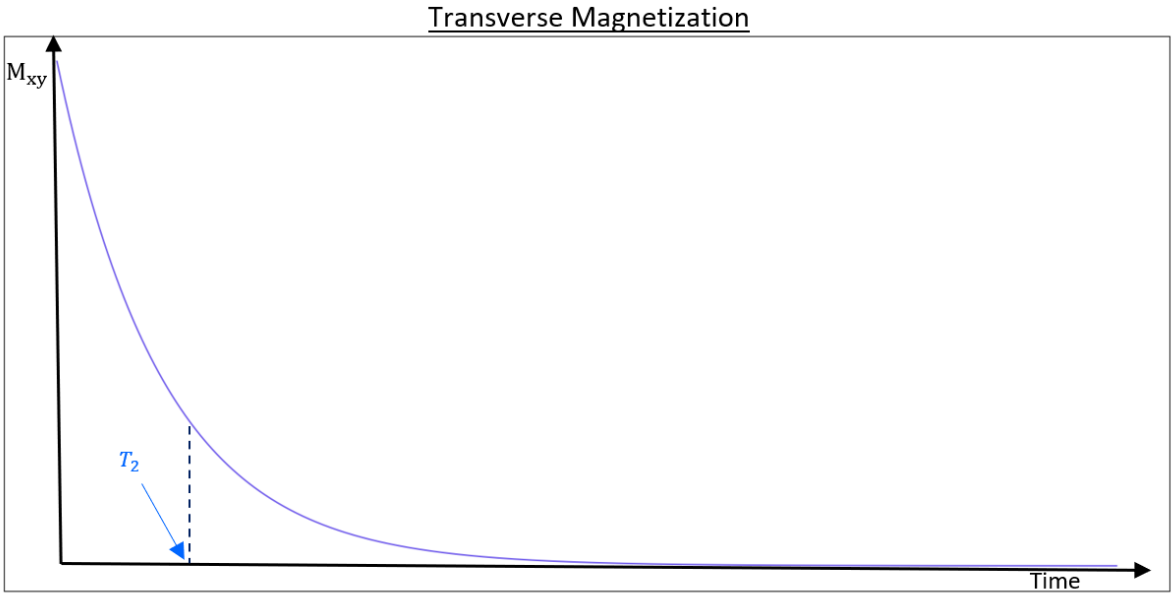

Fig. 2.4 Transverse magnetization (M_{xy}) across time.

$$\frac{1}{T_2^*} = \frac{1}{T_2} + \frac{1}{T_2'} \tag{2.7}$$

T_1-weighted images refer to MR images where the contrast depends on T_1 values for tissues. T_1 is manipulated by changing the TR in a sequence. Repeated RF pulses at a TR much shorter than T_1 cause a different steady state magnetisation. Differences in T_1 then result in varying signal strength. T_2-weighted images are a result of manipulating the TE value in a sequence using longer TRs. The choice of contrast depends on the purpose of the image as each contrast is suited to different clinical applications (Symms, 2004).

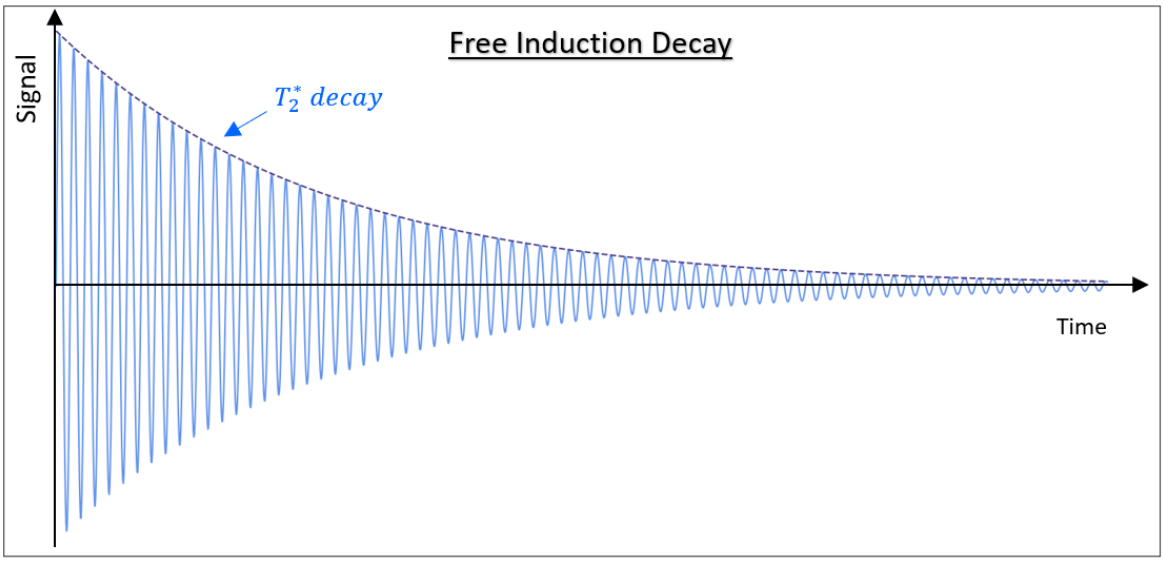

Fig. 2.5 Free Induction Decay signal across time.

Magnetic Field Gradients

Gradient fields are applied in a sequence to obtain spatial information about the MR signal. The gradient fields are combined with the main magnetic field, varying the strength of the field in the direction of the gradient, causing a spatially varying Larmor frequency. Slice selection, frequency encoding and phase encoding gradients are required to encode spatial data to form a 3D image. Gradients are applied in the x,y and z directions to introduce linear variations in the magnetic field along the specified axis (Buxton, 2009).

The resonant frequency depends on the gyromagnetic ratio and the magnetic field strength (Eq. 2.3). Hence, varying the field strength across space results in the resonant frequency varying as a function of spatial position. A gradient applied in the z-axis results in spins with a Larmor frequency that is dependent on their position along the z-axis (Eq. 2.8) (Jezzard et al., 2003). When combined with the B_0 field, the magnetic field will increase in the positive z-direction and decrease in the negative z-direction (Eq. 2.9). This is depicted in Fig. 2.6.

$$\omega(z) = \gamma B(z) \tag{2.8}$$

$$B(z) = B_0 + G_z z \tag{2.9}$$

A slice selection gradient is applied along the slice selection axis which is perpendicular to the plane of the desired slice. This varies the Larmor frequency of the protons along this axis. When a radiofrequency pulse with the same frequency as the resonant frequency of the protons in the slice is applied, only the protons within the slice are excited. The RF pulse is applied as a range of frequencies which excites a slice of a chosen thickness. Therefore, slice thickness can

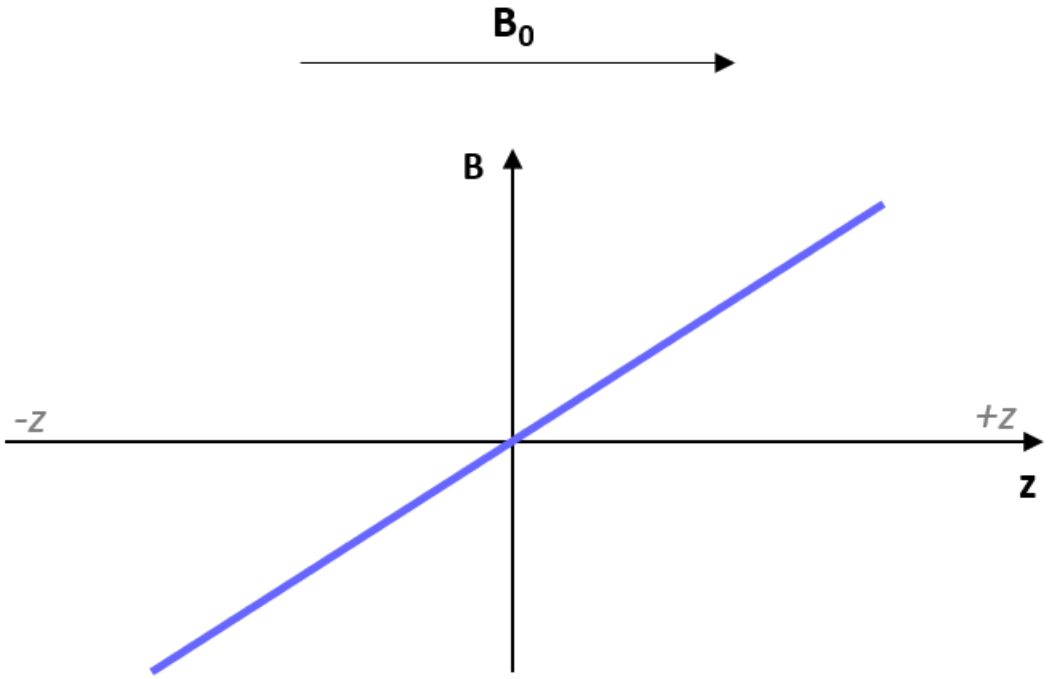

Fig. 2.6 Positive gradient applied in the z direction.

be altered by changing the frequency bandwidth of the RF pulse. Alternatively, slice thickness can be modified by changing the steepness of the gradient field (Currie et al., 2013).

A phase-encoding gradient is used to alter the phase of the spins along the chosen gradient axis, which is perpendicular to the direction of the slice selection gradient. Spins are in phase before the gradient is applied and are out of phase once the gradient is switched off. The phase varies linearly in the direction of the gradient, providing further information about the spatial location (Buxton, 2009).

A frequency-encoding gradient is used to obtain spatial information along the remaining axis and is applied in the orthogonal direction to the previous gradients. The MR signal is measured when the frequency-encoding gradient is applied (Buxton, 2009).

The frequency and phase encoded spatial information is held in a data matrix called k-space. Low spatial frequency information is stored towards the centre of k-space whilst high spatial frequency information is stored in the periphery (Hennig, 1999). The pulse sequence is repeated until all lines of k-space are filled with the same slice selection and frequency-encoding steps, but varying the magnitude of the phase-encoding gradient (Currie et al., 2013).

Sequences

MRI sequences consist of a combination of RF pulses and gradients. The choice of sequence is dependent on the desired image contrast, as well as the speed of acquisition amongst other factors (Jackson et al., 1997). After an RF pulse is applied, the measurable signal decays due

to dephasing. There are two approaches to refocus the signal at the time of measurement, thus increasing the signal to noise. This is called an echo, either a spin echo or a gradient echo.

In a standard Spin Echo (SE) sequence, an RF pulse of 90° is applied to excite the spins, tipping the net magnetization vector into the transverse plane. At this time, M_{xy} is at its maximum value and spins precess in phase with each other. As described above, spins start to dephase over time. To overcome this a refocusing pulse, typically a 180° RF pulse, is applied bringing the spins into phase with each other once again and M_{xy} returns to its maximum value. The signal from this spin echo is measured at the echo time, TE. The refocusing pulse is applied at time TE/2. The sequence is repeated after the repetition time, TR (Jung and Weigel, 2013). Since this sequence refocuses dephasing due to spin-spin interactions, it is a T_2-weighted signal.

Gradient Echo (GRE) sequences differ to Spin Echo sequences as a refocusing pulse is no longer applied to get the spins to rephase. Instead this is achieved by dephasing and rephasing gradients (Hargreaves, 2012). An initial RF pulse, typically with a flip angle less than 90° is used to excite the spins. A negative gradient is then applied to accelerate the dephasing of the spins by introducing a variation in the magnetic field. A positive gradient of equal strength is applied for twice the amount of time to allow spins to rephase. The gradient echo signal is then obtained (Markl and Leupold, 2012). Since this sequence refocuses dephasing due to local field inhomogeneities, it is a T_2^*-weighted signal.

Echo Planar Imaging (EPI) is a fast GE imaging technique which differs to other conventional sequences since multiple lines of k-space are filled after a single RF pulse (Fig. 2.7). This is achieved by employing a rapidly oscillating frequency-encoding gradient and phase "blips" to jump between different frequency-encoding lines in k-space (Schmitt et al., 1998). Since the acquisition speed greatly increases, EPI sequences are well suited to measuring physiological processes (Poustchi-Amin et al., 2001).

Acceleration techniques can be used to speed up the acquisition of MR data. One example is parallel imaging which involves the use of multiple receiver coils with known spatial sensitivities to provide additional spatial information. Employing this technique reduces acquisition time as less phase-encoding steps are required in the sequence, reducing the amount of k-space data that is collected (Deshmane et al., 2012). GeneRalized Autocalibrating Partially Parallel Acquisitions (GRAPPA) is a parallel imaging algorithm which uses the undersampled k-space data to reconstruct the image (Griswold et al., 2002). Partial Fourier reconstruction algorithms can also be used to reduce acquisition time. Data within a section of k-space is acquired, with the remaining data generated from this data owing to the conjugate symmetry of k-space (McGibney et al., 1993).

Image Formation

An inverse Fourier transform (Eq. 2.10) is used to form an MR image by transforming the spatial data stored in k-space in the frequency domain to the time domain (Gallagher et al., 2008).

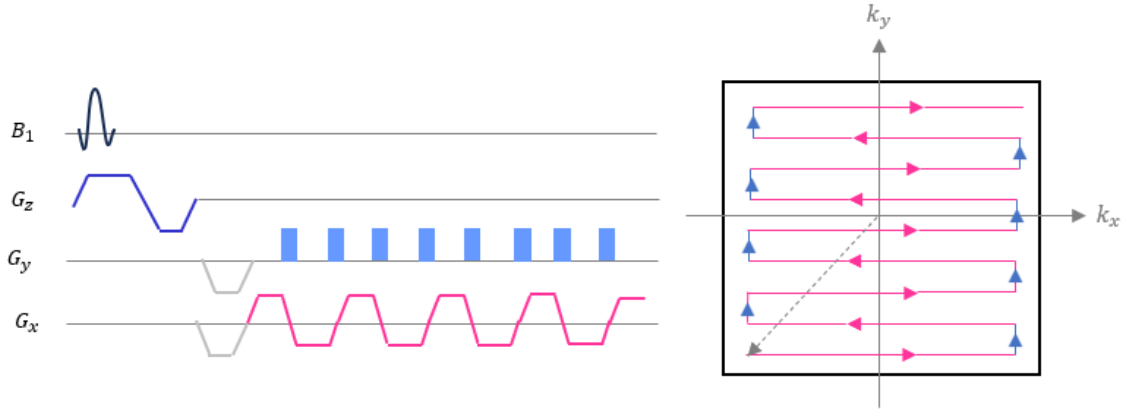

Fig. 2.7 EPI pulse sequence and k-space trajectory diagram. Following the application of an RF pulse, data is acquired with the use of an oscillating frequency-encoding gradient and phase-encoding blips. The frequency-encoding gradient oscillates along the x-axis and the phase "blips" move the trajectory along k_y. Based on figure by Jezzard et al. (2003).

$$f(t) = \frac{1}{2\pi} \int_{-\infty}^{\infty} F(\omega) e^{i\omega t} \, d\omega \tag{2.10}$$

2.3.2 MR Methods for Imaging Blood Flow

MRI methods for imaging blood flow can be split into two categories: inflow contrast methods or phase contrast methods.

Inflow Contrast

The inflow contrast, also referred to as time-of-flight contrast, relies on the partial saturation of stationary spins following the application of multiple RF pulses to provide a contrast between blood moving in vessels and the surrounding tissue. RF pulses are repeatedly applied to the imaging slice using a short TR. Therefore the longitudinal magnetization of any stationary spins is not fully recovered. On the other hand, spins flowing into the imaging plane have not experienced the applied RF pulses and hence contribute more greatly to the MR signal due to having a fully relaxed initial magnetisation. Depending on their velocity, flowing spins may be fully refreshed between repetition times or, if moving more slowly, may experience fewer RF pulses than static spins. To achieve optimal results, the imaging plane should be perpendicular to the vessel of interest (Ferreira and Ramalho, 2014).

One application of inflow contrast techniques is to image blood vessels. Magnetic Resonance Angiography (MRA) is a non-invasive approach to visualising blood vessels which is useful for studying vascular disease. When inflow contrast techniques are used in MRA, the images are

referred to as time-of-flight images in which blood appears bright compared to the surrounding tissue when a GRE sequence is used (Yucel et al., 1999).

Phase Contrast Methods

Phase contrast methods use magnetic field gradients to create a contrast between moving and stationary spins. A simple approach to this is through the use of a bipolar gradient. Application of the first gradient causes a phase shift for the stationary and flowing spins. The second gradient is then applied to restore the phase but will only rephase fully if the spins are stationary. As the flowing spins are moving along the magnetic field gradient and hence their location varies along the gradient, the degree of phase shift will also vary. The phase shift is proportional to the velocity of the flowing spins (Wymer et al., 2020). Velocity encoding gradients can be used to quantify blood flow in vessels.

Quantification of flow in the x,y and z directions in a single sequence is referred to as 4D-flow imaging. These are highly accelerated phase contrast images with encoding in the three directions that can be acquired quickly to give a temporal dimension as well. Studies have demonstrated the feasibility of measuring pulsatility (Holmgren et al., 2020) and pulse wave velocity (PWV) (Björnfot et al., 2021) using 4D-flow MRI. A study by Holmgren et al. (2020) investigated the practicality of 4D-flow MRI to measure pulsatility and compliance in cerebral arteries. Measurements of the pulsatile flow waveform were acquired and values for the flow waveform amplitude and pulsatile volume load and pulsatility index were calculated. The values were compared to those obtained from 2D phase contrast MRI to assess the validity of the method. A limitation of this method was the requirement for low-pass filtering to reduce high-frequency noise which could filter physiological variations, reducing the accuracy of the pulsatility calculations. A study by Björnfot et al. (2021) used 4D-flow to estimate a global measure of PWV in intracranial arteries using flow waveforms sampled at different parts of the vasculature and the distance between the points. The methods highlight the potential of phase contrast methods in measuring important markers of cerebrovascular health. However, averaging the data over multiple phase encoding images limits the accuracy for pulsatility and PWV applications.

DIMAC

Dynamic Inflow Magnitude Contrast (DIMAC) is an MR technique based on the inflow contrast which was developed to measure pulsatile flow in real time (Whittaker et al., 2022). Using a very short TR to suppress signals from static spins and a flip angle of 90° ensures that the signal is sensitive to changes in blood flow velocity. The mechanism is further explained in Fig. 2.8.

The image plane is oriented perpendicularly to the blood vessel. Repeated excitation following a train of RF pulses and a short TR leads to the partial saturation of stationary spins in the tissue surrounding the blood vessel. Spins in the blood vessel flowing into the imaging plane

produce a stronger signal in comparison as they have not experienced the same saturation, i.e., the same number of excitation pulses. Pulsatile flow is measured as the observed MR signal is dependent on the velocity of spins flowing into the imaging slice and the chosen TR. Spins flowing into the imaging slab are excited by RF pulses. The number of RF pulses the spins experience, and therefore the degree of excitation, depends on their velocity. Spins flowing at a greater velocity than the critical velocity, v_c (determined by the slice thickness divided by the TR), experience only one RF excitation and hence their longitudinal magnetization is at equilibrium, thus have no velocity related contrast.

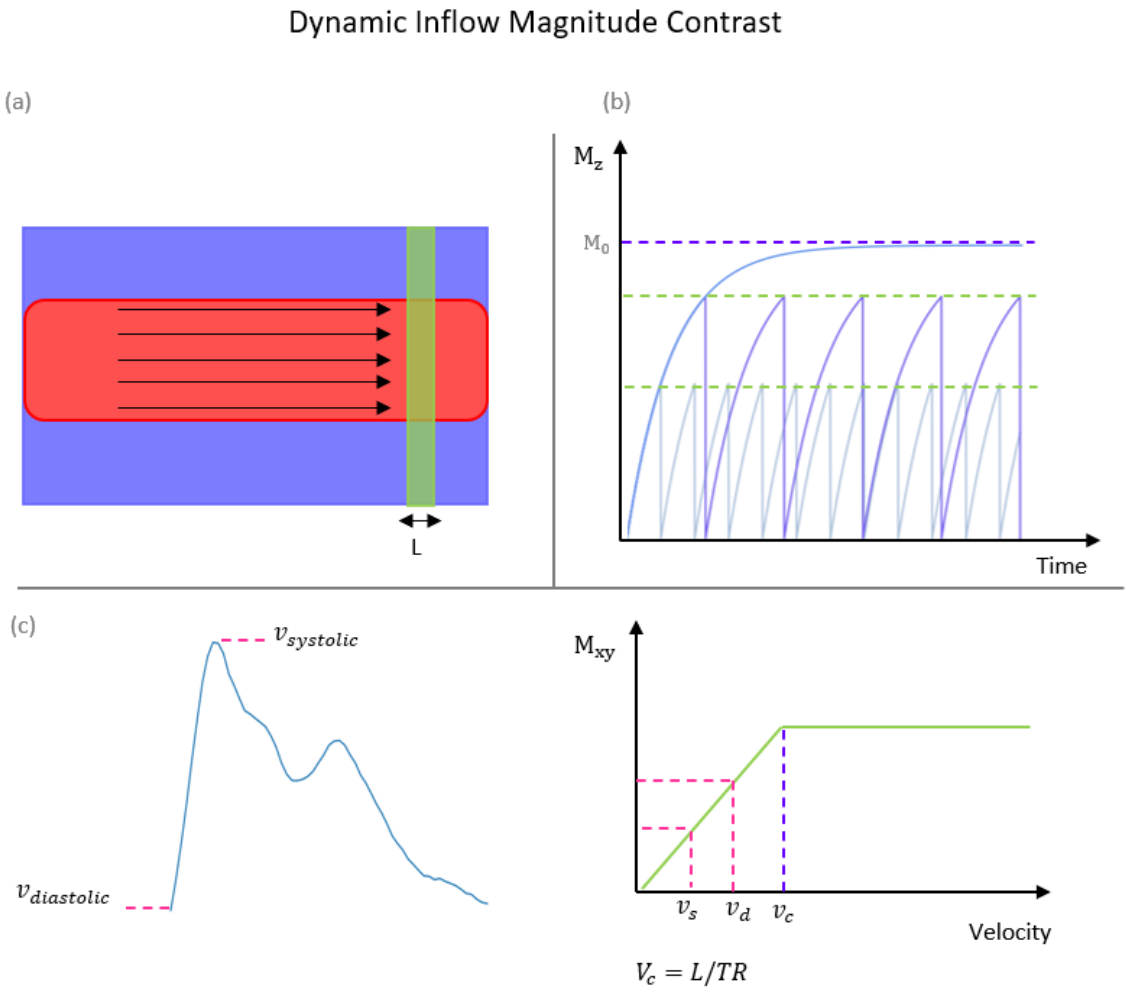

Fig. 2.8 Measuring pulsatile flow using DIMAC. (a) A slice of thickness, L, is selected perpendicularly to the vessel of interest. Blood flow is assumed to have the same velocity across the vessel (plug flow). (b) A short TR results in the partial saturation of stationary spins. Inflowing spins experience fewer RF excitations and so the observed signal is stronger. The recovery of M_z depends on the chosen TR. (c) The observed signal is dependent on the velocity of inflowing spins which allows pulsatile flow to be measured. Spins with velocities greater than the critical velocity, v_c, only experience one RF pulse when flowing through the slice and thus have no velocity related contrast.

One advantage of this technique is that DIMAC can be used to measure pulsatile flow in large arteries as well as smaller vessels (Whittaker et al., 2022). Therefore, pulsatility can be assessed across the cerebral vascular tree which may provide further information about how pulsatility propagates across vessels. This is important for understanding the relationship between arterial stiffness and the buffering of pulsatile energy which is related to the development and progression of cerebrovascular disease. As DIMAC is based on the inflow effect, acquisitions are faster than equivalent phase contrast methods as the addition of velocity encoding gradients are not required. As a result, pulsatile flow is measured with a higher temporal resolution when using DIMAC. By measuring pulsatile flow in two different slices using DIMAC, the time delay and path length between two intracranial vessels such as the ICA and MCA can be used to measure pulse wave velocity.

2.4 Summary

An overview of the key methods used to measure pulsatility and arterial stiffness in cerebral vessels has been presented in this chapter. Despite TCD being a relatively inexpensive and accessible technique, assessment of cerebrovascular health relies on measuring cerebral blood flow indirectly through measures of cerebral blood flow velocity. This requires knowledge of the vessel diameter which is assumed to be constant across time, potentially limiting the accuracy of the measure. Furthermore, TCD is restricted to measuring flow velocity in large cerebral arteries. Consequently, pulsatility cannot be assessed across the vascular tree. Finally, pulse wave velocity cannot be measured using TCD. Due to the limitations of the technique, TCD is not well suited to studying the effect of arterial stiffness on the propagation of pulsatility across cerebral vessels.

MRI is a versatile technique which can be used to measure pulsatile flow in cerebral vessels. Unlike TCD, PWV can be measured using MRI. This is advantageous as PWV is the gold-standard method for measuring systemic arterial stiffness, motivating the need for a brain based measure. Phase contrast methods can be used to quantify blood flow, however obtaining measures of pulsatile flow requires averaging data over cardiac cycles (Pelc et al., 1991). This does not take into account the variability that exists between heartbeats. Additionally, phase contrast methods require the application of a velocity encoding gradient which increases the acquisition time. DIMAC was developed to measure pulsatile flow with very high temporal resolution. By acquiring beat-to-beat pulsatile flow waveforms in cerebral vessels, important measures of arterial stiffness such as pulse wave velocity can be obtained, providing a specific assessment of the health of blood vessels in the brain.

Pulsatile flow waveforms in the ICA and MCA can be used to obtain estimates of compliance and pulse wave velocity which are important indicators of arterial stiffness. Data collected in these vessels using DIMAC will be used in the model to obtain estimates of vessel compliance by comparing shape changes in simulated flow waveforms with expected changes seen in the DIMAC data.

Chapter 3

Existing Models of Blood Flow

Chapter Overview

Existing models of blood flow may be categorised as 0D, 1D, 3D or multi-scale models. There are advantages and disadvantages to each approach, and the choice of method depends on the purpose of the model. The aim of the computational model developed in this thesis is to simulate dynamic pulsatile flow in a branched network of brain vessels from the large arteries to the veins to better understand the consequences of pulsatility and arterial stiffness, using the simplest approach possible. In this chapter, an overview of each type of model will be given, along with some examples of existing models of blood flow. The aims of the computational model described in this thesis will be introduced, along with an explanation of the key models used in the development of this model.

3.1 Introduction

3.1.1 Criteria for a Blood Flow Model

A dynamic model of pulsatile blood flow could provide a powerful tool to improve understanding of the deterioration of cerebrovascular health with age and disease. To model pulsatile flow accurately, it is important to account for local changes in blood flow across a network of vessels resulting from changes in blood volume in compliant vessels, as a response to changes in blood pressure. Modelling dynamic flow is important for understanding changes in flow behaviour across time in relation to vessel compliance, and how variations in flow in one section of the network may influence the rest of the network. Furthermore, a model of pulsatile blood flow could be used alongside pulsatile flow data acquired with MRI to obtain estimates of compliance and pulse wave velocity in intracranial vessels, both of which are important markers of cerebrovascular health. Simulating flow waveforms across a network could also provide estimates of flow behaviour in smaller vessels which can't be easily measured with current imaging methods.

Modelling pulsatile flow across a vascular network requires the use of multiple vessels with different properties. To construct a large enough network of vessels to model pulsatile flow from the arteries to the veins in an anatomically realistic way quickly becomes complicated, requiring large amounts of computational power to run. To alleviate the high computational costs required for a realistic and complete network, a more simplistic network may be constructed. The model developed in this thesis aims to simulate dynamic flow across a network of vessels in the brain consisting of arteries, microvessels and veins in order to better understand the consequences of flow pulsatility and arterial stiffness. To achieve this, elements of existing models were used to construct this model using the simplest approach possible.

3.2 Existing Models

Existing models of blood flow may be categorised as either 0D, 1D, 3D or multi-scale coupled models depending on the complexity of the underlying equations (Korte et al., 2024). Each type of model has strengths and limitations and the choice of model is determined by its application. An overview of each type of model is provided in the following subsections.

3.2.1 Zero-Dimensional Models

Zero-dimensional models were developed as a simplified approach for modelling blood flow through the heart and the vessels by treating the system as one or more compartments. In this category of models, the relationship between pressure, P, flow, F, and resistance, R, is analogous to an electric circuit, such that the flow through a vessel can be calculated by dividing the pressure gradient, ΔP, by the resistance to flow (Eq. 3.1). The change in blood volume, V, in a compartment per unit time is equal to the the difference between the flow into the compartment, F_{in}, and the flow out, F_{out} (Eq. 3.2). Lumped parameter/compartmental models are categorised as 0D models (Shi et al., 2011).

$$F = \frac{\Delta P}{R} \tag{3.1}$$

$$\frac{dV(t)}{dt} = F_{in}(t) - F_{out}(t) \tag{3.2}$$

Lumped parameter models characterise sections of the vascular network into compartments. The 2-compartment Windkessel model, developed by Otto Frank in 1899, is one of the earliest attempts to model the behaviour of the pressure wave across the arterial system using this type of model. Consisting of a resistance compartment to represent the peripheral resistance resulting from downstream arteries and arterioles and a capacitance compartment to take into account the storage capacity of the large elastic arteries (i.e. compliance), the 2-compartment Windkessel was used to model the shape of the pulse pressure across the cardiac cycle (Westerhof et al., 2009).

Further developments of the Windkessel model were made with the addition of compartments to improve accuracy. The 3-compartment Windkessel model includes a compartment to represent the resistance due to the aorta and the 4-compartment Windkessel model includes an inductor compartment to represent inertia of blood flow (Westerhof et al., 2009). RLC models incorporating resistance (R), capacitance (C) and inductance (L) consider resistance to blood flow, vessel elasticity and blood inertia and therefore may be used to capture the effects of pulsatility and wave propagation. Values for R, C and L depend on the geometry of the vessel and the wall mechanics and can be calculated using Eqs. 3.3, 3.4 and 3.5 respectively (Korte et al., 2024). Here, η is the blood viscosity, l is the length of the vessel, d is the diameter of the vessel, r is the vessel radius, E is the elasticity module, h is the vessel thickness and ρ is the fluid density.

$$R = \frac{128\eta l}{\pi d^4} \tag{3.3}$$

$$C = \frac{3\pi l r^3}{2Eh} \tag{3.4}$$

$$L = \frac{9\rho l}{4\pi r^2} \tag{3.5}$$

0D models can represent the entire system or sections of the system such as the arterial tree. Applications include studying conditions such as arterial hypertension by increasing the resistances of compartments, and simulating the effect of occlusion on blood flow in intracranial arteries (Liu et al., 2020). A 0D model by Abdi et al. (2013) aimed to model the pressure waveform in vessels in the Circle of Willis in both normal and pathological (e.g stenosis) conditions using resistance, capacitance and inductance components. The model simulated pressure changes in arteries in the Circle of Willis after increasing the resistance in the internal carotid artery, highlighting how changes in vessel properties can impact the pressure and flow dynamics in downstream vessels.

Some advantages of 0D models include the simplicity of solving the governing equations which require less computational power compared to the higher dimensional methods and the ability to model behaviour of the cardiovascular system on a global scale. However, one key disadvantage of these models is that they are not suited to modelling the propagation of the pressure wave and the associated haemodynamic changes across the vessels (Liu et al., 2020). As pressure, volume and flow are assumed to be uniform and constant across a compartment, 0D models are not the most appropriate for simulating local dynamic changes in flow in a network of vessels. For this reason, more complicated 1D and 3D models may be favoured, especially when modelling pulse wave propagation along a vessel or vascular network (Liu et al., 2020).

3.2.2 One-Dimensional Models

One-dimensional models of blood flow were developed to model haemodynamic changes across vessels in a single dimension. As blood flow is only considered in one dimension, the complexity

of the governing equations can be reduced to a set of partial differential equations. The resulting equations require less computational power when compared to more complex 3D models. A key assumption used in 1D models is that blood flow does not vary across the cross-sectional area of the vessel, and instead only varies across the length of the vessel. Following this assumption, the Navier-Stokes equations can be simplified to a linearised version to model blood flow across the length of the vessel (Liu et al., 2020). The simplified mass and momentum conservation equations used in 1D models are shown in Eqs. 3.6 and 3.7 respectively. Here A is cross-sectional area of the vessel, Q is flow, P is pressure, ρ is blood density, K_R is blood resistance and z is the length along the vessel axis (Korte et al., 2024). To solve the system, an equation that indicates the material property of the vessel wall and relates vessel area to pressure is required. An example of this type of equation is shown in Eq. 3.8 where E is Young's modulus, σ is the Poisson ratio, r is the radial coordinate, and P_0, h_0 and A_0 are reference values for pressure, wall thickness and area respectively (Liu et al., 2020).

$$\frac{\delta A}{\delta t} + \frac{\delta Q}{\delta z} = 0 \tag{3.6}$$

$$\frac{\delta Q}{\delta t} + \frac{\delta}{\delta z}\left(\frac{Q^2}{A}\right) + \frac{A}{\rho}\frac{\delta P}{\delta z} + K_R\frac{Q}{A} = 0 \tag{3.7}$$

$$P - P_0 = \frac{Eh_0}{r_o(1-\sigma^2)}\left(\sqrt{\frac{A}{A_0}} - 1\right) \tag{3.8}$$

1D models of blood flow may be favoured over 0D models when modelling pulse wave transmission (Shi et al., 2011). A 1D model developed by Alastruey et al. (2007) simulated flow and pressure waveforms in the largest arteries in the Circle of Willis to better understand collateral pathways and vessel occlusion. The model generated pressure and flow waveforms for a number of cerebral arteries to compare the effect of occlusion in different vessels, however neglected mechanisms such as vasodilation and vasoconstriction.

Simulating pressure and flow across a vessel or vascular network requires the use of more complex equations, incorporating changes across the length of the blood vessel. Hence 1D models can more accurately represent flow dynamics in comparison to more simplistic 0D models. While higher dimensional models can also provide information on pressure and flow characteristics, taking into account more complex flow patterns such as turbulence, this is often limited to a section of the vessel due to high computational demands. Therefore 1D models of blood flow may be favoured when assessing changes in pressure and flow across a larger network of vessels.

3.2.3 Three-Dimensional Models

The Navier-Stokes equations (Eq. 3.9 & 3.10) are used in three-dimensional models to simulate the local flow field. Eq. 3.9 represents the conservation of mass, where u is the blood velocity. Eq. 3.10 is the momentum equation where ρ is blood density, u is blood velocity, p is pressure, μ is blood viscosity and f is the body force (Liu et al., 2020). With the use of appropriate boundary conditions, the Navier-Stokes equations are used in 3D models to predict complex flow patterns such as turbulent flow and this is particularly useful at vessel bifurcations (Liu et al., 2020). Furthermore, 3D models of blood flow are used to provide more accurate information for better surgical planning. 3D models require more complex vessel geometry and greater computational power is needed to solve these equations (Korte et al., 2024). As a result, these models are better suited to studying local changes in flow, such as a single vessel, as opposed to a large network of connected vessels.

$$-\nabla u = 0 \tag{3.9}$$

$$\rho\left(\frac{du}{dt} + u \cdot \nabla u\right) = -\nabla p + \mu\nabla^2 u + f \tag{3.10}$$

A model by Ren et al. (2015) was developed to investigate the collateral capacity of the Circle of Willis and its effect on perfusion with a range of anatomical variations in the posterior circulation. 3D models were reconstructed from magnetic resonance angiography (MRA) data and finite element analysis was used to solve the Navier-Stokes equations to simulate blood flow. The use of a 3D model allowed for more complex flow patterns such as secondary flows, usually observed at vessel bifurcations to be simulated, increasing the accuracy of the haemodynamic outputs. This is useful for clinical applications such as evaluating a patient's risk of stroke as a result of an incomplete Circle of Willis and selecting the most appropriate treatments for vessel occlusion. However, to reduce the computational power required to run complex 3D simulations and to simplify the overall governing equations, vessels were treated as rigid which neglected the influence of vessel compliance on flow. By focusing on the larger arteries in the Circle of Willis, peripheral resistance in the downstream microvessels was also simplified.

3.2.4 Multi-Scale Coupled Models

Multi-scale models of blood flow involve the coupling of either 0D, 1D or 3D models, with the lower scale models often used to supply appropriate boundary conditions to 3D models (Korte et al., 2024). The type of model can vary across sections of the chosen vasculature, resulting in the most appropriate model being used for each part of the network. A model by Xiao et al. (2013) simulated flow within a deformable full-body arterial network, combining 0D, 1D and 3D models. 3D models were used to capture complex flow patterns such as turbulence at vessel

bifurcations, whereas 1D models were used to simulate pressure and flow wave propagation along the length of the arteries. Simplified 0D models were used to describe the peripheral resistance of the smaller downstream arteries.

3.2.5 Further Applications of Blood Flow Models

Models have also been developed to simulate local changes in blood flow as a way of better understanding the Blood Oxygenation Level Dependent (BOLD) response. The Balloon Model by Buxton et al. (1998) is an early example of this type of model, which aimed to understand the changes in blood flow and volume following neural activation. Here, the venous compartment is treated as a balloon which can expand to accommodate output flow from the capillaries.

A model by Piechnik et al. (2008) was developed to study the relationship between cerebral blood flow and cerebral blood volume to better understand vascular reactivity. The network used in the model was constructed with larger arteries and veins in addition to the microvessels. Vessels were grouped into compartments with different compliance properties to take into consideration the non-linear relationship between blood flow and volume across the network. Understanding vascular reactivity is useful for improved interpretation of the BOLD signal.

3.2.6 Comparison of Models

The category of model used to simulate blood flow in the brain is highly dependent on the purpose and application of the model. While simplistic zero-dimensional models are limited to investigating flow on a global scale, they may be used in conjunction with more complex models to provide appropriate boundary conditions. One-dimensional models can be used to model changes in pressure and flow along a vessel, and are especially useful when modelling flow across a larger network as they require less computational power to run in comparison to 3D models. Three-dimensional models are most appropriate when modelling complex geometries and flow patterns and can therefore simulate flow in blood vessels realistically. However, 3D models are greatly limited by computational inefficiency, making large-scale models less feasible.

3.3 Key Existing Models

The models summarised in the following section are key to the development of the model described in this thesis. An overview of the Delayed Compliance Windkessel model by Mandeville et al. (1999) and the Vascular Anatomical Network (VAN) model by Boas et al. (2008) will be provided.

3.3.1 Delayed Compliance Windkessel Model

A Windkessel model was developed by Mandeville et al. (1999) to study the temporal dynamics between CBF and CBV in order to better understand the BOLD signal. Previous models such as the balloon model developed by Buxton et al. (1998) also attempted to understand changes across CBF and CBV following neural activity, however may be considered less accurate as it is assumed that changes in blood flow and volume in the venous compartment are instantaneous. The concept of a Windkessel was applied to the post-arteriole vessels in this model to represent the flow of blood across the venous compartment over time, taking venous compliance and the associated changes in venous volume into account. The model aimed to investigate the haemodynamic response related to the BOLD signal and the coupling of cerebral blood flow, blood volume and oxygen metabolism.

The venous compartment was treated as a Windkessel, incorporating compliance to accommodate increased blood volume in the compartment and create a delay in the corresponding change in flow. This is important when modelling the haemodynamic response function. Windkessel volume varied passively in response to changes in pressure following changes arteriole dilation and contraction. The relationship between pressure and volume is shown in Eq. 3.11, where V is volume, A is a constant, P_{w} is the pressure across the Windkessel and β is the compliance parameter. The power law equation characterises the non-linear relationship between pressure and volume, representing the elasticity of blood vessels.

$$V = AP_w^{1/\beta} \tag{3.11}$$

3.3.2 Vascular Anatomical Network Model

Network models were developed as a method of progressing beyond the lumped parameter and equivalent electrical circuit models consisting of a small number of compartments to a more realistic representation of the anatomy and connectivity of the cerebral vasculature. A key benefit of a network model is the ability to compare flow across different sections of the vasculature.

The VAN model by Boas et al. (2008) was developed to investigate dynamic vascular changes and the oxygen response to neural activity to better understand the BOLD signal. To model pressure and flow along the microvessels, a network consisting of arterioles, capillaries and venules was constructed, with each vessel branching into two vessels up to the capillaries. The remaining section of the network was formed of a series of converging venules, ending the network with a single vessel. Using the Poiseuille equation (Eq. 3.12), resistance can be calculated for a vessel with diameter, d, length, l, and blood viscosity, η. To calculate the pressure distribution across the network, i.e. the pressure at the start of each level of vessels, and the corresponding flow through each vessel, a system of linear equations was formed using Eq.3.13. Flow was assumed to be split equally between all vessels within a level in steady state.

$$R = \frac{128\eta l}{\pi d^4} \tag{3.12}$$

$$\Delta P = F \times R \tag{3.13}$$

The non-linear relationship between pressure, P, and volume, V, in compliant vessels is based on the relationship used in the Windkessel model by (Mandeville et al., 1999) and is shown in Eq. 3.14. The compliance parameter is represented by β. The constant, A_0, is calculated using the initial pressure, P_0 and volume, V_0 and P_{IC} is the intracranial pressure. The equations are explained in further detail in Chapter 4.

$$\begin{aligned} V &= A_0(P - P_{IC})^{\frac{1}{\beta}} \\ A_0 &= \frac{V_0}{(P_0 - P_{IC})^{\frac{1}{\beta}}} \end{aligned} \tag{3.14}$$

The VAN model (Boas et al., 2008) may be categorised as a 0D model in its steady state form due to the use of electrical components to simplistically construct the network. However, as the network consists of levels of individual vessels it is possible to simulate flow across different parts of the network. Furthermore, as levels are split into individual vessels, advancing on conventional lumped parameter 0D models, it is possible to treat each vessel independently, which in theory could introduce local variations in vessel properties within the network. In that respect, the VAN model has the potential to act as a 1D model if appropriate modifications are made.

3.4 Outline of Model and Rationale for Approach

The model described in this thesis was developed using the simplest approach possible while incorporating dynamic flow and vessel compliance. Key aims of the model include investigating changes in shape in the pulsatile flow waveform from the arteries to the microvessels in relation to vessel compliance and fitting pulsatile DIMAC MRI data to obtain estimates of compliance and pulse wave velocity. The VAN model by Boas et al. (2008) created a network of arterioles, capillaries and veins using a simple branching pattern and was therefore used a base for this model. The network structure was also chosen as each vessel can be treated independently, allowing properties to vary in different vessels. This is useful when modelling the effects of vessel diseases such as arteriosclerosis. The network was modified by splitting each vessel into a number of individual segments, therefore introducing a method to track pressure and flow in the network across time. By introducing a time component and tracking variables in individual segments at each time step, the model progresses beyond the lumped parameter compartmental

concepts typically used in 0D models while still offering a simplified approach to modelling local changes in blood flow in a vascular network in the brain. A detailed explanation of the development of the model is given in Chapter 4.

While more complex 3D models have been constructed to simulate flow realistically in vessels in the Circle of Willis, this approach was not necessary for the purpose of our model. The pulsatile flow waveforms to be incorporated into this model were obtained in large vessels using 2D MRI. A 3D model would not be required for this purpose as the MRI data does not provide the spatial information within the vessel and for that reason a lower dimensional model is sufficient. In addition, 3D models are best suited to simulating flow within a vessel and would not be computationally feasible for following the pulse wave along a network. The model was developed with the aim of simulating flow from the large arteries to the capillaries in compliant vessels. Comparing the shape of the flow profile across vessels is useful for understanding how arterial stiffness affects the dampening of pulsatility across the network.

3.5 Summary

Computational models have the potential to be an effective tool in aiding the study of vascular health and its relationship with brain health. Previous studies by Boas et al. (2008) and Piechnik et al. (2008) have demonstrated that it is possible to model blood flow across a network of cerebral vessels, advancing on earlier Windkessel models which lumped sections of the vasculature into compartments. However, existing 0D and 1D models have mainly focused on simulating flow globally in steady state and are therefore limited in their ability to model local changes in flow due to the omission of blood volume changes caused by vessel compliance. Higher-dimensional models were developed to obtain more realistic flow profiles for blood travelling through vessels, however are better suited to single vessels instead of larger vascular networks due to the complexity of the equations that need to be solved in these models.

A dynamic model of flow across the cerebrovascular network could help to better understand the dissipation of pulsatile energy. The model developed in this thesis aims to simulate flow across a network of vessels from the arteries to the veins, taking into account pressure-driven volume changes and compliance, using the simplest approach possible. The model will be paired with DIMAC MRI data to estimate useful indicators of cerebrovascular health such as vessel compliance.

Chapter 4

Development of the Model

Chapter Overview

A computational model was developed to study pulsatility across the vascular network to better understand changes in the dissipation of pulsatile energy in the brain as vascular health deteriorates. The Vascular Anatomical Network model by Boas et al. (2008) was chosen as the basis for this model due to the ability to construct a network of branched vessels with different properties such as diameter and length and the addition of a compliance parameter to account for changes in flow in compliant vessels, using a relatively simplistic approach. The VAN model was replicated and modified to obtain flow waveforms across a network of vessels, with the eventual aim of simulating dynamic flow in a network of vessels from the large arteries to the capillaries. This is a crucial development in order to study pulsatile flow, how it traverses a network of cerebral blood vessels and how it is related to arterial stiffness. In this chapter, each stage of the development of the model will be outlined, from the replication of the VAN model to the addition of the time component, and the rationale behind the developments and extensions will be discussed.

4.1 Introduction

A computational model was developed to simulate blood flow in a network of cerebral vessels. The model was based on the Vascular Anatomical Network (VAN) model created by Boas et al. (2008) which simulates flow through a branched network of microvessels. This model was chosen to form the basis of the model detailed below due to its bifurcating branched vessel structure. The model developed in this thesis was designed with the aim of simulating pulsatile flow through a vascular network from the large arteries in the Circle of Willis to the capillaries, in order to investigate the influence of compliance on the dampening of the pulsatile energy across the vascular tree. To achieve this, the VAN model (Boas et al., 2008) was modified in a number of ways. Firstly, a time-varying component was added to the model to obtain

pressure-driven changes in flow across the vessels. Compliance was also incorporated into the model by taking into account changes in volume and resistance following pressure changes. To study the distribution of flow in a network of vessels with different properties, vessels within a branch and within a level of the network were treated independently. The microvascular network from the VAN model (Boas et al., 2008) is replicated here and used in simulations presented in Chapter 5 for the purpose of setting up the model and carrying out an initial validation. The network is extended in Chapter 6 to include the larger arteries and veins to study pulsatile flow across a more extensive network of blood vessels in the brain.

The development of this model was achieved in four stages:

1. replicating the microvascular steady state VAN model (Boas et al., 2008)
2. extending the VAN model (Boas et al., 2008) with the addition of vessel compliance to investigate steady state flow in a single vessel and a small branched network
3. adding a time component to obtain dynamic flow waveforms for a compliant single vessel and small branched network
4. running simulations for the large branched microvascular network used in the VAN model (Boas et al., 2008) with the addition of compliance.

Steady state outputs from our model were compared to the results from the VAN model (Boas et al., 2008) as an initial method of validation.

4.2 Replication of the VAN Model

Blood flow was first simulated in the microvasculature to replicate the method outlined by Boas et al. (2008). A network of multiple arterioles, capillaries and venules of various sizes was arranged in a symmetrical branched pattern, with each vessel splitting into two vessels at every branch point for six branches (Fig. 4.1). Therefore there was a maximum of 64 vessels within a branch level, with vessels from the arterioles to the capillaries decreasing in diameter by 20% at each branch point. Here, a branch level refers to the vessels between branching points. In the first level there is one vessel, in the second there are two vessels and so on. To model the remaining vessels in the network from the capillaries to the venules, vessels converged at every branch point to return to a single vessel, with vessel diameters increasing after each converging branch point. Vessel lengths and diameters were taken from the VAN model along with blood viscosities and used as inputs into the model. Output values for flow, velocity and input pressure were obtained for each level of the network in steady state.

Assuming a steady, laminar flow, values for the vessel length, l, diameter, d and viscosity, η were used in the Poiseuille equation (Eq. 4.1) to calculate the resistance, R, of each corresponding vessel. Due to the conservation of flow, flow was assumed to be split equally between all vessels

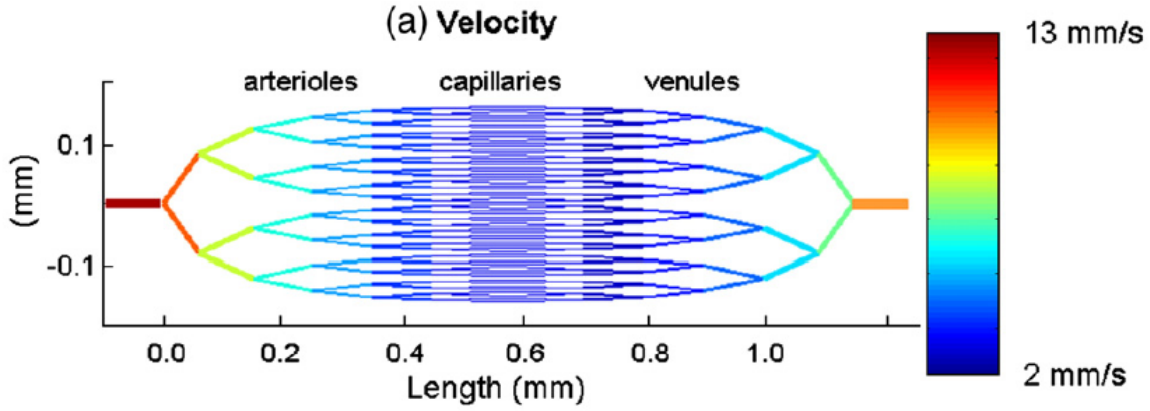

Fig. 4.1 Diagram of the microvascular network used in the VAN model (Boas et al., 2008). The network includes arterioles, capillaries and veins. Vessels branch into two across the arterioles and converge across the venules. Figure taken from Boas et al. (2008).

within a branch level. Using the pressure-flow relationship (Eq. 4.2), a system of linear equations was solved to obtain the pressure distribution across the network and the flow through the vessels for each level. Flow velocity, v, was calculated using Eq. 4.3, where F is the flow and A is the cross-sectional area of the vessel.

$$R = \frac{128\eta l}{\pi d^4} \tag{4.1}$$

$$\Delta P = F \times R \tag{4.2}$$

$$v = F/A \tag{4.3}$$

The pressure distribution along the microvascular network was obtained from the model along with blood flow velocities for vessels in each level and plotted against vessel diameter as shown in Fig. 4.2. Results from this model were in agreement with those presented by Boas et al. (2008).

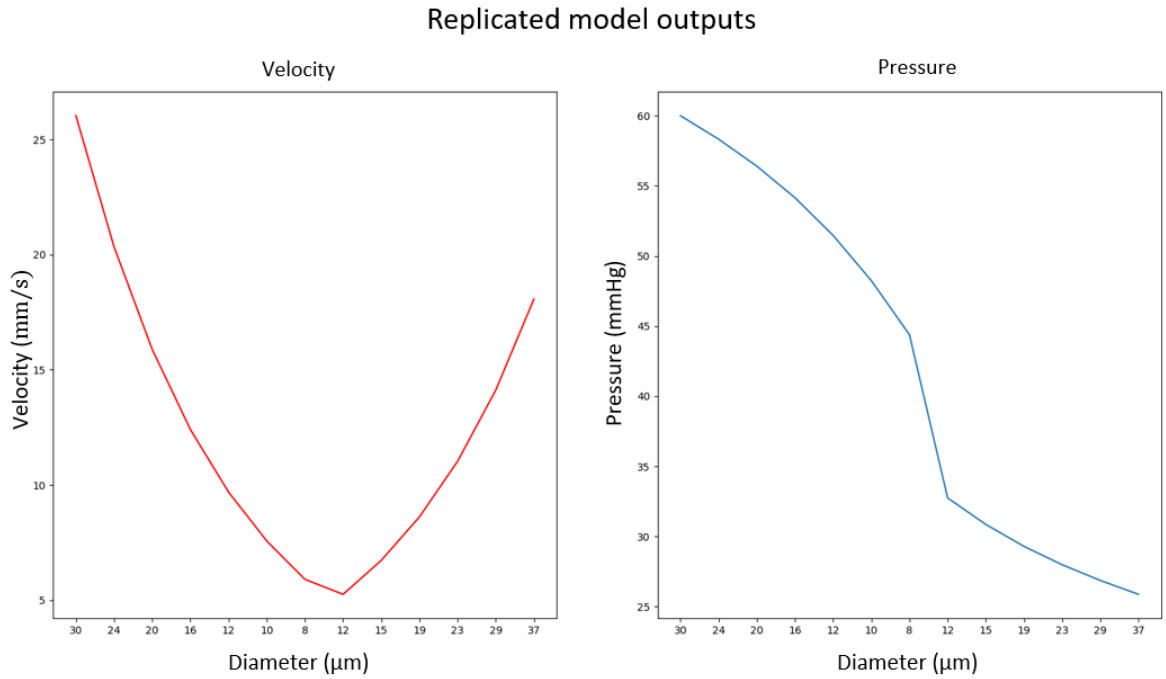

Fig. 4.2 Velocity and input pressure values plotted against vessel diameter in the steady state microvascular network.

4.3 Steady State Models

In zero-dimensional models of blood flow, compliance is typically incorporated into the model using a capacitor to represent the elasticity of vessels and their ability to store blood (Liu et al., 2020). However, this approach is usually applied to model whole compartments, thus neglecting local pressure-driven changes in flow. Another approach is to use a pressure-volume equation which represents the non-linear elasticity of blood vessels. Vessel compliance was incorporated into the model using Eq. 4.4, where β is the compliance, P is the input pressure, V is the vessel volume and P_{IC} is the intracranial pressure. A_0 is calculated using the baseline input pressure, P_0 and volume, V_0 at t=0 (Boas et al., 2008). A compliance value of β=1 represents infinite compliance, with vessel compliance decreasing as β increases.

The power law pressure-volume relationship represents the non-linear elasticity of blood vessels. As pressure increases, the volume increases (i.e. the vessel distends). For a vessel with greater compliance, there is a larger increase in volume for a given increase in pressure. At higher pressures, the increase in volume for a given increase in pressure decreases as vessels resist further expansion (see Fig. 4.3).

$$\begin{aligned} V &= A_0(P - P_{IC})^{\frac{1}{\beta}} \\ A_0 &= \frac{V_0}{(P_0 - P_{IC})^{\frac{1}{\beta}}} \end{aligned} \tag{4.4}$$

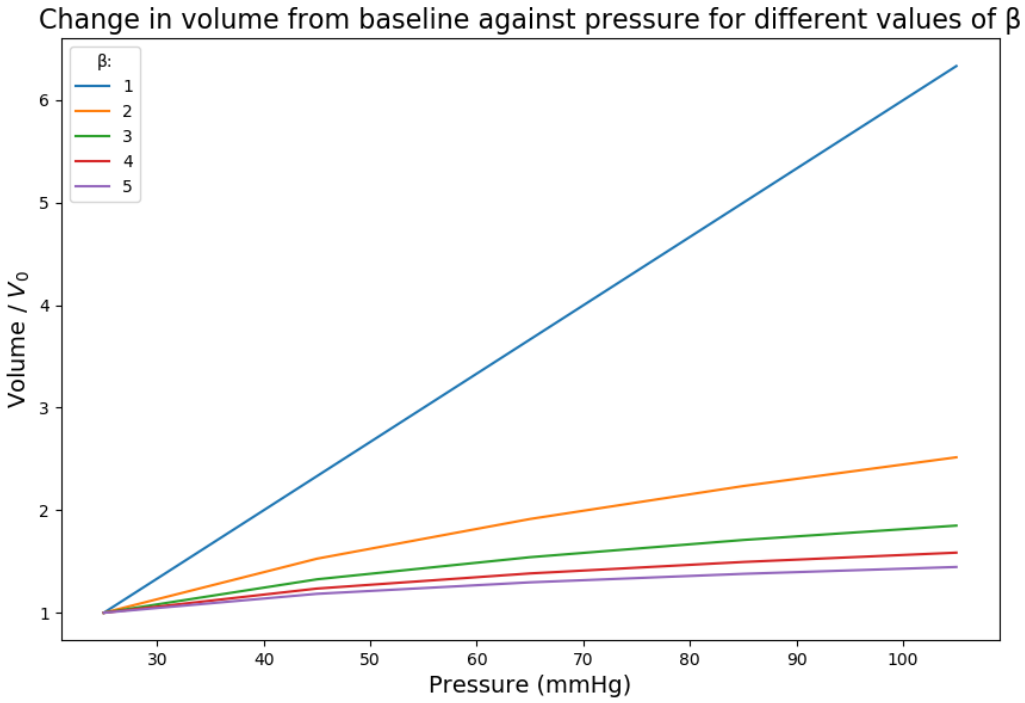

Fig. 4.3 Change in volume from baseline against pressure for β=1, 2, 3, 4 and 5. A compliance parameter value of β=1 represents a linear relationship between volume and pressure which is not realistic for blood vessels. As β increases (and compliance decreases), the volume change for a given pressure change decreases. At lower pressures, there is a greater change in volume compared to higher pressures.

A study by Warnert et al. (2015) used short inversion time pulsed arterial spin labelling (ASL) to estimate arterial compliance in arteries in the Circle of Willis. Changes in arterial blood volume associated with the cardiac cycle were measured and compliance was calculated for the right and left middle cerebral arteries, right and left posterior cerebral arteries and the anterior cerebral artery. Compliance values were reported as a change in volume per mmHg change in blood pressure.

The pressure-volume equations above offer a simple method for incorporating compliance into the model and allow changes in volume to be calculated locally when changes in pressure occur. While 0D models can account for more complex characteristics of blood flow such as vessel compliance and inertia by utilising capacitors and inductors, outputs are representative of the global flow dynamics as vessels are grouped into compartments. In this model, vessels are split into smaller segments, introducing a time parameter and allowing the pressure wave to be tracked across the network. The associated changes in volume and resistance are dependent on the compliance of the vessels and are updated at every time step following a change in pressure. Therefore, local changes in pressure and flow in every segment can be simulated using this approach. The development of the model is described in greater detail in the following sections.

Vessel compliance was added to the steady state models to simulate flow for a single vessel and a small branched network. Pressure changes were applied to investigate instantaneous changes in vessel volume for different compliance values.

4.3.1 Single Vessel

Compliance was initially investigated by modelling flow through a single vessel. Values for the vessel properties were taken from the VAN model (Boas et al., 2008) with vessel diameter initially set as 30.5 μm and vessel length as 100 μm. A value of 2.49 cP was used for the blood viscosity. Resistance to flow in the vessel was calculated using Eq. 4.1 and flow was calculated using Eq. 4.2 with 60 mmHg and 58 mmHg as the input and output pressures respectively.

The single vessel model was used to investigate the effect of pressure changes on volume for a compliant vessel. Pressure was increased by 10, 20, 30, 40 and 50% and the corresponding percentage volume changes were calculated using Eq. 4.4 for β values of 1, 2 and 3 (Fig. 4.4). As expected, the greatest increase in volume for a given pressure increase was for a compliance value of β=1, with increases in volume becoming smaller as compliance decreased.

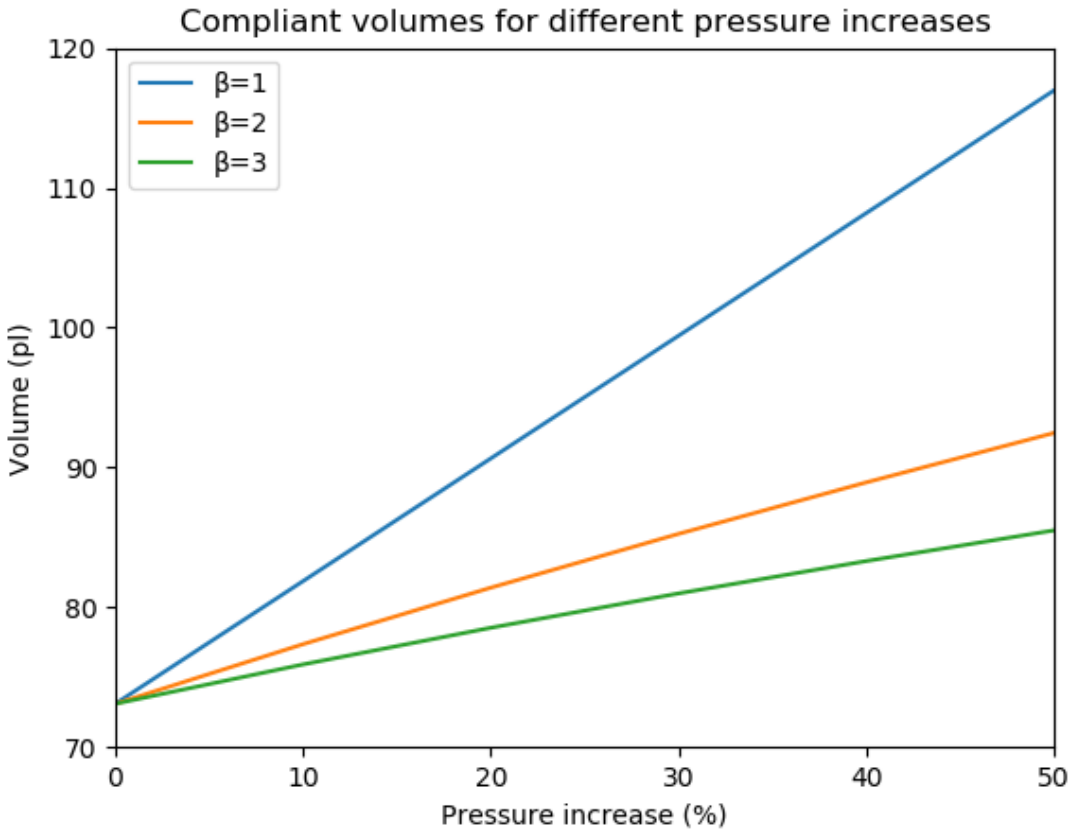

Fig. 4.4 Vessel volumes for percentage pressure increases of 10, 20, 30, 40 and 50% compared across compliance values of β=1, 2 and 3.

4.3.2 Small Branched Network

A small branched network was constructed from a single vessel branching into two vessels and joining to form a single vessel as shown in Fig. 4.5. The 1-2-1 vessel structure was chosen as a simplified approach to modelling flow across a branched vessel structure such as the ICA, MCA and the remaining vessels contributing to the Circle of Willis. The initial aim of this model was to investigate the distribution of flow through vessels with different properties within a branch.

As with the single vessel model, steady state values were calculated using the diameters and lengths of the vessels and the blood viscosity, with values taken from the VAN model (Boas et al., 2008). All vessels were the same length with the diameter of the branched vessels decreasing by 20%. Volumes and resistances were calculated for each vessel and inputted into a 4x4 system of linear equations using Eq. 4.2. A 4x4 system of equations was used instead of the 3x3 system which would have resulted from directly following the method described by Boas et al. (2008) as flow was no longer assumed to be split equally between branched vessels (F2 and F3), therefore vessels could be treated independently.

Compliance was incorporated into the model using the pressure-volume relationship (Eq. 4.4). Assuming an increase in pressure in the first vessel would be experienced by the remaining vessels in the network, corresponding volume changes were calculated for each vessel. For example, following an increase in pressure of 10%, vessel volume becomes $1.1{V_0}^{1/\beta}$ where V_0 is the initial volume of the vessel. Volumes were used to calculate resistances which were substituted into the 4x4 system of linear equations to calculate the pressure distribution across the network and flow through each vessel. Values of β were varied for the two branched vessels.

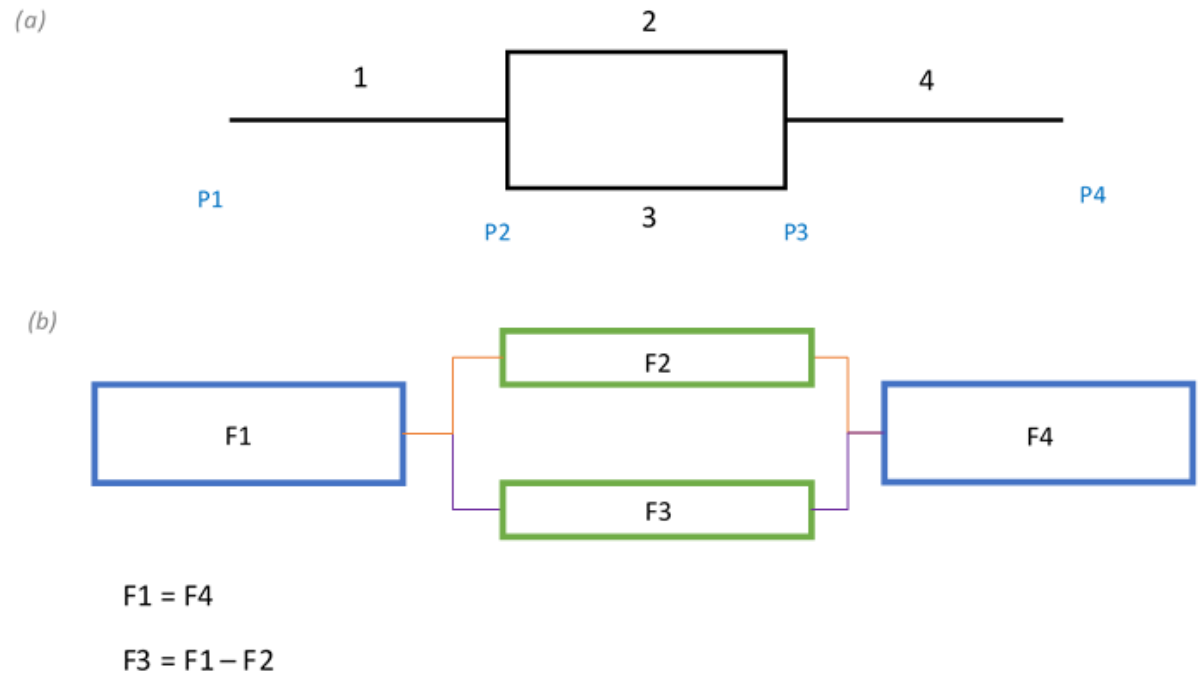

Fig. 4.5 (a) Pressure in relation to vessel segments in the small branched network model, (b) Distribution of flow in the network. Flow values in each vessel are related as described by the equations.

4.4 Dynamic Models

4.4.1 Time-varying Single Vessel Model

The next stage of development was to extend the previous models to explore changes in the vessel network across time. To simulate changes in flow due to changes in pressure and to study the effect of vessel compliance on flow, a pressure wave was introduced to the model. This enabled pressure to vary with time. Several pressure waves, including a sine wave and a step increase, were used as inputs in the model to replicate a pulse wave travelling through a vessel. The pressure waves chosen as inputs at this stage of development were not physiologically plausible, however this was adequate as the main objective was to develop the model and ensure that it was working as expected.

To model instantaneous changes in the properties of compliant vessels, the single vessel was split arbitrarily into 10 segments of equal length. The pressure wave was assumed to move across the vessel one segment per time step, therefore introducing a varying pressure component with time. Values for length and diameter of the vessel and the blood viscosity were taken from the VAN model (Boas et al., 2008). The length of the single vessel was 100 µm and the diameter was 30.5 µm. The value of blood viscosity was 2.49 cP. The length of each segment in the single vessel was 10 µm. Resistance in each segment was calculated using Eq. 4.1. The output pressure for the vessel was fixed at 80 mmHg. Various pressure waves were used as pressure inputs.

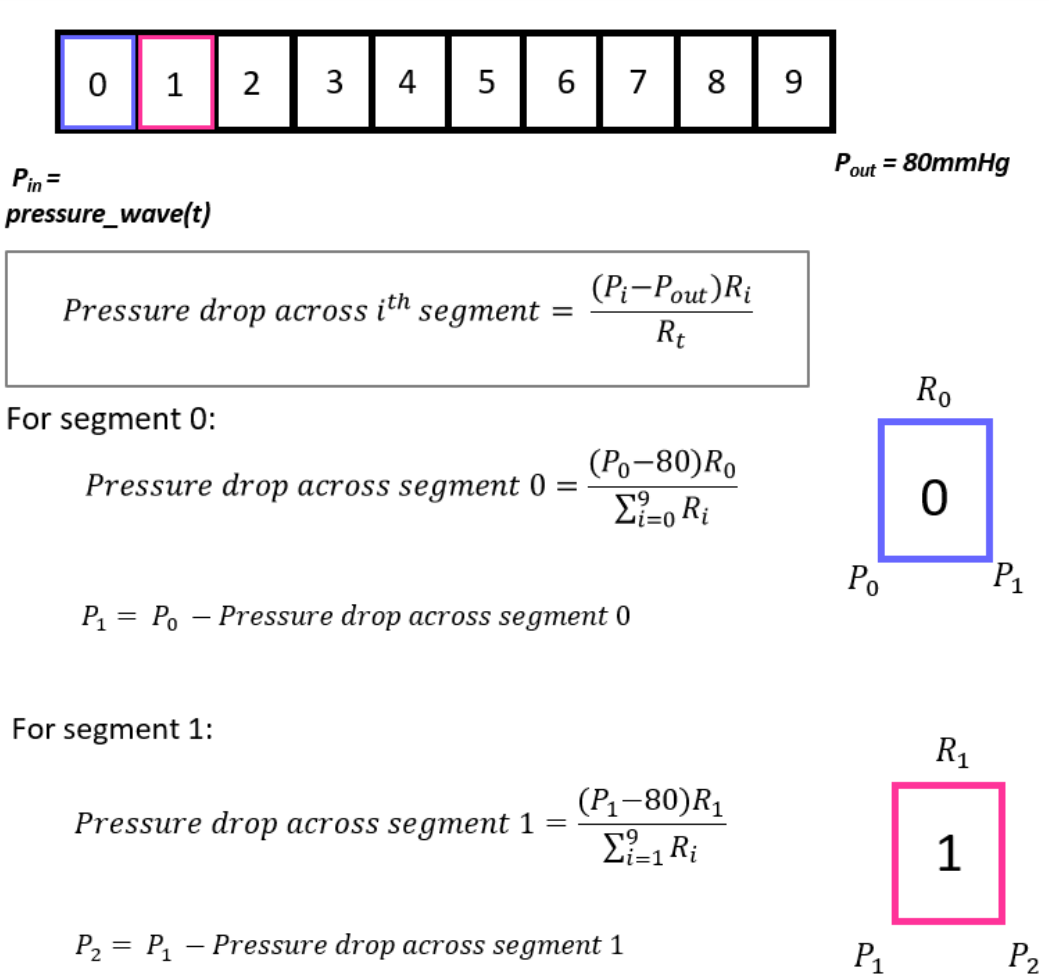

Fig. 4.6 Diagram explaining how pressure was calculated across the segments in a single vessel.

For input pressure at the start of the vessel to reach output pressure at the end, pressure has to decrease across vessel segments. The pressure drop across each segment at every time point was calculated using Eq. 4.5 where P_i is the input pressure for the i^{th} segment, P_{output} is the output pressure for the vessel, R_i is the resistance in the i^{th} segment and R_T is the total remaining resistance from the i^{th} segment to the end of the vessel. The pressure distribution (i.e. the input pressures for every segment) across the whole vessel was updated at every time point, using the pressure output for the i^{th} segment as the input pressure for the $(i+1)^{th}$ segment at the following time point (Fig 4.6). The volume of each segment was calculated using Eq. 4.4 and resistance was calculated using the updated value for volume. Using pressure and resistance, flow was calculated across each segment (Eq. 4.2). Therefore by iterating over time, flow waveforms for every segment were obtained. Values of β were varied to allow for comparisons of flow for different amounts of vessel compliance.

$$Pressure\ drop\ across\ i^{th}\ segment = (P_i - P_{output})\frac{R_i}{R_T} \tag{4.5}$$

4.4.2 Time-varying Branched Vessel Model

The dynamic model was extended to model flow through a branched vessel network, with the initial aim of comparing flow between two branched vessels with different compliance values. This was initially achieved using two simple, branched networks: (i) a single vessel splitting into two smaller vessels (1-2 network) and (ii) a vessel splitting into two smaller vessels and rejoining to form a single vessel (1-2-1 network). Each vessel was split into 10 segments of equal length. Initial input and output pressures at t=0 were set as 80mmHg. Branched vessels were initially modelled to be equal in size.

A pressure wave was inputted into the model and the pressure drop across each of the segments was calculated using Eq. 4.5. Using the pressure out of the single vessel as the pressure input for the branched vessels, flow was calculated in each of the segments at every time step. The pressure wave was assumed to move across a segment at every time step, as with the single vessel model. In the case of the 1-2-1 model, pressures out of the two branched vessels were averaged together and used as input pressure into the single vessel following the branch.

The distribution of flow in a branched (1-2) network consisting of vessels with different compliance values is shown in Fig. 4.7. A sine wave was used as the input pressure wave in this case. The effect of compliance is demonstrated as flow was greater in the more compliant vessel (a_2) across time due to the larger increase in vessel volume following a change in pressure. Therefore more flow was distributed to this vessel.

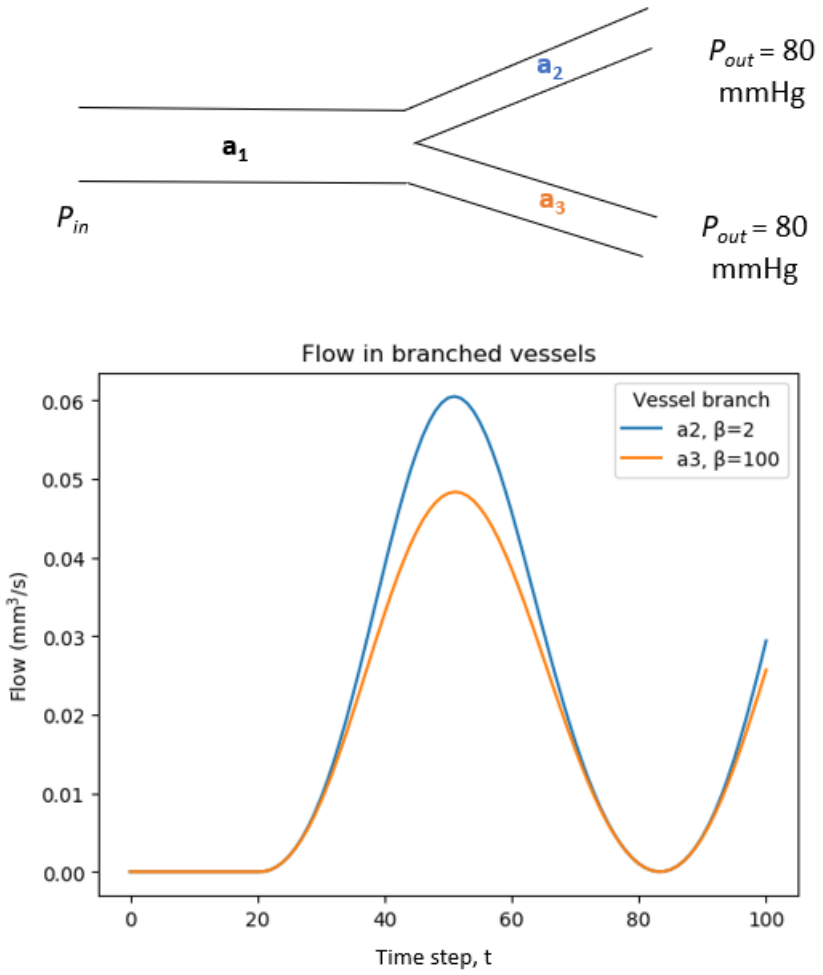

Fig. 4.7 Flow across time compared for two vessels within a branch, a_2 and a_3, with compliance values β=2 and 100 respectively. A sine wave was used as the time-varying input pressure wave in this case.

4.5 Modelling Blood Flow in the Large Microvascular Network

Using a similar approach, the dynamic small branched network model was extended to model flow across the large microvascular model created in the VAN model (Boas et al., 2008). The output pressure distribution and velocity profile were then compared with values obtained from the original steady state model to check that the dynamic simulation had been set up correctly.

4.5.1 Components of the Vessel Network - Terminology

The large vessel network was split into components: levels, branches, vessels and segments as shown in Fig. 4.8. Levels refer to the vessels between each branching point. Here, 14 levels were used to replicate the vessel network used in the VAN model (Boas et al., 2008), numbered from 0 to 13. Levels 0 to 5 represent the arterioles, 6 and 7 represent the capillaries and 8 to 13 represent the venules. Each level consists of either a single vessel or diverging (if in the first half of the network) and converging (if in the second half of the network) branched vessels. Branches are constructed from two equal length vessels. Each vessel was then split into a number of equally sized segments.

Diverging branches were used to represent pairs of vessels across the arterioles and converging branches were used for venules. Two levels in the network were used to represent the capillary level, as this was constructed from pairs of diverging and converging branches. Single vessels were used to represent the first arteriole and last venule in the network. For the purpose of obtaining initial results for the pressure distribution and velocity profile outputs, all vessels were split into 10 segments of equal length, with an initial input and output pressure of 25 mmHg at t=0. Diameter and length values taken from the VAN model (Boas et al., 2008) were used as inputs for each vessel, with the volume and resistance for each segment in the vessel calculated from these values. Compliance was initially set as β=100000 to ensure that the vessel volume and associated resistance would not change over time, hence allowing flow to be modelled in steady state as in the VAN model. A pressure wave consisting of constant values of 60 mmHg was used as an input into the model, and was assumed to move across the network one segment per time step. The pressure drop across each segment was calculated using the remaining resistance in the network (Eq. 4.5) at every time step and the pressure distribution across the whole network was updated.

The pressure distribution in steady state was obtained from the input pressure for vessels in each level at the last time point in the simulation. This was after the pressure wave had travelled across the whole network and values were constant. Flow was calculated for each vessel using the pressure gradient and the resistance (Eq. 4.2). Flow velocity was calculated from the flow and cross-sectional area of the vessel using Eq. 4.3. Initial simulations were run assuming that every vessel in a branch had equal properties. However, the model also permits vessel properties

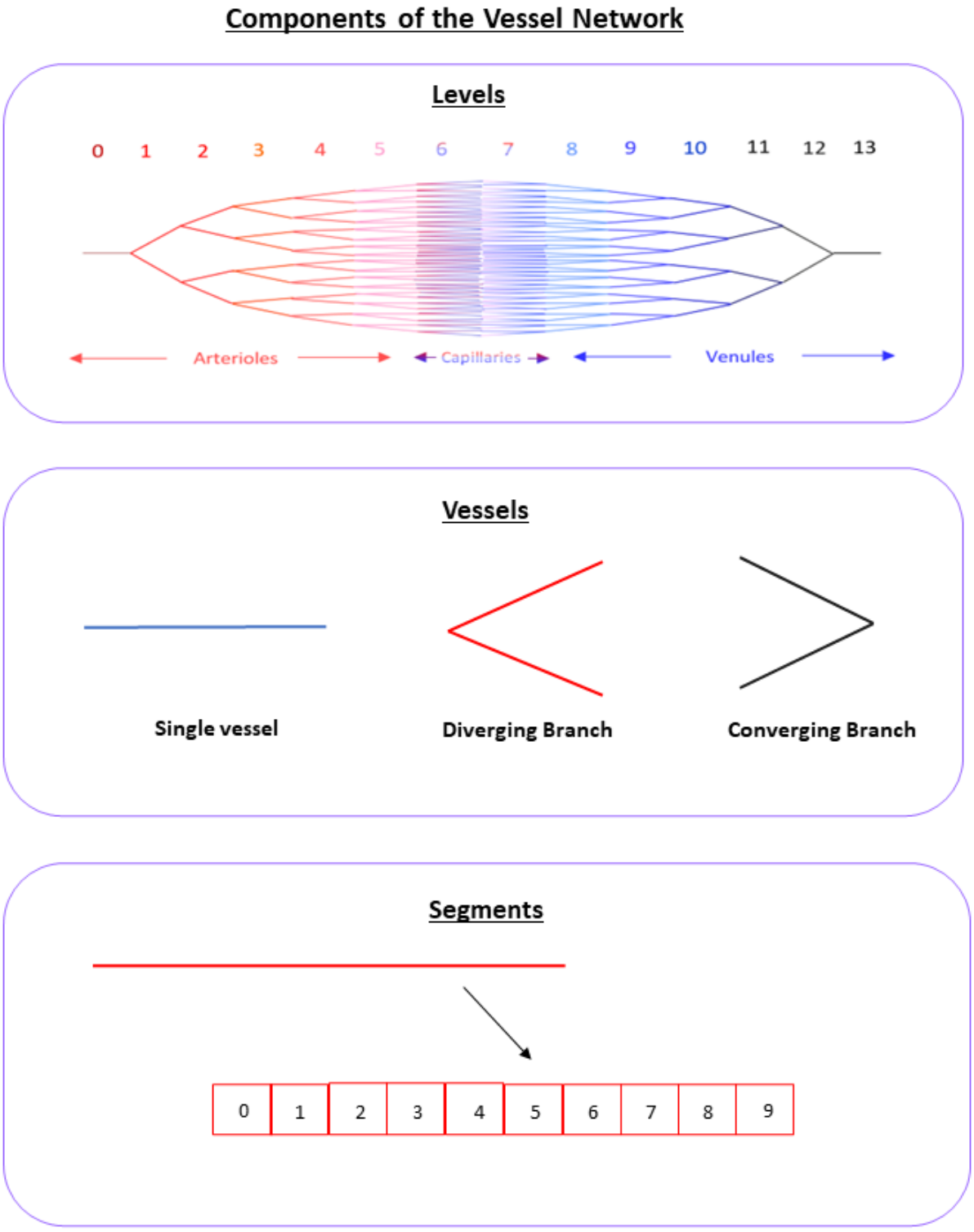

Fig. 4.8 Components of the Vessel Network - The network is split into levels, branches, vessels and segments.

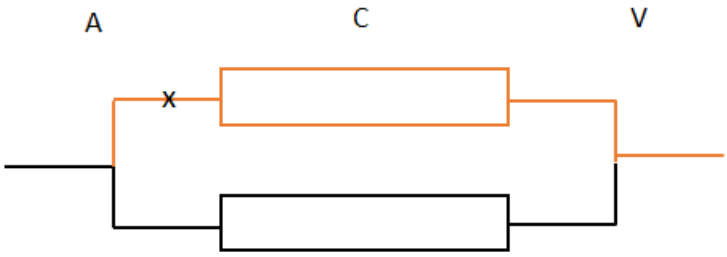

Fig. 4.9 Diagram of the path of blood flow (orange) for an arbitrarily chosen vessel (marked by x) within a small, branched network consisting of 5 levels.

to differ within a level, allowing for pressure and flow to be simulated in a pathological condition such as a blocked vessel.

4.5.2 Calculating Remaining Resistance in the Network

A key challenge faced when recreating the large network of microvessels with our dynamic model was the calculation of the pressure drop across the vessels in the network at every time point. This was due to the uncertainty in defining the remaining resistance in a network involving branches of vessels within a level. It was initially hypothesised that the pressure drop along a vessel could be calculated using the ratio of the resistance in the current vessel and the resistance in the remaining vessels in the network, as calculated in the single vessel (Eq. 4.5). The remaining resistance in the single vessel was defined as the resistance in segments including and following the current segment within the vessel.

To apply this method to the large microvascular network, a path of blood flow was defined for every vessel within the network which identified the vessels in the following levels that were connected to the vessel of interest. This was computed for every vessel within the network. An example of this can be seen in Fig. 4.9, which demonstrates the vessels in the path of blood flow for an arbitrarily chosen vessel within a network constructed from five levels. Once the path of blood flow was defined for each vessel in the network, the remaining resistance was calculated by finding the sum of the resistances of these vessels to obtain one value for total remaining resistance in the network for each vessel. Comparisons were made with the pressure distribution from the steady state replication of the VAN model (Boas et al., 2008).

Fig. 4.10 compares the pressure distribution obtained from the simulation with the pressure distribution from the VAN model (Boas et al., 2008). Values were not in agreement and this was particularly evident across the arteriole levels. Pressures obtained from the dynamic model were approximately constant along the arterioles and decreased greatly at the capillaries. This was because the value of the total remaining resistance in the network was too large when calculating the pressure drop across the arterioles, as the majority of the resistance in the network

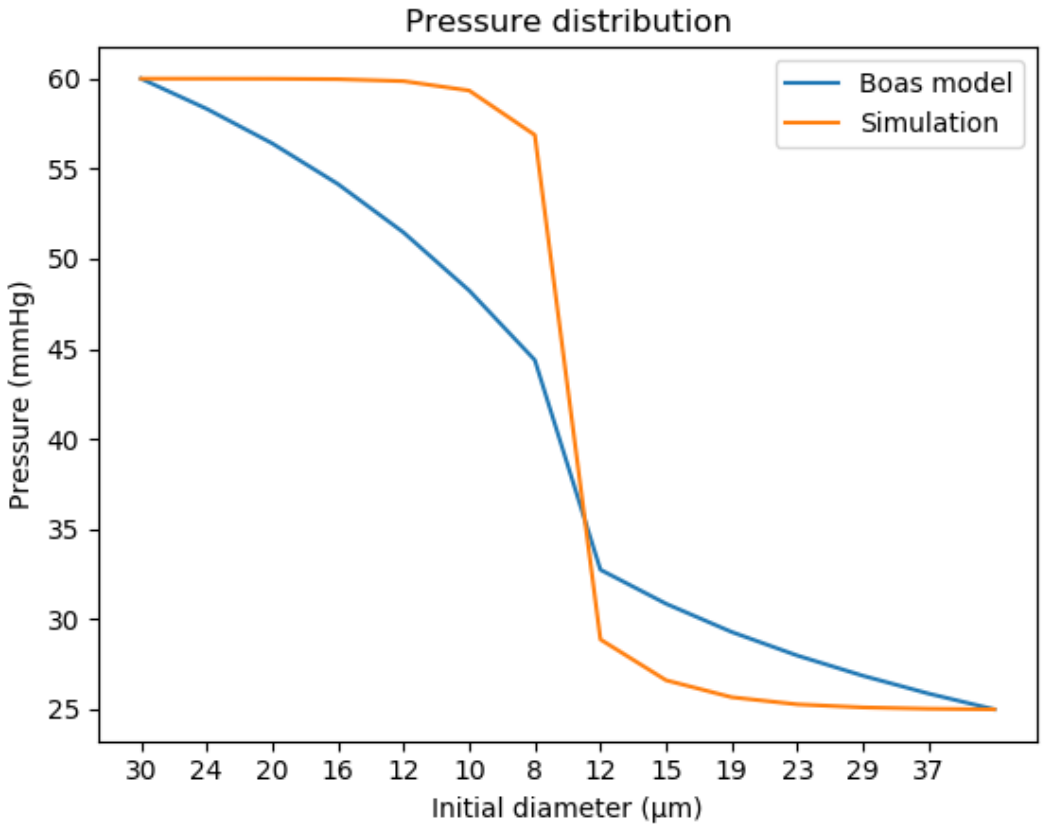

Fig. 4.10 Pressure distribution compared for the Boas model and our simulation using remaining resistance calculated in series.

was contributing to the calculation. Hence it was unlikely that remaining resistance should be calculated in this way.

$$\begin{aligned} \textit{Pressure drop across } i^{th} \textit{ vessel} &= (P_i - P_{diastolic})\frac{R_i}{R_T} \\ \textit{where } R_T &= \sum_{n=l}^{L_{max}} R_n \end{aligned} \tag{4.6}$$

A second approach to calculating the remaining resistance in the network involved computing the resistance, firstly within a level and then across all the remaining levels in the network, as shown in Eq. 4.6. Here, R_{T} refers to the total remaining resistance across all remaining levels with l defined as the level of the current vessel and $L_{\max}$ is the total number of levels in the network. As remaining resistance values were too high in the previous method, a value for R_{n} was obtained by calculating the total resistance across the vessels in a level in parallel. Furthermore, treating the cerebral vasculature as an electrical circuit suggests that the resistance should be combined either in series or in parallel depending on the geometry of the network (Secomb, 2016). Therefore, the total resistance of the vessels within a level was found by calculating the parallel resistance of two vessels within a branch using Eq. 4.7 and then finding the parallel resistance of pairs of branches until one value of total resistance per level was obtained. This was deemed a better approach to calculating remaining resistance compared to the previous method, as calculating the resistance in parallel meant that the number of possible paths for blood flow in a level involving branches of vessels was taken into account. Therefore, remaining resistance values were smaller than in the previous method, especially across the arteriole levels. Once a value of total resistance had been obtained for each level, total remaining resistance was found by adding up the total resistance values for the levels following the current level in series using Eq. 4.8, which was equivalent to finding the sum of R_{n} across all the levels (Eq. 4.6).

$$R_{parallel} = \frac{R_1 R_2}{R_1 + R_2} \tag{4.7}$$

$$R_{series} = R_1 + R_2 \tag{4.8}$$

Expected remaining resistance values were calculated using the pressure distribution outputted from the replication of the steady state VAN model and compared with values calculated in this method. Values from the dynamic model were out by a factor equal to the number of vessels within the level of the current vessel. For example, in the case of the capillary level in the large microvascular network, the total remaining resistance obtained from the parallel and series calculations would need to be multiplied by 64 to equal the expected values. By correcting the values of total remaining resistance within the simulation for every pressure drop calculation, a pressure distribution in agreement with the values stated in Boas et al. (2008) was obtained across the microvascular network, as shown in Fig. 4.11.

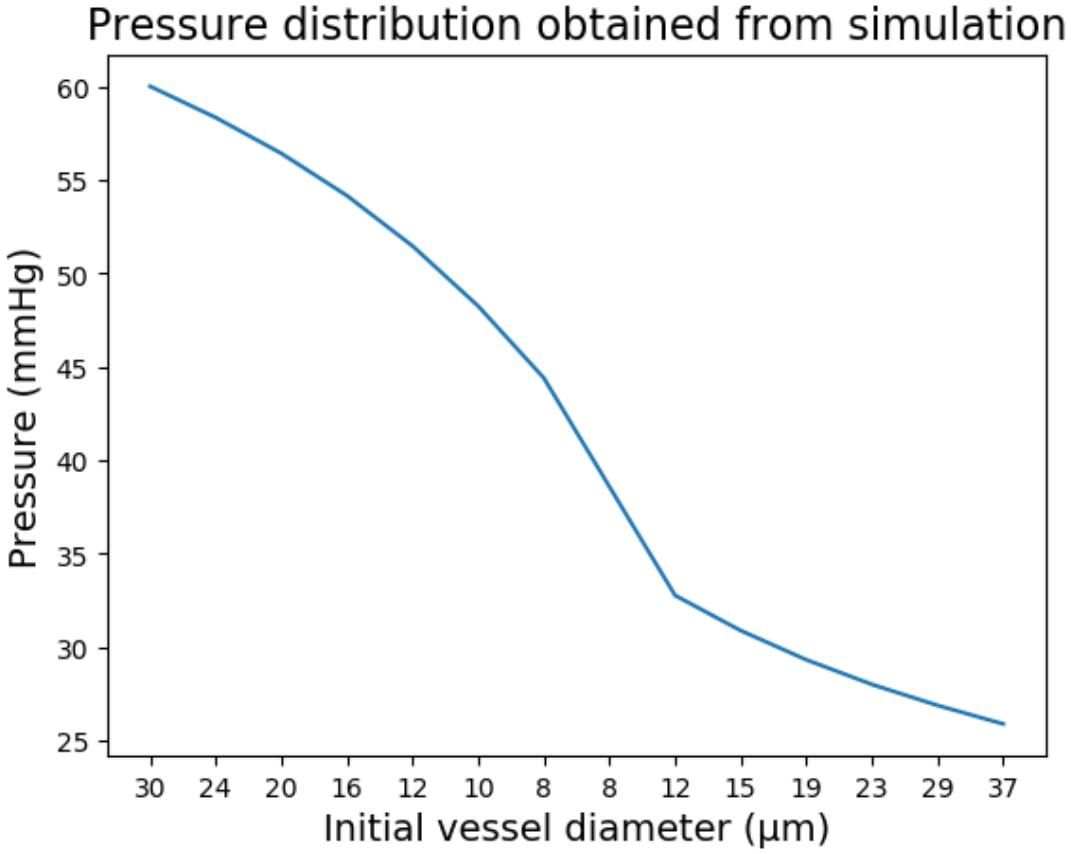

Fig. 4.11 Pressure distribution for values obtained from our dynamic simulation model using the second approach for calculating total remaining resistance in the network. This is the expected pressure distribution, matching the pressures obtained from the VAN model (See Fig. 4.2). The simulated pressure distribution suggests that the model is now working correctly.

4.5.3 The Equivalent Single Vessel (ESV)

The next stage in the development of the model was to incorporate cases in which vessel properties differed within a level. One aim of the model was to investigate changes in pressure and flow for different compliant networks. To do this, a more generalised method of calculating the remaining resistance in the network was required, as the previous method only holds under the assumption that all vessels within a level have the same properties, resulting in the same pressure drop across every vessel in a level.

The Equivalent Single Vessel (ESV) model was created as an approach to solve this problem. Here, the network was reduced to a single vessel, with the number of segments equal to the number of levels within the network. Each level in the network was defined to have one total resistance value, with the total resistance in each branch calculated in parallel (Eq. 4.7), representing the value of resistance for the segment within the single vessel. Using the resistance values and the pressure input, pressure distribution was obtained across the vessel using the method described in the dynamic single vessel model. Using the pressure distribution and resistance, flow was calculated through each segment using Eq. 4.2 and was used as the bulk flow through a level. Returning to the large branched network, the bulk flow through a level was distributed across the individual vessels within that level using the ratio of the resistance in the path of flow to the ratio of the total remaining resistance in the network. Ratios were calculated for each branch of vessels, such that the distribution of flow at each previous branching point was taken into consideration in the calculation. Using the individual resistances for each vessel along with the values of distributed flow through the vessel, the change in pressure was calculated using Eq. 4.2 and pressure distribution was obtained across the whole network. See Fig. 4.12 for a visual representation of the framework.

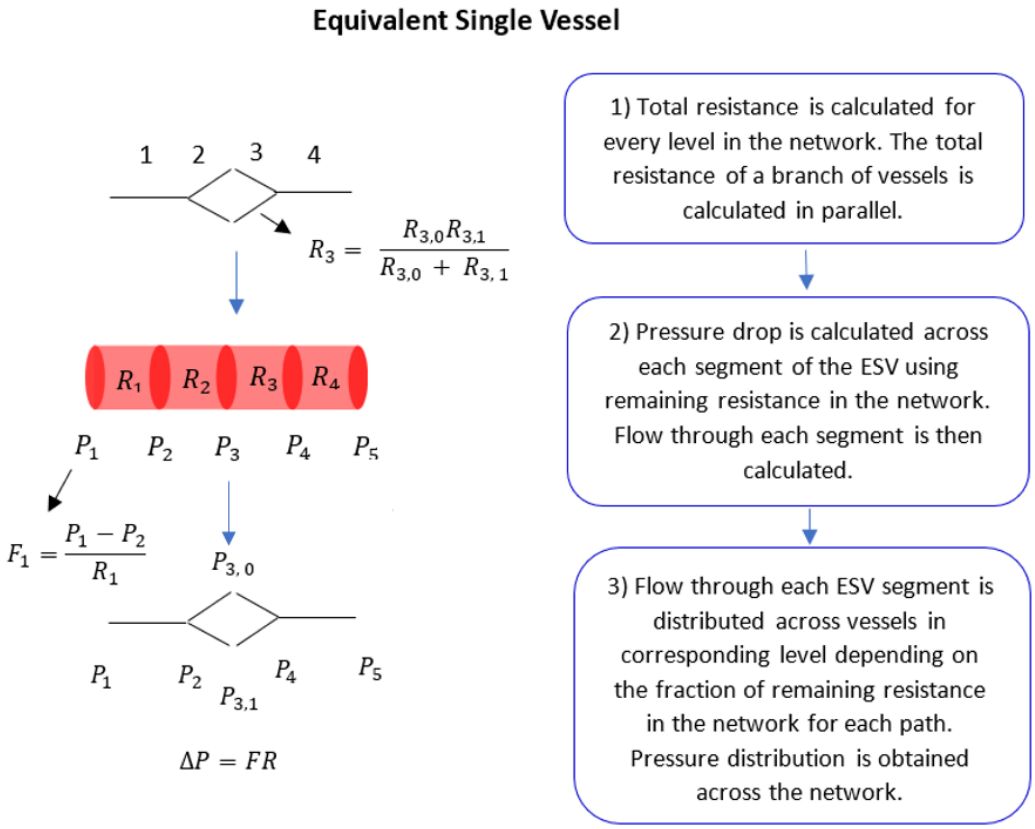

Fig. 4.12 The Equivalent Single Vessel Model - A branched network is reduced to a single vessel and pressure is obtained. Flow through each segment is calculated using pressure gradient and resistance and distributed across vessels in corresponding levels of the branched network. Therefore the pressure distribution across the branched network can be obtained.

4.6 Features and Advantages of the Model

The model was based on the existing VAN model (Boas et al., 2008), but modified to increase the potential applications. Features were added for the purpose of modelling dynamic pressure-driven changes in volume and flow in a network of compliant vessels. Furthermore, the model was created to allow vessel properties to differ across paths of the network. To achieve this, the following features were incorporated into the model:

1. The addition of a time-varying pressure component to model pressure-driven changes in flow across the network.
2. Changes in volume and resistance following changes in pressure to reflect individual vessel compliance.
3. Setting the number of segments in an individual vessel. This is related to the pulse wave velocity.
4. Treating vessels within a branch and within a level independently, and calculating pressures and flows to reflect these differences. This was achieved with the Equivalent Single Vessel.

A high-level description of the algorithm used in the model is presented as a flowchart in Fig. 4.13.

4.7 Summary

The development of the computational model has been described in this chapter, from replication of the steady state VAN model (Boas et al., 2008) to a model that simulates dynamic flow in a branched network of cerebral vessels. The VAN model was replicated by obtaining steady state pressure and flow outputs by solving a system of linear equations as described by Boas et al. (2008). Once this was achieved, the addition of compliance was investigated for a single vessel and a small, branched network. A time component was added to the model and simulations were run for a single vessel and branched network as a first step validation.

The model was extended to dynamically model flow in the large microvascular network used in the VAN model with the intention of investigating pressure-driven flow changes in compliant cerebral blood vessels. This was achieved by updating the volume and resistance of every segment at every time step following changes in pressure. Results were initially obtained for a non-compliant network of vessels and compared to those obtained from replicating the VAN model to validate the model. Another possible application of the model was to investigate changes in the distribution of flow across a network for vessels with different properties, for example if one vessel in a branch was more compliant than the other. The ESV was incorporated into the model as a more general method of calculating flow and pressure across vessels in the

network. The ESV was also developed to simplify the calculation of flow and pressure in a network with different vessel properties, departing from methods requiring a system of linear equations to be solved which would have become more complicated as the number of unknown variables increased. Using the model described in this chapter, simulations will be run for a range of compliant networks for steady state (Chapter 5) and pulsatile flow inputs (Chapter 7).

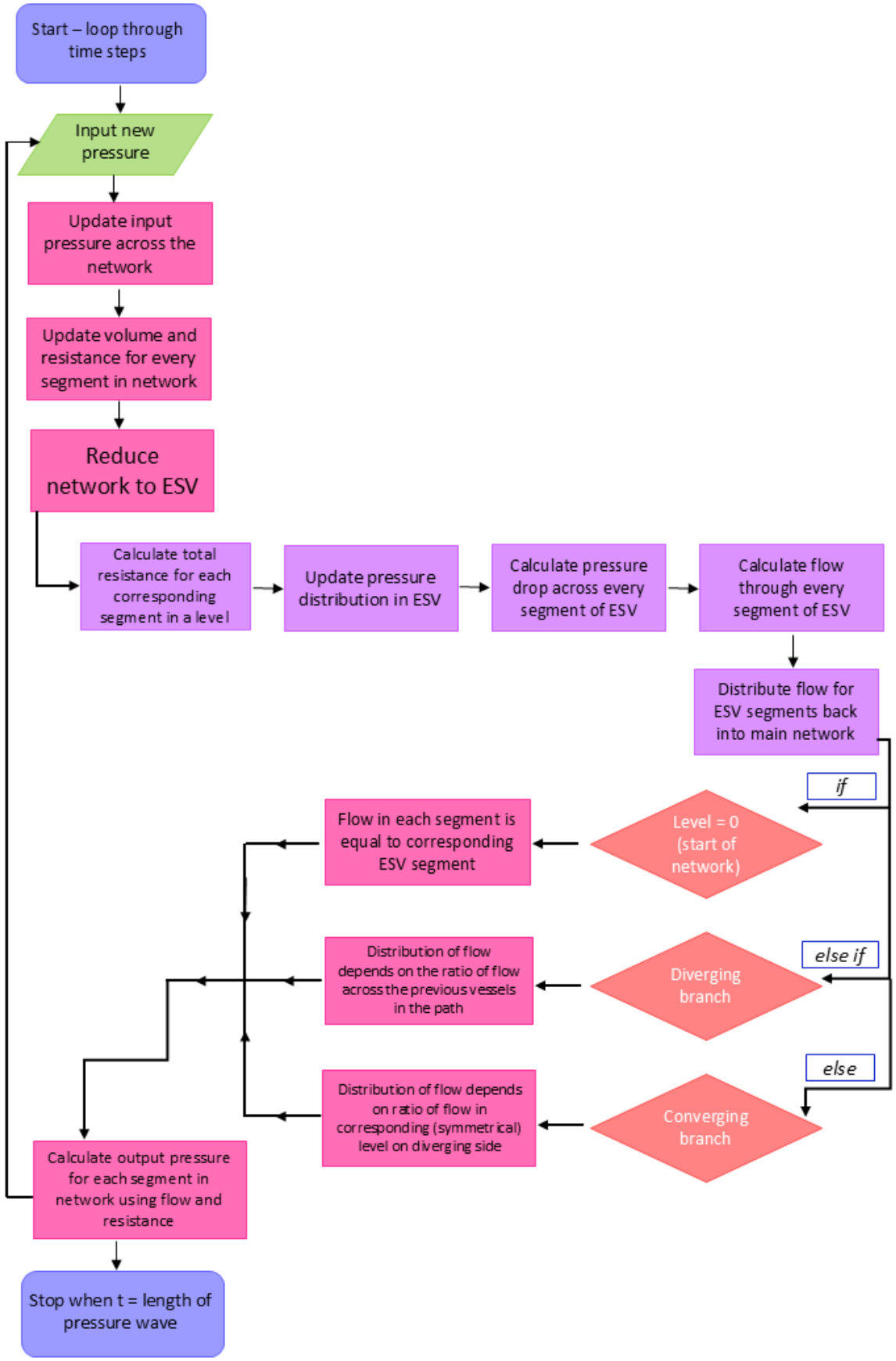

Fig. 4.13 High-level description of algorithm used in model to update variables at every time step, from inputting the new pressure to calculating flow through every segment. Output pressures are calculated using flow and resistance. At the next time step, the output pressure for a segment is used as the input pressure for the next segment.

Chapter 5

Steady State Simulations

Chapter Overview

Compliant vessels dilate and contract as a response to changes in pressure, dampening the pulsatile energy across the vessel network. This is an important process which ensures that harmful pulsatile energy does not reach the smaller, more delicate vessels in the brain. To understand how pulsatile energy is dissipated across a network, and how this changes as vascular health declines, it is important to appropriately account for changes in flow in the computational model. To achieve this, simulations were run in steady state for four different vessel structures/networks with a range of compliance values. The purpose of the simulations was to check that the model was working as expected, by comparing results to the non-compliant steady state network, and to characterise the model in order to pick suitable compliance values for the vessels, hence reducing the number of free parameters required for future simulations. Results from the first set of simulations in steady state are presented in this chapter and the effect of compliance across the network is discussed. Outputs from the simulations suggest that arterioles and capillaries influence flow greater than the venules, and flow across the network is affected not just by local changes but also changes along the network, highlighting the importance of modelling flow across a large compliant network of vessels. Conclusions from this chapter will be used to limit the model parameters for the dynamic simulations presented in Chapter 7.

5.1 Introduction

To study the effect of compliance on pressure and flow across the vessel network, a compliance parameter, β, was added to the model to account for instantaneous changes in segment volume, thus flow, following changes in pressure. As a key aim of the model is to study how compliance affects the dampening of pulsatile flow across the network, it is important to first understand the changes in the network behaviour in steady state. Steady state simulations were initially run

using a range of compliance values to characterise the model. Using the 14-level microvascular network described in the VAN model (Boas et al., 2008) as the basis for the input vessel network, compliance was varied across the network in different cases which were divided into the following categories:

i Compliance in the whole network

ii Compliance in different sections of the network

iii Compliance varying across levels of the network

iv Compliance varying across branches of vessels within a level.

Pressure and flow outputs were obtained from the model and compared for each of the compliant network categories.

The purpose of running steady state simulations was firstly to check that the model was working as expected, and secondly to characterise the model in order to pick suitable compliance values across the microvessels in the network. Therefore, it was important to gain an understanding of how pressure and flow varied for different amounts of compliance and whether this was dependent on where in the network compliance was added. Furthermore, the results from the steady state simulations were used to set parameter values for the microvessels to limit the degrees of freedom for the larger scale macrovascular dynamic simulations in Chapter 5. Further simulations were run to observe how differences in compliance as well as vessel properties within a level influenced the dynamics of the system, highlighting the power of our model.

5.2 Methods

Pressure and flow outputs were obtained for a symmetrical network of microvessels consisting of 14 levels in total. Changes in segment volume following changes in pressure were calculated as described in Chapter 3 to incorporate the effect of vessel compliance on the model outputs. Vessel networks were created for a range of compliance cases and simulations were run to obtain pressure and flow outputs across 500 time steps. Values of 60 mmHg and 25 mmHg were used as input and output pressures for the network respectively and a value of 10 mmHg was used as the intracranial pressure to replicate the VAN model (Boas et al., 2008). To imitate a pressure wave travelling through the vessel network, a value of 60 mmHg was inputted as the pressure at the start of the network at every time step and the drop in pressure across each vessel segment was calculated (refer to Chapter 3 for further details).

5.2.1 Microvascular Network Parameters

The microvascular network was created from 14 levels of bifurcating vessels with values for vessel diameter, length and blood viscosity taken from the VAN model (Boas et al., 2008).

Level	Number of Vessels	Vessel Category	Diameter (μm)	Length (μm)	Viscosity (cP)	Number of segments
0	1	Arteriole	30.5	100.0	2.49	10
1	2	Arteriole	24.2	100.0	2.34	10
2	4	Arteriole	19.5	100.0	2.25	10
3	8	Arteriole	15.6	100.0	2.20	10
4	16	Arteriole	12.5	100.0	2.16	10
5	32	Arteriole	10.0	100.0	2.12	10
6	64	Capillary	8.0	125.0	2.10	5
7	64	Capillary	8.0	125.0	2.10	5
8	32	Venule	12.0	100.0	2.15	10
9	16	Venule	15.0	100.0	2.18	10
10	8	Venule	18.7	100.0	2.22	10
11	4	Venule	23.4	100.0	2.32	10
12	2	Venule	29.3	100.0	2.51	10
13	1	Venule	36.6	100.0	2.70	10

Table 5.1 Baseline values for microvascular network parameters. Values for diameter, length and blood viscosity taken from Boas et al. (2008). The methods used by Boas et al. (2008) to obtain the values are summarised - Vessel lengths were taken from Turner (2002) and Vovenko (1999). Capillary diameter was obtained from Lipowsky (2005). Arteriole diameters were calculated to obtain the expected decrease in red blood cell velocity from the arterioles to the capillaries, decreasing in diameter by 20% at every branch. Similarly, venule diameters were calculated by increasing the diameter by 20% at every branch, resulting in a final venule diameter that was greater than the largest arteriole. Viscosity values were calculated using diameter and haematocrit (Pries et al., 1992).

The network is a simplistic representation of a real anatomical vascular network in the brain, however it was replicated exactly from the VAN model in order to compare model outputs to investigate the effect of vessel compliance. While the branching pattern and the number of levels is unrealistic, the network was created in this way to increase computational efficiency and to replicate the VAN model. Increasing the number of levels may increase the accuracy of this model but would increase the time required for the model to run. Arteriole and venule vessels were split into 10 segments. Each capillary level was split into five segments, resulting in a total of 10 segments across the capillaries. The number of segments for each vessel was chosen arbitrarily. Vessels were split into segments to track the propagation of the pressure wave as it was designed to move across the network one segment per time step. As the number of segments approaches infinity, the model would become continuous. However, as the number of segments increases, the computational power required to run the model increases. The number of segments chosen was computationally efficient and introduced a time parameter into the model. Initial values for every level of the network are given in Table 5.1. Baseline values for vessel diameter, length and blood viscosity were initially equal for all vessels within a level.

5.2.2 Compliant Network Categories

Flow was simulated in four categories:

i Whole network compliance

ii Compliance in sections of the network (arteriole only, capillary only and venule only compliance)

iii Compliance in a level of the network

iv Varying compliance across branches within a level.

Fig. 5.1 illustrates the compliant vessels corresponding to each category. Figs. 5.2 and 5.3 explain how compliance in each case relates to the vessels across the network.

The addition of compliance in the model was first studied by allowing the whole network to be compliant. In this case, all vessels in the network had the same compliance value. Values of the compliance parameter, β, were varied for every simulation in order to fully characterise the model behaviour and pick a suitable value for the network. Simulations were run for β=2, 3, 5, 10, 100 and 100000 and pressure, flow, volume and resistance distributions were compared. A value of β=100000 was used to represent non-compliant vessels. The β values were chosen to investigate the influence of compliance on the behaviour of the model, hence this initial exploratory analysis was carried out with a range of compliance values from compliant vessels (β=2) to non-compliant vessels (β=100000). As stated in existing literature (Boas et al., 2008; Mandeville et al., 1999), realistic compliance values for the microvessels are between 2 and 3. Simulations were repeated for β=2, 2.2, 2.4, 2.6, 2.8 and 3 and pressure and flow were obtained as outputs.

Compliance was then investigated across sections of the network, firstly by comparing 'arteriole only compliance' to 'capillary only compliance' and 'venule only compliance' with the aim of examining whether compliance in one location of the network could influence pressure and flow in the remaining sections. As each level of the network can be categorised into a type of vessel, levels corresponding to a vessel category were either classed as compliant or non-compliant. Values of β between 2 and 3 were used for vessels in the chosen compliant section and β=100000 was used as the non-compliant value.

A more realistic approach was then applied by varying compliance across levels using a ramp up and ramp down in β values between 2 and 3. Pressure and flow outputs were compared across two cases:

1. Ramp down in β from 3 to 2 across the arterioles and back up to 3 across the venules (β=2 in the capillaries)

2. Ramp up in β from 2 to 3 across the arterioles and down to 2 across the venules (β=3 in the capillaries).

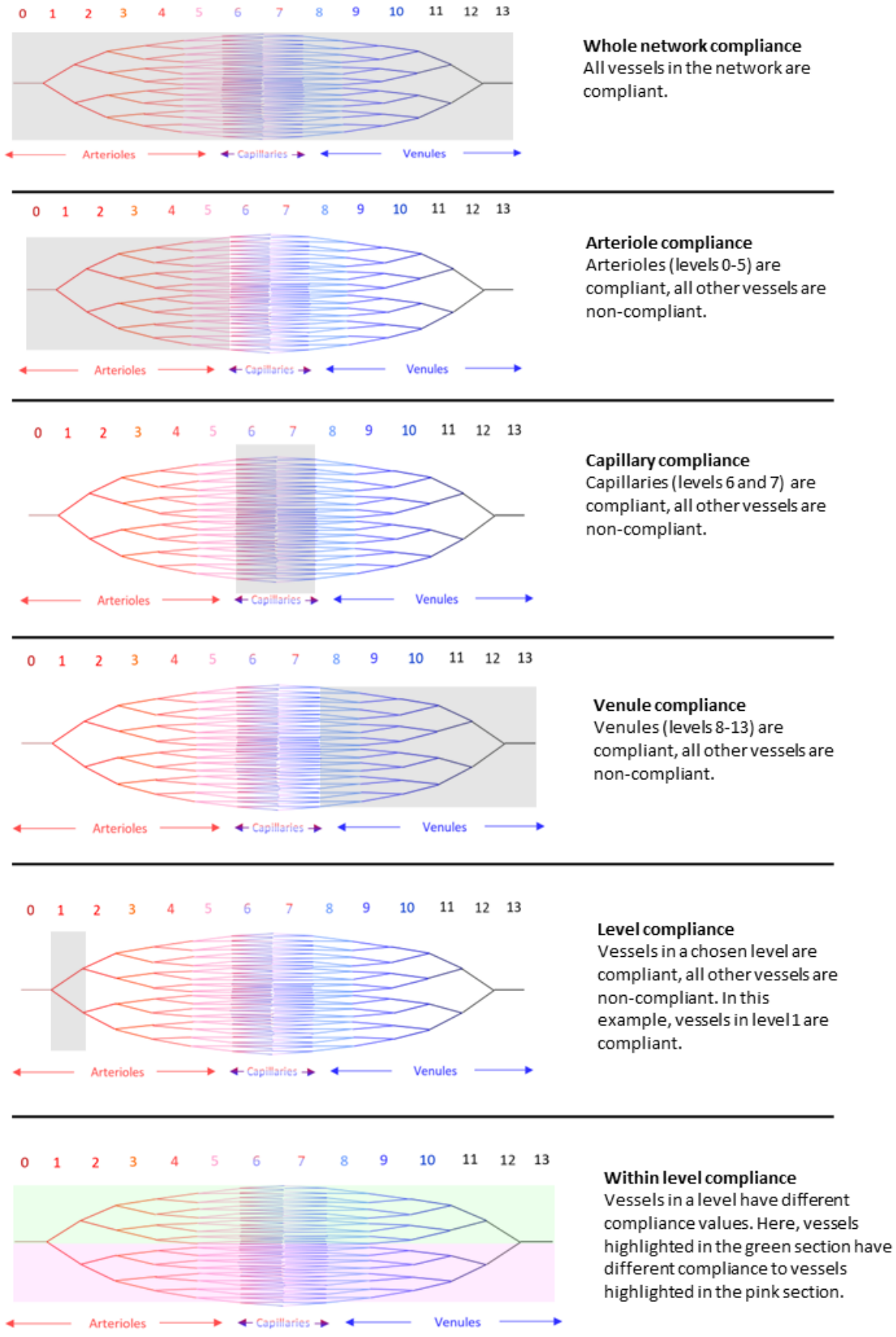

Fig. 5.1 Visualisation of the compliant network categories used in this chapter. The compliant vessels are highlighted in each case.

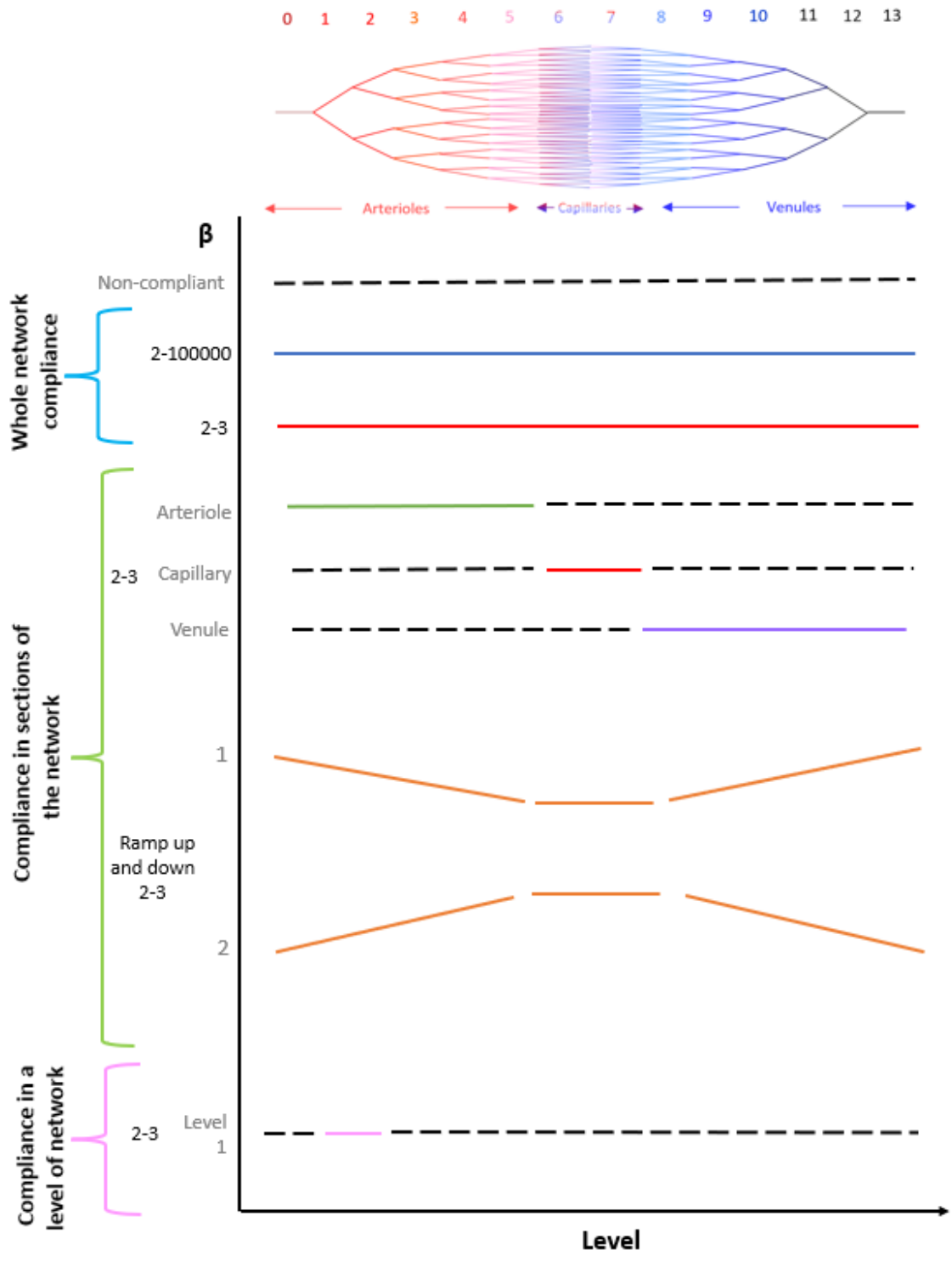

Fig. 5.2 Visual representation of compliance in the network for categories i-iii. Lines represent the compliance values used in the corresponding sections of the network; straight lines represent constant compliance values, diagonal lines represent varying compliance and dashed lines represent no compliance (β=100000).

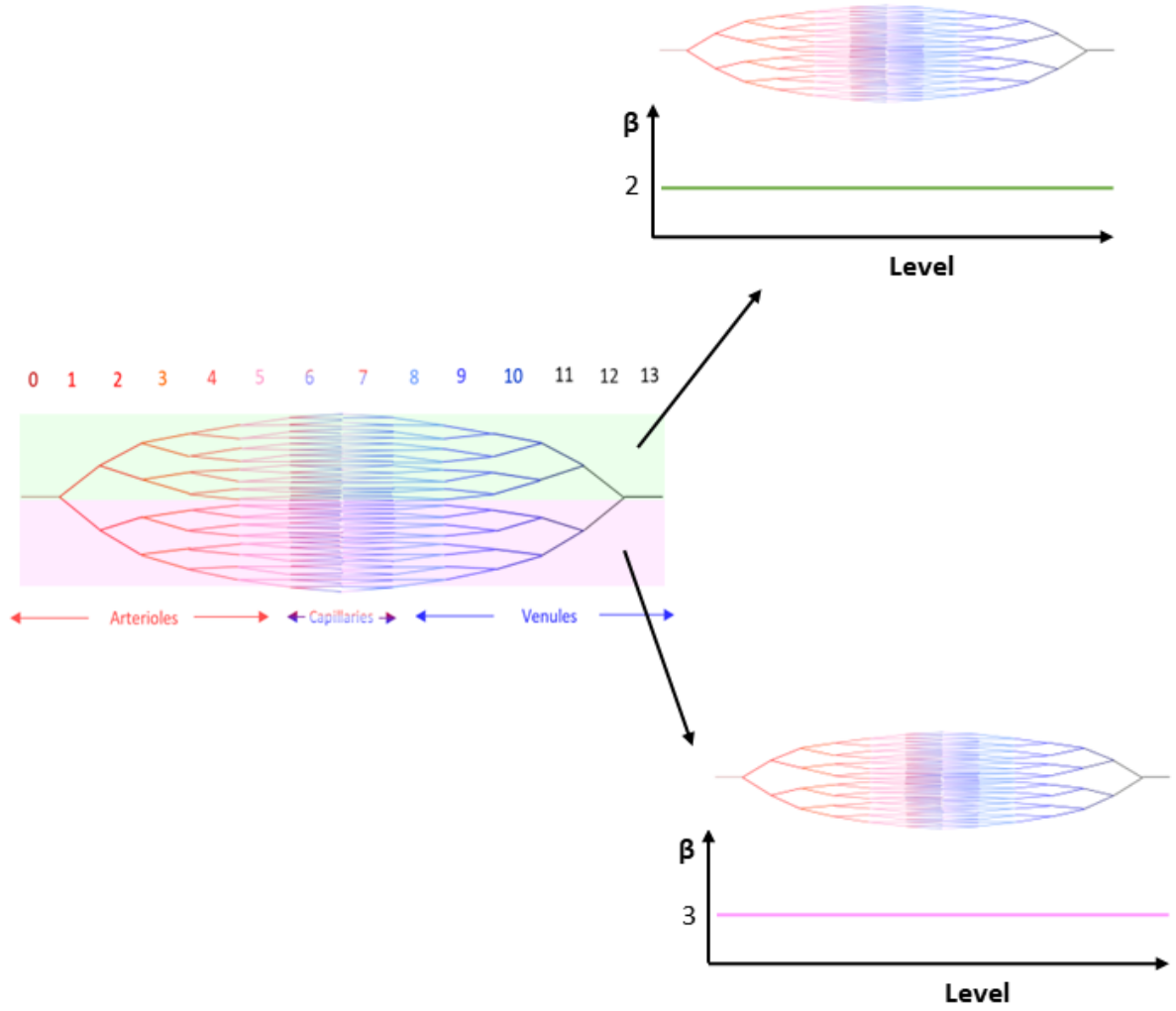

Fig. 5.3 Visual representation of the compliant network used for the simulations in category iv. Vessels in the top half of the network (highlighted in green) have a compliance value of β=2 and vessels in the bottom half of the network (highlighted in pink) have a compliance value of β=3.

See Fig. 5.2 for a detailed explanation of the compliant network cases. Compliance values were varied in both directions as it was unclear how compliant the capillaries should be in relation to the arterioles and venules and therefore outputs could be compared for capillaries having a compliance value of 2 and 3.

To investigate the influence of individual levels of compliant vessels on network flow, β was varied across levels. Here, all vessels in a chosen level were compliant and all other vessels in the network were non-compliant (β=100000). Simulations were run 14 times, with each level in turn having a compliance value of β= 2 while all other levels were non-compliant. The simulations were then repeated using a compliance value of β=3 in the chosen compliant level.

Finally, compliance was varied across branches within a level to compare pressure and flow along different paths of the network. The purpose of this was to investigate the distribution of flow across vessels in a branch with different properties and how this affected pressure and flow across the whole network. Furthermore, the simulations in this category highlight how the model has been extended beyond the VAN model (Boas et al., 2008) as here vessel properties can differ within levels. This is particularly useful when considering how flow adapts to changes in the vasculature, for example if there was a blockage in a particular path of blood flow. For the purpose of validating and characterising the model, differences in vessel compliance were applied across two paths. This was achieved by splitting the vessels in the network across the horizontal axis. Pressure and flow values were compared for two paths, A and B. Path A refers to the first (top) vessel in every level of the network and path B refers to the last (bottom) vessel in every level. Vessels in the top half of the network were given a compliance value of β=2 and vessels in the bottom half of the network were given a compliance value of β=3.

To further explore the distribution of flow in the network, vessel properties were varied for vessels within a branch of a level. In this case, the diameter of the first vessel in the first branch of level 2 was initially set to be half the diameter of the other vessels in the level, therefore creating a network where there was greater resistance in one vessel compared to the remaining vessels in the level. This imitates a network whereby one vessel is partially blocked. All vessels in the network were compliant (β=2). Pressure and flow were compared for paths A and B.

Pressure and flow distributions were obtained as outputs from the model and compared across compliant network cases. A particular emphasis was placed on flow in the capillaries as a key aim of the model is to assess how pulsatility is dampened across the vascular tree before reaching the capillaries. Therefore capillary flow across time was also compared for different compliant networks. In all results, capillary flow refers to the flow through the corresponding vessel in level 6. Finally, relative flow difference was calculated comparing flow in the compliant networks to the corresponding values in non-compliant (β=100000) networks.

5.3 Results

5.3.1 Compliance across the whole network

Initially, all vessels in the network were compliant. Pressure and flow distributions across the network for β=2, 3, 5, 10, 100 and 100000 are presented in Fig. 5.4. Here, pressure refers to the input pressure for the first segment of the vessel and flow refers to the value of flow in the middle segment of the vessel. Volume and resistance values refer to the total volume and resistance across all segments in a vessel. Therefore, the volume and resistance plotted against each level represents a single path across the network. As compliance was the same in every vessel in a level, output values across every path of blood flow were equal. Therefore, steady state values were arbitrarily taken from the first vessel across every level at the last time point (t=500) to obtain the distributions. Initially, pressure and flow distributions for the non-compliant network (β=100000) were compared to the results from the VAN model (Boas et al., 2008) to check the model was working as expected.

Pressure and flow values were higher for greater compliance values in every level of the network. The volume distribution shows that volume was greater across the arteriole levels for more compliant vessels and decreased as vessels became less compliant. Volume was the lowest at the capillaries due to these vessels having the smallest diameter and increased across the venous levels as vessel diameter increased. Volumes were similar across all compliance values for the venous levels as the pressure differences between the venule input pressures and the intracranial pressure were small. This differs to the vessels on the arteriole side as pressure differences between the arteriole input pressures and intracranial pressure are much greater, hence there is a variation in volumes across β values. Resistance increased along the arteriole levels and was highest for the capillaries in the non-compliant vessels. As expected, resistance decreased across the venules as vessel diameters increased. These steady state distributions validate that the model is working as expected.

Simulations were repeated for more realistic microvascular β values between 2 and 3. The steady state pressure and flow distributions and relative pressure and flow differences for five β values between 2 and 3 are shown in Fig. 5.5. Small differences can be seen between absolute pressure and flow values for compliance values between 2 and 3, however greater differences can be seen in the relative difference plots comparing flow and pressure in compliant vessels to the corresponding values for the non-compliant vessels, emphasising the variation in results for β values between 2 and 3. Again, steady state pressure and flow values were greatest when vessels were the most compliant and decreased as compliance in the network decreased, further highlighting that the model was working as expected. Results from this point on will compare compliant vessels for β values between 2 and 3 and β=100000 will be used for non-compliant vessels.

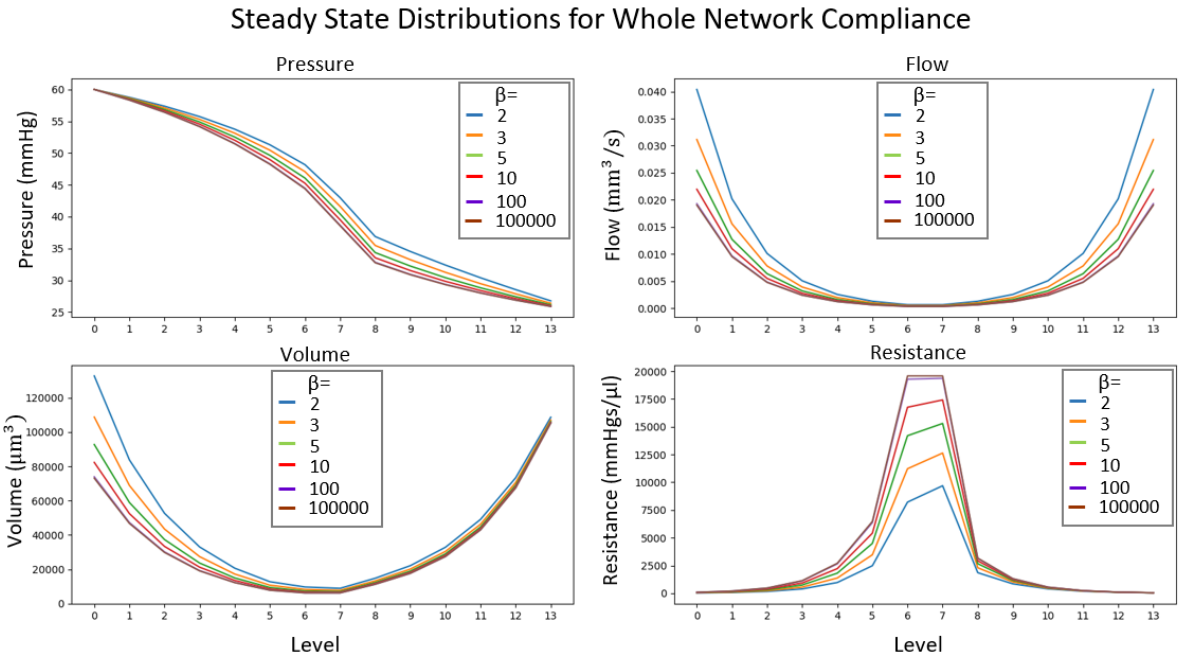

Fig. 5.4 Steady state pressure flow, volume and resistance distributions for β=2, 3, 5, 10, 100 and 100000. Values were obtained at t=500 in the first vessel of each level. Pressure values represent the pressure in the first segment and flow values represent flow in the middle segment of the chosen vessel in each level. Volumes and resistances represent the sum of the volumes and resistances in each segment of the chosen vessel. Therefore, the volumes and resistances plotted against each level represent a single path across the network.

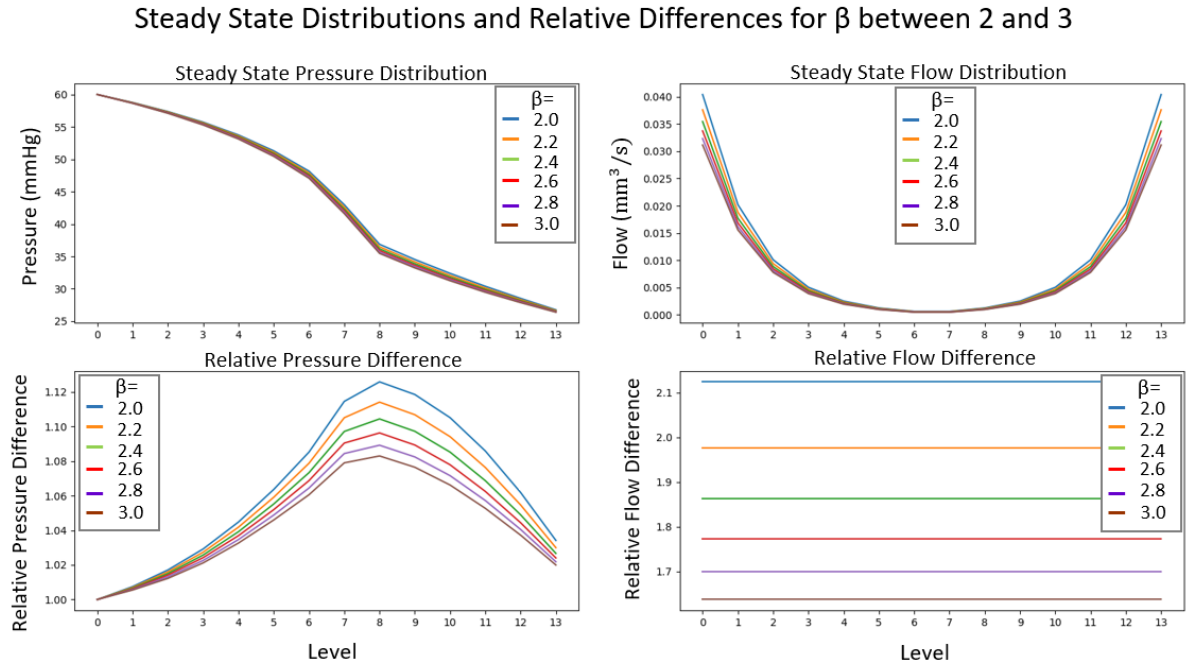

Fig. 5.5 Pressure and flow distributions (top panel) and relative pressure and flow differences (bottom panel) for β values between 2 and 3.

5.3.2 Compliance in sections of the vascular tree

Compliance was varied in sections of the network to investigate how changes in one part of the network influenced pressure and flow across the whole network. Initially, compliance was compared across five cases: no compliance, whole network compliance, arteriole only compliance, capillary only compliance and venule only compliance. In all cases the same β value was used for all vessels in the compliant section of the network and every other vessel was treated as non-compliant.

Pressure and flow distributions are compared across each compliant network case for β=2 and 3 (Fig. 5.6). It is evident from the variation in the distributions across all cases that the location of compliance within the network affects steady state pressure and flow. Distributions for both β=2 and 3 follow the same pattern, however absolute flow is greater for β=2 as expected. The pressure and flow distributions for the venule only compliance case showed the smallest difference to the non-compliant network distributions, suggesting that compliant venules influence the network the least. Arteriole only compliance gave the second highest values in flow across all levels of the network after whole network compliance. This is further evident in Fig. 5.7 which compares the magnitude of flow in the capillary (level 6) in steady state across the five compliance cases.

Fig 5.8 shows absolute flow across time in the first capillary level for the five cases. Values of β=100000 and β=2 were used to represent non-compliant and compliant vessels respectively. As expected, absolute flow was the highest when all vessels in the network were compliant. Arteriole only and capillary only compliance also increased flow compared to the non-compliant network whereas venule only compliance had the smallest increase in flow. All increases in flow occurred as soon as the pressure wave reached the capillary level with all values plateauing to a constant value once the system had reached steady state. In all the compliant network cases, flow did not instantly reach a steady state value which suggests that dynamic network changes following pressure changes downstream in the network also affect the capillaries. This is particularly apparent in capillary flow across time for both the arteriole only compliance and capillary only compliance cases which indicate that there is feedback in the system and that the dynamics of the network are not only influenced by changes upstream but also changes across the remaining sections of the network.

Relative flow difference is shown for the four compliant cases in Fig. 5.9 for compliance values of β=2 and β=3. Relative flow difference was calculated by dividing flow values across time for each compliance case by the corresponding flow values outputted from the non-compliant network. Differences in relative flow difference over time can be seen across all compliant cases, again suggesting that the location of the compliance within the network influences flow. Furthermore, in all compliant network cases flow did not instantly reach a constant value. This implies that in the dynamic situation where input pressure changes across time, many complicated changes in flow across the network will take place.

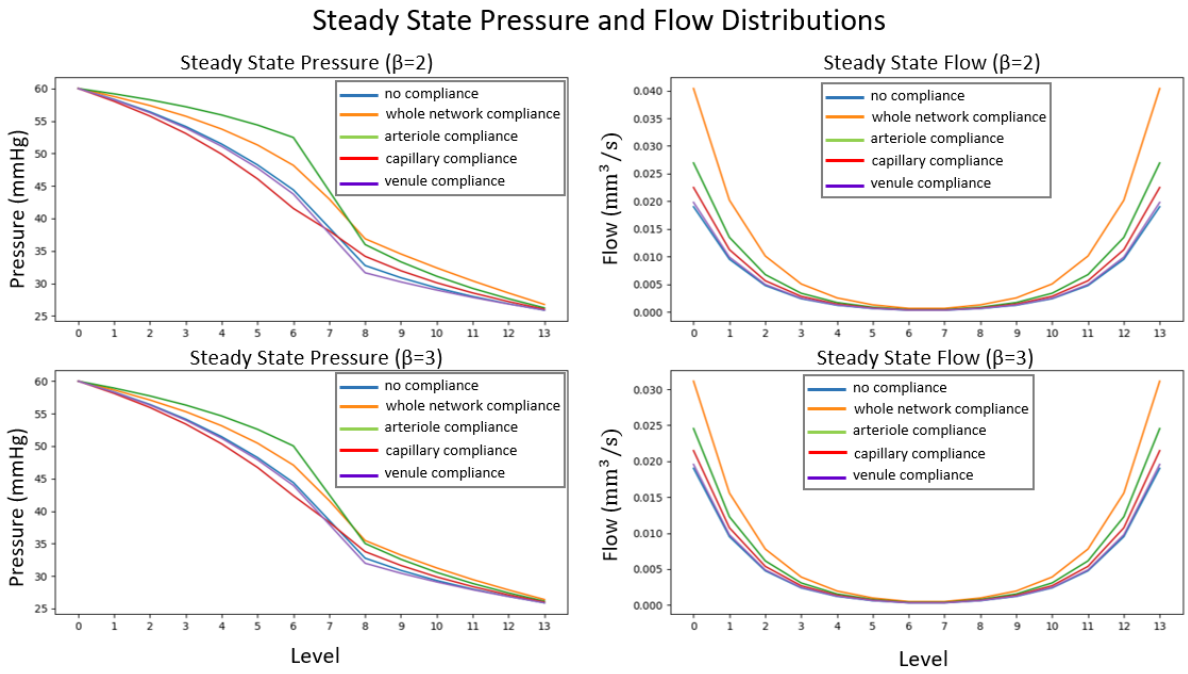

Fig. 5.6 Pressure and flow distributions for compliant network cases: (1) no compliance, (2) whole network compliance, (3) arteriole only compliance, (4) capillary only compliance and (5) venule only compliance for β=2 (top panel) and β=3 (bottom panel).

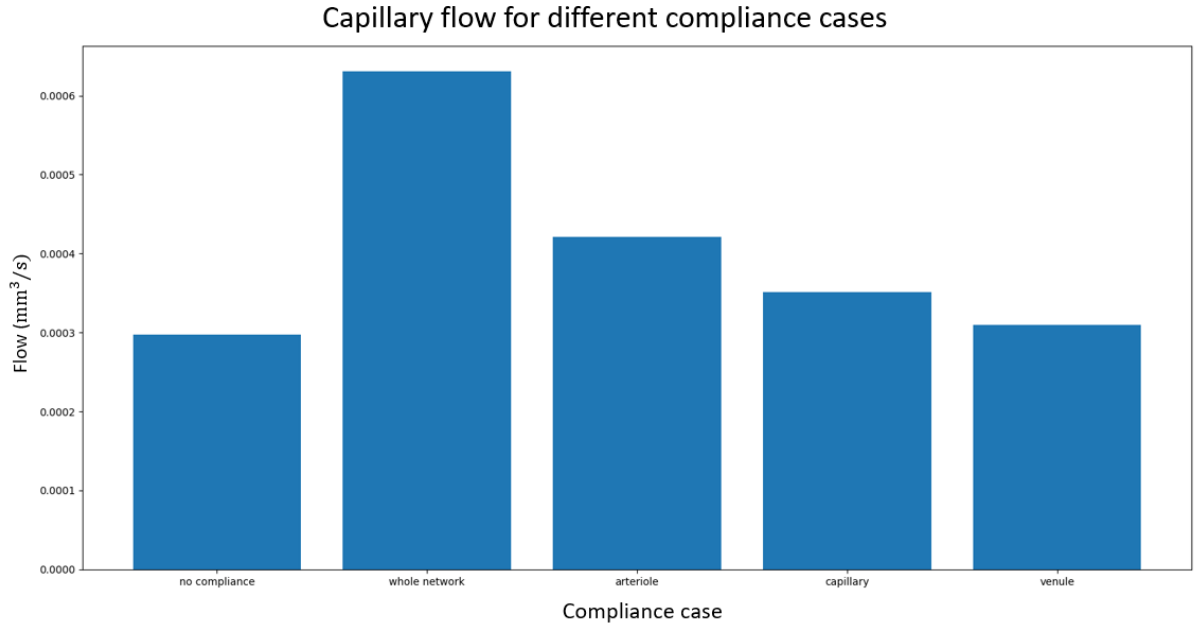

Fig. 5.7 Magnitude of flow in the capillary (level 6) in steady state for five compliant network cases: (1) no compliance, (2) whole network compliance, (3) arteriole only compliance, (4) capillary only compliance and (5) venule only compliance. A compliance value of β=2 was used for the corresponding compliant vessels in each case.

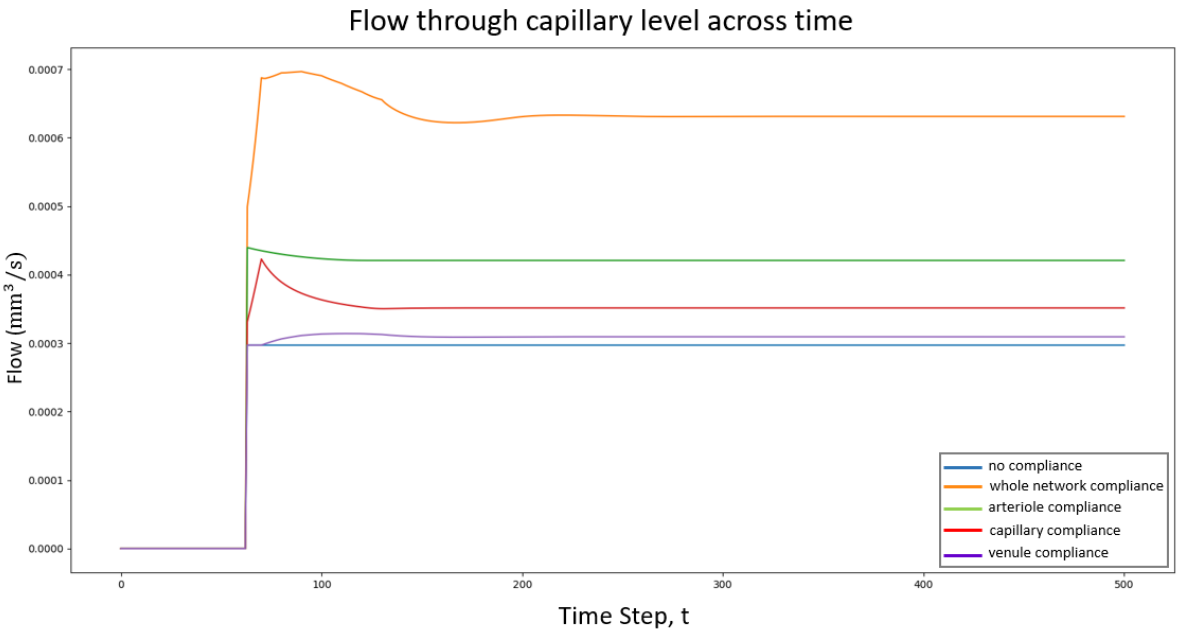

Fig. 5.8 Absolute flow through the capillary (level 6) across time is compared across five compliant network cases: (1) no compliance, (2) whole network compliance, (3) arteriole only compliance, (4) capillary only compliance and (5) venule only compliance.

In order to model vessel compliance more realistically, compliance was varied across levels of the network using a ramp up and down in β values between 2 and 3. The steady state pressure and flow distributions are compared across four cases in Fig. 5.10. Small differences can be seen in the pressure and flow distributions across all four cases, with the whole network compliance of β=2 giving the greatest flow values and the whole network compliance of β=3 giving the smallest flow values as expected. Flow values were higher for case 1 compared to case 2 when the capillaries were more compliant. This is further highlighted in Fig. 5.11 which compares steady state flow in the capillary across the compliant cases and Fig. 5.12 comparing capillary flow across time. Results suggest that capillary compliance is an important factor in the system.

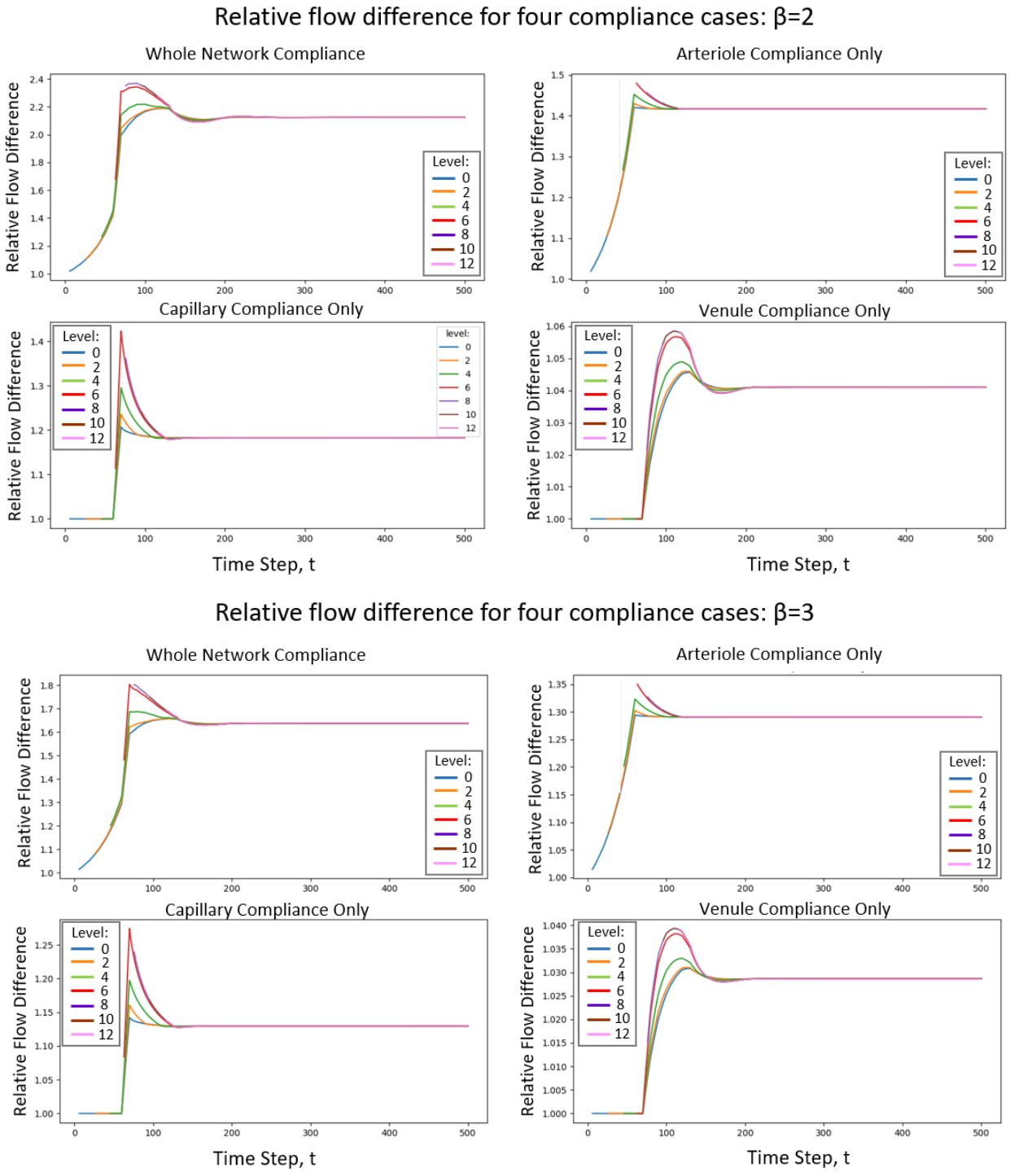

Fig. 5.9 Relative flow difference for four compliant cases: (1) whole network compliance, (2) arteriole only compliance (3) capillary only compliance and (4) venule only compliance for β=2 and β=3. Relative flow difference was calculated using the corresponding values for the non-compliant (β=100000) network.

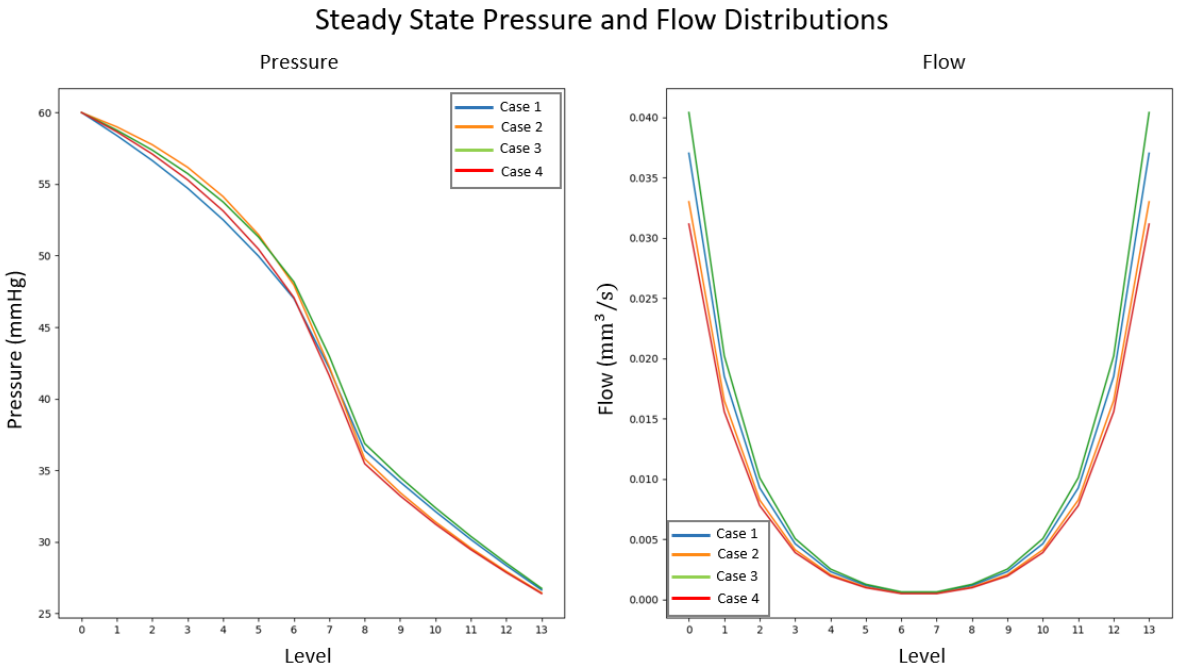

Fig. 5.10 Steady state pressure and flow distributions compared for four compliant networks: (1) ramp down from β=3 to 2 across arterioles, ramp up to 3 across venules, (2) ramp up from β=2 to 3 across arterioles, ramp down to 2 across venules, (3) whole network compliance β=2 and (4) whole network compliance β=3.

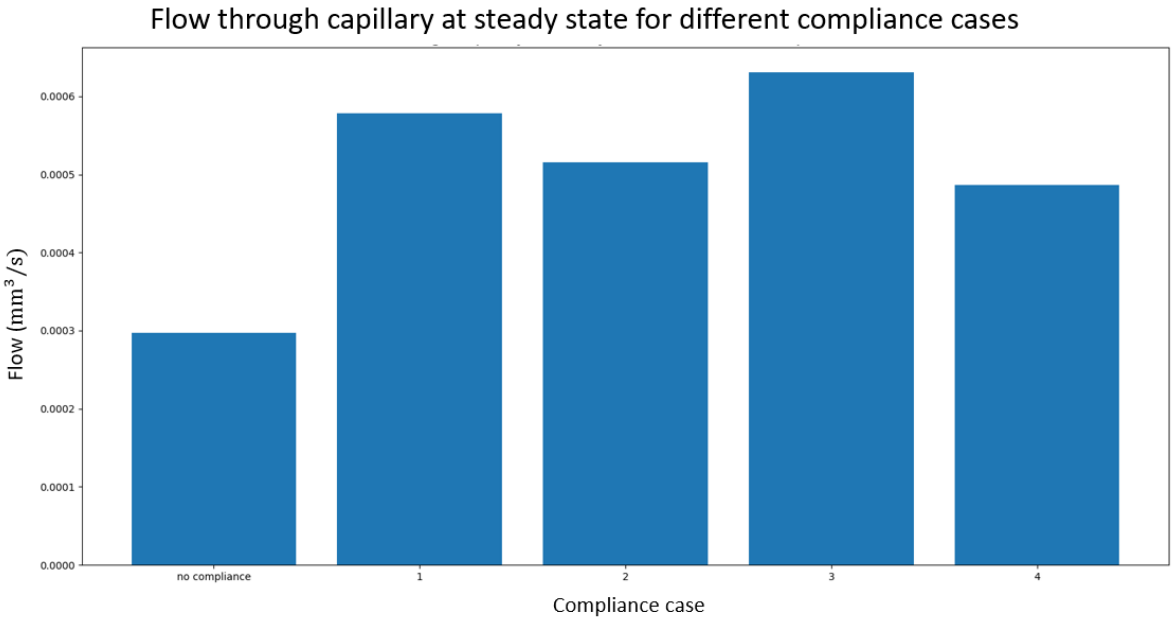

Fig. 5.11 Magnitude of flow in the capillary compared across five compliant networks: (0) non-compliant (1) ramp down from β=3 to 2 across arterioles, ramp up to 3 across venules, (2) ramp up from β=2 to 3 across arterioles, ramp down to 2 across venules, (3) whole network compliance β=2 and (4) whole network compliance β=3.

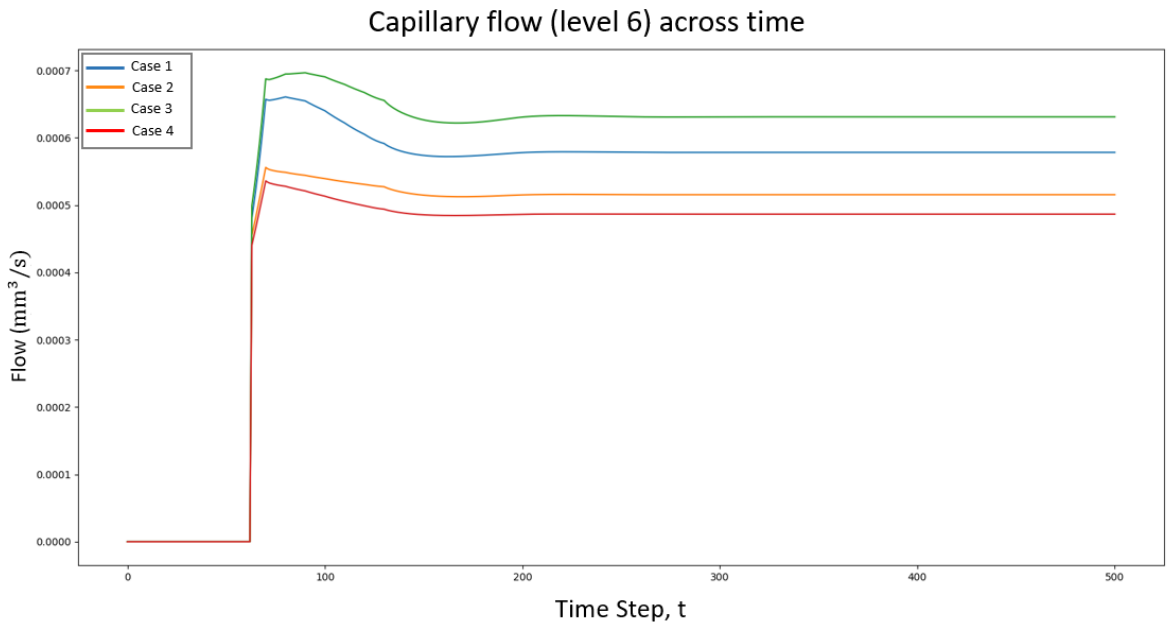

Fig. 5.12 Flow in the capillary across time for four compliant networks: (1) ramp down from β=3 to 2 across arterioles, ramp up to 3 across venules, (2) ramp up from β=2 to 3 across arterioles, ramp down to 2 across venules, (3) whole network compliance β=2 and (4) whole network compliance β=3.

5.3.3 Varying compliance in levels of the network

Compliance was added to the model one level at a time and pressure and flow were obtained as outputs. The steady state pressure and flow distributions are shown in Fig. 5.13. Pressure and flow are similar across all compliant levels. Fig. 5.14 shows the absolute value of flow in the capillary at steady state compared across compliant levels. Compliance in levels closest to the capillaries had greater flow values whilst compliant venules resulted in little difference in the magnitude of flow when compared to the steady state flow in the non-compliant network. This can also be observed when comparing capillary flow across time for all compliant levels (Fig. 5.15). Again, results suggest that venule compliance has the least influence on the network and can be discarded for future dynamic simulations.

5.3.4 Varying compliance across paths of the network

Compliance was varied across branches of vessels within a level and the distribution of flow for two paths, A and B were compared. Compliance was originally investigated by using a value of β=2 for vessels in the top half of the network and β=3 for vessels in the bottom half of the network. Fig. 5.16 shows the steady state pressure, flow, volume and resistance distributions across the network after 500 time steps for vessels in paths A and B. As expected, volume was greater across path A compared to path B since the vessels are more compliant, resulting in less resistance in path A. Flow was greater in path A than in path B since flow takes the path of least resistance. This is a demonstration that the model functions correctly. The difference in the

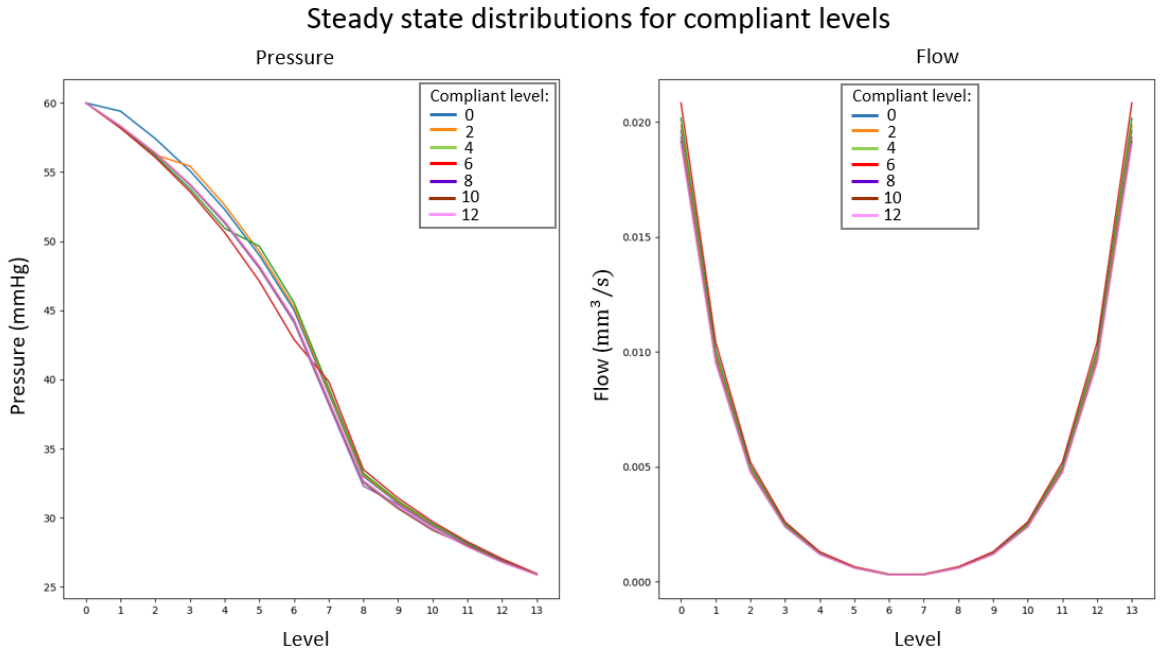

Fig. 5.13 Steady state pressure and flow distributions for compliant levels (β=2).

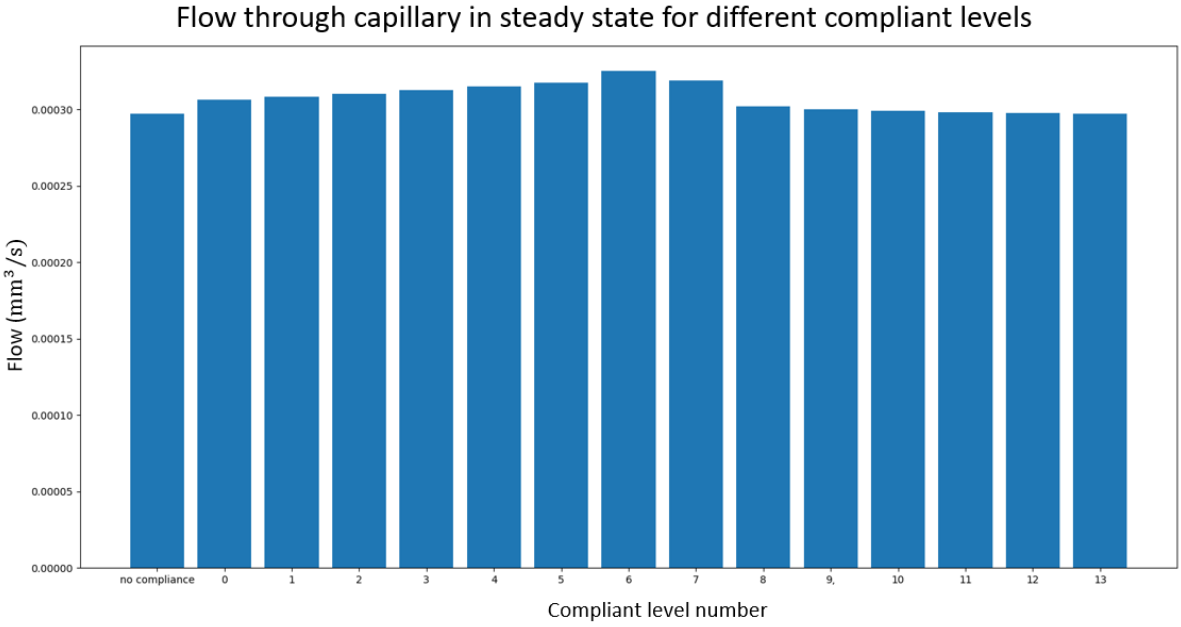

Fig. 5.14 Magnitude of absolute flow in the capillary at steady state for every compliant level.

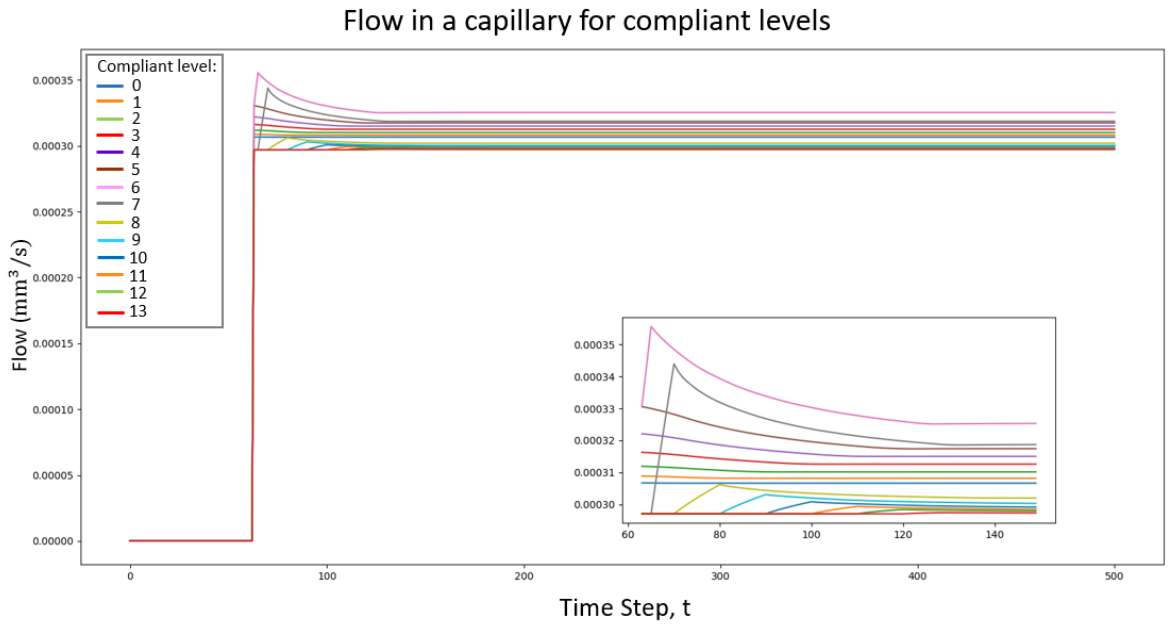

Fig. 5.15 Capillary flow against time shown for every compliant level.

distribution of flow between vessels with different compliance values is further highlighted in Fig. 5.17. After 61 time steps, when the pressure wave had reached the capillary (level 6), flow through the capillary in path A was greater than capillary flow in path B. Flow in path A was also greater than path B once the system reached steady state.

As a proof of concept, vessel diameter was varied in a branch of vessels in a level and pressure and flow through path A and path B were compared. Vessel diameter was halved for the first vessel of the first branch in level 2, simulating arteriosclerosis in that vessel. All vessels in the network has a compliance value of β=2. Steady state pressure and flow distributions are shown in Fig. 5.18. As illustrated in the figure, there is a clear difference in both the pressure and flow distributions for path A and path B with greater pressure and flow in path B due to less resistance encountered in this path. Fig. 5.19 shows capillary flow across time for paths A and B. Again, flow through path B is greater than path A. The dashed line in both figures represents the outputs for the case where diameter size is equal across all vessels within a level for a whole network compliance of β=2. A difference in pressure and flow can also be seen across these cases. This may be a result of the model predicting unstable flow dynamics in downstream capillaries due to arteriosclerosis in larger feeding arteries.

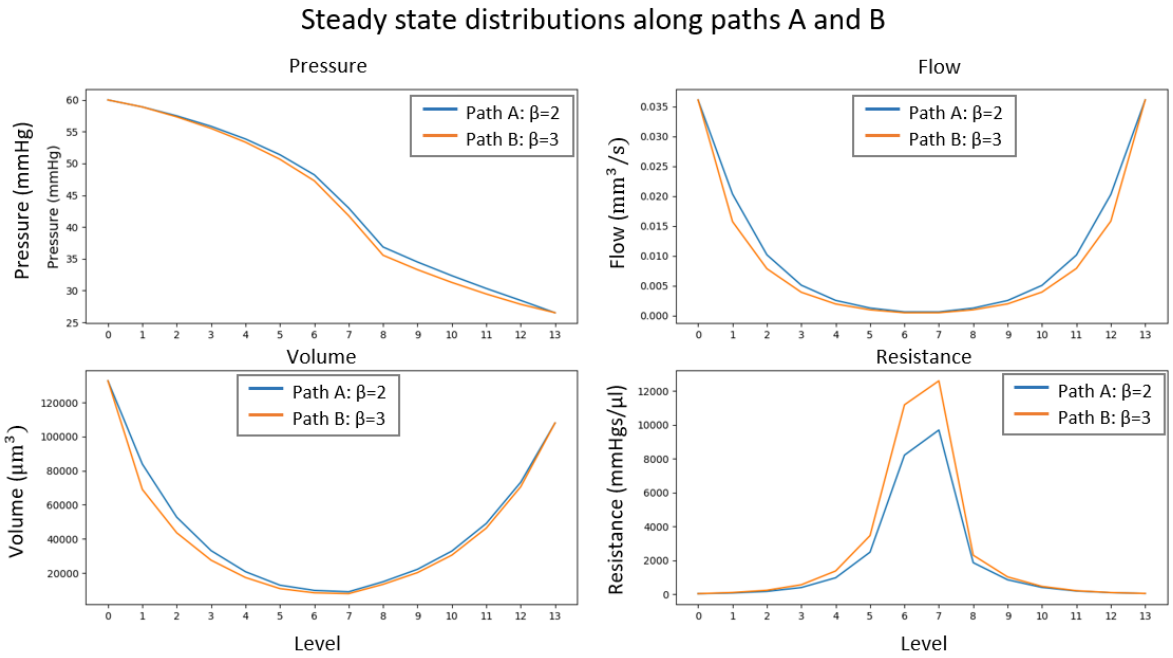

Fig. 5.16 Pressure and flow compared for paths A and B in the network. Vessels in the top half of the network have a compliance value of β=2 and vessels in the bottom half of the network have a compliance value of β=3.

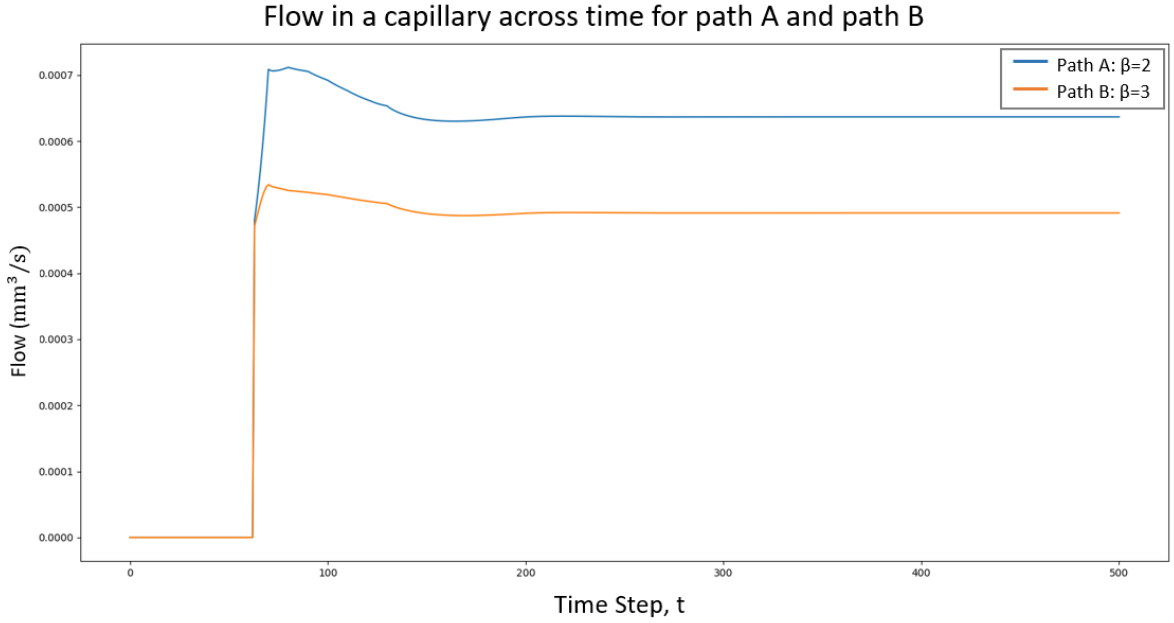

Fig. 5.17 Flow through the capillary across time compared for corresponding vessels in paths A and B. Compliance values for vessels in paths A and B are β=2 and β=3 respectively.

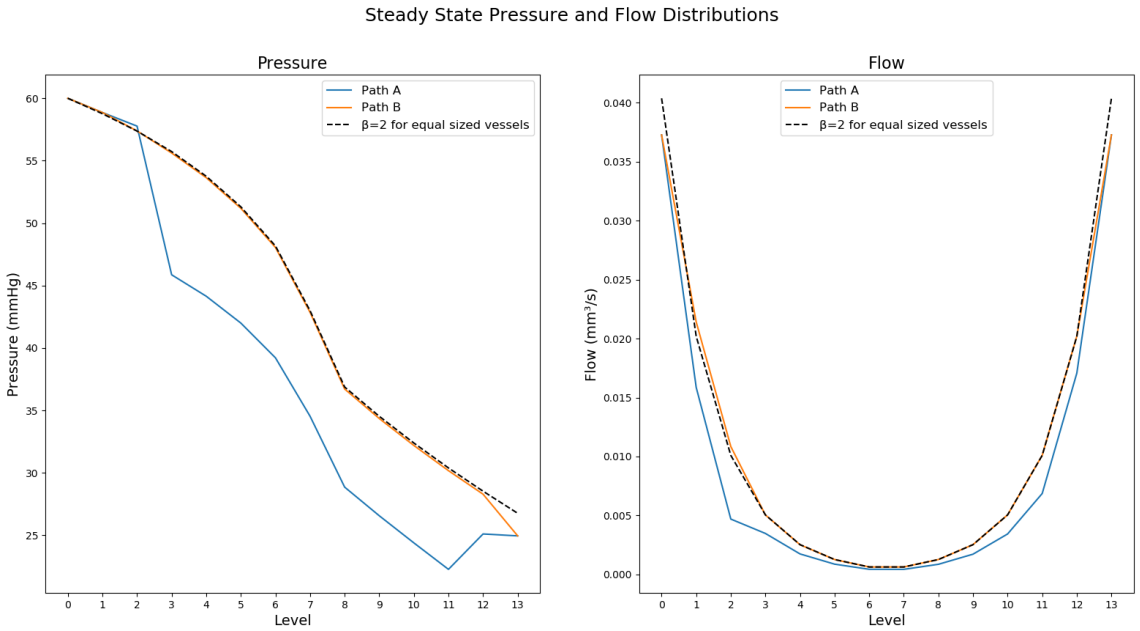

Fig. 5.18 Steady state pressure and flow distributions for path A and path B. Corresponding results for the case where vessel diameters are equal are shown by the dashed line for comparison.

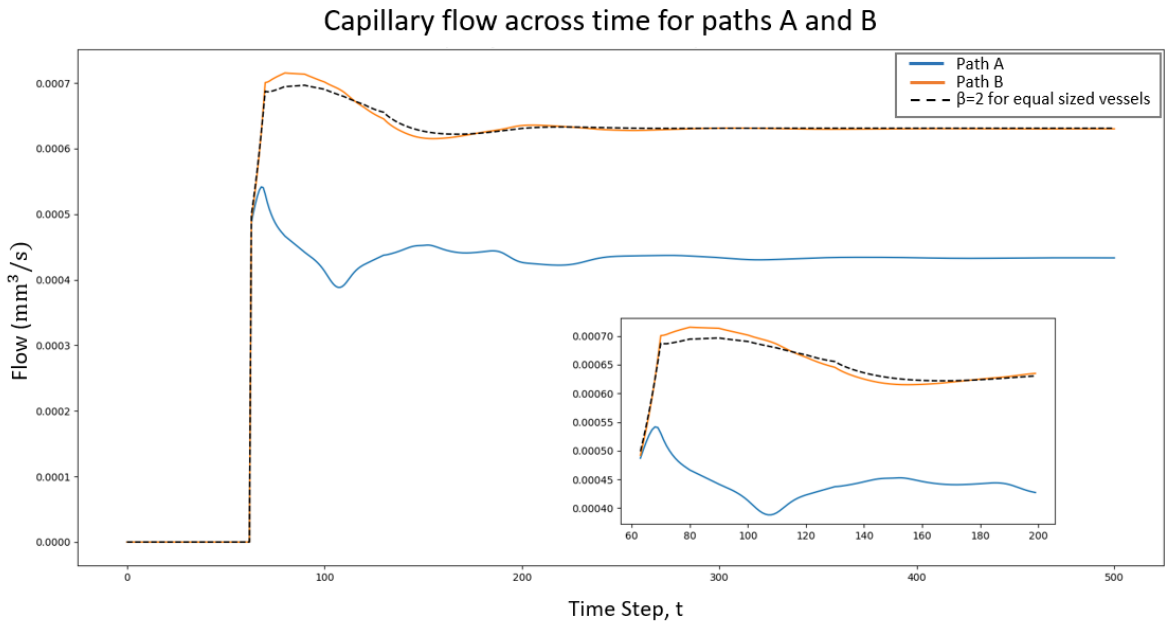

Fig. 5.19 Capillary flow across time for path A and path B. Corresponding results for the case where vessel diameters are equal are shown by the dashed line for comparison.

5.4 Discussion

Results presented in this chapter emphasise the importance of vessel compliance as a factor that should be taken into account when realistically modelling blood flow in cerebral vessels. To understand how pulsatility propagates through the network and how this is related to arterial stiffness, it is necessary to model changes in volume following changes in pressure. Existing models are limited in their ability to accurately model dynamic compliance related changes in flow. For this reason, passive changes in flow due to pressure changes were initially investigated in a large network of microvessels for a range of compliant network cases. Steady state simulations were carried out, firstly to validate the model by determining whether the model outputs were as expected and secondly, to limit model parameters for the microvascular section of the network for future macrovascular simulations.

Comparisons of the pressure and flow distributions across compliance values suggest that the model is working as expected. Pressure and flow values were greater for more compliant vessels (β=2) due to the greater volume increases for a given pressure increase. This relationship was also apparent when limiting values of compliance between 2 and 3. Results also highlight that flow in the network is influenced by the location of compliance in the network. The outputs obtained from varying compliance in sections of the network suggest that venule compliance had the smallest effect on flow in the whole network whilst arteriole and capillary compliance change the dynamics of whole network flow. Furthermore, capillaries appear to act as the bottleneck in the network. When exploring the effects of a compliant level of the network, flow values for compliant venule levels were closest to the corresponding values in the non-compliant network, suggesting that venule compliance can be disregarded in future simulations. Overall, results from the steady state simulations highlight the importance of knowing the state of the whole network.

Compliance was varied across levels of the network in a ramp up and down in β values as this was a more realistic approach to incorporating compliance in the model. Simulations were run for up and down ramps in compliance in both directions, so outputs for a capillary compliance of β=2 could be compared to β=3. Comparisons were made between capillary compliance values as it is unclear how compliant capillaries are in relation to the other vessels in the network due to the mechanisms that control capillary flow in the brain (Itoh and Suzuki, 2012). Results show that capillary compliance does have an effect on the pressure and flow distributions, with more compliant capillaries leading to greater flow in the network, as would be expected since they are the site of greatest resistance.

As a proof of concept, compliance was varied within vessels in a level to investigate how this influenced the distribution of flow across the network. Flow distribution through the network changed depending on the compliance of the vessels in each path. As expected, a greater amount of flow travelled through the more compliant vessels as this was the path of least resistance. In addition, flow in a network of vessels where vessel properties differed across a branch of a level was simulated. This was implemented by halving the diameter of a vessel in the branch to imitate

arteriosclerosis in the network. Again, pressure and flow were influenced by differences in volume and resistance within a level of the network with more flow in the path of least resistance. Interestingly, differences could also be seen between the flow in the unaffected path B in this case and flow in the corresponding compliance case where vessel properties within a level were equal. While the results appear to show the expected behaviour across the network, particularly when considering the distribution of flow across a network with different vessel properties, the validity of the outputs is limited by the lack of comparable studies. However, the results from this set of simulations demonstrate the potential of the model to simulate dynamic flow, particularly in pathological situations such as a vessel blockage.

5.5 Summary

In this chapter, simulations were run to explore the effects of vessel compliance on steady state pressure and flow in a network of cerebral microvessels. Compliance was varied across the network in a variety of ways, firstly to validate the model and secondly to characterise the model by investigating the influence of compliance in different sections of the network on changes in flow across the network. Outputs from the model suggest that arterioles and capillaries have a greater influence on changes in flow in the network compared to venules. Changes in flow across time indicate that flow is not just affected by local changes but also changes further along the network and therefore it is important to know the state of the whole network when modelling flow in compliant vessels. In addition, it was shown that the model can be used to investigate the distribution of flow in a network where vessel properties differ between vessels in a level. Conclusions from the steady state simulations presented in this chapter will be used in the next to limit the model for the dynamic simulations in a realistic network of cerebral vessels.

Chapter 6

Creating a Plausible Vessel Network

Chapter Overview

The network of microvessels created for the VAN model (Boas et al., 2008) offers a simplistic method for simulating flow through a group of branched vessels. However, to understand how the dissipation of pulsatile flow is related to arterial stiffness, a larger network of vessels is required, incorporating arteries and veins in addition to the microvessels. In this chapter, a more appropriate network, titled the 'Plausible Vessel Network', was constructed to model pulsatile flow across a larger section of the vascular network from the ICA and MCA to the microvessels. The stages of network development, including modifications made to the microvascular VAN network (Boas et al., 2008) will be explained in detail and initial outputs from the model using the Plausible Vessel Network will be presented. Values for vessel diameter, blood velocity and compliance found in existing literature were incorporated into the network when available and remaining values were calculated to ensure the expected flow and pressure distributions were achieved. The Plausible Vessel Network will be used to simulate flow across the ICA, MCA and microvessels to study the effect of vessel compliance on flow pulsatility in the brain. Dynamic simulations will then be paired with DIMAC data to estimate vessel compliance.

6.1 Introduction

The propagation of pulsatile energy from the large arteries to the smallest cerebral vessels is associated with cerebrovascular damage and the deterioration of brain health (O'Rourke, 2007). A key aim of the computational model developed for this thesis is to investigate pulsatility across the cerebrovascular tree, with a focus on blood travelling from the large arteries in the Circle of Willis to the capillaries. In a healthy network of vessels, pulsatile flow becomes steady once it reaches the capillaries. However, as a consequence of arterial stiffness this process becomes less efficient, leaving the cerebral microvessels exposed to potential damage caused by excessive pulsatile energy (Shirwany and Zou, 2010). Despite the mounting evidence suggesting that

arterial stiffness and pulsatility have a detrimental effect on brain health, it is still unclear how stiffness manifests within the cerebral vasculature. Additionally, studies are typically limited to measuring stiffness across the central systemic arterial system as a result of the methods available, and hence are not necessarily suitable for studying pulsatility in cerebral arteries.

A vessel network incorporating arteries, microvessels and veins was created in order to investigate the flow dynamics from the ICA to the microvessels using our model. The network was designed with the intention of fitting MRI data to the model which was collected in the ICA and MCA using DIMAC (Chapter 7). The updated network, titled the Plausible Vessel Network (PVN), maintained the structure of the bifurcating 14-level microvascular network used in the steady state simulations presented in Chapter 4, but was modified such that the first three and last three levels were now representative of the cerebral arteries and veins respectively. Values for vessel diameter, blood viscosity and blood velocity were taken from existing literature when possible (Boas et al., 2008; Donahue et al., 2017; Piechnik et al., 2008).

While the network is not physiologically accurate, the aim of the model was to estimate compliance in vessels using DIMAC data, along with PWV, rather than represent an anatomically accurate cerebral vascular network. Therefore, values for vessel lengths were set to achieve the chosen pressure gradients and flows along the network in order to replicate the experimental results from the DIMAC data. The network was also designed in such a way that the ICA bifurcated into the MCA and the remaining vessels in the Circle of Wills. This was to simplify the model while fitting DIMAC data collected in the ICA and MCA. While the inclusion of more vessels to represent the whole Circle of Willis would be more realistic, this would also introduce more unknown parameters into the model, greatly increasing the complexity. Given the aims of the model in this thesis, it was deemed sufficient to simplistically represent the vessel network in terms of the ICA and MCA.

Steady state simulations were run using the Plausible Vessel Network and pressure and flow outputs were compared across paths of blood flow and for a range of compliance values. Results from the steady state simulations were then used to choose appropriate values for vessel compliance across levels of the network.

6.2 Methods

The Plausible Vessel Network was developed and used as an input in the model to investigate flow pulsatility in the brain. Arterial and venous levels were defined in the new network to represent a larger region of the brain's vasculature. As before, a total of 14 levels of bifurcating branched vessels were used to represent the vessels of interest in the network. The network was split into three compartments: arteries (levels 0-2), microvessels (levels 3-10) and veins (levels 11-13). The pressure distribution across the network was updated to range between 120 mmHg and 11 mmHg to account for the inclusion of the larger vessels across a greater section of the vascular tree. Intracranial pressure was also adjusted to establish a large enough difference between this

Level	Number of Vessels	Vessel Category	Diameter Path A, Path B (μm)	Length (μm)	Viscosity Path A, Path B (cP)	Number of segments
0	1	Artery	4000.0	426630	2.5	10
1	2	Artery	4013.51, 1920.0	455072	2.5, 2.5	10
2	4	Artery	3374.95, 1614.52	455072	2.5, 2.5	10
3	8	Arteriole	69.8, 30.0	0.0175612	3.84, 2.5	10
4	16	Arteriole	44.8, 20.0	0.0199284	2.98, 2.26	10
5	32	Arteriole	21.3, 10.0	0.00149206	2.28, 2.12	10
6	64	Capillary	11.8, 5.6	0.000258512	2.15, 2.08	5
7	64	Capillary	11.8, 5.6	0.000543993	2.15, 2.08	5
8	32	Venule	32.7, 15.0	0.00640784	2.57, 2.18	10
9	16	Venule	69.8, 30.0	0.0204383	3.84, 2.5	10
10	8	Venule	99.9, 45.0	0.0199257	4.88, 2.99	10
11	4	Vein	752.5, 360.0	202.2	2.99, 2.99	10
12	2	Vein	6020.3, 2880.0	423777	2.99, 2.99	10
13	1	Vein	4500.0	122848	2.99	10

Table 6.1 Baseline input values for the Plausible Vessel Network. Diameter values for the MCA and ICA in blue were taken from Donahue et al. (2017). The diameter for the vein in level 13 (green) was taken from existing literature (Larson et al., 2020). Diameter values in orange were taken from the model by Piechnik et al. (2008). Diameter values in purple were calculated using Eqs. 6.2 & 6.3 for a given pressure gradient, flow and resistance. The diameters in Path A are larger to account for greater flow through this path due to the large vessel volume in level 1. Viscosity values in red were estimated using a linear interpolation function with viscosity values from Boas et al. (2008). Vessel lengths are unphysiological but were calculated to obtain the expected pressure distribution and flow values. Lengths were calculated from resistances which were obtained for a given pressure gradient and flow across each vessel (Eqs. 6.2 & 6.3). Lengths were kept equal across all vessels in a level.

value and the network output pressure for the model to run without errors. The methods used to obtain the network parameters for each compartment are described in the following subsections. Parameters for the Plausible Vessel Network are summarised in Table 6.1.

6.2.1 Compartment 1: Arteries

Cerebral arteries of interest were represented across the first three levels of the Plausible Vessel Network. In order to model pulsatile flow entering the brain, a network incorporating the ICA and the Circle of Willis was desired. To achieve this, the first level of the network represented the ICA which branched into two vessels in the second level: the MCA and a single vessel representing the remaining vessels in the Circle of Willis. The MCA was isolated from the remaining arteries in the Circle of Willis in level 1 for the purpose of incorporating DIMAC data obtained for the ICA and MCA in Chapter 7. Each vessel in level 1 branched into a further two vessels in the following level resulting in a total of 7 vessels in Compartment 1, representing the arterial side of the vascular tree. See Fig. 6.1 for further detail.

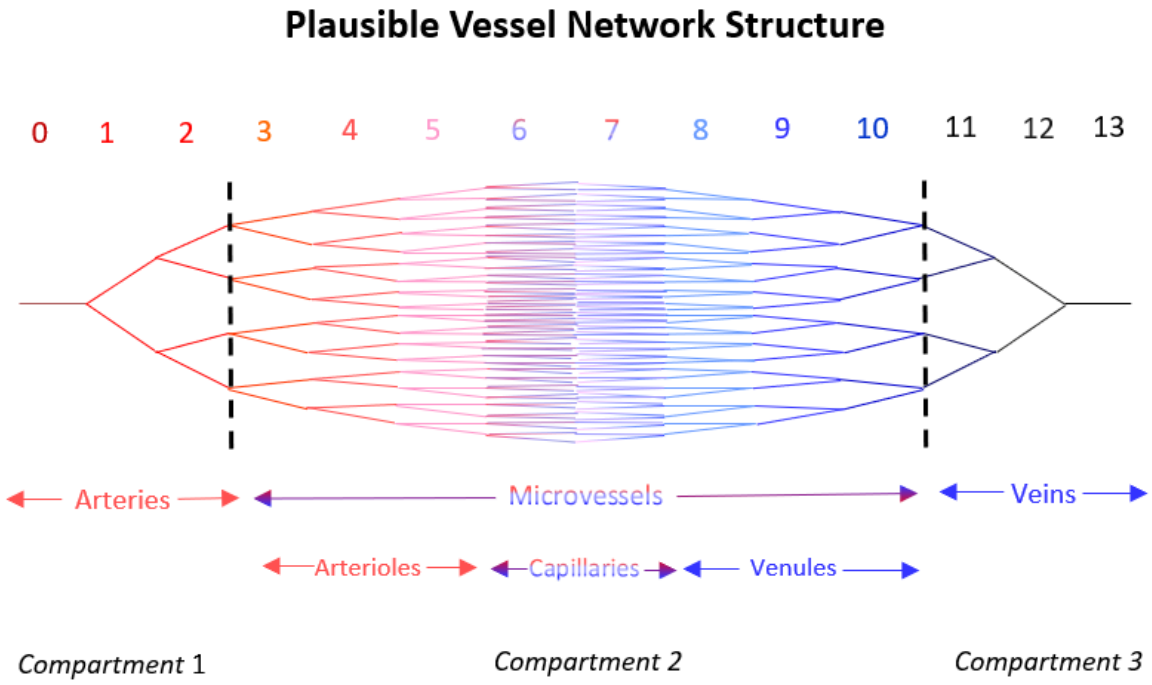

Fig. 6.1 Diagram showing the corresponding levels to each compartment within the Plausible Vessel Network.

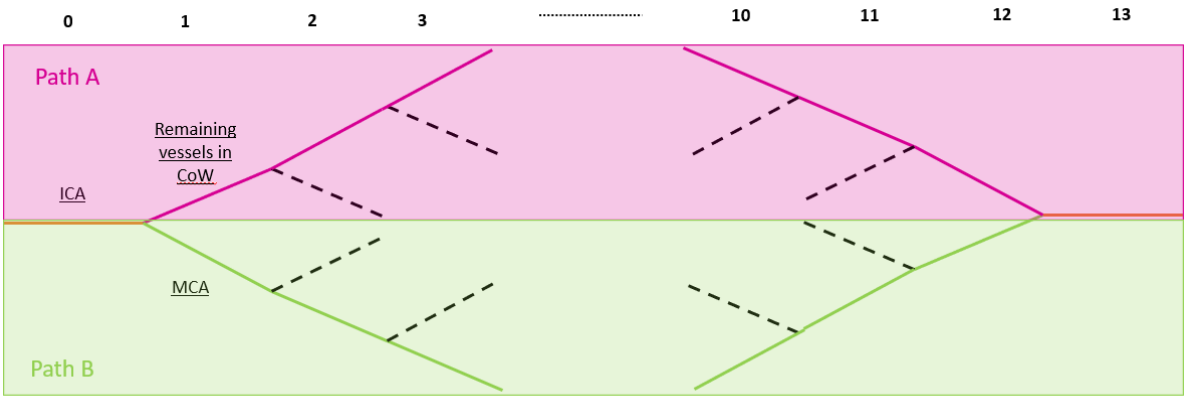

Fig. 6.2 Diagram indicating the vessels belonging to Path A (pink lines) and Path B (green lines) in the network. The first and last vessel in the network belong to both paths.

Values for the vessel diameters and corresponding blood velocities for the ICA and MCA were taken from existing literature (Donahue et al., 2017; Piechnik et al., 2008). The baseline ICA diameter was chosen to be 4 mm with a blood velocity of 1250 mm/s and baseline MCA diameter was 1.92 mm with a blood velocity of 270 mm/s. A viscosity value of 2.5 cP was used for all vessels in this compartment as this was the viscosity for the largest arteriole in the microvascular compartment. Viscosity was assumed to stay constant across diameter changes in the macrovessels. Eq.6.1 was used to calculate flow through the ICA, which was the total bulk flow through the system in steady state. Flow through the MCA was calculated using the same method. As the ICA in level 0 was designed to split into the MCA and the remaining vessels in the Circle of Willis, due to the conservation of flow, flow through the remaining vessel in level 1 was calculated by subtracting the MCA flow from the ICA flow.

$$F = vA \tag{6.1}$$

Assuming a linear pressure drop from 120 mmHg to 60 mmHg across the arteries (to match the starting pressure in the microvasculature), pressure inputs for each level were fixed as 120 mmHg, 100 mmHg and 80 mmHg for levels 0, 1 and 2 respectively. Using the change in pressure across levels 0 and 1 and the flow in level 0, resistance to flow in the ICA was calculated using Eq. 6.2. Diameter and viscosity values were used to calculate a suitable length for the ICA using the Poiseuille equation (Eq. 6.3). The method was repeated to calculate a length for the MCA. To keep lengths equal across all vessels within a level, the same length was used for the remaining vessel in level 1. Using the resistance across the vessel (Eq. 6.2) and the blood viscosity and length, a corresponding vessel diameter was calculated (Eq. 6.3) for this vessel. Vessel lengths are not anatomically accurate but were calculated to obtain the expected pressure distribution and flow values, thus are only representative of the corresponding vessel(s).

$$R = \frac{\Delta P}{F} \tag{6.2}$$

$$R = \frac{128\eta l}{\pi d^4} \tag{6.3}$$

A similar approach was followed to obtain diameters for the vessels in level 2. Flow through the corresponding vessel in the previous level was assumed to be split equally across each branched vessel, hence flow was greater in the vessels in the first branch due to the larger volume of the first vessel in the preceding level. Resistance for each vessel was calculated using flow and the difference between the input pressure (80 mmHg) and output pressure (60 mmHg) for the level. Lengths were kept equal to the values in level 1. Vessel diameters were calculated using length, viscosity and resistance (Eq. 6.3).

6.2.2 Compartment 2: Microvessels

Arterioles, capillaries and venules were represented in levels 3-10 of the Plausible Vessel Network. Vessel diameters were taken from the vascular network developed by Piechnik et al. (2008). Feasible input pressures for the 8 microvascular levels in the network were interpolated from the steady state input pressures and diameters in the VAN model (Boas et al., 2008) using a spline function.

In every diverging level, flow from the previous vessel in the corresponding path was split equally between the vessels in subsequent branches. Flow values from corresponding vessels in the previous levels were added together for vessels in the converging levels. Resistance was calculated using the pressure gradient and flow across a vessel. A linear interpolation function was used with viscosity and diameter values from the VAN model (Boas et al., 2008) to estimate blood viscosities for the microvessel diameters in this network. Vessel lengths were calculated using the Poiseuille equation (Eq. 6.3).

To keep vessel lengths equal within a level as in Compartment 1, vessel diameters for the top half of the network were recalculated to accommodate a greater amount of flow across this section of the network. Recalculating diameters in the top half of the network required a modified approach for vessels in Compartment 2 due to blood viscosity varying with diameter in the microvessels. The apparent viscosity of blood in vessels with diameters typically less than 300 μm decreases with decreasing diameter due to the Fahraeus-Lindqvist effect. Haematocrit (the volume percentage of red blood cells in the blood) is reduced in vessels of this size compared to larger arteries as red blood cells move towards the centre of the vessel where they also travel faster (Secomb, 2017). A reduction in haematocrit contributes to a lower viscosity.

For a given resistance, calculated previously using the pressure gradient and flow, and vessel length taken from vessels in the bottom half of the same level, resistance was calculated for a range of appropriate diameters using Eq. 6.3. Suitable diameters for vessels in each level were selected by choosing the closest matching diameter for the required value of resistance. Viscosity was calculated for each chosen diameter using the interpolation function described above.

6.2.3 Compartment 3: Veins

The final vessel in the network (level 13) was chosen to represent the superior sagittal sinus with a diameter of 4.5 mm (Larson et al., 2020). Suitable diameters between this and the vessels in the last level of Compartment 2 were chosen for vessels in levels 11 and 12 and were taken from the vascular network developed by Piechnik et al. (2008). A value of 2.99 cP was used for blood viscosity for all vessels in this compartment. The viscosity value was selected by using the same approach as for the arteries (using the viscosity for the largest venule in the VAN model (Boas et al., 2008)) and was kept the same for all vessels in this compartment. Blood viscosity was larger in the veins in comparison to the microvessels and arteries as the veins have larger diameters. Flow into each vessel was calculated as the sum of the flow values from vessels in

the corresponding path of flow in the previous level. Pressure was assumed to decrease linearly across the veins, starting at 24 mmHg and ending at 11 mmHg. Resistance in each vessel was calculated using the pressure difference and flow (Eq. 6.2) and vessel length was calculated using Eq. 6.3, as described for the previous compartments. Vessel diameters in the top half of the network were adjusted to keep lengths consistent across levels using the same method described for Compartment 1.

6.2.4 Vessel Compliance

Realistic values for vessel compliance were determined for vessels in each compartment of the updated network. Appropriate values for ICA and MCA compliance were obtained from existing literature and converted to units complying with our model. Arterial compliance values are commonly reported as a change in cross-sectional diameter or volume per mmHg change in blood pressure. In a study by Warnert et al. (2015) which assessed compliance in the cerebral arteries using ASL, left MCA compliance was calculated as a 0.5% change in arterial blood volume per mmHg change in blood pressure. A value of 9.79 μm per mmHg was measured as the change in cross-sectional diameter in the carotid artery in a study by Salvi et al. (2022). Using 4 mm as the baseline diameter for the ICA in the network, the equivalent ICA compliance was calculated as a 0.49% change in volume per mmHg.

$$\frac{P_i - P_{IC}}{P_0 - P_{IC}} = \left(\frac{V_i}{V_0}\right)^{\beta} \tag{6.4}$$

The values of compliance stated above were converted to corresponding β values for use in this model using Eq. 6.4, taken from the VAN model (Boas et al., 2008) and defining V_i in terms of V_0 (See Chapter 4 for further details). Using 120 mmHg as the input pressure, P_i, 60 mmHg as the baseline arterial pressure, P_0 and 7 mmHg as the intracranial pressure, P_IC, ICA compliance was calculated as β=151.8. To obtain a suitable input pressure for level 1, the steady pressure distribution was simulated using the Plausible Vessel Network with ICA compliance, whilst all remaining vessels were non-compliant (β=100000). Following this, a value of 100.6 mmHg was used as the input pressure, P_0, into the MCA and a value of β=114.1 was calculated as the compliance for this vessel. The MCA compliance was also used for the remaining vessel in level 1 as vessels in close proximity to each other are expected to be similarly compliant.

Venous compliances were chosen to match corresponding symmetrical arterial values, for example the compliance in level 13 was equivalent to level 0. Following the results from the steady state simulations presented in Chapter 4, it is apparent that venule compliance has little effect on the dynamics of the system and therefore it can be assumed that compliant veins also do not affect the system significantly. Setting venous compliance to match arterial compliance was deemed appropriate as this allows the veins to adjust their volume enough to allow flow out of the system. To choose a suitable value of compliance for level 2, steady state simulations were

run for β values of 10, 50 and 100 in level 2 (and 11) with microvascular compliances of β=2, 3 and 100000, and the simulated pressure distribution was compared to the expected pressure distribution for each case. The expected pressure distribution was defined as the input pressures chosen for the development of the Plausible Vessel Network (see Methods section).

Initial outputs obtained from the steady state simulations suggest the microvascular compliance values used for the simulations presented in Chapter 4 were no longer appropriate for the updated network. To further investigate the effect of microvascular compliance on the steady state pressure distribution for the network, simulations were run for β=3, 10, 50 and 100 in the microvessels. A compliance value of β=100 was used for the vessels in level 2 as this was similar to the compliances for levels 0 and 1. Simulated pressure distributions were compared to the expected pressure distribution for paths A and B. See Fig.6.2 for diagram showing vessels in paths A and B. After examining the outputs, simulations were run for values of β between 3 and 10 in Compartment 2 (microvessels) and Root Mean Square Error was calculated for each case using the expected pressure distribution to select the most appropriate compliance value for the microvessels (i.e. the compliance value that resulted in the smallest error).

6.3 Results

Steady state pressure distributions were obtained for a range of compliant networks to select the most suitable values for each compartment. Level 2 compliance was determined by obtaining the simulated pressure distribution for β values of 10, 50 and 100 in level 2 for microvascular compliances β=2, 3 and 100000. Pressure distributions were compared to the expected pressure distribution for the network (i.e. the chosen input pressures for every vessel to create the PVN) and are presented in Fig. 6.3. For both paths A and B, the pressure dropped considerably across the arteries in the cases where β=2 and 3 in the microvessels while the pressures were more closely matched to the expected pressure distribution when microvessels were non-compliant (β=100000). In addition, compliance values of β=50 and 100 in level 2 resulted in similar output pressure distributions which suggests the amount of compliance in this level does not have a significant effect on the system. Therefore level 2 compliance was chosen as β=100 as this was similar to the compliance values used for the other vessels in Compartment 1.

After setting level 2 compliance as β=100, the effect of microvascular compliance on the steady state pressure distribution was further explored by obtaining simulated pressure distributions for values of β=3, 10, 50 and 100 in the microvessels. The pressure distribution was compared to the expected pressure distribution for paths A and B and shown in Fig. 6.4. For both paths A and B, the simulated pressure distribution was closest to the expected pressure distribution when the microvessels had a compliance of β=10. Microvessel compliances were then compared for β values between 3 and 10. Pressure distributions are compared to the expected pressure distribution in Fig. 6.5. Root Mean Square Error was calculated for each compliance value and results were plotted against values of β (Fig. 6.6). The results confirm that β=10 is the

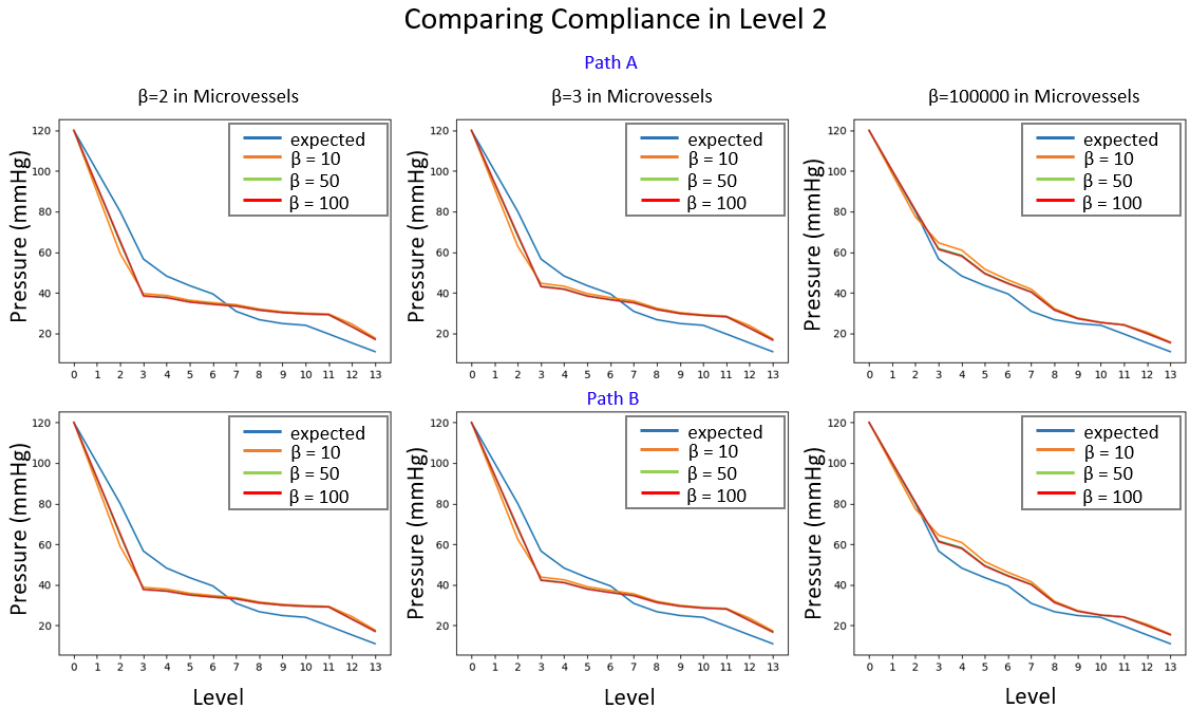

Fig. 6.3 Steady state pressure distributions along path A (top panel) and path B (bottom panel) compared for different compliance values (β=10, 50, 100) in level 2 for three microvascular compliances (β=2, 3, and 100000). The pressure distribution is compared to the expected pressure distribution in each case.

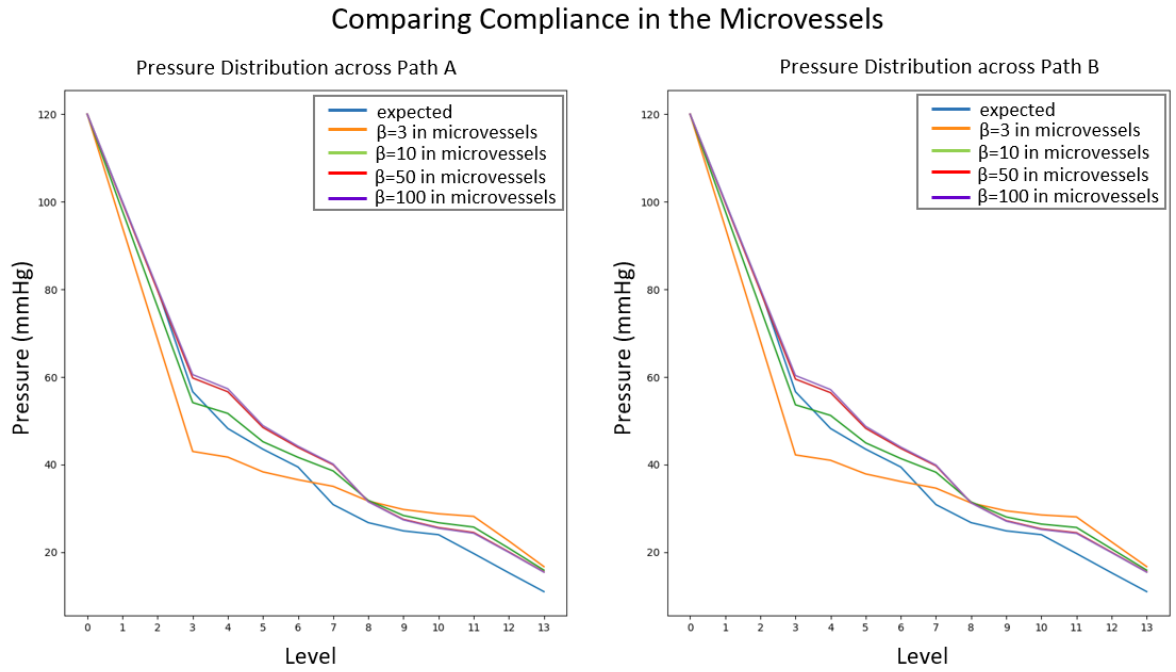

Fig. 6.4 Steady state pressure distributions along path A (left) and path B (right) compared for values of microvessel compliance (β=3, 10, 50 and 100).

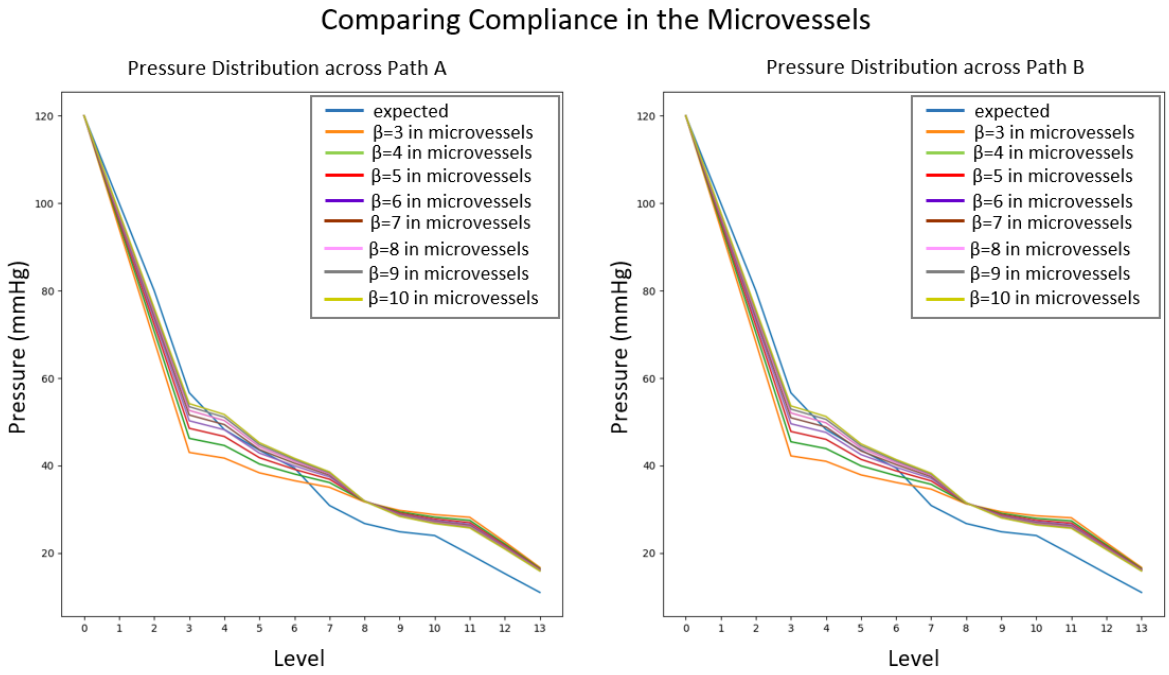

Fig. 6.5 Steady state pressure distributions along path A (left) and path B (right) compared for values of microvessel compliance (β=3, 4, 5, 6, 7, 8, 9 and 10).

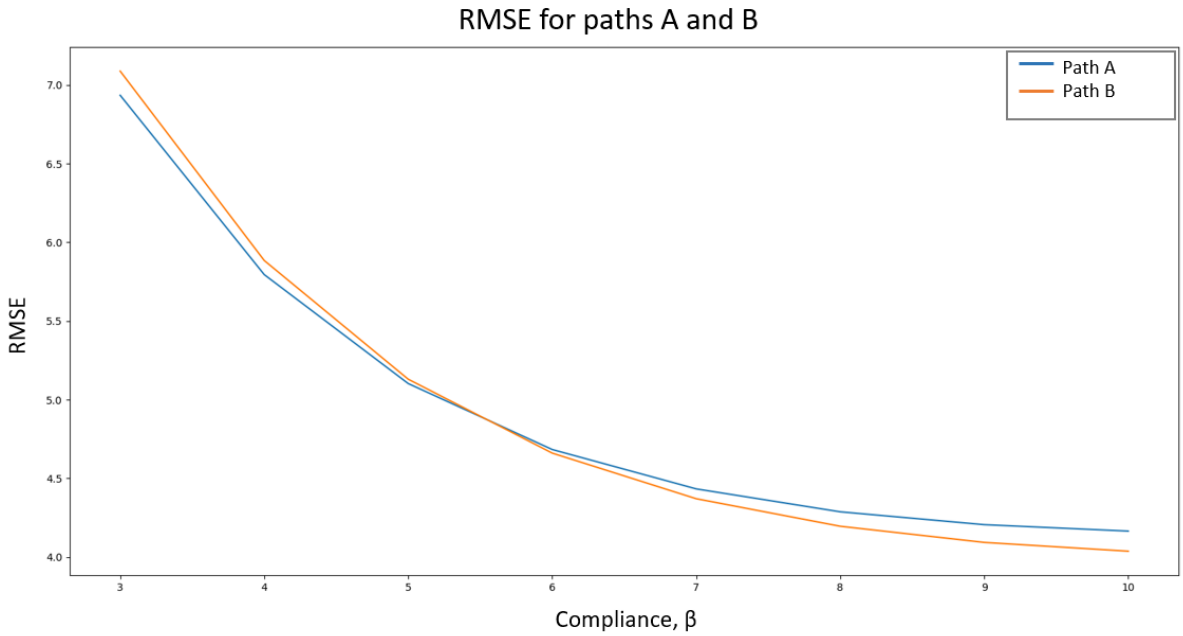

Fig. 6.6 Root Mean Square Error calculated using the expected pressure distribution for β=3, 4, 5, 6, 7, 8, 9 and 10 in the microvessels.

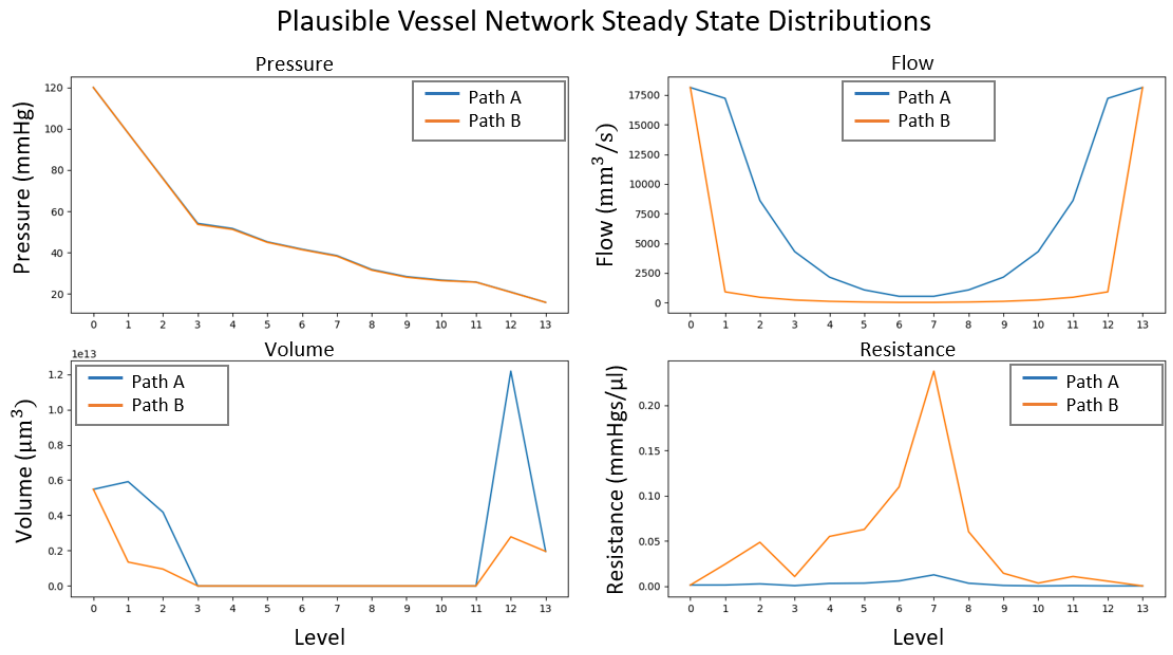

Fig. 6.7 Steady State Pressure, Flow, Volume and Resistance distributions for the Plausible Vessel Network using the chosen compliance values in each compartment.

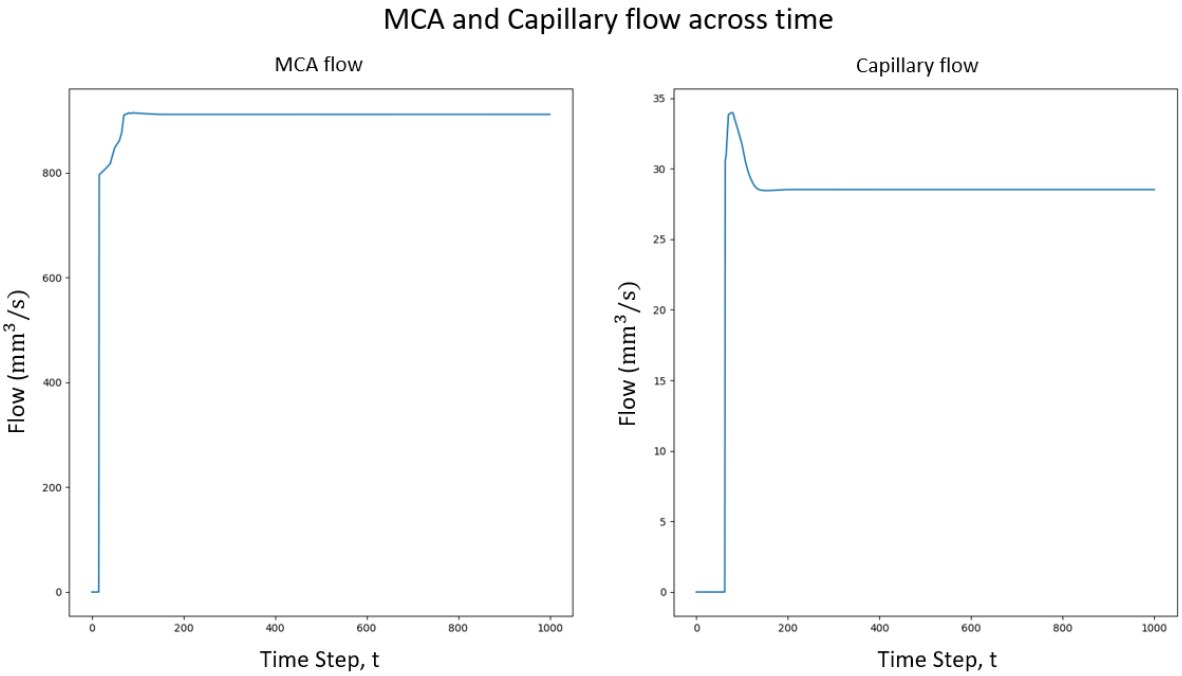

Fig. 6.8 Flow in the MCA and capillary (level 6) across time.

most appropriate compliance value for the microvessels (when β=100 in level 2) as the RMSE was the smallest for this case for both paths A and B.

Simulations were run using the chosen compliance values for the network and steady state pressure, flow, volume and resistance distributions were obtained. Fig. 6.7 compares the distributions along paths A and B. As expected, there is a difference between paths A and B for all distributions. Due to the larger volume of the vessels and therefore less resistance in path A, there is greater flow through this path compared to path B.

Flow in path B was compared across time for a step change in pressure for two vessels, the MCA and the capillary (level 6) and results are shown in Fig. 6.8. Similarly to outputs from simulations in the microvascular network, flow in both the MCA and the capillary did not reach a steady value instantaneously and instead increased across time due to compliance in the network before becoming constant and reaching an equilibrium.

6.4 Discussion

Compliance values for Compartment 1 of the Plausible Vessel Network were calculated using arterial compliance values found in existing literature and simulations were run to choose a reasonable compliance value for vessels in level 2. Comparisons between the simulated pressure distributions suggest that compliance in level 2 of the network is not as influential on the system as initially expected. Level 2 compliance was compared across three values of β in the microvessels. In each case there was a small difference in pressure distributions for β=10, 50 and 100 in level 2, however a greater difference could be observed depending on whether the microvessels were compliant (β=2 and 3) or non-compliant (β=100000). Results highlight that microvessel compliance is more significant than level 2 compliance when considering the dynamics of the system for this network.

Results from steady state simulations suggest that vessel compliance for the microvascular compartment of the network required adjustment compared to the microvessel network used in Chapter 4. Initially, β for the microvessels was thought to be between values of 2 and 3. However, comparing the simulated pressure distributions to the expected pressure distribution suggests that the microvessels are too compliant in this network for compliance values in this range. This is likely to be a consequence of the addition of substantially larger vessels in the Plausible Vessel Network. The adjusted microvascular compliance values in this network reflect the considerable influence of the larger vessels on the dynamics of the system.

Simulations were run once compliance values had been chosen for each compartment of the network. Steady state distributions highlight the differences in pressure, flow, volume and resistance across paths A and B as a result of splitting the vessel volume and hence flow disproportionately in level 1 of the network. The steady state outputs from the model indicate that flow is much greater in path A compared to path B due to the larger diameter of the vessels and hence less resistance encountered through this path. Flow through the MCA and

capillary was also plotted. Similarly to results obtained from the steady state microvascular simulations presented in Chapter 4, both MCA and capillary flow did not reach a constant value instantaneously, suggesting that flow in the realistic network is also influenced by the dynamics of the system due to compliance and flow across other parts of the network may affect what is happening at a particular level.

The Plausible Vessel Network was created by choosing realistic parameters where possible, with values for vessel diameter, blood velocity, blood viscosity and compliance taken from existing literature when available. In the remaining cases, appropriate values were estimated using a variety of methods to match the outputs to expected results. Therefore the network is not completely realistic in nature due to the fact that there are many degrees of freedom and no unique solution. In addition, limitations were placed on the structure of the network and therefore does not accurately reflect the true anatomy of the vessels in the brain.

One example of this is only allowing the vessels to bifurcate at branch points. However, it has been suggested that capillaries split into more than two vessels (Smith et al., 2019), hence the network could be considered too simplistic. Furthermore, all vessels in the network had branched structures which may also be considered as a simplification as this is not representative of the vascular structures in the brain. While other models have incorporated mesh-like connections at the capillary bed (Linninger et al., 2013), this feature is not necessary for the purposes of this model as the aim is to understand the propagation of pulsatility from the large arteries up to the capillaries. Therefore, the specific anatomical details at the capillaries are not needed in this model, however, would be highly relevant when modelling processes such as oxygen exchange at the capillary bed. Treating all types of vessels within the network the same limits the accuracy of the model in comparison to other models of blood flow in the Circle of Willis, however the network was designed using the simplest approach possible to obtain estimates of compliance from DIMAC data.

A simplified approach was also taken to isolate the MCA from adjacent vessels by treating the remaining vessels as one lumped vessel within the level. The grouping of multiple arteries forming the Circle of Willis is unrealistic in terms of vessel anatomy, but was chosen to allow for MRI data to be fitted to the model in future simulations in Chapter 7. This is not a dissimilar approach to lumped parameter models that exist in the literature (Buxton et al., 1998; Mandeville et al., 1999).

The total number of levels in the network was preserved from the microvascular network. This meant that there was an unrealistic jump between the arteries and arterioles due to using fewer branches than expected between the two categories of vessels. This is particularly evident in the steady state volume and resistance distributions. Levels could be added to construct a more realistic vascular network. However this was not necessary for the purpose of the simulations presented in this thesis as we are interested in changes in flow across large arteries and the capillaries. Changes could be made to the Plausible Vessel Network to more accurately represent

the cerebral vasculature but the purpose of the simulations and the computational running costs should be considered.

Due to the complexity of the cerebral vascular tree it was necessary to place these limitations on the structure for use in our model. Our approach of updating segments throughout the network for each time step to determine compliance-related volume and flow changes, would make any advances towards a more realistic vascular network very computationally expensive. Despite this, the network produces outputs that are sufficient for the purpose of our simulations as demonstrated by the outputs from initial steady state simulations. Moreover, the network has been set up to distribute flow appropriately between the ICA, MCA and remaining vessels in the Circle of Willis and this is an important factor for future simulations presented in Chapter 7.

6.5 Summary

The Plausible Vessel Network was created to investigate blood flow dynamics across a larger region of the cerebrovascular tree, from the large arterial structures such as the ICA and the Circle of Willis to the capillaries. Values for vessel diameter, blood velocity and arterial compliance, found in existing literature, were incorporated into the network to represent the vasculature more accurately. Remaining vessel properties were calculated to ensure that the expected pressure and flow distributions along the network were achieved. The network was constructed in such a way to allow for flow to be simulated through the ICA, MCA and microvessels which is important when investigating pulsatile flow across time in a compliant network of vessels. Initial results from the steady state simulations highlight differences in pressure, flow, volume and resistance across paths of the network.

The development of the Plausible Vessel Network will allow for pulsatility to be investigated across the cerebral vasculature, with a focus on blood flow in the ICA, MCA and the capillaries (Chapter 7). In addition, dynamic simulations using the network will be paired with DIMAC data to estimate vessel compliance (Chapter 8).

Chapter 7

Dynamic Simulations

Chapter Overview

Pulsatile flow is dampened as blood travels from the large arteries to the capillaries in order to reduce damage at the blood-brain barrier due to increased shear stress at the endothelial surface. As arteries become stiffer with age and disease, this process becomes less efficient. Studying changes in the flow profile across a network of vessels may aid the understanding of where pulsatility is dampened and how this corresponds to changes in cerebrovascular health. In this chapter, the results from dynamic simulations are presented for two investigations where compliance is varied across the network. Changes in the shape of the flow profile were compared across large arteries and the capillaries and quantitative values of flow pulsatility were calculated. Results from the dynamic simulations highlight the importance of considering the input pressure wave, including the length of the wave and the number of time steps across a beat in relation to the number of segments in the vessel. Simulations were run to study flow pulsatility and results suggest that pulsatile energy was dampened across the compliant network to some extent, despite the flow profile still appearing pulsatile in the capillaries. Understanding the dynamic behaviour of the network, such as the corresponding changes in flow following a pressure change, is an initial step in using the model to analyse DIMAC MRI data.

7.1 Introduction

Blood flow varies across the cerebral vessels with pulsatile flow from the arteries becoming more steady and continuous once it has reached the microvessels. Changes in the flow profile can be investigated to assess the health of blood vessels in the brain, with flow pulsatility becoming an increasingly important clinical marker of cerebrovascular health due to its association with increased arterial stiffness. Changes in blood flow across a network of vessels may aid the understanding of where pulsatility is dampened within the network, as well as the corresponding changes when vessels become less compliant. This, in turn, could contribute to understanding

the mechanisms behind declining vessel health in the brain relating to the development and progression of cerebrovascular disease.

Simulations were previously run for a network of microvessels to compare steady state flow for a range of compliant network cases (Chapter 4). Steady state flow was also investigated in a network of vessels encompassing a greater section of the vasculature to find suitable compliance values for vessels (Chapter 5). In this chapter, to explore changes in flow across time in the Plausible Vessel Network (PVN), dynamic simulations were run for a range of compliant network cases. A pulsatile pressure wave was inputted into the model to assess changes in flow in the network, with a particular focus on flow in the ICA, MCA and capillaries. Compliant vessels are expected to dampen pulsatility across the arteries, resulting in blood flow becoming steadier when it reaches the capillaries. Compliance was varied in different levels of the network and output flow waveforms obtained from the model were compared across time. Outputs from the simulations were used to characterise the dynamic behaviour in a compliant network of vessels. Understanding the dynamic behaviour is an initial step in using the model to analyse DIMAC data collected in the ICA and MCA (Chapter 7).

7.2 Methods

Simulations were run to characterise the dynamic behaviour of flow through compliant vessels for an input pressure wave varying with time. A pulsatile pressure wave was used as an input into the model to represent a pulse wave travelling from the heart towards the cerebral vessels. The purpose of this was to simulate changes in flow across time resulting from the changes in pressure related to the cardiac cycle. A key aim of the model is to investigate the pulsatility of flow across the network and the effect of vessel compliance. For this reason simulations were run, firstly to assess whether changes in the flow profile shape could be observed when comparing flow at the start of the network in the ICA to flow in the microvessels (capillaries), and secondly to investigate whether this was dependent on the amount of vessel compliance and the location of the compliant vessels within the network. The dampening of pulsatility was investigated across the network by comparing the output flow time series in the ICA, MCA and capillary, and also in the vessels of interest across time by comparing flow across beats. All simulations were run using the Plausible Vessel Network defined in Chapter 5 as the input vessel network.

7.2.1 Investigation 1: Changes in the shape of the flow profile

One approach to assessing pulsatility across the network is to investigate changes in the shape of the flow profile across vessels. As pulsatile flow travels through a network of compliant cerebral vessels it becomes less pulsatile, with flow becoming steadier once it reaches the capillaries due to the dampening of the pulsatile energy across the arteries. This was expected to be observed through changes in the the shape of the flow profile, firstly across levels in the network and

secondly across time. For example, flow was expected to look pulsatile at the start of the network in the ICA and eventually flatline in the capillaries following the attenuation of the pulse wave travelling through the vasculature as a result of vessel compliance.

Initial simulations were run using the baseline compliance values determined for the Plausible Vessel Network in steady state (refer to Chapter 5). Compliance was then added to chosen levels of the network, firstly one level at a time and then as a combination of levels. Compliance in the chosen level(s) was initially set as a value of β=2.

Investigating Arterial and Capillary Compliance

The addition of arterial compliance and venous compliance was initially investigated separately to assess whether compliance in either of these locations caused a significant change in flow. Compliance was originally varied in levels 1, 2, 6 and 7 to investigate whether shape changes in flow could be achieved by increasing the amount of compliance in the MCA (and the remaining vessel in level 1), downstream arteries (vessels in level 2) and capillaries (levels 6 & 7) respectively.

Investigating Venous Compliance

Compliance was added to the venules and veins to explore whether changes in flow across the ICA, MCA and capillaries were dependent on the amount of downstream resistance in the network. Compliant venules and veins in the network may act as a sink to absorb pulsatile energy from the system. This was assessed, firstly by making levels 11 and 12 compliant one at a time, and then setting all venules and veins to be compliant. The amount of venous compliance was also compared by varying values of β between 1 and 2. Flow profiles for each compliant network case were compared to the output flow for the baseline compliance values.

Investigating Compliance in Multiple Levels of the Network

Further simulations were run to explore whether shape changes occurred when compliance was added to a single level as well as the venous levels. Compliance was then added to the MCA, level 2 and capillaries as well as the venules and veins and outputs were compared across each case.

Modifying the Input Pressure Wave

Outputs from the first set of simulations show large jumps and fluctuations in flow within approximately the first 200 time steps, with flow settling after this point to reach an equilibrium state. The reason behind this pattern is unclear. To see whether the large fluctuations in flow at the beginning of the simulations were a result of the sudden increase in pressure from 11 mmHg (at t=0) to 80 mmHg, the range of the pulsatile pressure input was adjusted to 15 and 55

mmHg. Another approach was to adjust the pressure wave by adding periods of constant diastolic pressure (80 mmHg) between beats. To investigate why flow was reaching an equilibrium state after approximately 200 time steps, Gaussian noise (mean=0, standard deviation=1) was added to the input pressure wave to introduce random changes in pressure across time. The purpose of this was to introduce measurement noise, rather than a change in the pressure wave. Output flow values for each of the modified input pressure waves was compared across different compliant network cases.

Introducing a Time Delay

A time delay was introduced to assess whether an instantaneous change in volume and resistance following a change in pressure was causing the system to reach an equilibrium state. This was achieved by repeating each value in the pressure wave either 2, 3, 4 or 10 times such that the pressure wave would appear to take 2, 3, 4 or 10 times as long to pass through the vessel. Simulations were run using the Plausible Vessel Network with a standard number of segments and then repeated with a network where the number of segments was also increased by the same multiple as the repeated points in the input pressure wave. For the first set of simulations where segments and pressure points were increased by a factor of 2, 3 and 4, outputs from the baseline compliant network were compared to the network with the addition of venous compliance (β= 2). In the case where segments and pressure points were increased by a factor of 10, an input network with venous and capillary compliance (β=2) was used.

The input pressure wave for the initial simulations is shown in Fig. 7.1. This was modified for the cases relating to the investigation of flow reaching an equilibrium state. Flow across time was plotted in the ICA, MCA and capillary to compare shape changes in the flow profile across the network and across time. The percentage change in flow was calculated using the mean flow for each vessel of interest and also plotted across time.

7.2.2 Investigation 2: Buffering of pulsatile energy across the network and across time

A quantitative measure was required to obtain a more detailed understanding of how pulsatility was dampened across time in the network. Initially, a modified version of the Pulsatility Index (PI) was considered. Flow Pulsatility Index (FPI) was defined in a similar way to PI, a metric commonly used in TCD studies, however in this case values of absolute flow obtained from the model were used instead of blood flow velocity values (Eq. 7.1). However, on reflection this was deemed to be an unsuitable index for comparing pulsatility across different vessels, as it normalises pulsatility to the mean signal, thus neglecting any reduction in pulsatile energy. Pulsatile power and steady state power were used as more appropriate measures.

Pulsatile power (Eq. 7.2) is defined as the product of the pressure and flow whilst steady state power (Eq. 7.3) is defined as the product of the mean pressure and mean flow over the cardiac

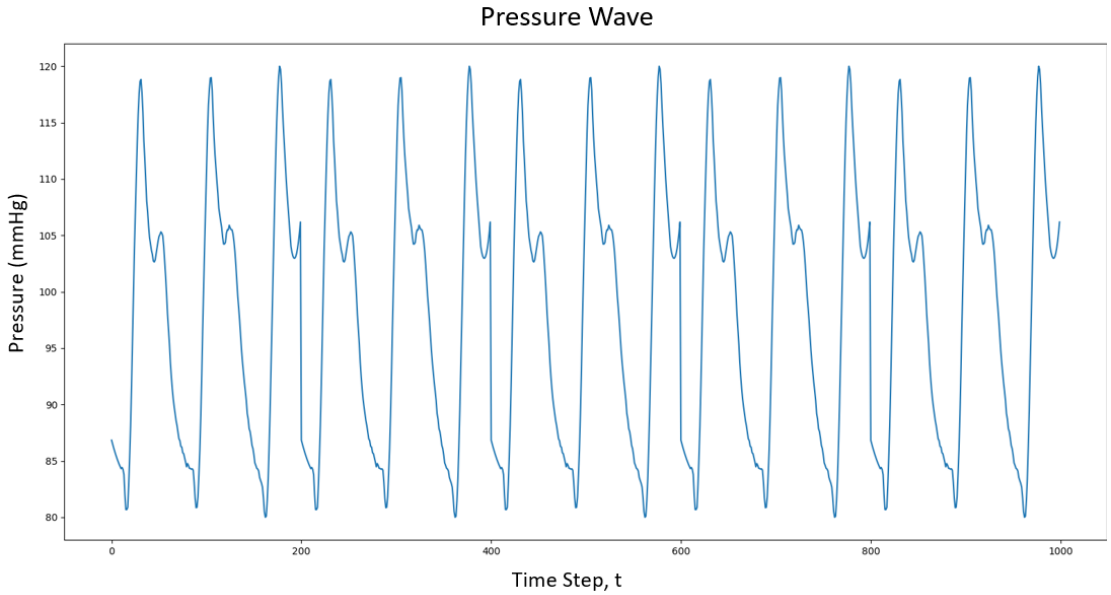

Fig. 7.1 Input pressure wave for simulations investigating shape changes in flow.

cycle (Song et al., 2023). Pulsatile power was calculated using values for pressure and flow at each time step and plotted across time. In a compliant network of vessels, pulsatile power was expected to decrease across the network as pulsatile energy is dampened. Flow and pressure values across time were used to calculate a pulsatile power time series. Mean pulsatile power was also compared across the ICA, MCA and capillary for a range of compliant networks. The compliant networks included:

- Baseline compliance in the PVN
- Capillary and venous compliance (β=2)
- MCA, capillary and venous compliance (β=2)
- Capillary (β=2) and venous (β=1.1) compliance

$$Flow\,Pulsatility\,Index = \frac{F_{max} - F_{min}}{F_{mean}} \tag{7.1}$$

$$Pulsatile\,Power = Pressure \times Flow \tag{7.2}$$

$$Steady\,State\,Power = P_{mean} \times F_{mean} \tag{7.3}$$

Following the conclusions obtained from the results in Investigation 1, simulations were now run using the Plausible Vessel Network with 100 segments in every arterial and venous vessel and 50 segments for each capillary vessel. Simulations were run using two input pressure waves: (i) a pressure wave with 50 beats and (ii) a pressure wave with return to diastolic (80

mmHg) pressure for varying lengths of time between each beat, termed the variable pressure wave (Fig. 7.2). The first pressure wave was created by repeating a single beat 50 times. From previous results it was decided that to accurately compare flow across beats, the same beat would need to be used across the pressure input. The second pressure wave was designed to introduce variability as a way of simulating flow more realistically. Lengths of the diastolic period were chosen at random, with a maximum length equal to the length of a single beat.

Shape changes in the flow profile were investigated by comparing flow across beats for simulations using the 50 beat pressure wave as the input. ICA, MCA and capillary flow time series were split into individual beats. For each beat, flow was normalised by dividing by the sum of the absolute flow values across the beat for each vessel. The shape of the flow profile across each beat was then compared to the beat in the input pressure wave by calculating the RMSE between the two sets of values. Beats were then split into four groups of eight and mean pulsatile power was calculated for the ICA, MCA and capillary across the groups. Output flow values from the simulations using the variable pressure wave were also split into four groups, but were split based on the timings of the beats using the 50 beat pressure wave instead of the number of beats. This was to allow comparisons to be made between the outputs for the two input pressure waves.

Investigation 2: Input pressure waves

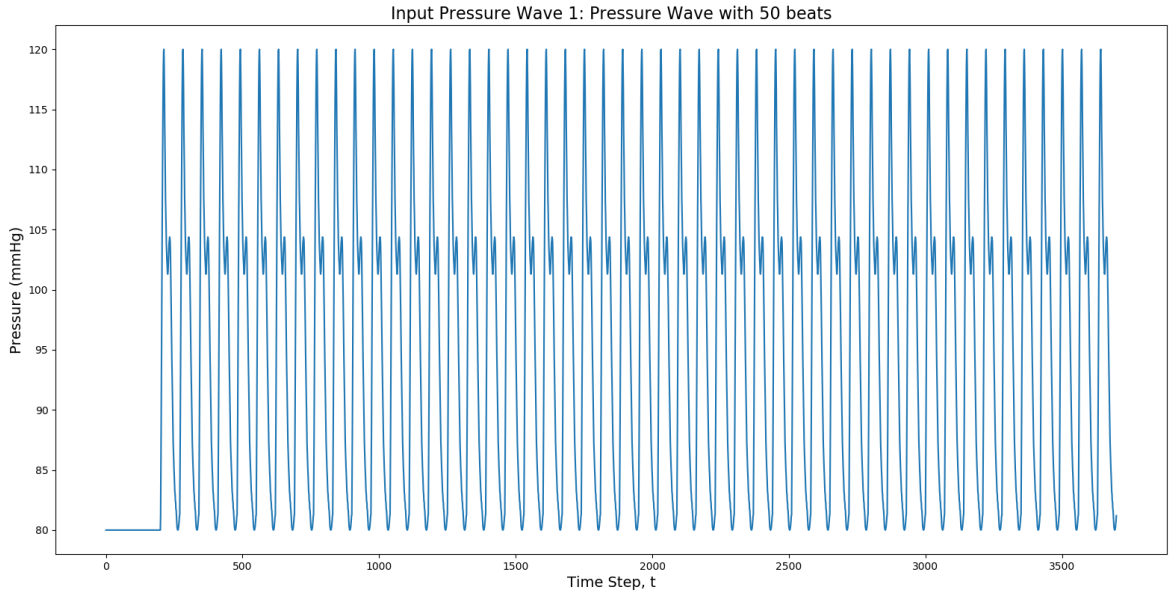

((a)) Input pressure wave consisting of a beat repeated 50 times.

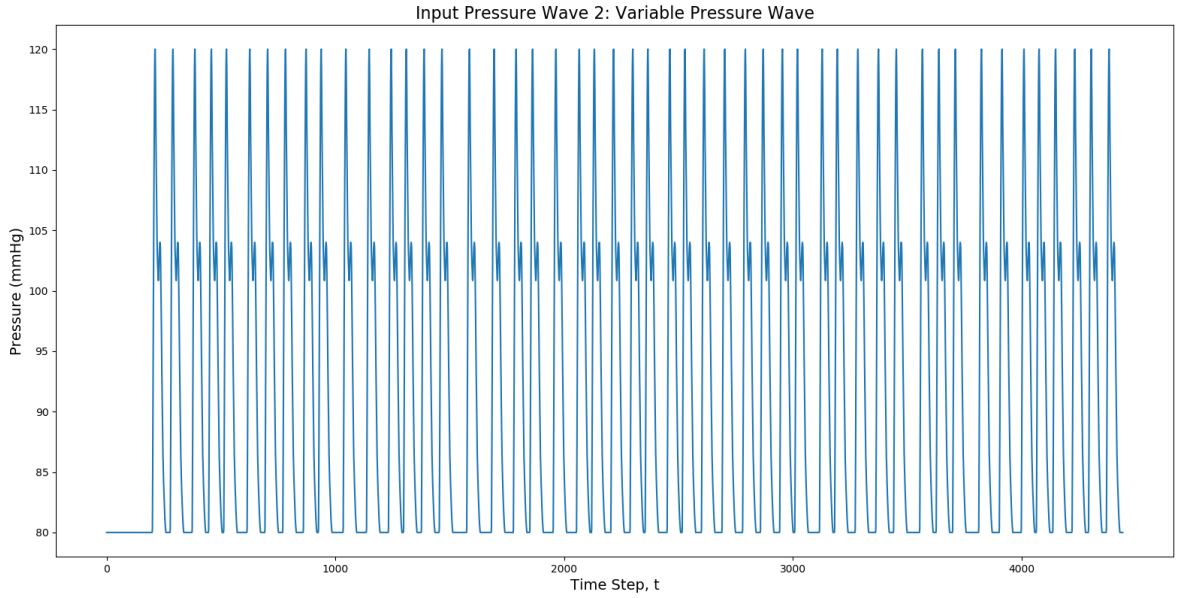

((b)) Input pressure wave consisting of a beat repeated 50 times with a return to diastolic pressure between each beat. The lengths of the diastolic pressures are random between beats.

Fig. 7.2 Two input pressure waves used for simulations in Investigation 2

7.3 Results

7.3.1 Investigation 1: Changes in the shape of the flow profile

Investigating Arterial and Capillary Compliance (Single Level)

Initial simulations were executed to investigate changes in flow in the ICA, MCA and capillary across time when adding compliance to the network in a single level. Compliance was added to the network in three cases: (1) the MCA (and corresponding vessel in level 1), (2) vessels in level 2 and (3) the capillaries. Flow time series for the ICA, MCA and capillary were compared across all compliant network cases, including the baseline compliance values determined for the Plausible Vessel Network (Chapter 6). Fig. 7.3 shows the absolute flow across time and percentage difference in flow for the ICA, MCA and capillary.

Fluctuations in flow, particularly in the capillary (highlighted by the blue box) can be seen within approximately the first 200 time steps. After this point flow reaches an equilibrium state. As expected, absolute flow increased as compliance was added to the network. The addition of compliance to vessels in level 2 and level 1 (MCA) resulted in similar flow time series and produced the greatest increase in flow compared to baseline compliance. Changes in the shape of the flow profile are only apparent across the first 200 time steps for all three vessels of interest in all compliant network cases, and this is further evident when comparing the percentage change in flow across time for each vessel. Results suggest the addition of compliance to a single level in the network may not be enough compliance to cause significant changes in the shape of the flow profile across time. Furthermore, the large increases in capillary flow at the start of the simulations may be due to the system responding to large and sudden jumps in pressure as opposed to dynamic responses to physiologically feasible changes in pressure in compliant vessels.

Investigating Venous Compliance (Single Level)

Venous compliance was also investigated by adding compliance to (1) vessels in level 11 and (2) vessels in level 12 and both cases were compared to the baseline compliance case (Fig. 7.4). Results suggest that venous compliance does not have a pronounced effect on the shape of the flow profile. Again this indicates that compliance added only to a singular level may not be enough to influence the dynamics of the system.

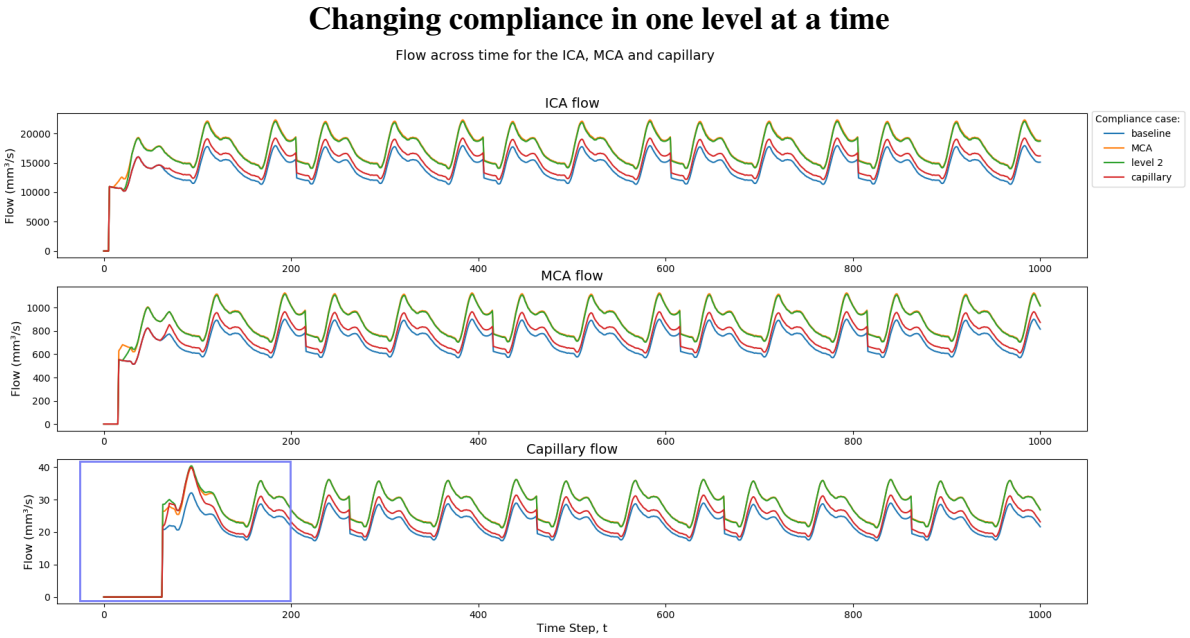

((a)) Flow across time in the ICA, MCA and capillary compared for different compliant network cases. Fluctuations in capillary flow within the first 200 time steps are highlighted by the box.

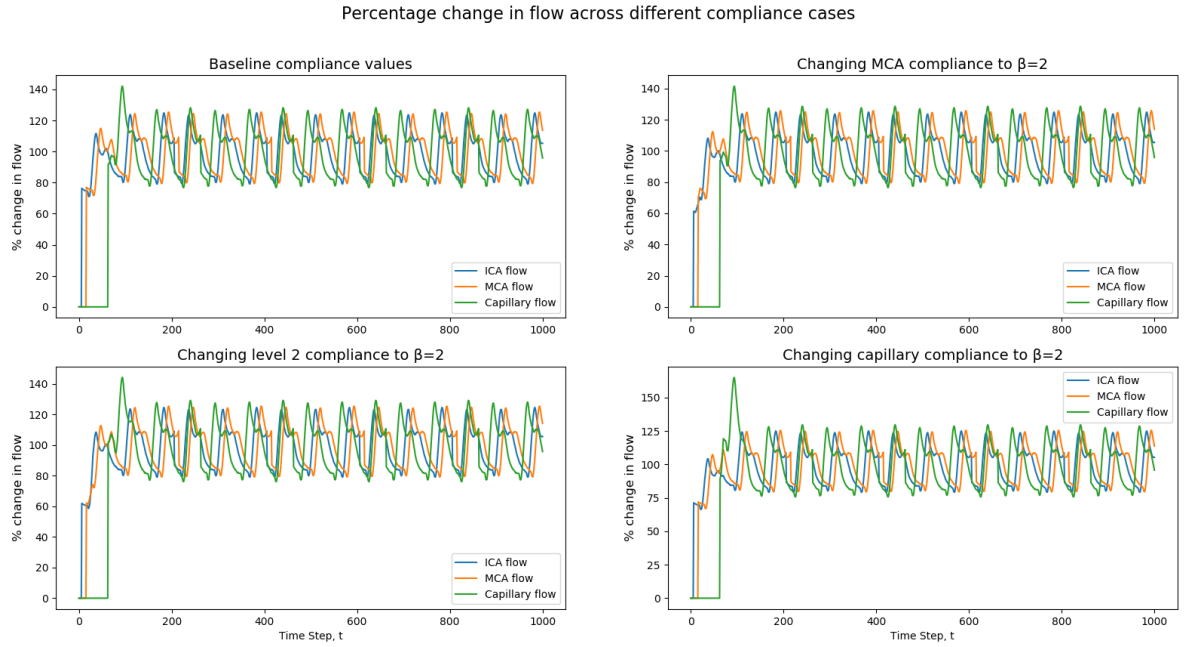

((b)) Percentage difference in flow compared for the ICA, MCA and capillary compared across different compliant network cases.

Fig. 7.3 (a) Flow across time and (b) percentage difference in flow in the ICA, MCA and capillary compared for compliant network cases: (0) baseline compliance, (1) addition of compliance in level 1 (MCA) (β=2), (2) addition of compliance in level 2 (β=2) and (3) addition of compliance in capillaries (β=2).

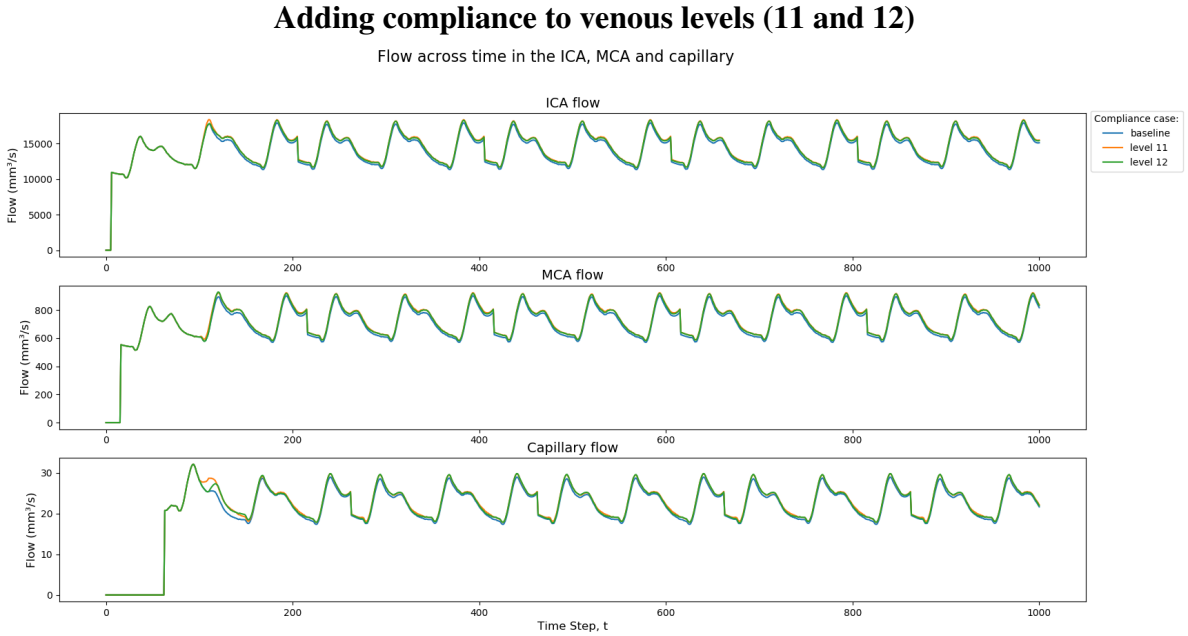

((a)) Flow across time in the ICA, MCA and capillary compared for different compliant network cases.

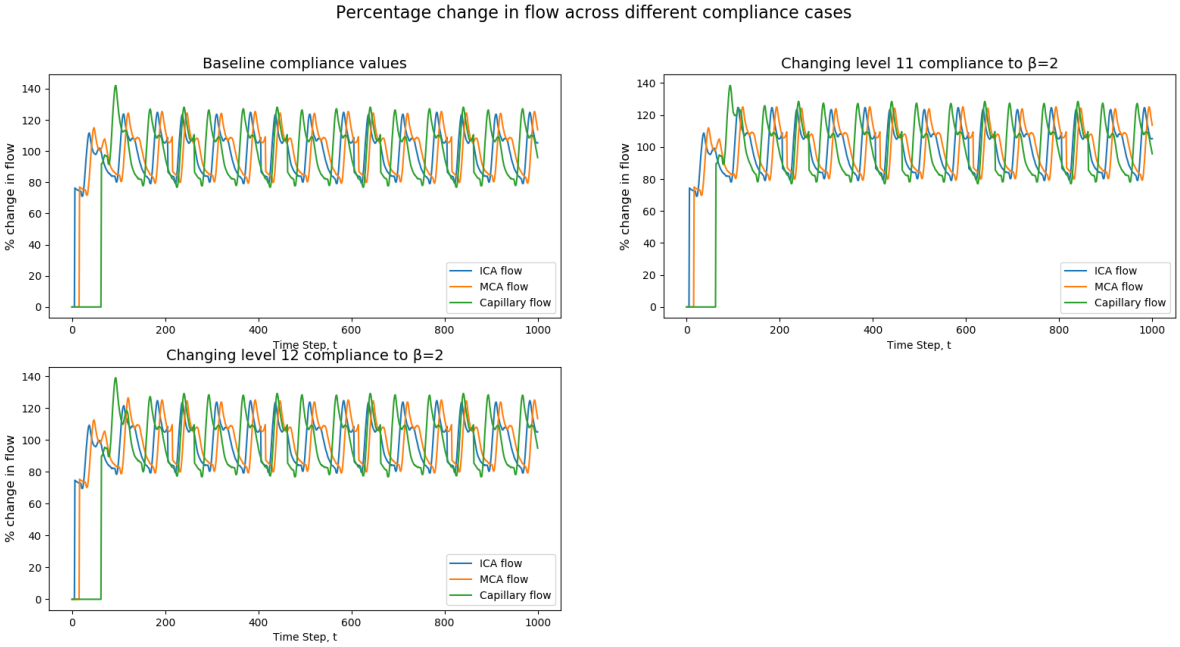

((b)) Percentage difference in flow compared for the ICA, MCA and capillary across different compliant network cases.

Fig. 7.4 (a) Flow across time and (b) percentage difference in flow in the ICA, MCA and capillary compared for compliant network cases: (0) baseline compliance, (1) addition of compliance in level 11 (β=2) and (2) addition of compliance in level 12 (β=2).

Investigating Compliance in Multiple Levels of the Network

Following the conclusions from the first two sets of simulations, compliance was added to multiple levels of the network and the flow time series and percentage changes in flow were compared (Fig. 7.5). As expected, absolute flow was greatest when compliance was added to three levels of the network (MCA, level 2 and capillaries). Similarly to the previous results, changes in the shape of the flow profile can be seen in the first 200 time steps with flow reaching an equilibrium state after this.

Compliance was added to all venous levels (8-13) and results are shown in Fig. 7.6. Initially a compliance value of β=2 was used in all venous levels and output flow was compared to the values obtained for the baseline compliance network. The blue box highlights considerable differences in flow across the two compliance conditions within the first 200 time steps. After this time point flow reached an equilibrium state.

To test whether a greater amount of venous compliance was required to achieve more significant shape changes, outputs were compared for (1) addition of venous compliance (β=2), (2) addition of venous compliance (β=2 in all venous levels apart from level 13 where β=1), (3) addition of venous compliance (β=1.1) and (4) addition of venous compliance (β=1.1 in all venous levels apart from level 13 where β=1). The results are shown in Fig. 7.7. Similarly to previous results, changes in flow can be seen within approximately the first 200 time steps and this is especially prominent in the capillary. The greatest change in flow compared to baseline can be seen for the case where compliance is equal to β=1.1 in levels 8-12 and β=1 in level 13. However, flow decreases suddenly at 1000 time steps. This suggests that there is too much compliance in the network which has caused unfeasible changes in pressure and therefore is not a realistic value.

The results suggest that venous compliance does affect the shape of flow and this is evident in the plots of percentage change in flow in the three compliance cases compared to the baseline, however the amount of compliance is not particularly significant. Therefore, to simplify further analyses, a value of β=2 was chosen for the venous levels in subsequent simulations.

The addition of compliance in the arteries and capillaries along with venous compliance was considered. Compliance was added to the compliant venous network in three cases: (1) MCA, (2) vessels in level 2 and (3) the capillaries and results were compared across cases (Fig. 7.8).

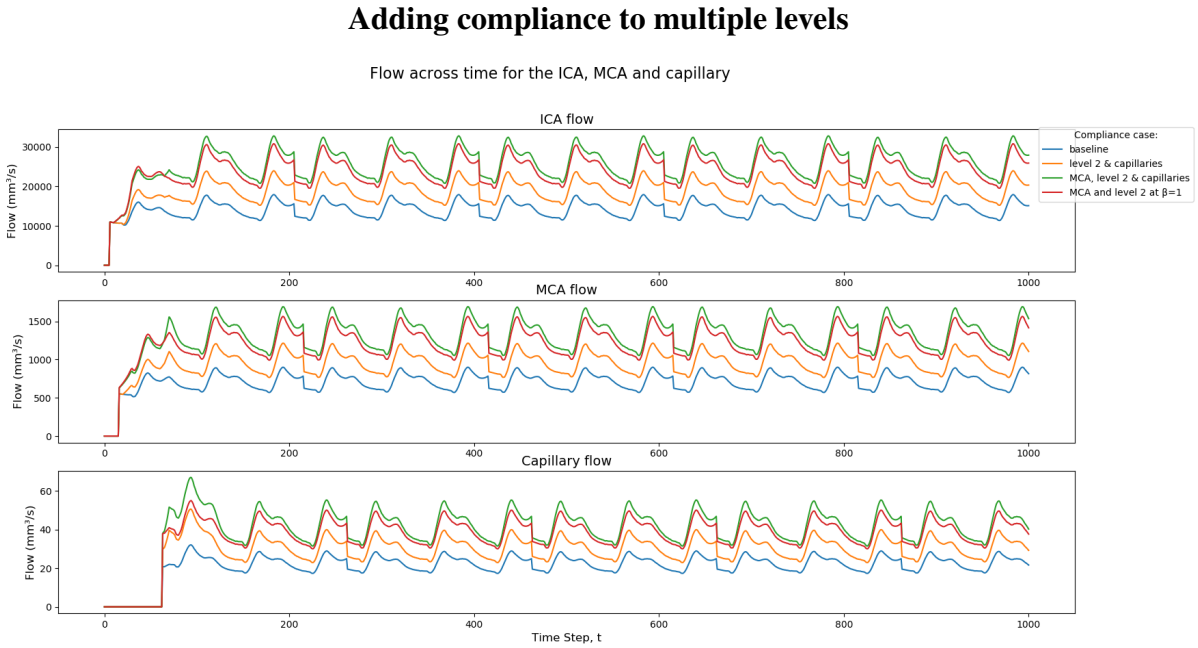

((a)) Flow across time in the ICA, MCA and capillary compared for different compliant network cases.

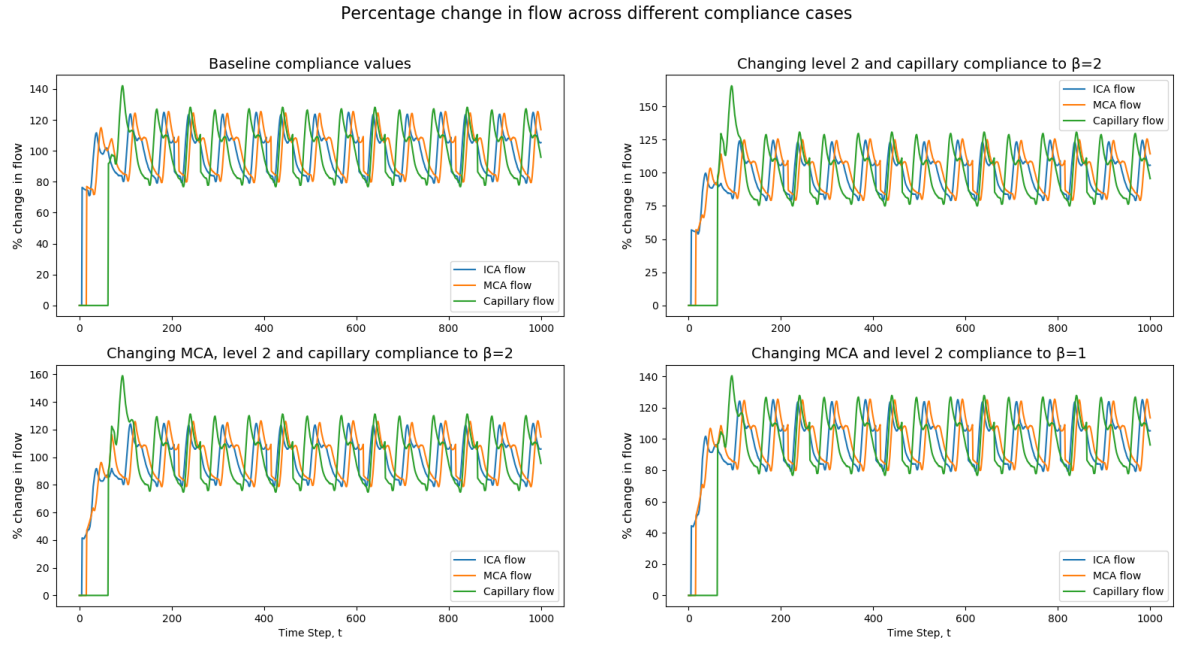

((b)) Percentage difference in flow compared for the ICA, MCA and capillary across different compliant network cases.

Fig. 7.5 (a) Flow across time and (b) percentage difference in flow in the ICA, MCA and capillary compared for compliant network cases: (0) baseline compliance, (1) addition of compliance in level 2 and the capillaries (β=2), (2) addition of compliance in the MCA, level 2 and capillaries (β=2) and (3) addition of compliance in the MCA and level 2 (β=1).

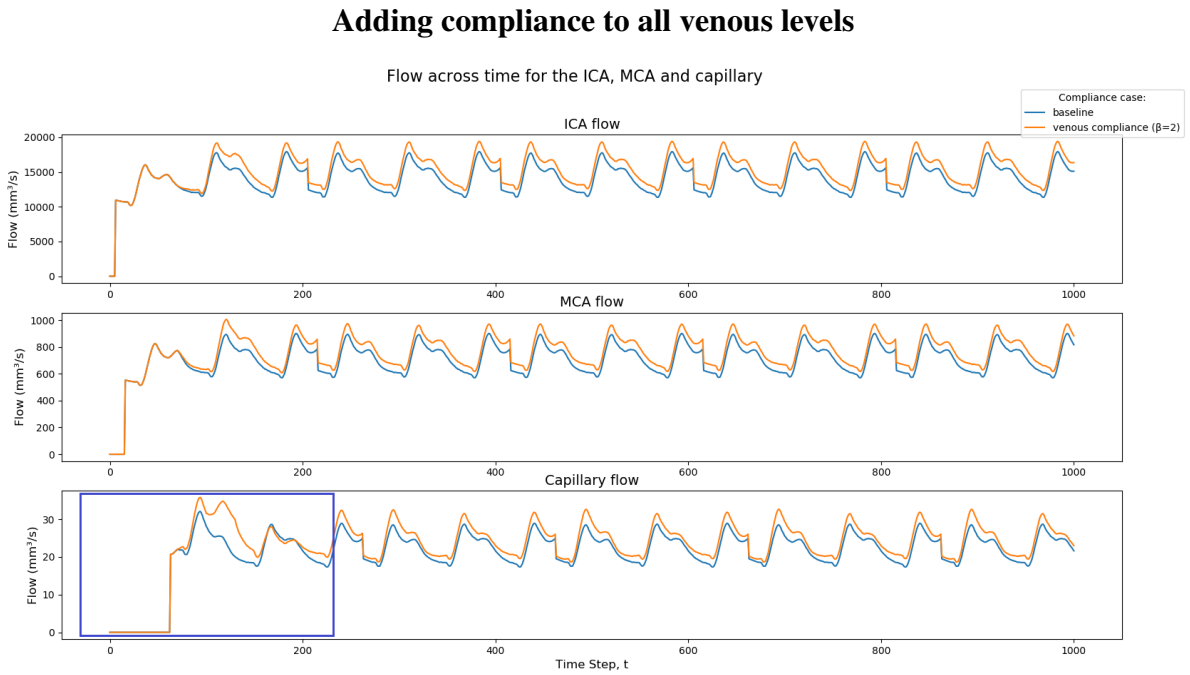

((a)) Flow across time in the ICA, MCA and capillary compared for different compliant network cases.

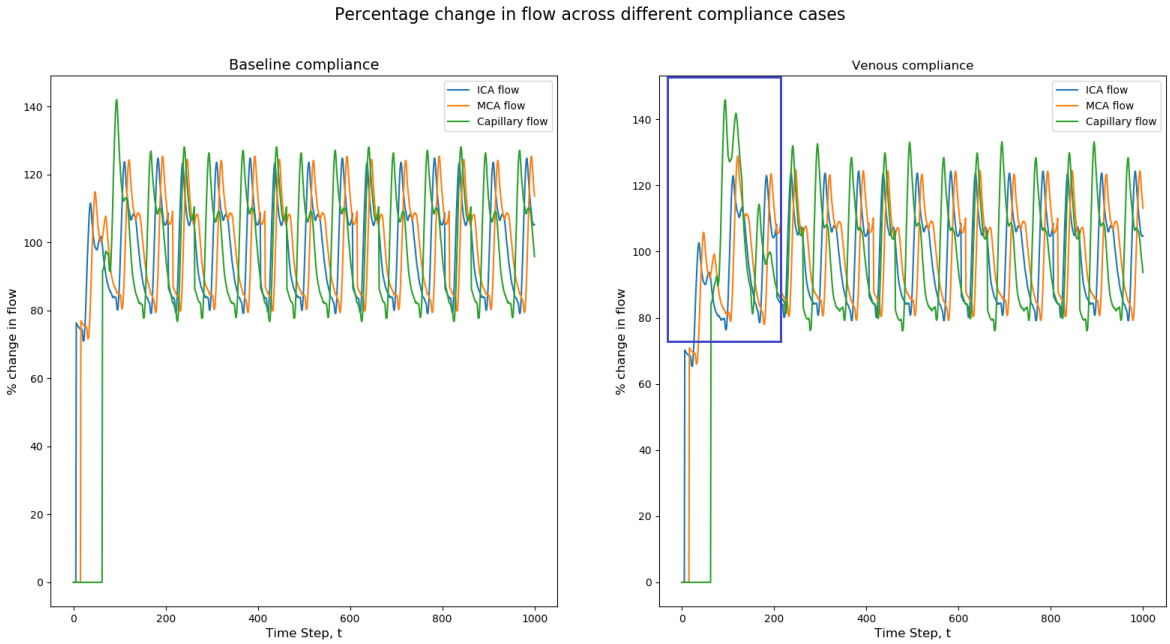

((b)) Percentage difference in flow compared for the ICA, MCA and capillary across different compliant network cases.

Fig. 7.6 (a) Flow across time and (b) percentage difference in flow in the ICA, MCA and capillary compared for compliant network cases: (0) baseline compliance and (1) addition of compliance in all venous levels (levels 8-13) (β=2).

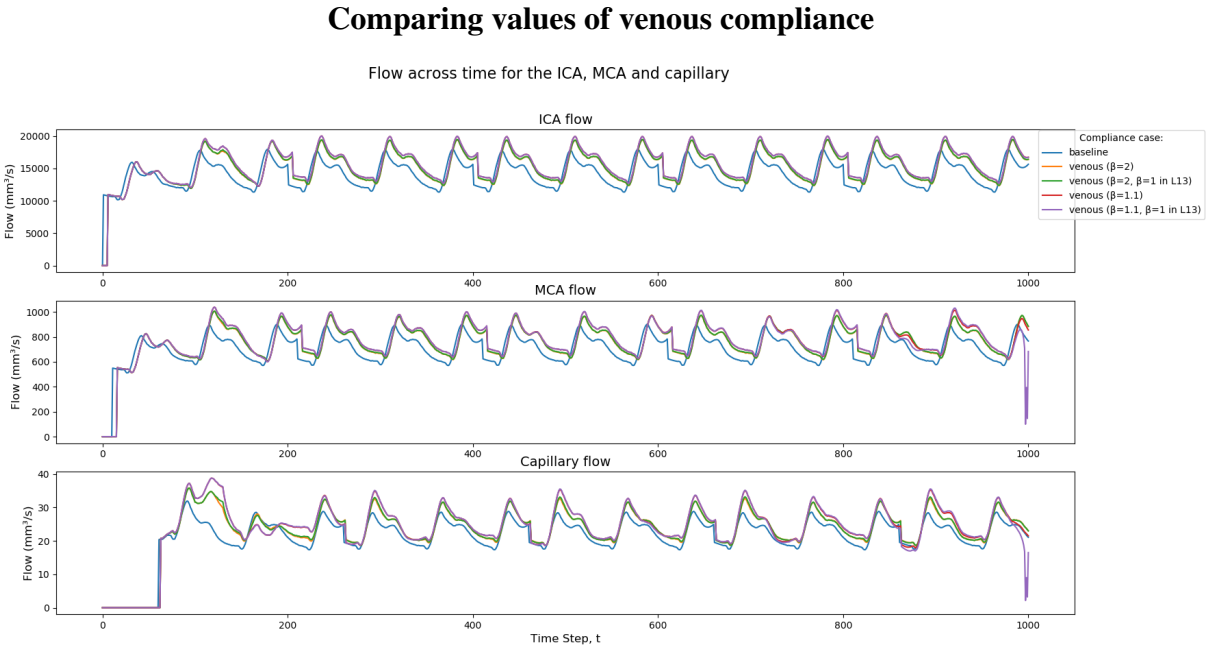

((a)) Flow across time in the ICA, MCA and capillary compared for different compliant network cases.

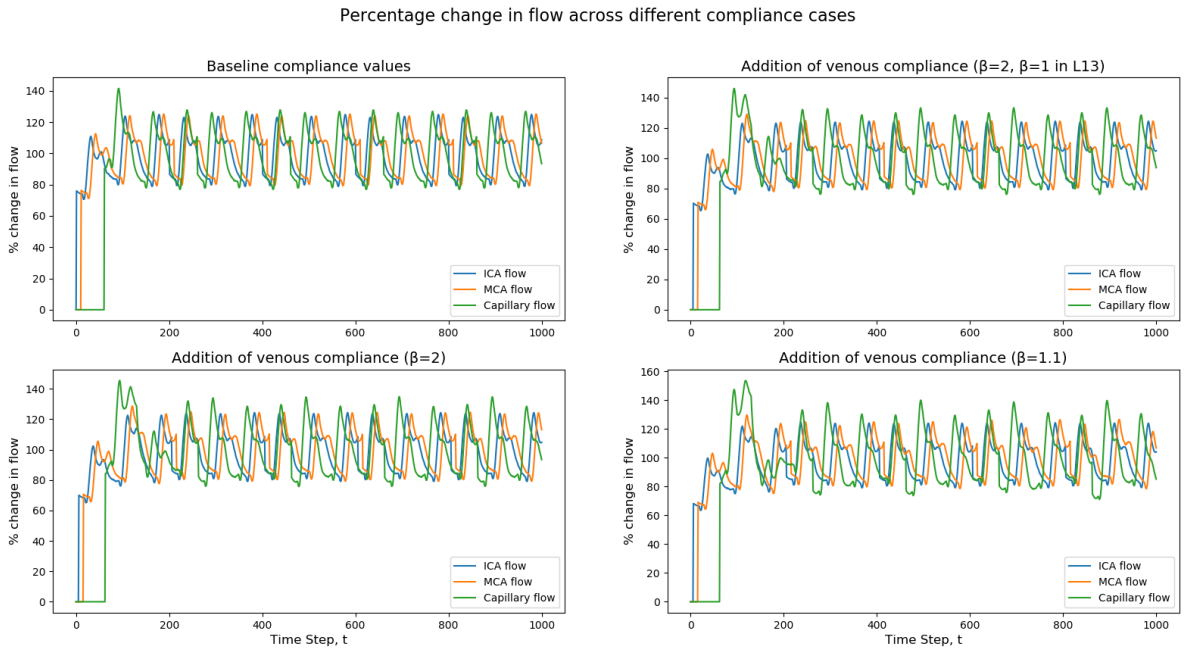

((b)) Percentage difference in flow compared for the ICA, MCA and capillary across different compliant network cases.

Fig. 7.7 (a) Flow across time and (b) percentage difference in flow in the ICA, MCA and capillary compared for compliant network cases: (0) baseline compliance, (1) addition of venous compliance (β=2), (2) addition of venous compliance (β=2 in all venous levels apart from level 13 where β=1), (3) addition of venous compliance (β=1.1) and (4) addition of venous compliance (β=1.1 in all venous levels apart from level 13 where β=1).

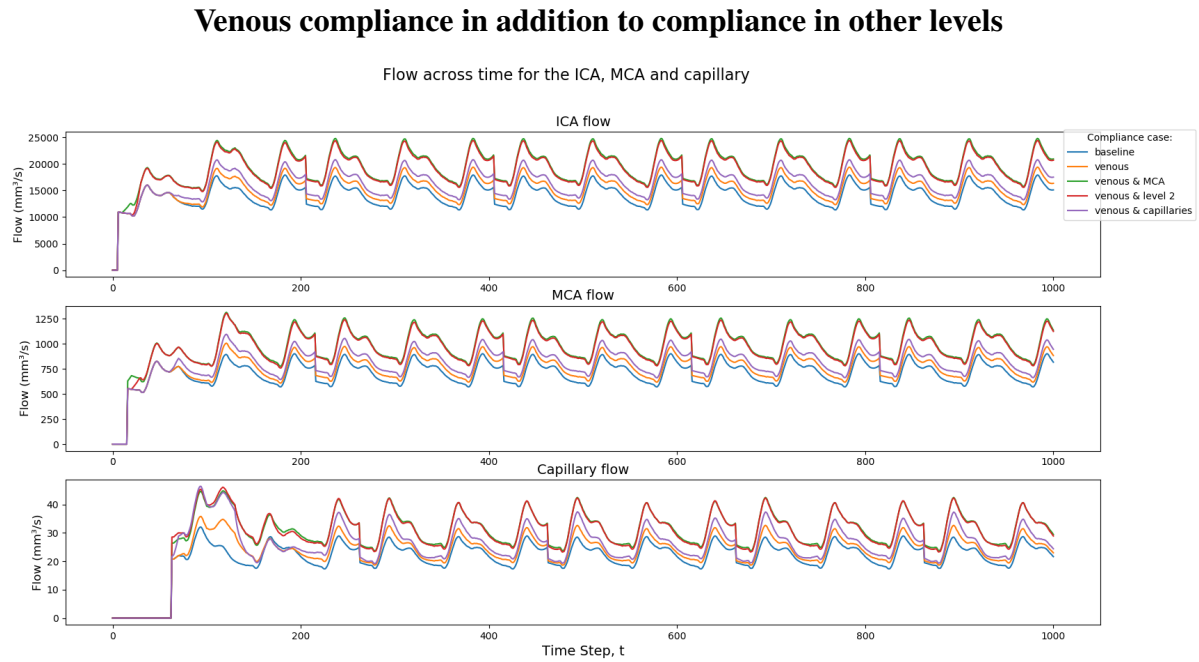

((a)) Flow across time in the ICA, MCA and capillary compared for different compliant network cases.

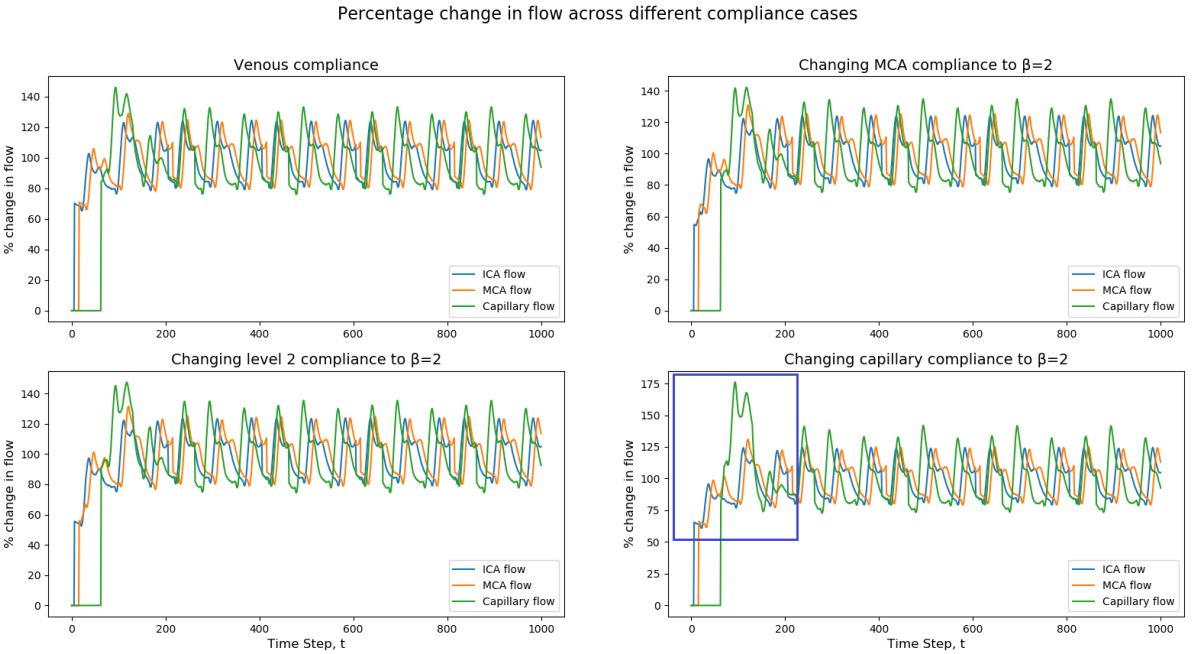

((b)) Percentage difference in flow compared for the ICA, MCA and capillary across different compliant network cases. The greatest change in flow in the capillary compared to the ICA and MCA is shown when capillaries are compliant (highlighted in the box).

Fig. 7.8 (a) Flow across time and (b) percentage difference in flow in the ICA, MCA and capillary compared for compliant network cases: (0.0) baseline compliance, (0.1) addition of compliance in all venous levels (β=2), (1) addition of compliance in all venous levels and the MCA (β=2), (2) addition of compliance in all venous levels and level 2 (β=2) and (3) addition of compliance in all venous levels and the capillaries (β=2).

Modifying the Input Pressure Wave

To investigate the cause of the large fluctuations in flow in the first 200 time steps, the input pressure wave was adjusted in a number of ways. The first approach was to shift the range of the pressure wave to 15 and 55 mmHg instead of 80 and 120 mmHg which was used in previous simulations. The purpose of this was to eliminate the large increase in pressure from baseline (11 mmHg at t=0) to 80 mmHg at the time point corresponding to when the pressure wave hits the vessel, as this was thought to be causing the changes in flow at the start of the simulation. Results in Fig. 7.9 suggest that this is the case as the large changes in flow are no longer apparent during the first 200 time steps. Although there are differences in the magnitude of flow across compliance cases, flow still reached an equilibrium state after this period of time.

The input pressure wave was also adjusted to include a period of constant diastolic pressure (80mmHg) before and between beats as an alternative approach to investigating the cause of the large fluctuations in flow at the beginning of the simulations (Fig. 7.10). Similarly to the case where the range of the pressure wave was adjusted, fluctuations can no longer be seen at the start of the flow time series, further suggesting that the changes in flow were a cause of the large jump in pressure from baseline (11mmHg at t=0) to 80mmHg at the start of each beat.

Random Gaussian noise was added to the input pressure wave to see whether flow would still reach an equilibrium state after a certain number of time steps. Flow was compared between the baseline compliance and venous compliance cases (See Appendix 1). The standard pressure wave (Fig. 7.1) was used for this simulation. As with previous results, changes in flow can be seen at the start of the time series for both compliant network cases. However following this point, flow still appears to reach an equilibrium across time.

Changing the range of the input pressure wave - pressure between 15 and 55mmHg

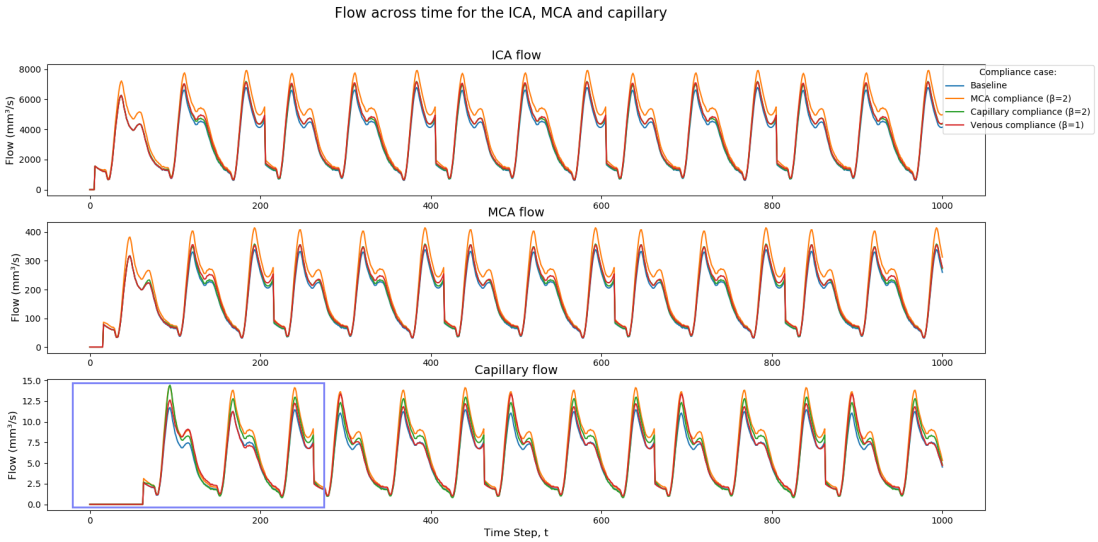

((a)) Flow across time in the ICA, MCA and capillary compared for different compliant network cases. The box highlights flow across the first three beats for the updated input pressure wave. Unlike previous cases, flow is no longer fluctuating across the first 200 time steps.

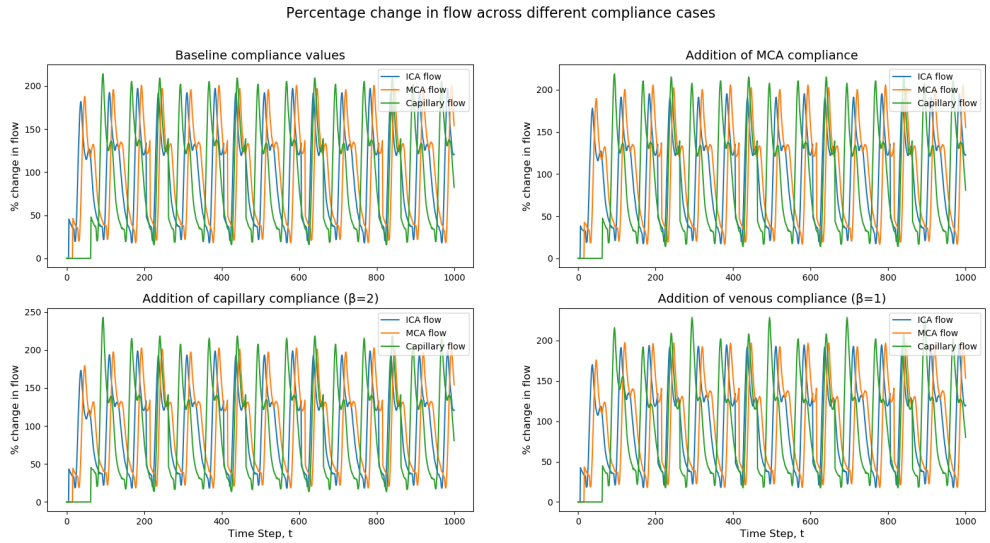

((b)) Percentage difference in flow compared for the ICA, MCA and capillary across different compliant network cases.

Fig. 7.9 (a) Flow across time and (b) percentage difference in flow in the ICA, MCA and capillary compared for compliant network cases: (0) baseline compliance, (1) addition of MCA compliance (β=2), (2) addition of capillary compliance (β=2) and (3) addition of venous compliance (β=1). The pressure wave was updated so that all input pressure values were between 15 and 55 mmHg.

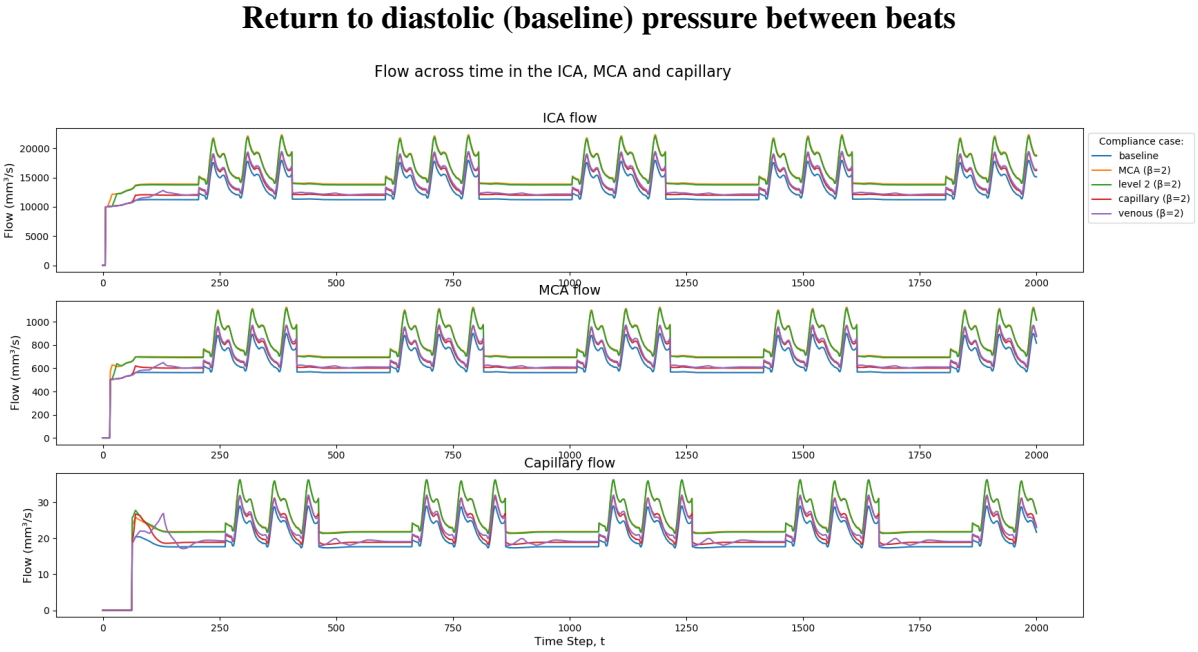

((a)) Flow across time in the ICA, MCA and capillary compared for different compliant network cases.

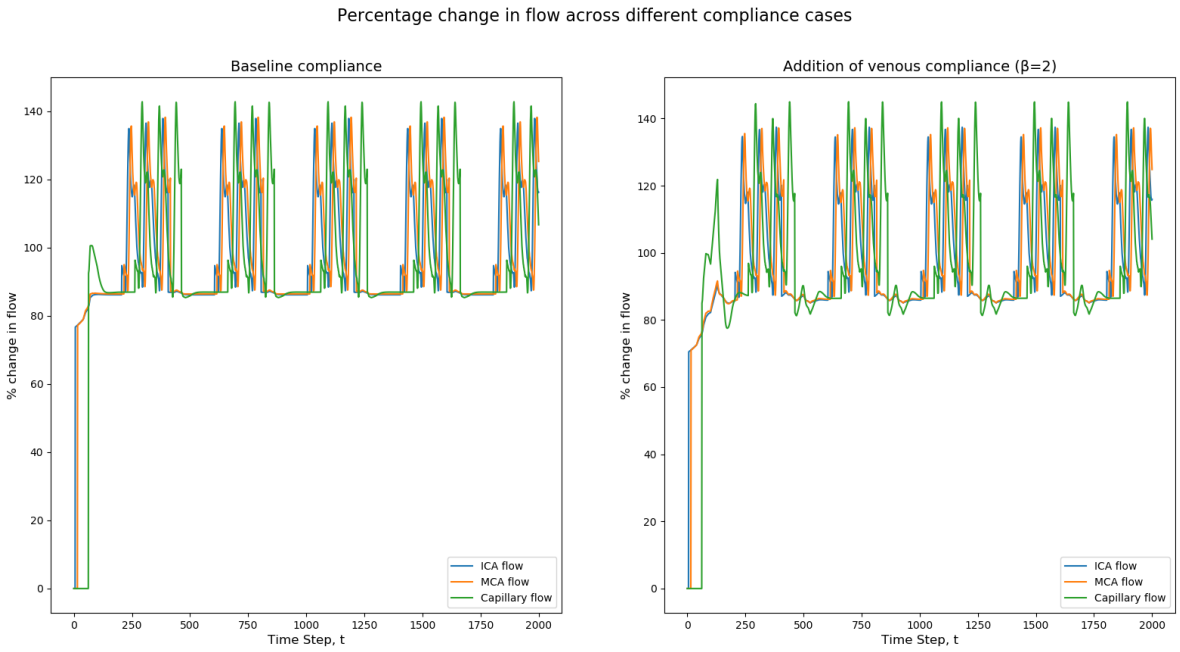

((b)) Percentage difference in flow compared for the ICA, MCA and capillary across different compliant network cases.

Fig. 7.10 (a) Flow across time and (b) percentage difference in flow in the ICA, MCA and capillary compared for compliant network cases: (0) baseline compliance, (1) addition of compliance in the MCA (β=2), (2) addition of compliance in level 2, (3) addition of compliance in the capillaries (β=2) and (4) addition of compliance in all venous levels (β=2).

Introducing a Time Delay

The number of points in the input pressure wave was varied as a way of imitating non-instantaneous changes in volume and resistance following changes in pressure to see whether this would influence the shape of the flow profile. This was achieved by repeating each value in the pressure wave. Initially the pressure wave was increased by a factor of 2, 3 and 4 and simulations were run for the Plausible Vessel Network with a standard number of segments (10 in arteries, arterioles, venules and veins and 5 in each capillary level). Flow in the ICA, MCA and capillary for baseline compliance and venous compliance was compared for each input pressure wave and results are presented in Fig. 7.11. Across all three cases there was an increase in flow in the capillary when venous compliance was added to the network. Flow profiles in the ICA and MCA are similar however some changes can be seen in capillary flow. It is important to note that flow was only simulated for two full beats so may have reached an equilibrium state after this.

Increasing the number of segments in the Plausible Vessel Network was also explored in addition to repeating values in the pressure wave. Simulations were run for the three pressure wave cases (repeating values two, three and four times) but this time the number of segments in the Plausible Vessel Network was also increased by the same factor. Flow was compared for baseline compliance and venous compliance and results are shown in Fig. 7.12. In all three cases, there appear to be no major changes in flow shape across the ICA, MCA and capillary and also across time for each vessel. This suggests that increasing the number of segments cancels out the effect of repeating values in the pressure wave.

In the previous two cases, the input pressure wave and number of segments was increased by a maximum factor of four. Results from the simulations indicate there may be some change in the shape of the flow profile following non-instantaneous responses to changes in pressure, however this is still inconclusive. For this reason, the number of segments was increased by a factor of 10 and results for the repeated pressure wave were compared to the standard pressure wave (Fig. 7.13). In the first case where values in the pressure wave were repeated, flow peaks in the capillary towards the start of the simulation and then reaches an equilibrium state. In contrast, the fluctuation in flow at the start of the capillary is no longer observed. Changes in pulsatile flow shape across time can be seen in the ICA, MCA and capillary.

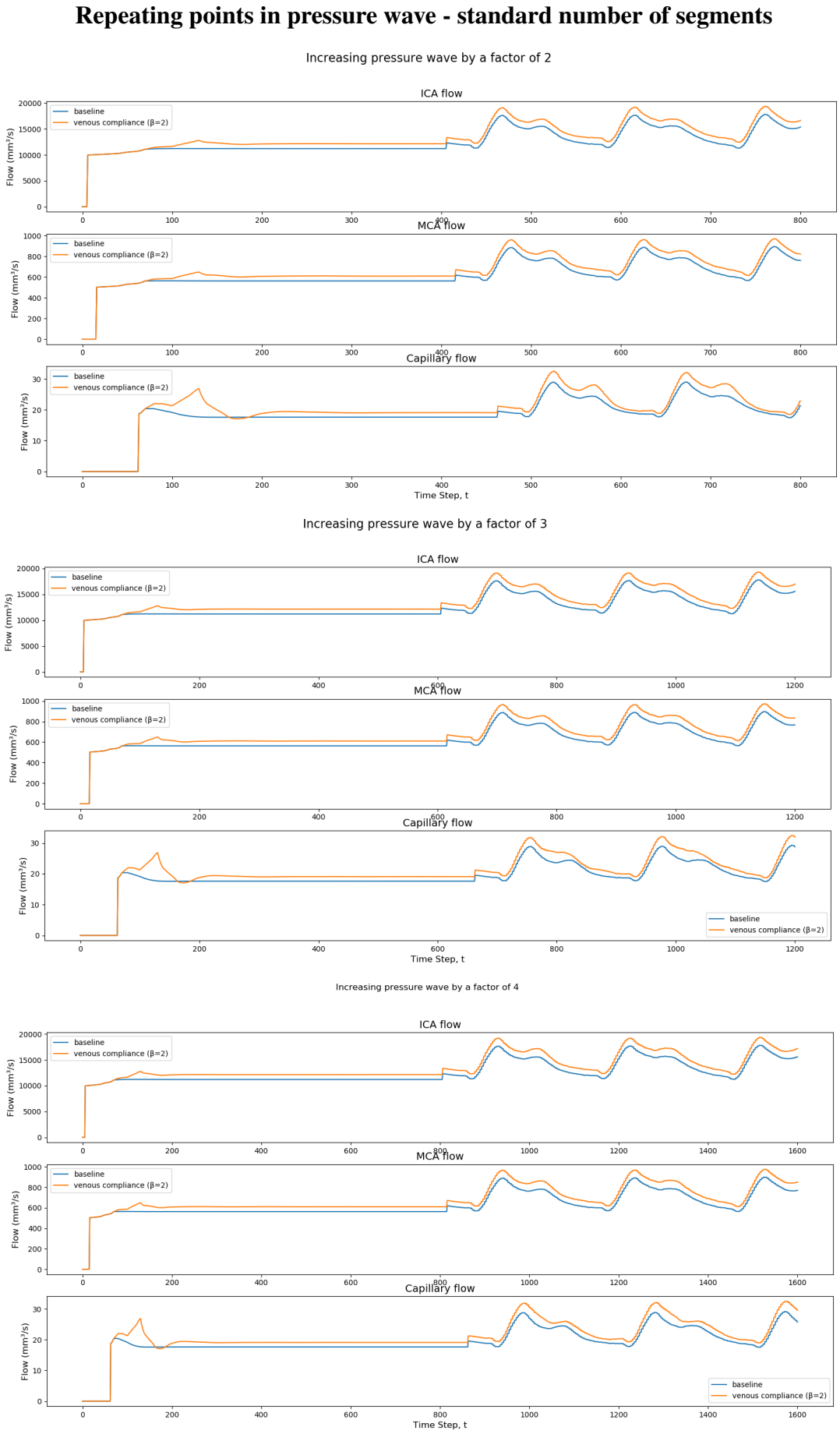

Fig. 7.11 Flow in the ICA, MCA and capillary across time compared for baseline compliance and venous compliance. The pressure wave was increased by a factor of 2, 3 and 4 and the number of segments was kept as standard.

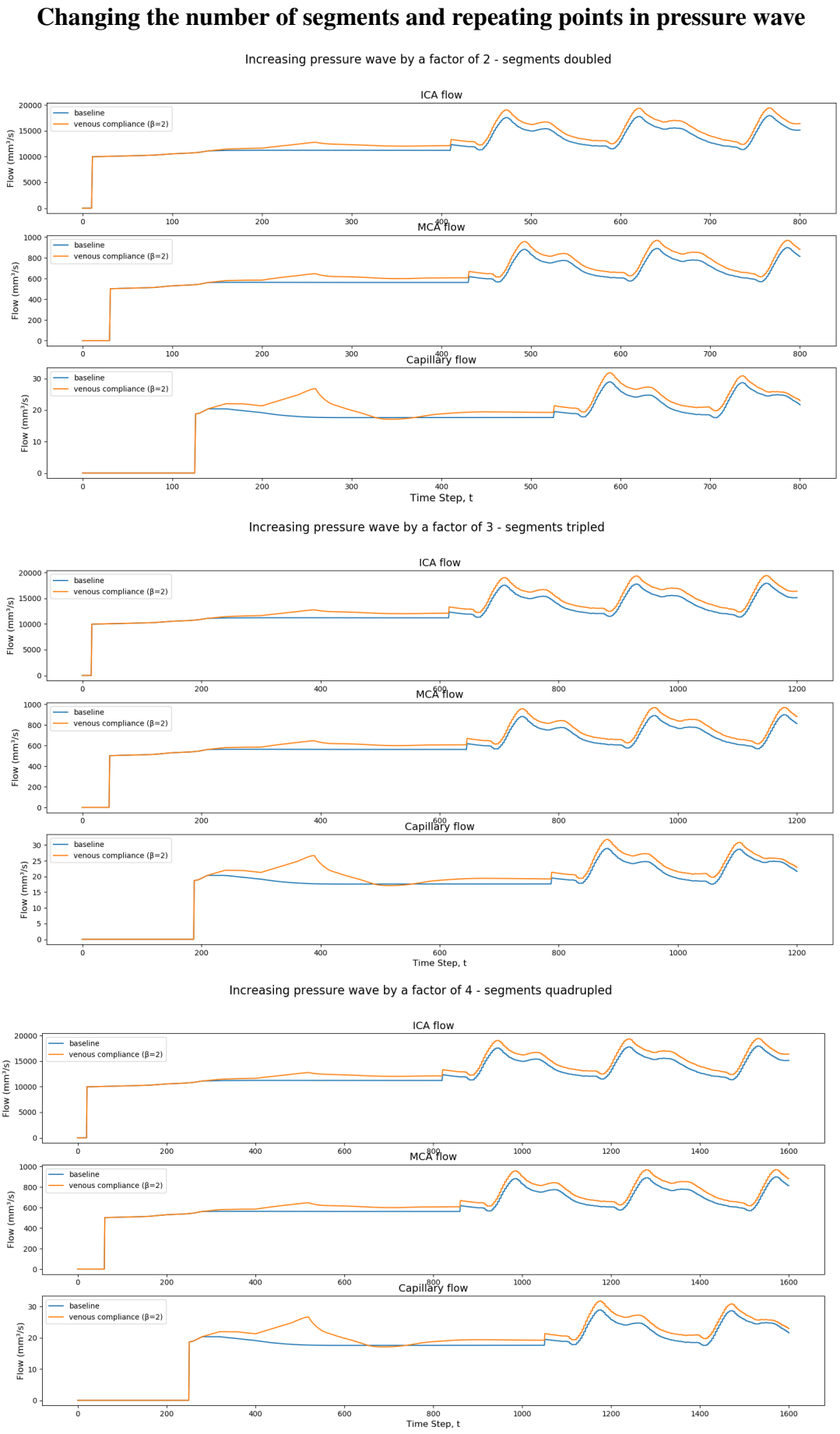

Fig. 7.12 Flow in the ICA, MCA and capillary across time compared for baseline compliance and venous compliance. The number of segments and values in the pressure wave were increased by a factor of 2, 3 and 4.

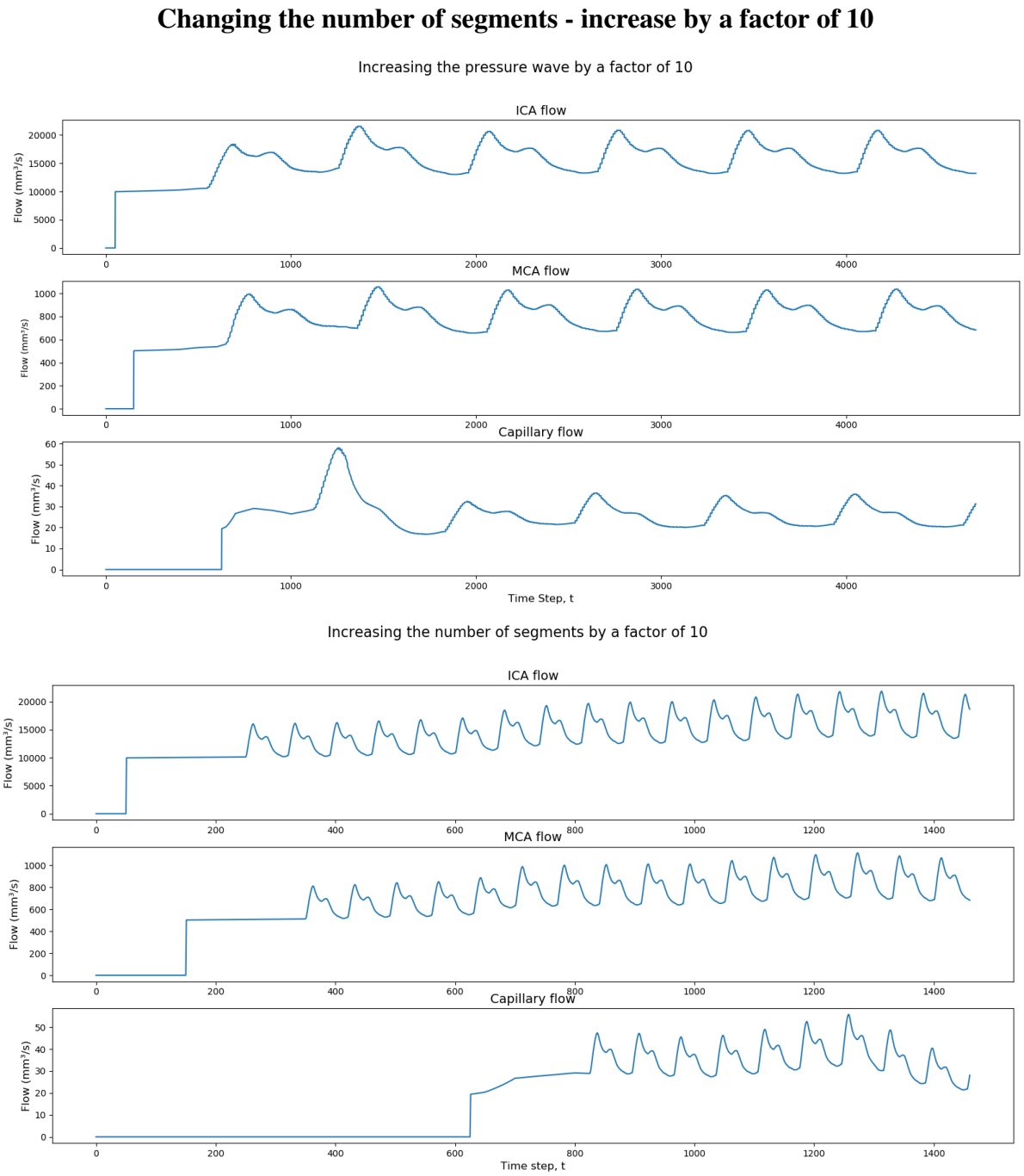

Fig. 7.13 Flow in the ICA, MCA and capillary across time. The number of segments in each vessel was increased by a factor of 10 and compared for two cases: (i) points in the pressure wave repeated 10 times and (ii) standard pressure wave.

Summary of Investigation 1 - Shape Changes

Simulations were run for a range of compliant network cases and flow was compared in the ICA, MCA and capillary to assess whether changes in the shape of the flow profile could be seen, firstly across the vessels of interest and secondly across time. Results from Investigation 1 suggest that obvious shape changes cannot be observed in outputs obtained from the model, particularly as flow appears to be pulsatile in the capillaries instead of flatlining as initially expected. The results suggest that compliance is required in all venous levels to reduce downstream resistance and to allow flow out of the network. This is comparable to treating the venous section of the network as a sink. Compliance was also added to the capillaries in order to accommodate the magnitude of flow from the arteries. A value of β=2 was chosen as a realistic value for compliance in both the venous vessels and the capillaries.

The number of vessel segments was also investigated. Results suggest that this is a significant factor to consider for dynamic simulations. The number of segments in each vessel was multiplied by 10 such that there were 100 segments in all arterial and venous vessels and 50 segments in vessels in each of the capillary levels. Following adjustments to both the number of segments in the Plausible Vessel Network and the inclusion of a constant diastolic period (for 200 time steps) before the start of the beats, large fluctuations in flow at the start of each simulation were no longer observed. This may indicate that the length of the vessel (number of segments) is important to consider in relation to the length of the beat in the input pressure wave.

Results from Investigation 1 were used to select appropriate values for vessel compliance as well as the number of segments for vessels in the Plausible Vessel Network for simulations in Investigation 2. In addition, the input pressure wave was adjusted in order to compare flow across beats, firstly across vessels and secondly across time. This was implemented by using a single beat repeated for the required duration of the pressure wave. The input pressure wave used for simulations in Investigation 1 was created by repeating three different beats which limited potential comparisons between results across time.

7.3.2 Investigation 2: Buffering of pulsatile energy across the network and across time

Results from the simulations carried out in Investigation 1 suggest that there are minimal changes in the shape of the flow profile for a range of compliant networks. Flow was expected to become steady in the capillaries such that it would appear to flatline across time as a result of the dampening of pulsatile energy across the arteries. Simulations in Investigation 2 were carried out to assess whether the apparent flow pulsatility in the capillaries was significant compared to pulsatility in the ICA and MCA. To achieve this, pulsatile power was calculated using the pressure and flow time series obtained from the model and compared across vessels. Mean pulsatile power was also compared across the ICA, MCA and capillary. Outputs from the model

were obtained for two input pressure waves: (i) a single beat repeated 50 times and (ii) the variable pressure wave with return to diastolic pressure between beats.

Pressure wave with 50 beats

Pressure and flow outputs were obtained across time and compared in the ICA, MCA and capillary. Results are shown in Fig. 7.14 and Fig. 7.15 respectively. Fluctuations can no longer be seen across the start of the simulation and this is likely due to increasing the number of segments per vessel. The results also highlight changes in pressure and flow across time in the capillary, particularly across the first 2500 time steps. Despite flow still appearing pulsatile in the capillary, changes in shape can be seen across time. This is particularly evident when comparing the magnitude of the beats across time. However, it is evident that both pressure and flow reach an equilibrium state after a certain number of time steps. Changes in flow across time are further highlighted in Fig. 7.16 where the percentage difference in flow with respect to the mean flow across time following the first beat is compared in the ICA, MCA and capillary.

Flow was compared in the ICA, MCA and capillary across individual beats. Flow in each beat was normalised by dividing absolute flow by the sum of the flow values across the beat and was compared in the vessels of interest for the first 32 beats. Results are presented in Figs. 7.17, 7.18, 7.19 and 7.20. Differences in the shape of the flow for the ICA, MCA and capillary can be seen up to beat number 24. After this point, the shape appears to be the same suggesting that flow has reached the equilibrium state. The most prominent differences in the shape of the flow profile compared to the input pressure beat are within the first 8 beats for all three vessels. RMSE was highest for beat number 7 in the ICA, beat number 6 for the MCA and beat number 8 for the capillary, indicating the greatest changes in flow shape occurred in these beats.

Pulsatile power was calculated across time and the results are shown in Fig. 7.21. Similarly to both the pressure and flow time series, changes in pulsatile power can be seen across time steps and are particularly evident in the capillary. Despite flow appearing pulsatile across time, comparisons between the amplitude of pulsatile power in the ICA, MCA and capillary suggest pulsatile energy is being buffered across the network. This is further evident in Fig. 7.22 which compares the mean pulsatile power across the three vessels. Mean pulsatile power decreases from the ICA to the MCA and capillary suggesting that the pulsatility has been dampened as expected, despite not manifesting as appreciable changes in the shape of the flow profile from pulsatile to steady flow. Mean pulsatile power was also compared across compliant network cases to assess whether changing the amount of compliance in the network influenced the dampening of the pulsatility across the network. Results highlight differences in mean pulsatile power across all compliant networks and across groups of beats. Compliance in the MCA, capillary and venous vessels resulted in the highest values of mean pulsatile power across all three vessels and this is likely a consequence of allowing a greater amount of flow through the network.

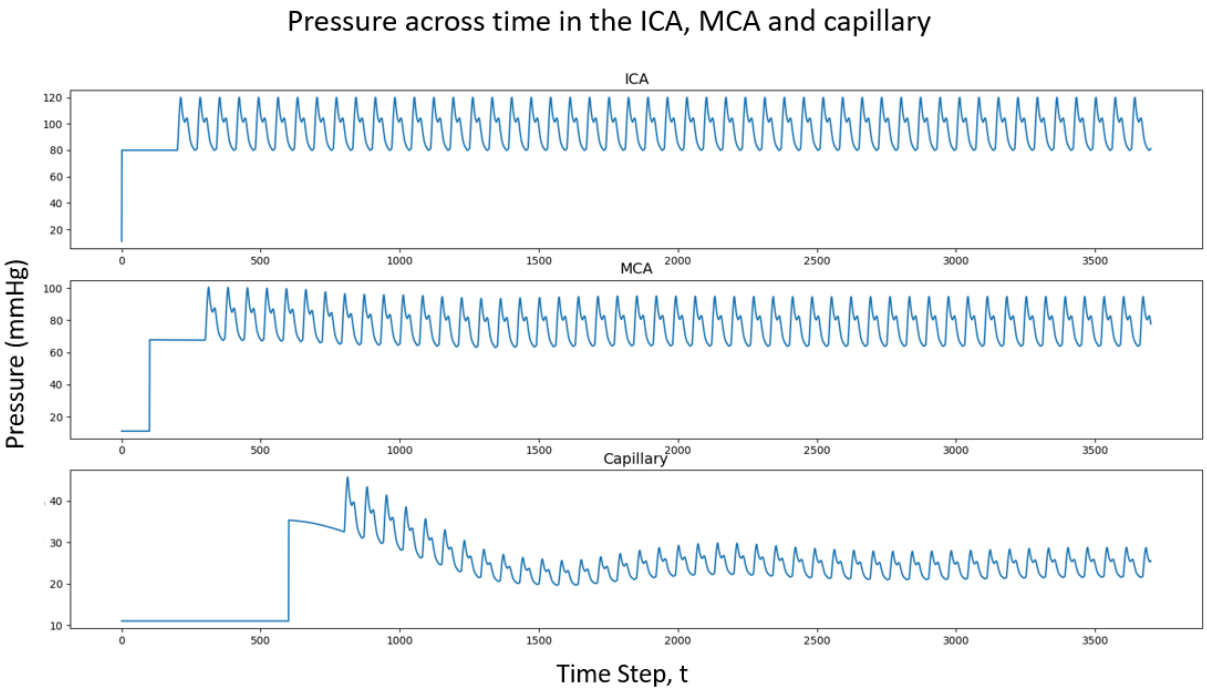

Fig. 7.14 Pressure across time in the ICA, MCA and capillary for 50 beat pressure wave.

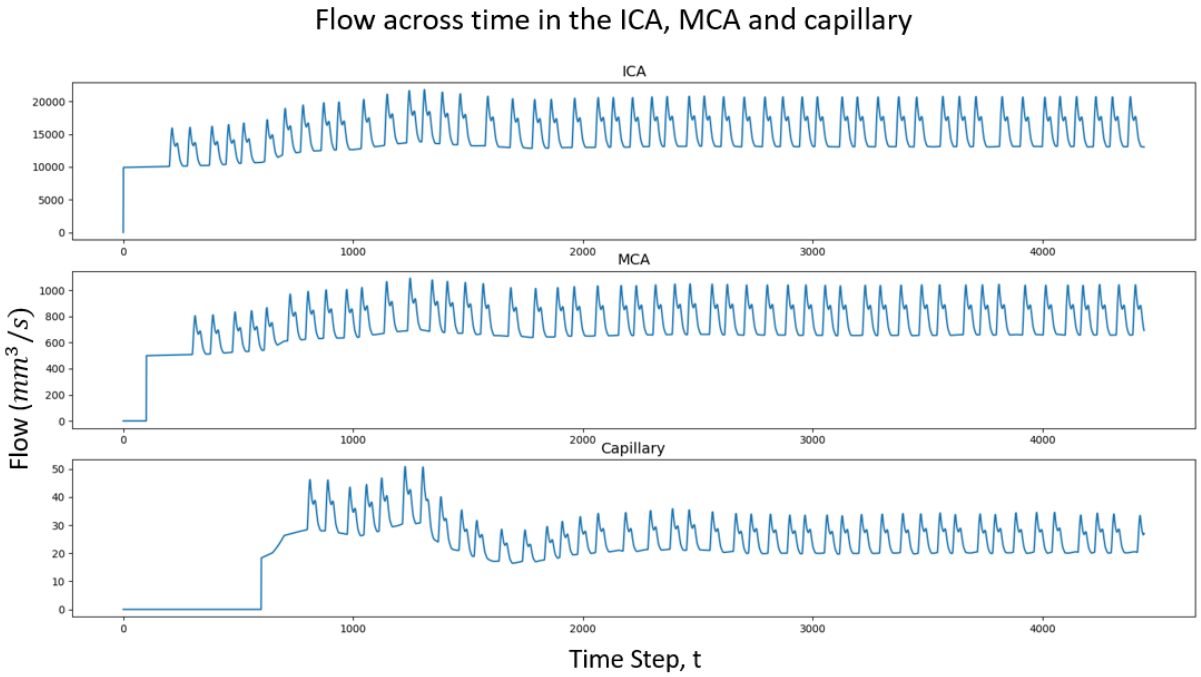

Fig. 7.15 Flow across time in the ICA, MCA and capillary for 50 beat pressure wave input.

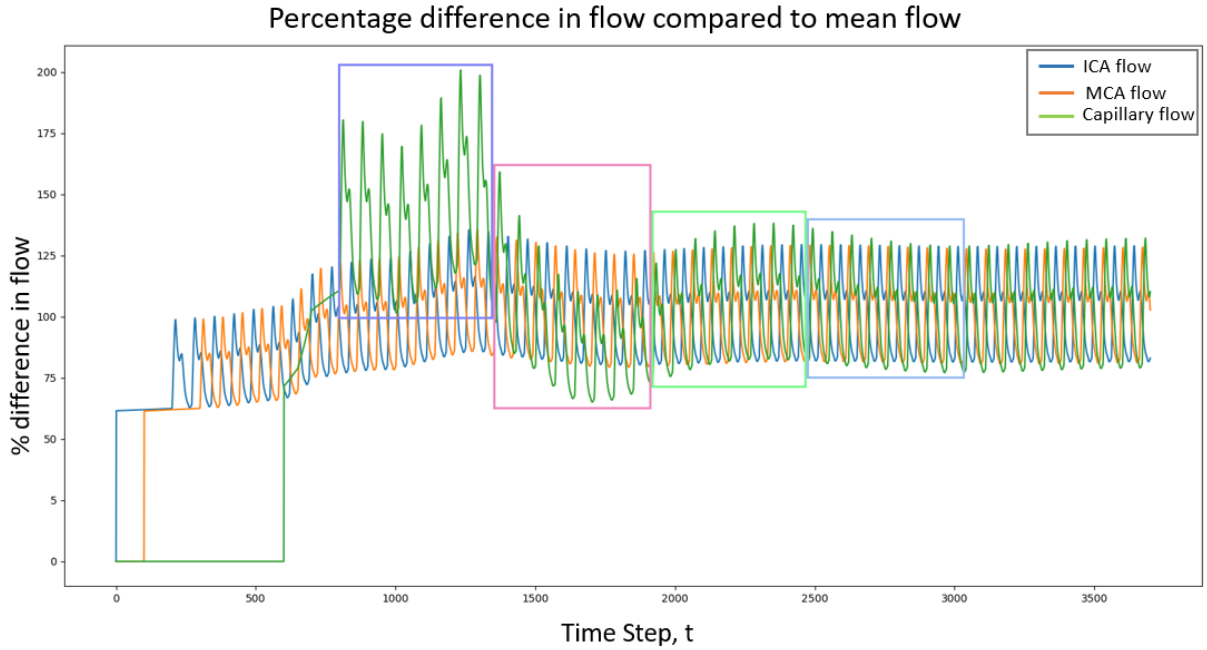

Fig. 7.16 Percentage difference in flow (calculated using the mean flow across time following the first beat) for the ICA, MCA and capillary. Capillary beats are split into groups of 8 from beat 1 to 32 and highlighted by the four boxes.

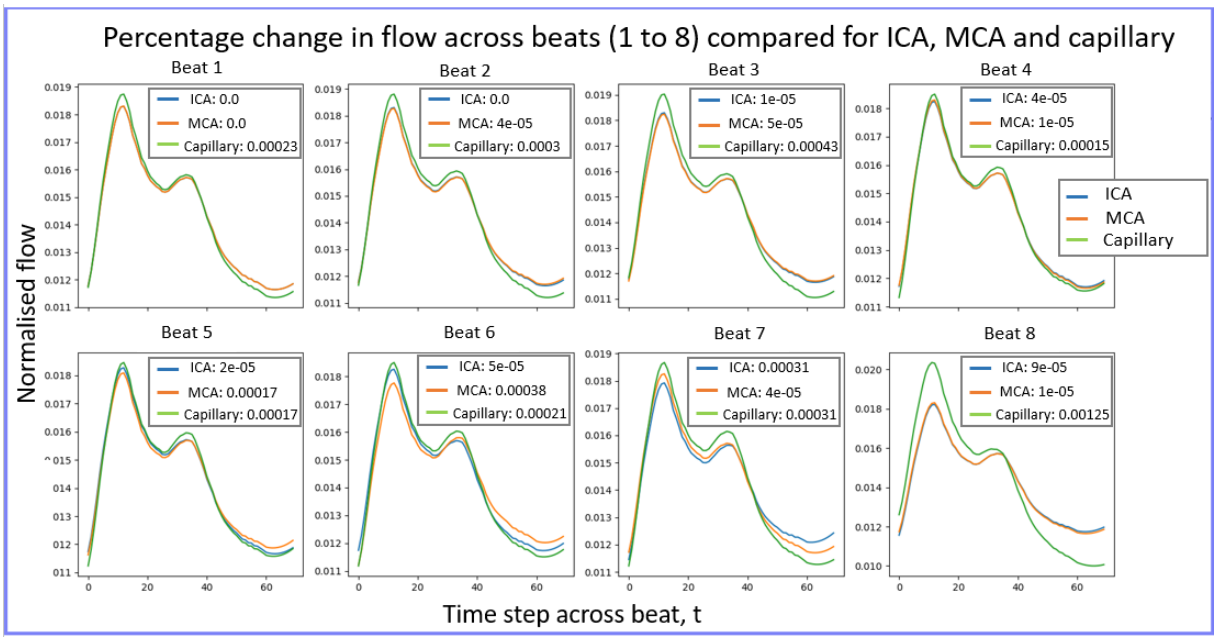

Fig. 7.17 Normalised flow in the ICA, MCA and capillary for beats 1 to 8. RMSE values are stated in the legend for each beat.

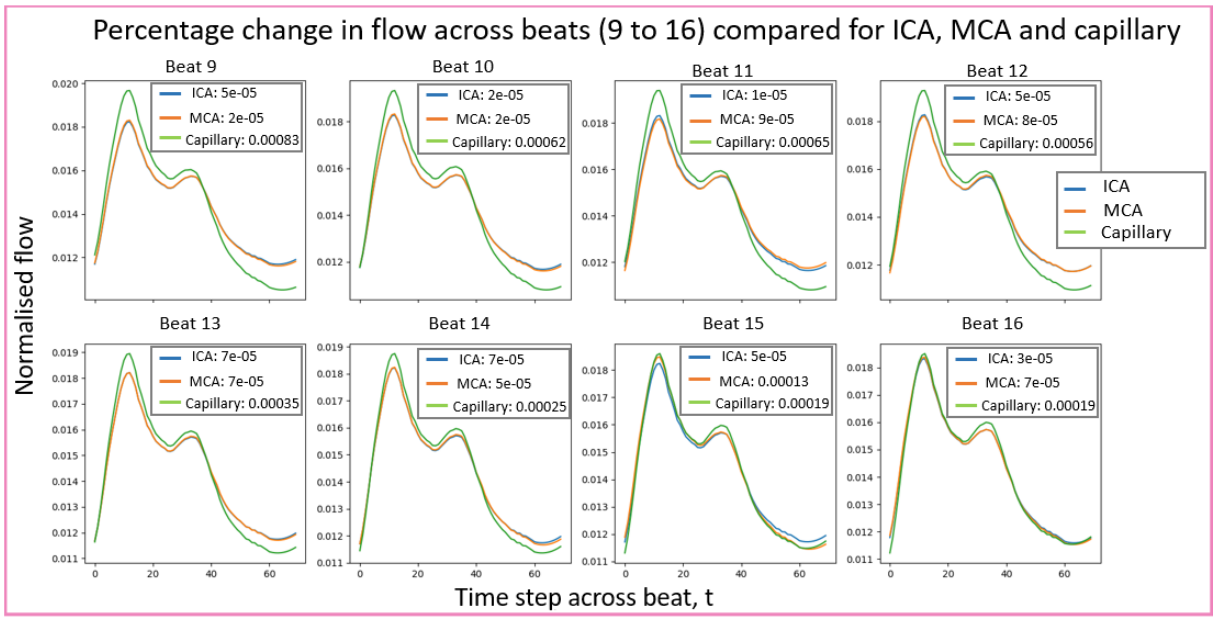

Fig. 7.18 Normalised flow in the ICA, MCA and capillary for beats 9 to 16. RMSE values are stated in the legend for each beat.

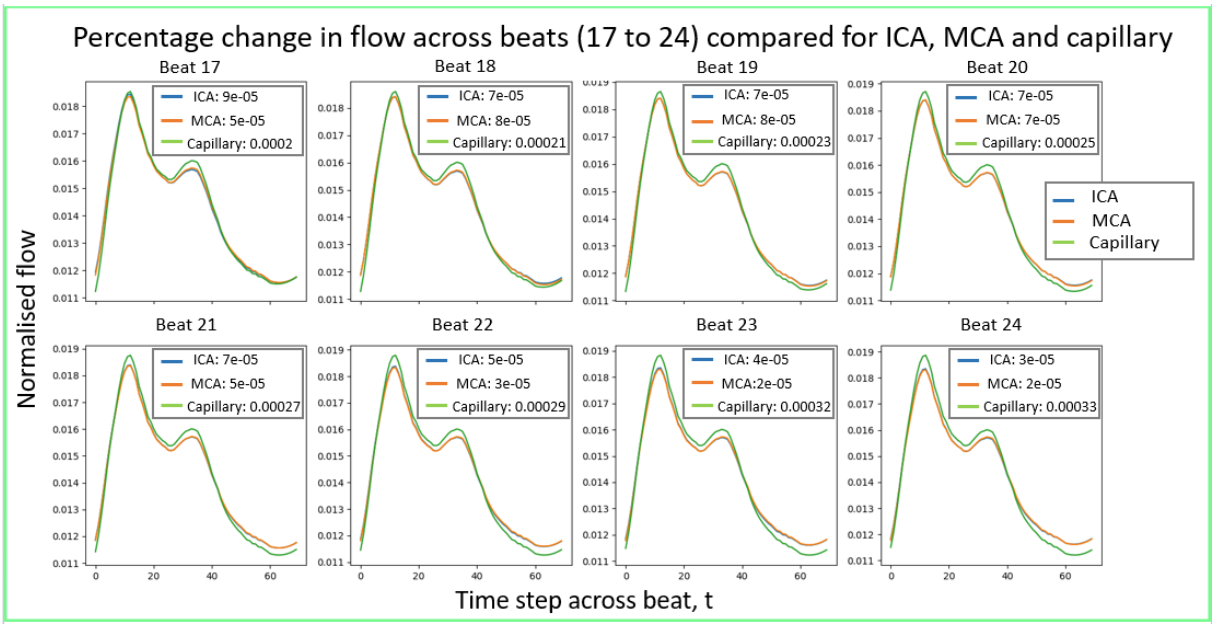

Fig. 7.19 Normalised flow in the ICA, MCA and capillary for beats 17 to 24. RMSE values are stated in the legend for each beat.

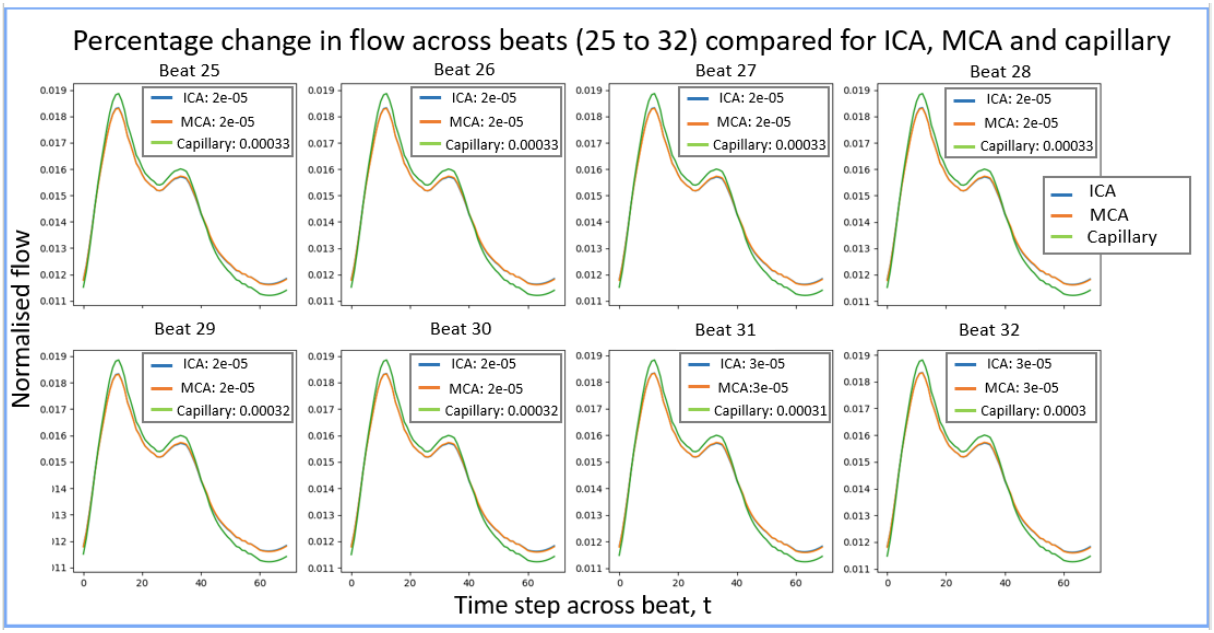

Fig. 7.20 Normalised flow in the ICA, MCA and capillary for beats 25 to 32. RMSE values are stated in the legend for each beat.

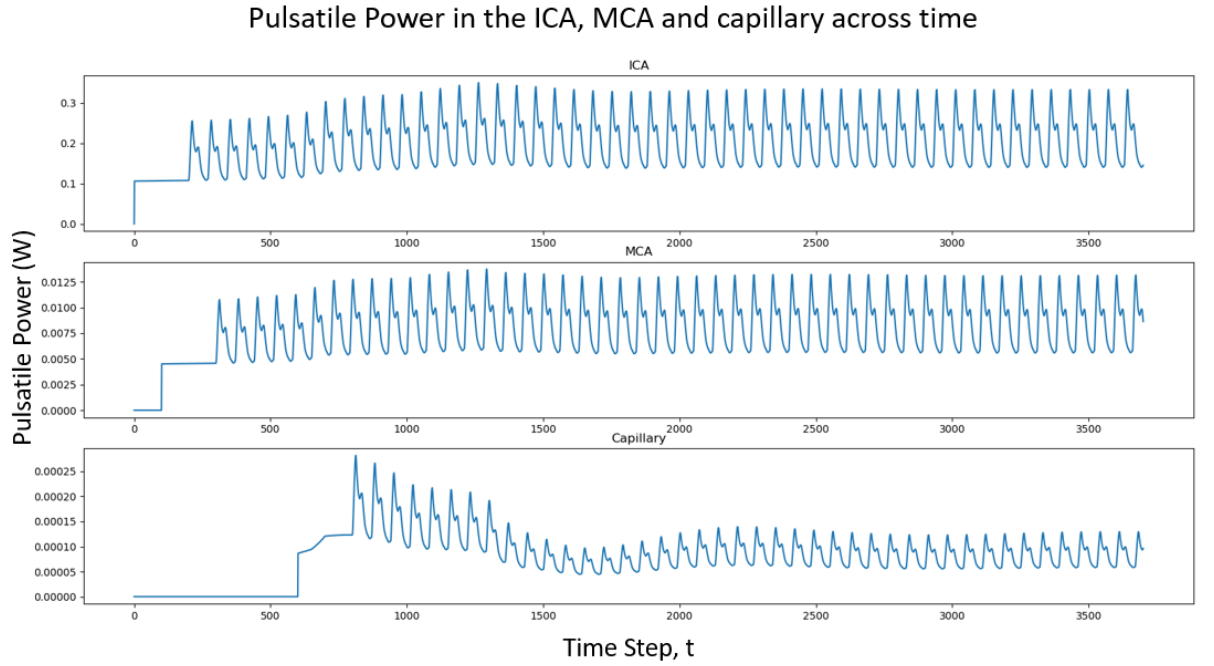

Fig. 7.21 Pulsatile power across time compared for the ICA, MCA and capillary.

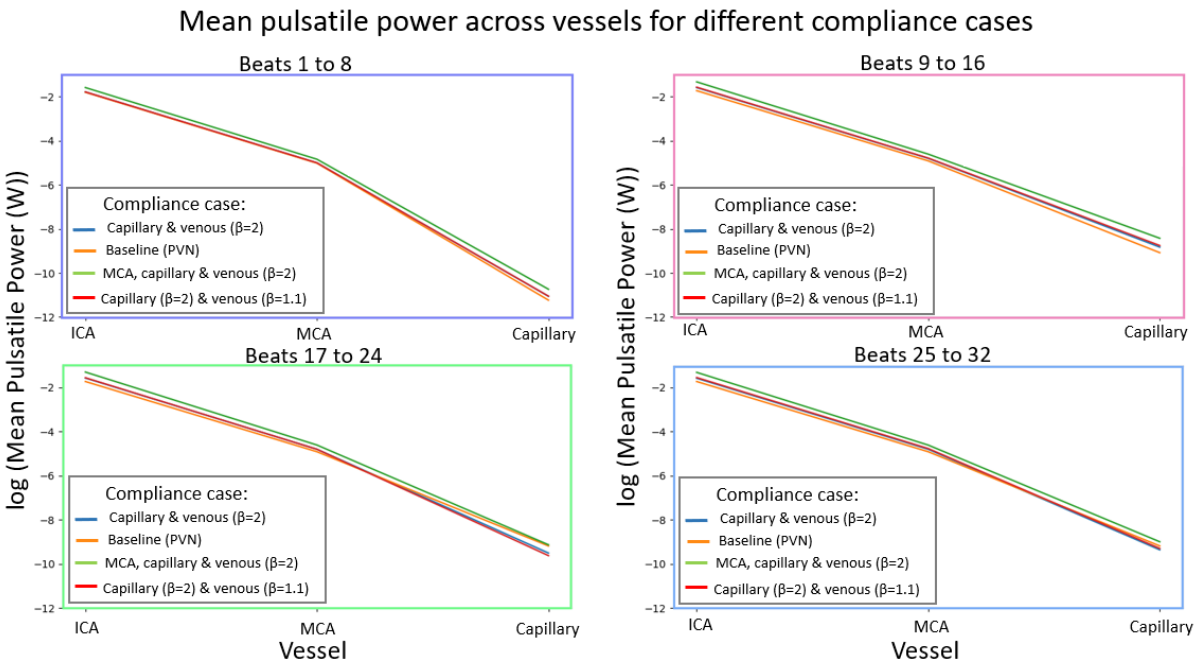

Fig. 7.22 Mean pulsatile power compared across the ICA, MCA and capillary. Mean pulsatile power was compared across groups of beats based on the beat number.

Pressure wave - variable heart beat

The pressure wave was adjusted to include periods of constant diastolic pressure in between beats. In this case, pressure returned to 80 mmHg with the length of this diastolic period varied randomly between beats. The purpose of this was to simulate flow more realistically by introducing variability into the input pressure wave. Pressure and flow values across time obtained from the model are presented in Figs. 7.23 and 7.24. Similarly to the results using the 50 beat pressure wave, small changes in flow can be seen across beats in both the output pressure and flow time series in the capillary until approximately 2500 time steps, at which point both pressure and flow fall into equilibrium. The percentage difference in flow also highlights this pattern (Fig. 7.25).

Pulsatile power across time is presented in Fig. 7.26. Pulsatile power decreases across the ICA, MCA and capillary which suggests that pulsatility is being dampened across the network, despite flow in the capillary still appearing pulsatile. Mean pulsatile power was also compared across groups of beats in the ICA, MCA and capillary for different compliant networks and results are shown in Fig. 7.27.

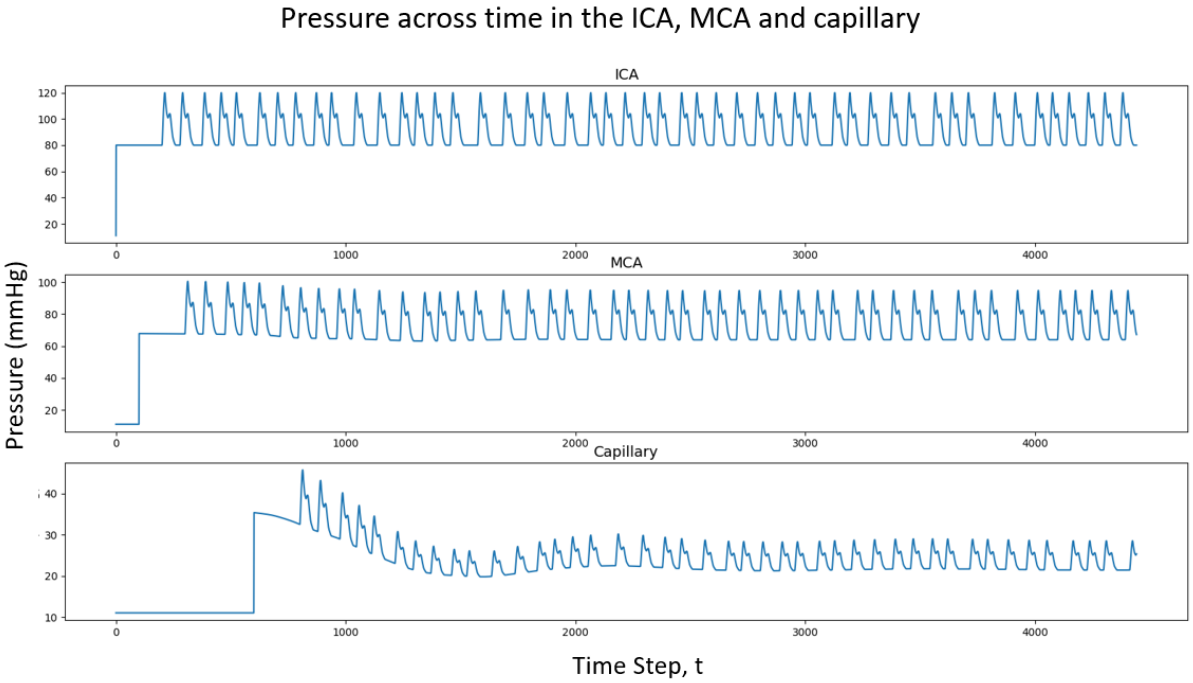

Fig. 7.23 Pressure across time in the ICA, MCA and capillary for pressure wave with return to diastolic pressure between beats.

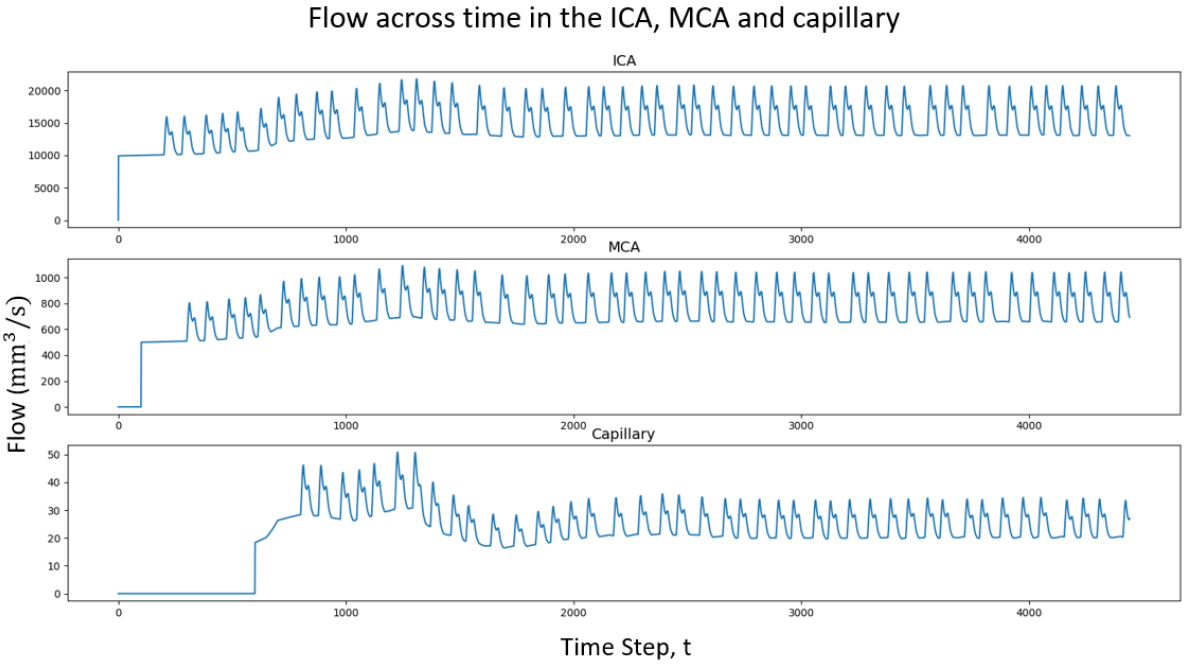

Fig. 7.24 Flow across time in the ICA, MCA and capillary for pressure wave with return to diastolic pressure between beats.

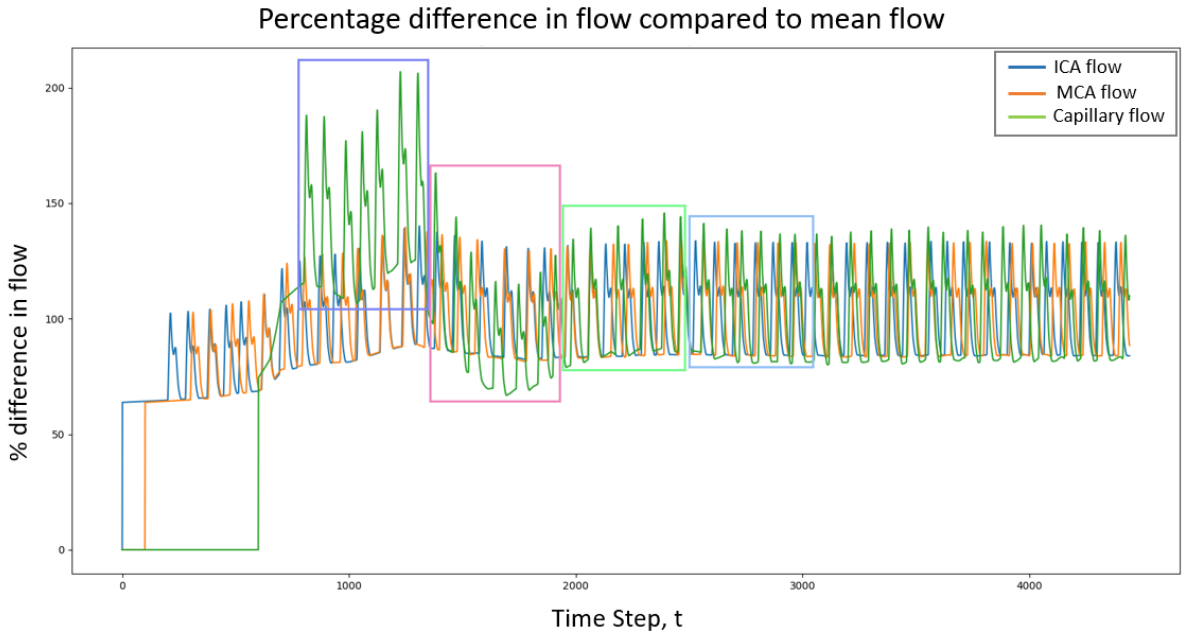

Fig. 7.25 Percentage difference in flow compared to mean flow across time for the ICA, MCA and capillary. The boxes highlight how the capillary time series was split into four groups corresponding to the timings for the groups of 8 beats using the 50 beat input pressure wave.

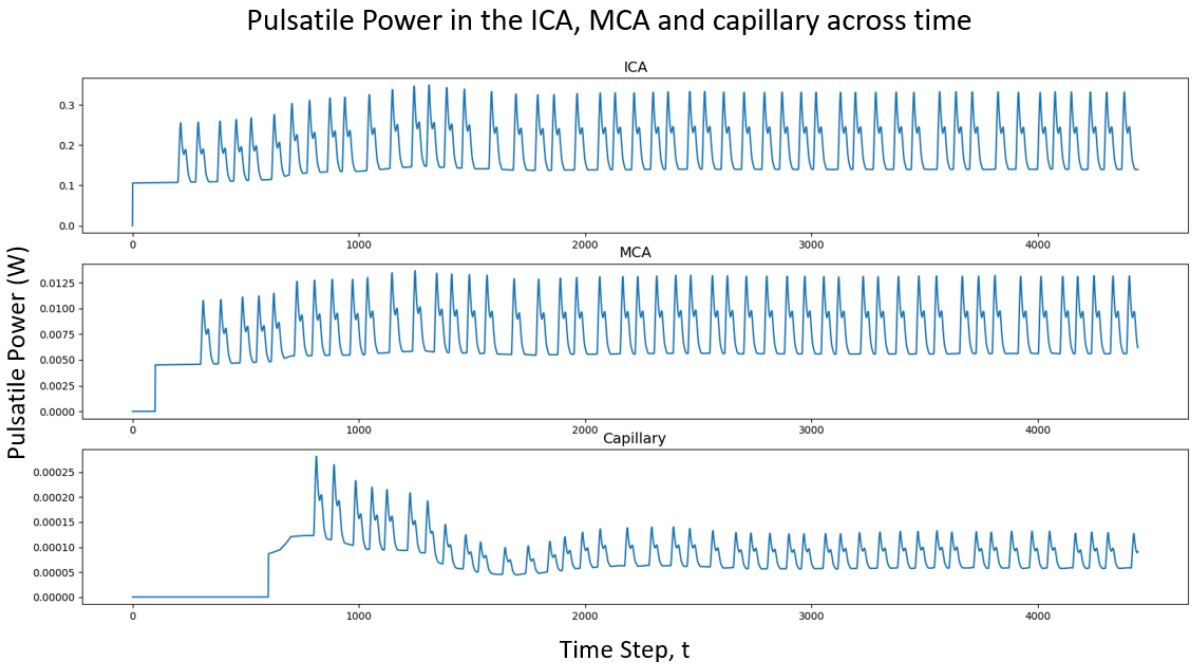

Fig. 7.26 Pulsatile power across time compared for the ICA, MCA and capillary.

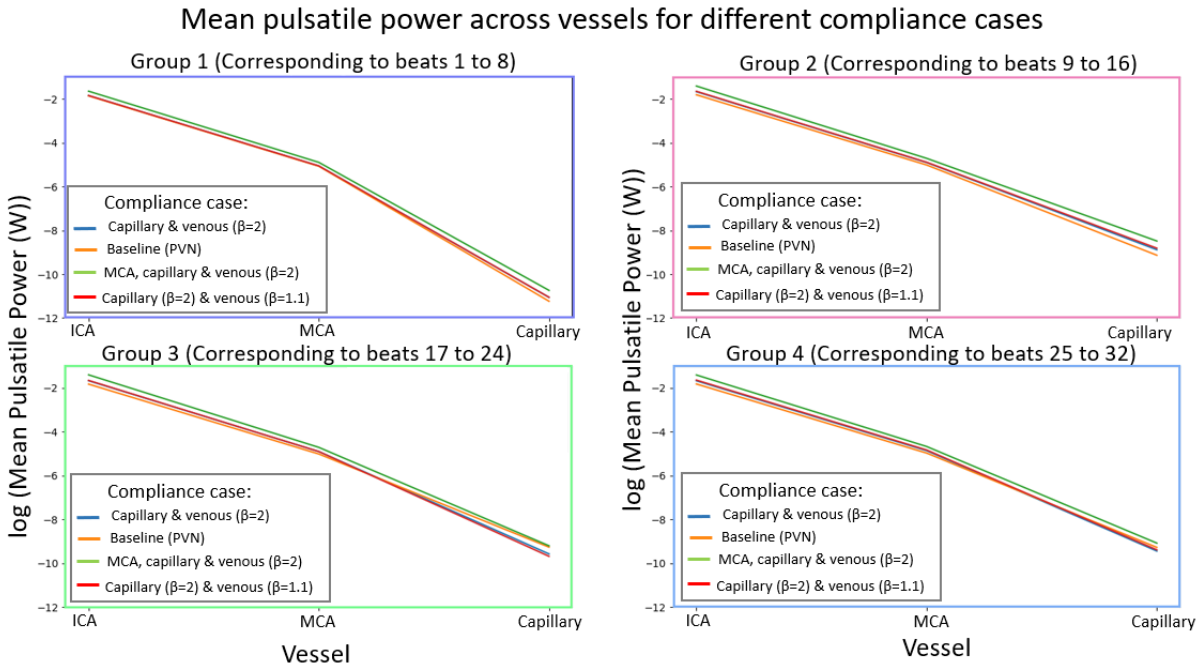

Fig. 7.27 Mean pulsatile power across the ICA, MCA and capillary for the variable pressure wave. Pressure and flow time series were split into four groups corresponding to the timings of the four groups of 8 beats for the 50 beat input pressure wave. Mean pulsatile power was calculated using pressure and flow for each group and is compared across each group.

Summary of Investigation 2 - Pulsatile energy across the network and across time

The buffering of pulsatile energy across a network of compliant cerebral vessels was investigated for two input pressure waves: (1) the pulsatile pressure wave with 50 identical beats and (2) the pulsatile variable pressure wave. Initial results from Investigation 1 suggested that flow remains pulsatile once it has reached the capillaries and therefore compliant vessels don't have an influence on the dynamics of the system. To assess whether the apparent pulsatile flow in the capillaries was meaningful, especially compared to flow pulsatility in the ICA, pulsatile power was compared across the three vessels. Results obtained for both input pressure waves suggest that there are dynamic changes in flow and that pulsatility does decrease across the network despite the shape of the flow profile still appearing pulsatile in the capillary. However, flow still reaches an equilibrium after a certain number of time steps and this suggests there are limitations of the model. Results from Investigation 2 highlight the need to consider the number of beats in the input pressure wave to observe changes in flow across time. The length of each beat in the input pressure wave in relation to the number of segments within a vessel should also be considered.

7.4 Discussion

Simulations were carried out to investigate changes in the shape of the flow profile for a range of compliant network cases. Compliance was added to different levels of the network to assess whether changes in flow could be seen across the ICA, MCA and capillary. Initially, compliance was added to one level of the network at a time and output flow values were compared to the baseline compliance case (determined for the Plausible Vessel Network in Chapter 5). Results highlight that there may not have been enough compliance in the network to influence the dynamics of flow when vessels in only one level of the network were compliant. Changes in the magnitude of the flow could be seen when compliance was added to the model, however changes in the shape of the flow profile were minimal after approximately the first 200 time steps.

Changes in the shape of the flow profile could be seen across the initial time steps for all cases in Investigation 1 using Fig. 7.1 as the input pressure wave. This was particularly prominent in the capillary. Large fluctuations in flow in compliant vessels within approximately the first 200 time steps are likely a result of the large increase in pressure from baseline (11 mmHg at t=0) to 80 mmHg at the start of the beat. Therefore the changes in flow shape are unlikely a result of the added compliance in the network and instead represent the system adjusting to large changes in pressure. This is further confirmed as flow reached an equilibrium state after this period of time in all cases. Results highlight the importance of adding a constant baseline period (e.g. period of diastolic pressure) to the input pressure wave before the start of the beats to allow the system to adjust to pressure changes.

The results suggest that compliance should be added to all venous vessels in order to decrease downstream resistance and allow flow out of the network. This is apparent as some changes in flow across the ICA, MCA and capillary were observed after the addition of venous compliance. This can be compared to the venous levels acting as a sink in the network. Compliance was also added to the capillaries in order for these vessels to accommodate a greater amount of flow. A value of β=2 was chosen for the capillaries and venous levels as this was deemed as realistic for the network, and compares to the original VAN network by Boas et al. (2008). This differs to the conclusion drawn from the steady state simulations in Chapter 5, but takes into account changes in pressure across time and the addition of venous compliance. While capillaries may not be compliant individually, they may appear compliant as a compartment. Changes in capillary transit time heterogeneity and capillary recruitment accompany increased metabolic demands, ensuring there is a sufficient supply of oxygen (Østergaard, 2020). Therefore, assuming a compliance value of β=2 accounts for these mechanisms. Results comparing flow for different values of compliance suggest that using values below β=2 does not have a significant effect on flow, however may cause an issue with the model execution due to errors caused by vessel pressures dropping below the assumed intracranial pressure.

The pressure wave was modified by repeating each value either 2, 3, 4 or 10 times as an approach to imitating non-instantaneous responses to pressure changes in the vessels. Simulations

were run using the standard number of segments in the Plausible Vessel Network and repeated using networks where the number of segments in all vessels were increased by the same factor. Initially it was hypothesised that increasing the number of points in the pressure wave would result in changes in the flow shape and therefore the aim was to compare results from the standard network with the corresponding modified network to test whether it was necessary to increase the number of segments. However the results suggest that increasing the number of segments along with the points in the pressure wave cancels out the effect of the imitated time delay.

Increasing the number of segments instead of repeating the number of points in the pressure wave has a greater effect on the flow across time. Results from this set of simulations suggest that the length of the pressure wave beat in relation to the number of segments, and therefore the number of time steps required for the pressure wave to travel across a vessel, is an important factor to consider. Furthermore, the number of beats within a pressure wave should be considered as changes can be seen across beats before flow reaches an equilibrium state. This also suggests that the pressure wave used for simulations in Investigation 1 did not include enough beats to be able to see a change in flow across time. From this set of simulations it was apparent that the input pressure wave should consist of a single beat repeated for the required number of time steps in order for accurate comparisons to be made across the time series. Furthermore, the pressure wave needs to consist of enough beats to be able to observe changes in pulsatility before flow reaches the equilibrium state in the system. Finally, the number of segments in the vessel should be greater than the length (number of time steps) of a beat within the pressure wave to allow for the vessel to respond to the pressure changes across the beat before the reaching the next vessel in the network.

Results obtained from Investigation 1 indicate that flow simulated in the model does not appear to show the shape changes we were expecting to observe. This is particularly evident as capillary flow continues to exhibit the pulsatile shape seen at the start of the network as opposed to flatlining which would signify flow becoming steady. This may have been a consequence of the input pressure wave being too short to observe dynamic changes in flow. This was taken into account when running simulations in Investigation 2. The main aim of the second set of simulations was to assess whether the pulsatility seen in the capillary in the previous results was comparable to flow pulsatility in the ICA, and therefore whether flow was still significantly pulsatile. This was achieved by comparing the shape of flow between each vessel and also across beats. Mean pulsatile power was also calculated to assess the buffering of pulsatile energy, firstly across the network from the ICA to the capillary, and secondly in the vessel across time. Results suggest that despite the shape of the capillary flow waveform still appearing pulsatile across time, pulsatility is dampened across the network as pulsatile power decreased from the ICA to the MCA and capillary. Furthermore, a study by Hahn et al. (1996) found red blood cell velocity to be pulsatile in capillaries in the skin. Although capillaries in the brain may exhibit different behaviour due to different physiological mechanisms, the study suggests that flow in

the microvessels does remain pulsatile to some extent and is in agreement with the results from this set of simulations.

The results from the dynamic simulations propose a number of potential limitations of the model. Changes in flow across the ICA, MCA and capillary were minimal, suggesting that the model may be too simplistic to observe the expected shape changes in compliant vessels. This could be due to the large number of parameters in the model for which values have been estimated. Values of arterial compliance were taken from existing literature for the purpose of creating a plausible network of vessels using empirical values where possible. However, capillary and venous compliance was estimated as the values are unknown. Furthermore, flow appeared to reach an equilibrium state in the ICA, MCA and capillary after a certain number of time steps which suggests that there is a point where vessel compliance no longer influences the dynamics of the system. Noise was added to the input pressure wave to introduce variability to explore this further. However it was found that flow still reached an equilibrium state for the modified input pressure wave. As compliance no longer influences the system after this equilibrium state is reached, the time for useful simulated outputs of flow is restricted.

Another limitation of the model is the use of a constant value for intracranial pressure (ICP). Intracranial pressure in the VAN model (Boas et al., 2008) was chosen to be 10 mmHg and a typical value of ICP falls between 7 and 15 mmHg (Steiner and Andrews, 2006). The value for ICP in this model was lowered to 7 mmHg to provide a large enough difference between the baseline pressure of 11 mmHg while still being plausible. However, keeping ICP constant across time does not take into account the dynamic changes in compliant vessels. As vessels in the network respond to changes in pressure resulting from the time-varying pressure wave, it is likely that ICP would also vary. Furthermore, the model is limited by using the same value of ICP across all vessels in the network. ICP could be varied across the different vessels to reflect the local dynamic behaviour in the network. Using a time-varying and localised value of intracranial pressure would make the model more realistic by reflecting dynamic and local changes in compliant vessels. However, vessel compliance would also need to be considered across time as dynamic changes in ICP would likely affect how compliant the vessel is and this would greatly increase the complexity of the model.

More levels could be added to the Plausible Vessel Network to make the model more realistic. The Plausible Vessel Network was designed to have 14 levels in total to represent arteries, microvessels and veins. However, results from the dynamic simulations show that flow appears pulsatile at the start of the microvessels which indicates that there may not be enough levels for the pulsatile energy to be buffered across the arteries and arterioles before reaching the capillaries. This could be implemented by adding more levels, such as adding all levels from the VAN model (Boas et al., 2008) to to the Plausible Vessel Network, hence creating a network with 20 levels in total. A more realistic network would require 100s, if not 1000s, of branching points. However, adding more levels to the network would increase the running time of the simulations and would

require suitable computational power. The model would also need to be re-characterised to choose appropriate compliance values for each level.

7.5 Summary

Dynamic simulations were run to investigate changes in pulsatility across levels of the Plausible Vessel Network. Pressure and flow values were simulated across time and compared in the ICA, MCA and capillary for a range of compliant networks. Changes in the shape of the flow profile were compared across vessels in the network and also within vessels across time. Results from Investigation 1 suggest that compliance should be added to the venous and capillary levels to achieve changes in flow across time. In addition, the results highlight the need to consider the input pressure wave. An example of this is the use of a single beat repeated across the length of the pressure wave if comparing the shape of the flow across time. The number of beats within the pressure wave should also be considered as using a short pressure wave may not exhibit dynamic changes in flow due to the inadequate duration of the simulation. The number of segments in a vessel in relation to the the length of a beat in the input pressure wave is another detail to consider. The aforementioned factors were considered in simulations in Investigation 2 which assessed the buffering of pulsatile energy across the network and across time. Despite flow still appearing pulsatile in the capillaries, results suggest that pulsatile energy is dampened across the network as indicated by the decrease in pulsatile power from the ICA to the capillary. Furthermore, shape changes can be observed across the ICA, MCA and capillary provided the input pressure wave consists of enough beats. Dynamic simulations will be run with data collected using DIMAC to investigate whether expected shape changes can be observed in the MCA (Chapter 8).

Chapter 8

Estimating Compliance in Cerebral Vessels from MR data

Chapter Overview

Arterial stiffness is typically measured using pulse wave velocity. However, this is limited to a small number of vessels as current methods are unable to spatially and temporally resolve the pulsatile flow waveform to obtain reliable measures. A proof of concept is presented in this chapter to estimate compliance in the ICA and MCA using DIMAC MRI data, applying a simple method. A number of input networks were created using a range of compliance values and output flow profiles obtained from the simulations were compared to the measured DIMAC flow waveforms to find the closest matching compliance values. Results suggest that there are many factors that need to be considered in order to accurately model flow across a network of vessels from the large arteries to the capillaries, however the method demonstrates the potential contribution of a dynamic model of blood flow in obtaining indicators of cerebrovascular health.

8.1 Introduction

Data were collected from seven participants using the DIMAC sequence to obtain pulsatile flow waveforms in the ICA and MCA. Imaging pulsatile flow in cerebral vessels can provide localised measures of arterial stiffness which indicate the health of blood vessels in the brain. Key measures of arterial stiffness include vessel compliance and pulse wave velocity (PWV), however current methods are unable to spatially and temporally resolve the pulsatile waveform accurately enough to obtain reliable estimates in many cerebral vessels.

In this chapter, a proof of concept to estimate compliance in cerebral vessels is presented, involving the use of DIMAC data and simulated data from the model. Pulsatile flow waveforms measured in the ICA using DIMAC were inputted into the model. Simulated flow waveforms in the MCA were compared to the measured DIMAC MCA waveforms for a range of compliant

networks. Compliance was varied in the MCA, capillaries, venules and veins in the Plausible Vessel Network to create a number of input network files, and output flow values were obtained from the model for each network. The shapes of the simulated MCA flow waveforms were compared to the measured flow waveforms obtained from DIMAC data to find the closest matching combination of compliance values and therefore obtain estimates of compliance in these vessels. The model was developed to follow the pressure wave across the network and track the corresponding changes in flow, making it suitable for obtaining simulated waveforms at different sections of the vascular network. The number of segments was also varied across levels of the network to investigate whether the shape of the flow waveforms was influenced by the speed of progression of the pulsatile waveform through the vascular tree, that is, the pulse wave velocity. The method described in this chapter demonstrates the potential contribution of a dynamic vascular model of blood flow when obtaining estimates of arterial stiffness, an important indicator of vessel health in the brain.

8.2 Methods

8.2.1 Data collection

DIMAC data were previously collected for a study investigating the influence of hormone changes throughout the menstrual cycle on cerebrovascular function. Data were collected in seven healthy female participants at three different phases of the menstrual cycle. The data used in this chapter were taken from the the early follicular phase, when hormone levels are low and thus won't have an influence on cerebrovascular function. Two separate DIMAC slices were positioned perpendicular to the right ICA and right MCA, and the following acquisition parameters were used: TR=15 ms, TE=7 ms, slice thickness=10 mm, matrix size=2x2 mm, GRAPPA=5, partial Fourier=6/8, number of repetitions=10. Pulse oximeter measures were acquired from the index finger whilst scanning to provide an independent cardiac measure.

Using a time-of-flight angiogram as a reference, 4 contiguous voxels in the ICA and 4 contiguous voxels in the MCA were chosen as masks. The DIMAC data were averaged across these masks to provide a 1 minute long time series of pulsatile waveforms on the ICA and the MCA, each representing approximately 60 cardiac beats (see See Fig.8.1). The pulse oximeter data were processed to detect cardiac peak timings. Each cardiac beat period was divided into 20 bins. The ICA DIMAC data were averaged across all cardiac beats by calculating the mean signal in each cardiac bin. The MCA DIMAC data were processed in a similar fashion. This resulted in an average cardiac pulsatile waveform lasting 20 time steps for both the ICA and MCA data.

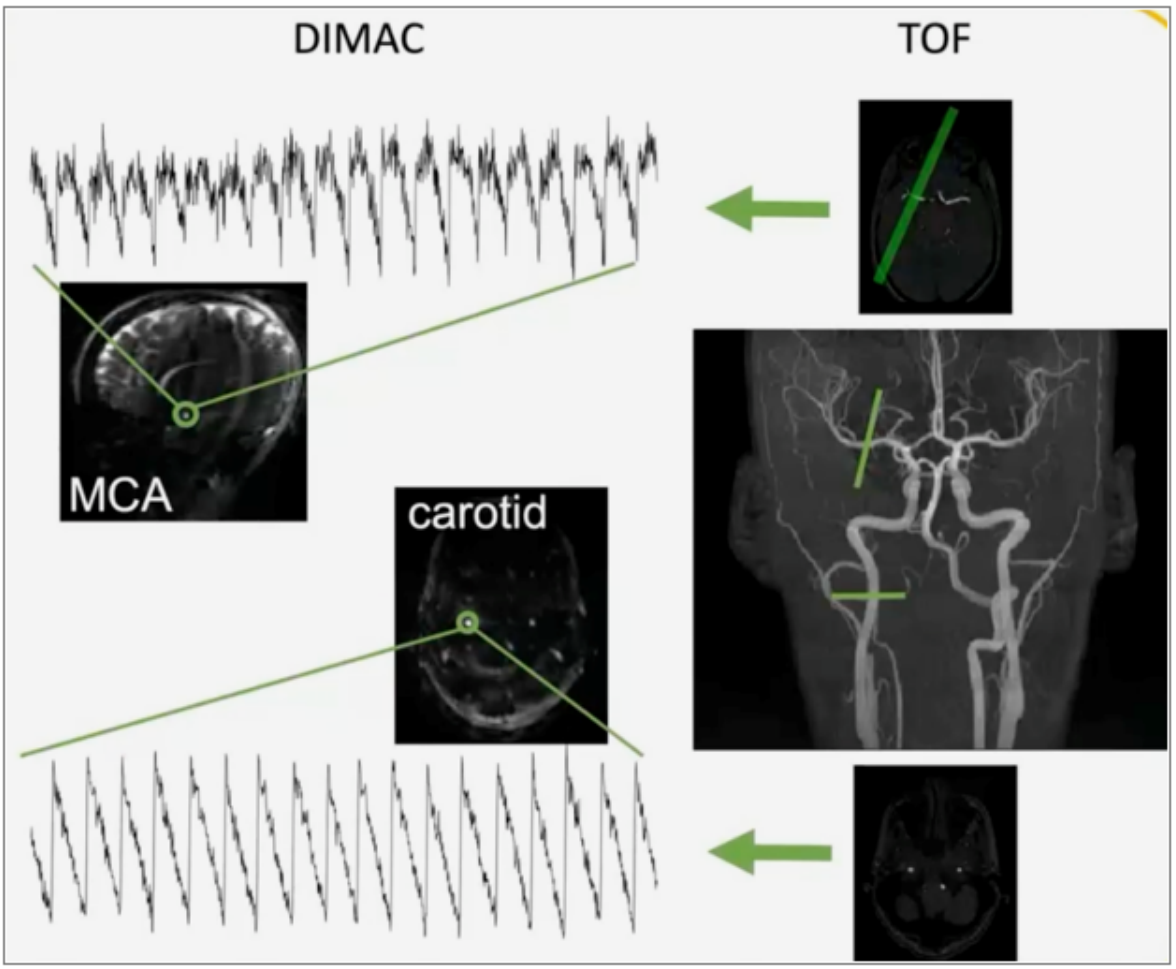

Fig. 8.1 DIMAC data were collected in the ICA and MCA. Time-of-flight angiography was used for slice positioning. Two DIMAC slices were positioned perpendicular to the right ICA and right MCA. Example DIMAC flow time series for each vessel are presented.

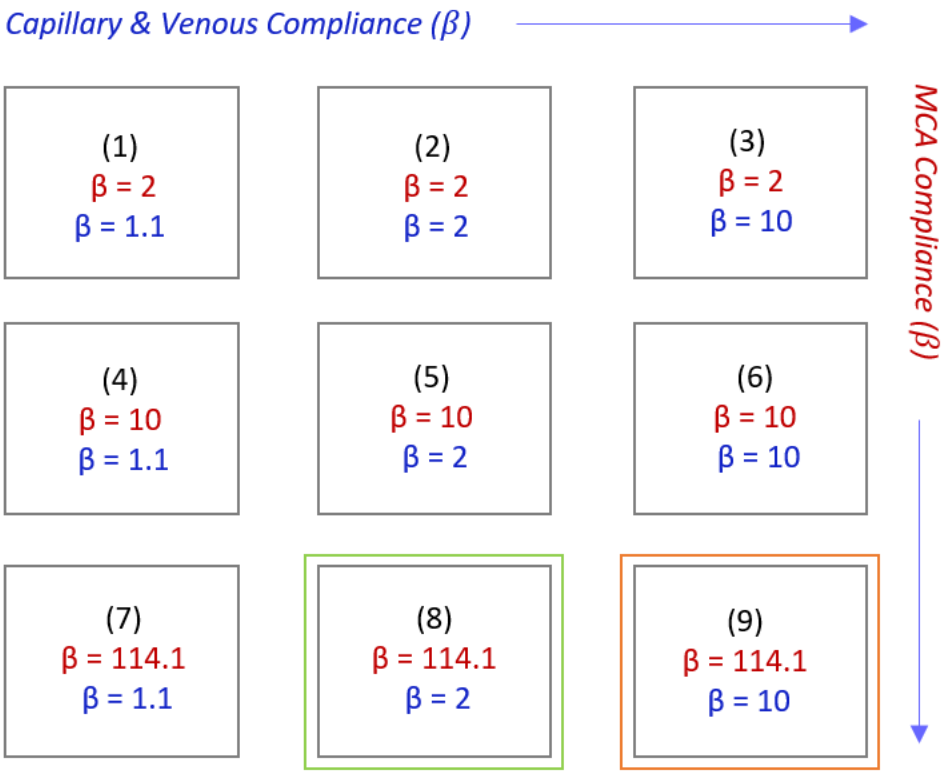

Fig. 8.2 Compliance (β) values for the MCA, capillaries, venules and veins for the nine compliant networks. The green box highlights the compliance values used in previous simulations presented in Chapter 6, Investigation 2. The orange box highlights the compliance values determined for the Plausible Vessel Network in steady state (Chapter 6).

8.2.2 Simulations

Estimating compliance using pulsatile waveforms obtained from DIMAC

Compliance was varied in the Plausible Vessel Network by changing values in the MCA, the capillary and the venous vessels. All simulations in this section were run using the Plausible Vessel Network with 100 segments in each vessel (50 segments in each capillary level). Capillary and venous vessels were grouped together with the same compliance value, following the conclusions drawn from the investigations presented in Chapter 7. Three different β values were used for each category (MCA and capillary/venous), with the combination of compliance values resulting in a total of nine different input networks (Fig. 8.2). Compliance values of β=2, 10 and 114.1 were used in the MCA and β=1.1, 2 and 10 in the capillaries and venous vessels. These were chosen to represent the extreme range of possible compliance values derived from Chapter 7.

Simulations were run for three participants (2, 4 and 6), who were determined to have trustworthy data in both the ICA and MCA (see Results section below). Here, trustworthy pulsatile waveforms were defined as feasible ICA and MCA waveforms that displayed the typical characteristics of a pressure wave i.e. there is a positive change in pressure in the MCA waveform in line with the ICA measurements and there is a clear systolic peak. While the data for participant 4 didn't fit this description due to the lack of a clear systolic peak in the MCA, the pulsatile waveforms were still used in the simulations to provide an extreme contrast to participants 2 and 6. Input pressure waves were created for each of the three participants using the averaged ICA waveform obtained from the DIMAC data. The process used to create the input pressure wave for participant 2 is shown in Fig. 8.3. The calculated cardiac average pulsatile waveform was scaled so that all pressure values were between 80 mmHg and 120 mmHg. The scaled waveform was then repeated to produce a pressure wave with 100 beats. A diastolic baseline period (using the minimum value of pressure in the waveform) equal to the length of 200 time steps was added to the start of the pressure wave to allow the system to adjust to large jumps in pressure before the start of the pulsatile beats. An example of an input pressure wave used for the simulations is shown in Fig. 8.4.

For each of the three chosen datasets, simulated flow waveforms in the MCA were compared across all nine compliant network cases. The output MCA time series was separated into individual beats and the shape of the output flow waveform was compared to the expected MCA flow waveform resolved from the DIMAC data. Correlation coefficients were calculated to compare each beat to the measured MCA waveform to see which beat in the time series matched the closest. Correlation values were also compared across the nine compliant networks to find the combination of compliance values that produced the closest matching simulated waveform to the expected waveform.

Investigating the effect of varying the number of segments in the network

The simulations described in the previous section were run using 100 segments in each arterial and venous level of the Plausible Vessel Network (50 segments in the each capillary level), following the conclusions from the initial dynamic simulations (Chapter 7). The number of segments in each level was chosen as 100 as this was longer than a beat in the input pressure wave (20 time steps), therefore ensuring that the whole beat would pass through the vessel in a level before reaching the next level.

Outputs from the first set of simulations, which were run to estimate vessel compliance, indicate there are some shape changes between the input ICA waveform and the simulated MCA waveform, however the changes are minimal. To investigate whether the number of segments in a level had an effect on the shape of the flow profile, and therefore whether setting the number of segments could produce more accurate simulated flow waveforms from the model, the number of segments was varied and output ICA, MCA and capillary flow was compared across beats. By

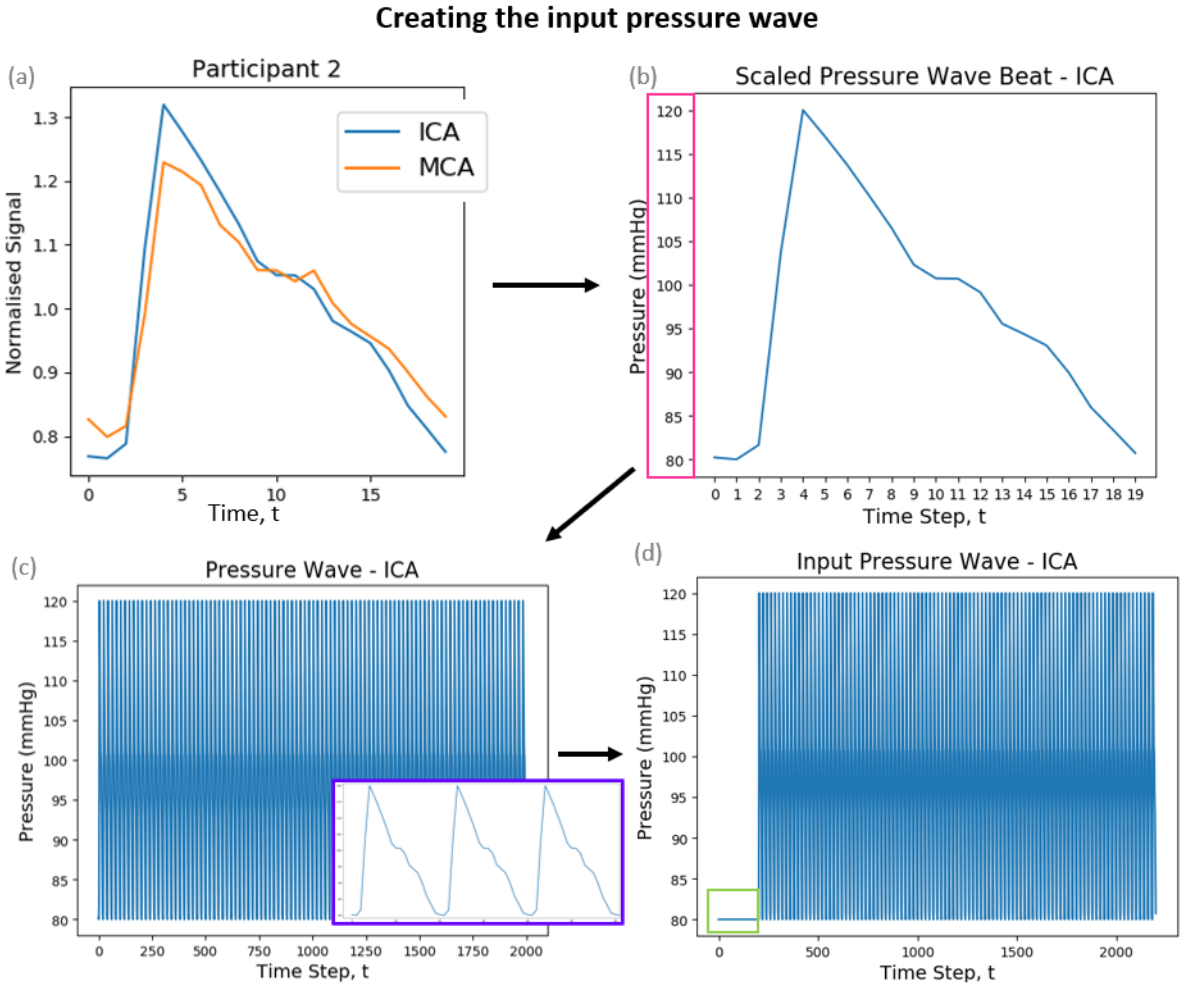

Fig. 8.3 Creating the input pressure wave from DIMAC data collected in the ICA for participant 2. The same process was repeated to create input pressure waves for participants 4 and 6. (a) Cardiac average ICA and MCA waveforms were obtained from DIMAC data, (b) The ICA waveform was scaled between 80 and 120 mmHg to create an appropriate pressure wave beat to use in the input pressure wave, (c) The scaled pressure wave beat was repeated 100 times to create a pulsatile pressure wave of length equal to 2000 time steps with values between 80 and 120 mmHg. The first three beats (first 60 time steps) are highlighted in the purple box, (d) A diastolic baseline period (80 mmHg) equal to the length of 200 time steps (highlighted by the green box) was added to the start of the pressure wave to allow the system to adapt to large changes in pressure before the start of the pulsatile beats. This was used as the input pressure wave for participant 2.

varying the number of segments in a vessel, we are effectively varying the speed at which the pressure wave travels through the vessel, that is, the pulse wave velocity.

Two different approaches were taken to assess whether changing the number of segments influenced the shape of the flow across time in the ICA, MCA and capillary. Firstly, the number of segments in the Plausible Vessel Network were set as their original values (Chapter 6). All arterial and venous levels had 10 segments in each vessel and capillary levels had 5 segments in each vessel. Since each individual pulse was 20 time steps long, the pulse wave would pass from one vessel to the next in less than one cardiac cycle. The second approach involved varying the number of segments across each level such that the vessel in level 0 consisted of 2 segments, vessels in level 1 had 3 segments, vessels in level 2 had 4 segments and so on, resulting in the vessel in the final level having 14 segments. The purpose of this was to imitate a decrease in pulse wave velocity as the pulse wave travels through the network. Since the model was designed to allow the pressure wave to travel through the the network one segment per time step, varying the number of segments varies the time required for the pressure wave to travel across a vessel. In this case, the pressure wave would take longer to travel across each level as the number of segments increased, taking the longest on the venous side as we would expect.

For the modified segment number analysis, simulations were run using the input pressure wave created from the averaged ICA DIMAC waveform for participant 2. Network 1 was chosen as the input network as this was the network that had the highest correlated simulated MCA flow waveform for participant 2. The number of segments was modified as appropriate for the two cases detailed above. Flow time series obtained from the model in the ICA, MCA and capillary were compared by splitting each time series into individual beats. Flow was normalised across each beat by dividing the flow values across the beat by the sum of the flow in the beat (i.e. normalising by the area under the curve).

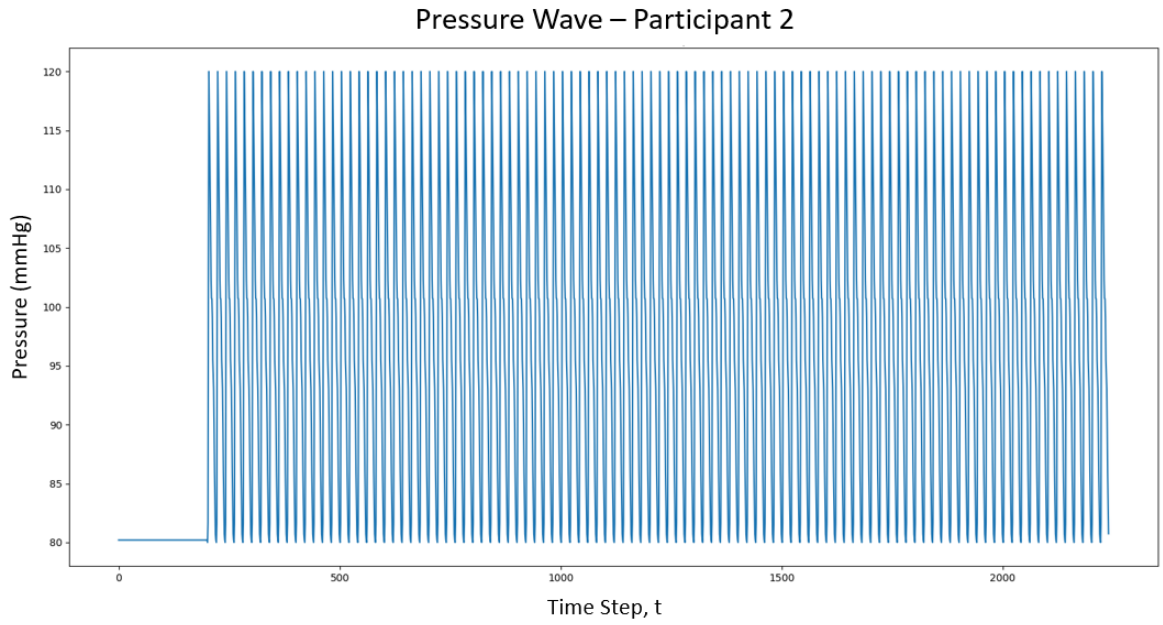

Fig. 8.4 Input pressure wave created from the averaged ICA pulsatile waveform obtained for participant 2.

8.3 Results

Example data collected using DIMAC is presented for a single participant in Fig. 8.5. The low frequency variations in the acquisitions may be a result of low frequency fluctuations in the blood pressure or heart rate variability changing the diastolic blood flow. A similar signal can be seen in DIMAC data obtained using a thigh cuff release challenge to produce changes in blood pressure (Whittaker et al., 2022).

Averaged pulsatile flow waveforms in the ICA and MCA for seven participants are shown in Fig. 8.6. When comparing data collected in the ICA and MCA, it is clear that there are differences in the shape of the flow waveforms across all seven participants, however the degree to which they differ varies. Flow waveforms for participants 2 and 6 show some differences between the ICA and MCA, particularly in terms of the magnitude of the signal, however follow approximately the same shape of a heartbeat. In contrast, data collected for participant 5 shows a large difference in the shape of the two waveforms.The MCA waveform suggests that the data is not accurate for this participant as the waveform is inverted and does not follow the shape of a typical pulsatile waveform. It is possible that the MCA flow in this participant was too high, exceeding the critical velocity of the DIMAC sequence, thus losing its pulsatile shape. In participants 3, 4 and 7, the MCA waveform appears flat at the point where the systolic peak is expected. This indicates a similar issue where part of the pulsatile flow has exceeded the critical velocity. ICA flow waveforms for participants 2, 4 and 6 were used to create input pressure waves for the model and simulations were run for a range of compliant networks.

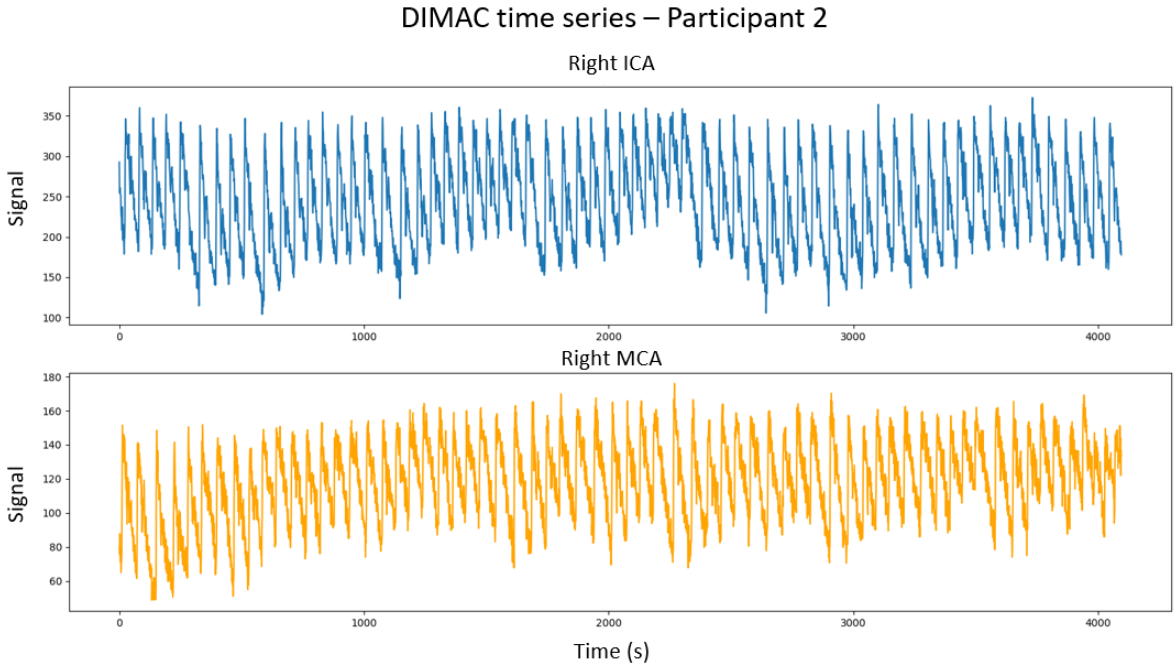

Fig. 8.5 Raw data obtained in the ICA and MCA using DIMAC for a participant.

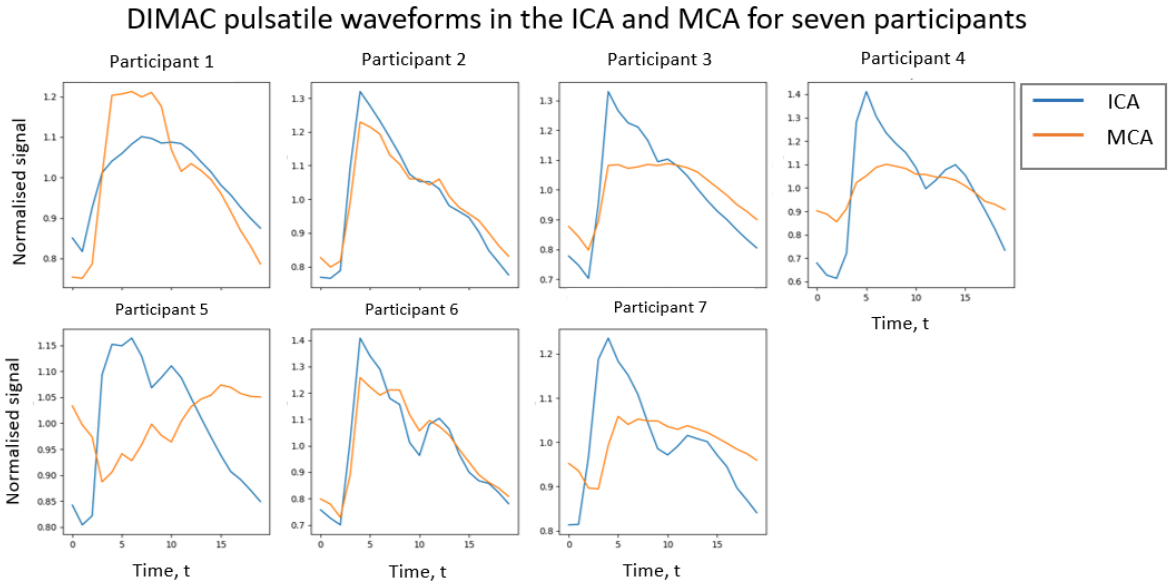

Fig. 8.6 Average pulsatile flow waveforms in the ICA and MCA compared for seven participants.

Estimating compliance using pulsatile waveforms obtained from DIMAC

Simulated MCA waveforms were compared to the measured MCA waveform for all nine compliant networks for each participant. The results for participants 2, 4 and 6 and are presented in Figs. 8.7, 8.8 and 8.9 respectively. Each normalised waveform represents a beat in the simulated MCA time series and is plotted in grey. The beat with the highest correlation coefficient is shown in red and the measured MCA DIMAC waveform is plotted in black. The number of the highest correlated beat and the correlation coefficient are stated in the figures for each compliant network.

The highest correlated waveform was found using Network 1 for participant 2, Network 8 for participant 4 and Networks 5 and 8 for participant 6. In almost all cases, the highest correlated beat is beat number 19. This suggests that the simulation needs to run for a minimum number of beats to obtain feasible shape changes in flow. Across the three participants, simulated MCA waveforms were the closest matching to the measured MCA waveforms in participant 2. However, this could be due to the minimal differences in the ICA and MCA DIMAC waveforms for this participant.

Simulated waveforms for each participant are compared to the corresponding ICA and MCA DIMAC waveforms in Fig. 8.10. The highest correlated waveform was plotted as the simulated MCA waveform for each participant. Overall, the results indicate that there are some shape changes which can be observed between the DIMAC ICA waveform and the simulated MCA waveform, suggesting that flow is influenced by compliance in the network. However, the DIMAC MCA waveform was not accurately reproduced using the model, and this is particularly evident for participant 4. This is not a particularly surprising result since minimal shape changes were observed in the simulations in Chapter 7.

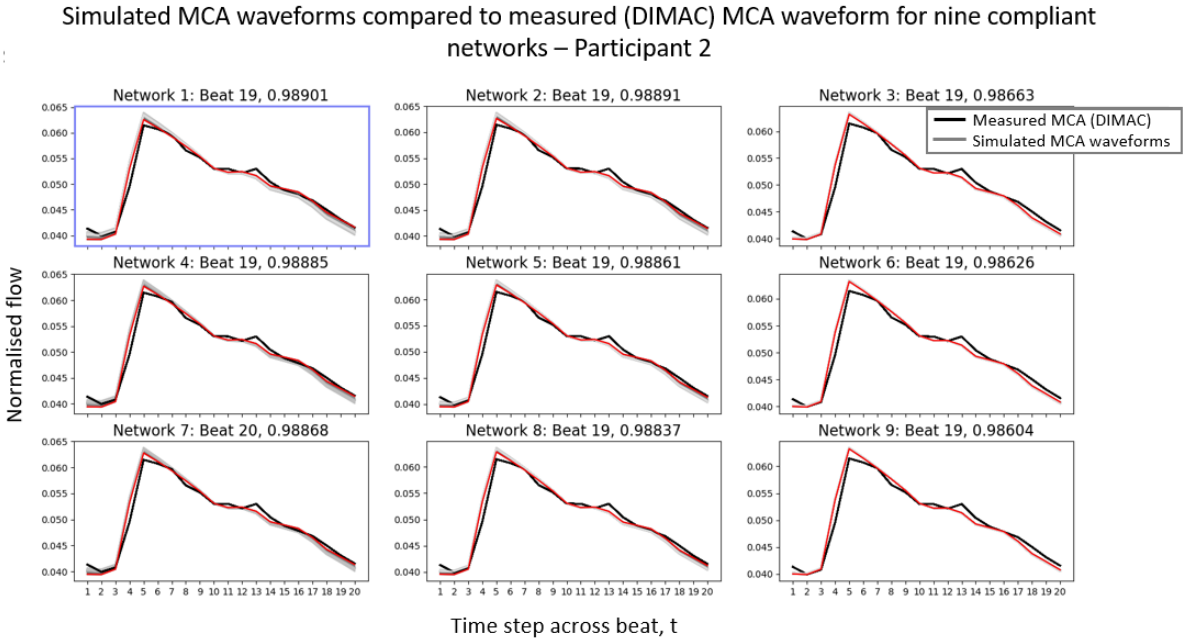

Fig. 8.7 Simulated pulsatile flow waveforms (grey) in the MCA compared to measured MCA flow waveform obtained from DIMAC (black) for participant 2 for nine compliant networks. The highest correlated simulated waveform for each network is plotted in red. The number of the highest correlated beat and the corresponding correlation coefficient are stated in the titles for each network. The blue box highlights the network with the highest correlated beat.

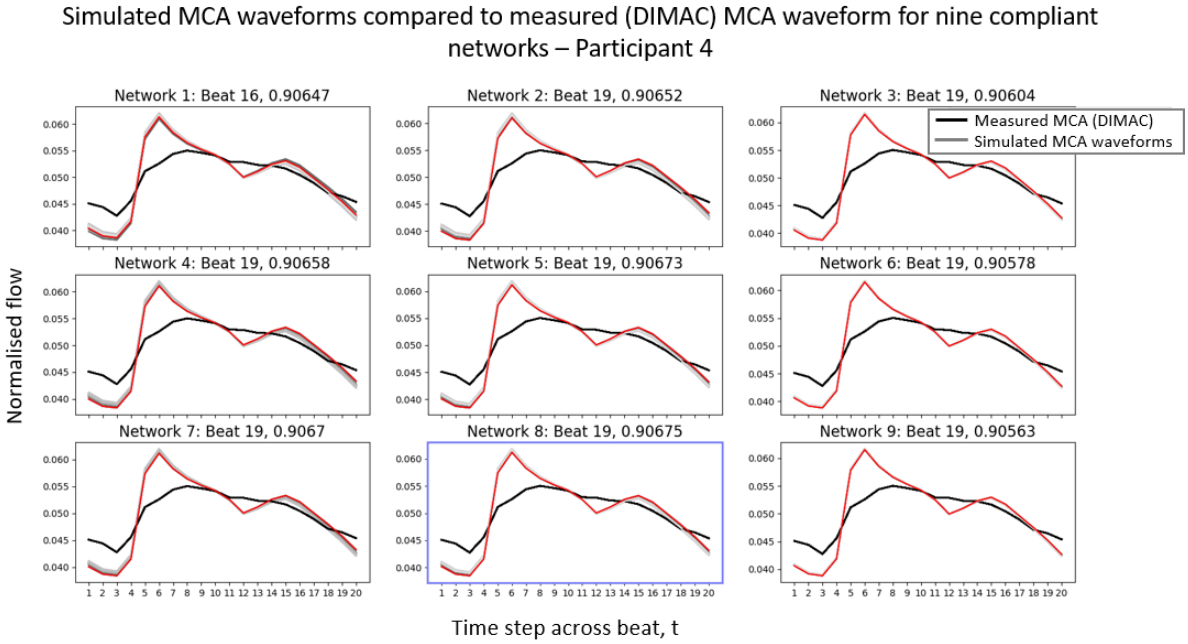

Fig. 8.8 Simulated pulsatile flow waveforms (grey) in the MCA compared to measured MCA flow waveform obtained from DIMAC (black) for participant 4 for nine compliant networks. The highest correlated simulated waveform for each network is plotted in red. The number of the highest correlated beat and the corresponding correlation coefficient are stated in the titles for each network. The blue box highlights the network with the highest correlated beat.

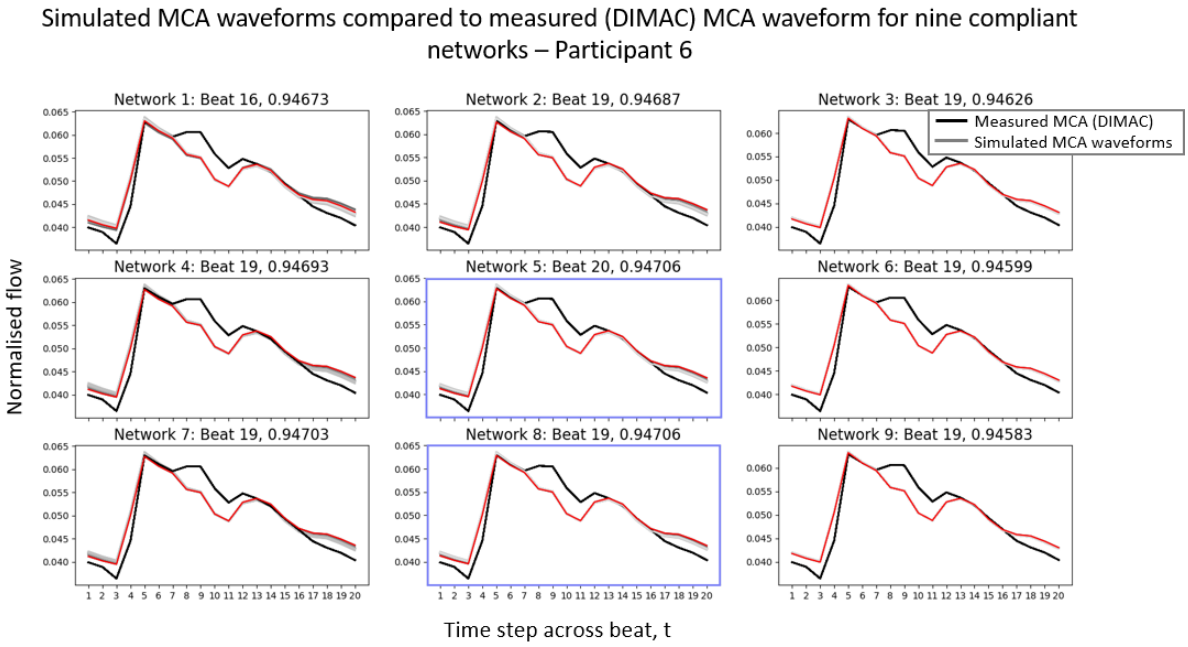

Fig. 8.9 Simulated pulsatile flow waveforms (grey) in the MCA compared to measured MCA flow waveform obtained from DIMAC (black) for participant 6 for nine compliant networks. The highest correlated simulated waveform for each network is plotted in red. The number of the highest correlated beat and the corresponding correlation coefficient are stated in the titles for each network. The blue box highlights the network with the highest correlated beat.

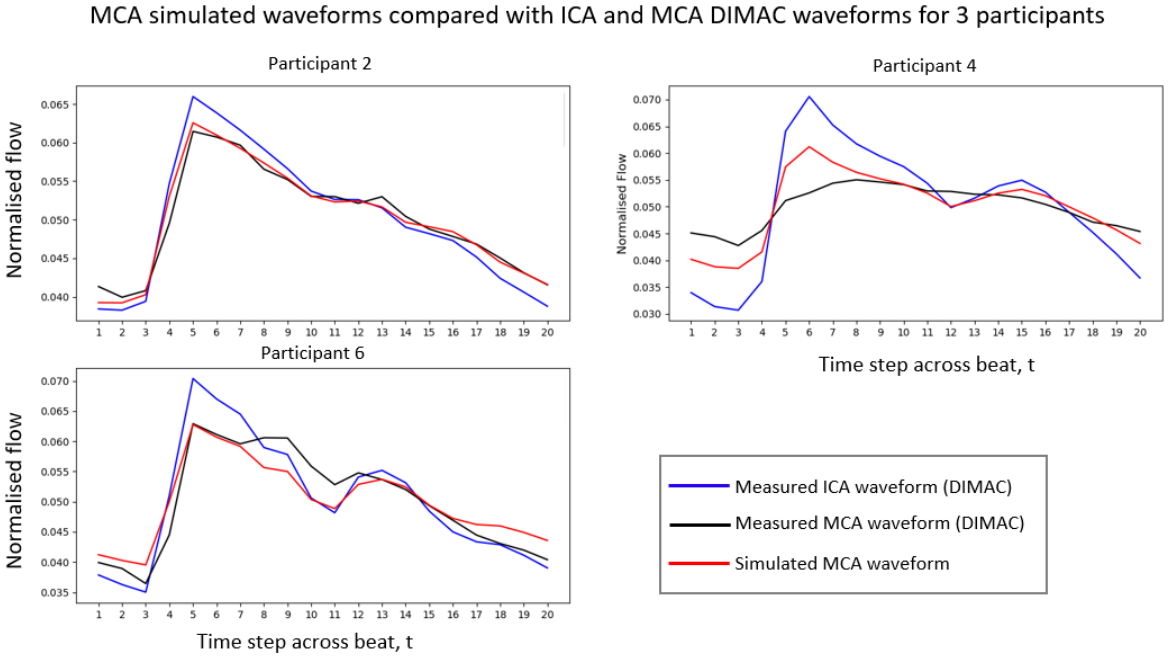

Fig. 8.10 Simulated MCA waveforms compared to the ICA and MCA waveforms obtained from DIMAC data in three participants. The highest correlated beat across all networks was plotted as the simulated MCA waveform for each participant.

Investigating the effect of varying the number of segments in the network

The effect of varying the number of segments across the Plausible Vessel Network on the shape of the flow profile was investigated using two approaches. The number of segments was decreased to 10 segments per level (5 for each capillary level) and the ICA, MCA and capillary flow time series were simulated. The flow time series was split into individual beats for each vessel and flow across the first nine beats is shown in Fig. 8.11. Shape changes are apparent across the network and across beats and this is particularly noticeable in the capillary, suggesting that the number of segments does have an effect on the simulated flow profile across time.

The number of segments in the Plausible Vessel Network was also varied across levels to investigate whether a slowing of the pulse wave would have an effect on the shape of flow across time and across vessels. The number of segments was increased across each level by one segment so that the input pressure wave would take longer to travel across a vessel as it travelled further across the network. ICA, MCA and capillary flow is compared across the first 9 beats in Fig.8.12. Similarly to the previous case, flow shape changes can be observed across vessels and across time and this is particularly evident in the capillary.

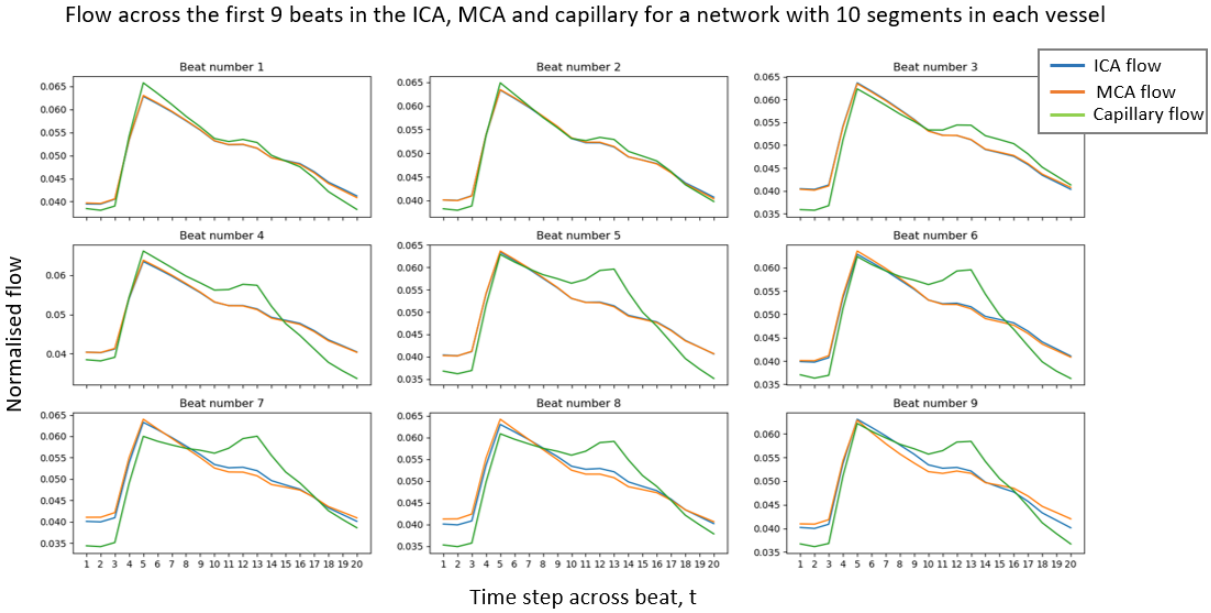

Fig. 8.11 Simulated ICA, MCA and capillary flow compared across the first 9 beats. Simulations were run using the Plausible Vessel Network with 10 segments in each arterial and venous vessel and 5 segments in each capillary level.

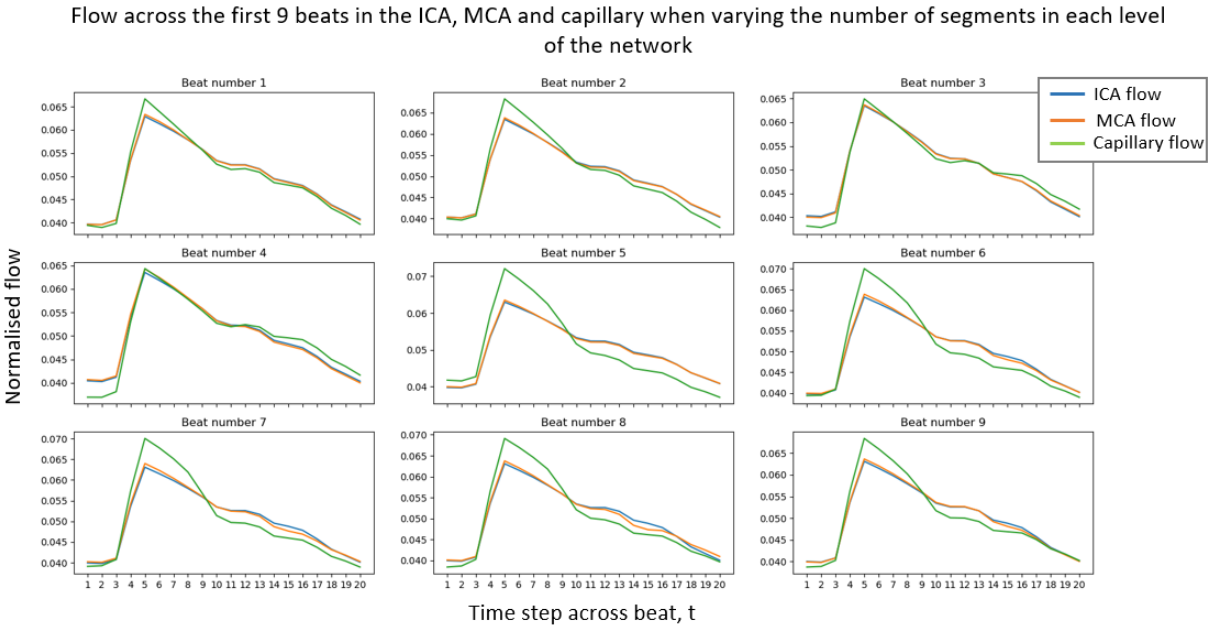

Fig. 8.12 Simulated ICA, MCA and capillary flow compared across the first 9 beats. Simulations were run using the Plausible Vessel Network, varying the number of segments across each level. The number of segments in the first level was chosen as 2, and this was increased by one segment across each of the remaining levels.

8.4 Discussion

A method for estimating vessel compliance in large arteries using pulsatile flow waveforms obtained with the DIMAC sequence is presented in this chapter. Simulations were run using ICA waveforms resolved from DIMAC data for three participants to create input pressure waves, and compliance values were altered in the MCA, capillaries and all venous vessels to create a dictionary of compliance combinations. The simulated MCA time series were obtained for each of the nine compliant networks and separated into individual beats which were compared to the measured average MCA waveform. The simulated MCA waveforms and measured DIMAC MCA waveforms were compared to see whether the model could accurately reproduce the shape of the MCA waveforms and the observed changes in the shape of the flow profile from the ICA to the MCA.

Initial results indicate that there were some shape differences between the ICA flow waveforms obtained from DIMAC and the the corresponding simulated MCA waveforms obtained from the model. However, when comparing the simulated MCA waveforms to the measured MCA waveforms from the DIMAC data, there are clear differences between the two, and this is particularly apparent for participant 4. This suggests that the model cannot accurately generate the DIMAC MCA waveform and was not successful for the purpose of estimating vessel compliance from DIMAC data.

The number of segments in the Plausible Vessel Network was varied to investigate whether greater differences in the shape of the simulated flow waveforms across vessels could be achieved. Results from this set of simulations suggest that the number of segments in each level of the network is another factor that should be considered to accurately simulate pulsatile waveforms. However, this adds another level of complexity to the model as it requires knowledge of how many segments are needed for each level (i.e. the pulse wave velocity across each level) and how this changes across vessels/sections of the network. It should be noted that the simulations in this section were exploratory to investigate whether changing the number of segments would affect the simulated flow time series. Therefore the number of segments in each level was chosen arbitrarily. Varying the number of segments appears to influence the output flow obtained from the model and this is mainly apparent in the capillaries. Further simulations should be carried out with a different number of segments to see whether this could result in larger differences between the simulated ICA and MCA waveforms. Results from this investigation, alongside the results presented in the previous chapter highlight the importance of accurate values for all the parameters in the model. While the simplistic mathematical model and network description may limit the accuracy of the model, the results suggest that there are too many parameters with unknown values that need to be estimated, such as the pulse wave velocity. The addition of more parameters would greatly increase the complexity of the model as more values would need to be known.

A method for estimating vessel compliance using a dictionary of compliance values is demonstrated here. To obtain a realistic estimate of compliance, a greater number of compliance values would be required for each vessel, as well as varying compliance in more levels of the network. This would result in a larger number of compliance combinations, and therefore more input networks. However, increasing the number of input networks would increase the risk of overfitting. The range of β values used in the network would depend on the sensitivity of the model. Outputs from the previous dynamic simulations presented in Chapter 7 suggest that changes in β of 0.1 (e.g. comparing β=1 and β=1.1) do not significantly change the flow time series. Therefore varying β by 1 would be sufficient for the purpose of these simulations.

Accuracy of the simulated flow time series was also limited by the quality of the DIMAC data used in the model. Input pressure waves were created for three out of the seven participants, and were chosen as the most reasonable expected shape changes to attempt to simulate using the model. The averaged MCA waveforms for other participants (e.g. 3 and 7) suggest that the velocity of blood was higher than the critical velocity in the chosen MCA DIMAC slice. Simulations for the purpose of estimating vessel compliance could be repeated using DIMAC data collected further along the arterial section of the vascular tree in order to prevent the blood flow exceeding the critical velocity. Flow waveforms could then be simulated in the corresponding level of the input network and compared to the measured waveforms for a range of compliance combinations to estimate vessel compliance. There is ongoing developmental work to acquire DIMAC data in more appropriate vessels such as the anterior cerebral artery (ACA) where flow isn't too fast or turbulent for the sequence. Data acquired from this vessel could be used in future simulations to determine whether more accurate and valid flow waveforms can be obtained from the model.

The method described in this chapter demonstrates the potential contribution of a dynamic model of blood flow in obtaining important indicators of cerebrovascular health. Previous studies have measured arterial compliance using TCD and MRI. Arterial compliance has been measured in intracranial arteries using TCD (Fu et al., 2016; Roher et al., 2011). Although TCD offers a cost-effective and widely available method for measuring compliance, measures are limited to several vessels and may not be feasible for all participants. Furthermore, flow measured indirectly through flow velocity. MRI offers a promising alternative technique that can provide whole-brain measures of compliance. A study by Warnert et al. (2015) demonstrated the feasibility of estimating compliance in arteries in the Circle of Willis using ASL to estimate the change in blood volume for a given change in pressure. Pulse wave velocity has been measured in intracranial arteries using 4D-flow MRI (Björnfot et al., 2021). The DIMAC sequence allows pulsatile flow to be measured in real time in large and small arteries (Whittaker et al., 2022). Using a model alongside DIMAC data could assist in estimating compliance in all vessels in the network. Further research into setting the parameters could help to increase the accuracy of the outputs, providing a useful tool for assessing the health of blood vessels in the brain.

8.5 Summary

A method to estimate vessel compliance using data collected with the DIMAC sequence is described in this chapter as a proof of concept. ICA waveforms obtained from DIMAC were used to create input pressure waves and the simulated MCA waveforms obtained from the model were compared to the measured MCA waveforms from DIMAC data. Initial outputs from the model show some shape changes in the simulated MCA waveform that compare with the expected MCA waveform, however simulated MCA waveforms did not accurately match the measured waveforms. The number of segments was varied in vessels to investigate whether this had an effect on the shape of the flow profile across vessels. Results from these simulations suggest that this is an important factor to consider when simulating realistic pulsatile flow waveforms, although it would dramatically increase complexity and the number of parameters that need to be set.

Chapter 9

Discussion

The declining health of vessels in the brain, often as a consequence of ageing, is associated with the development and progression of cerebrovascular disease. Arterial stiffness is related to the pulsatility of blood flow. Pulsatile energy is dampened less efficiently as arteries become less compliant, resulting in pulsatile flow reaching the microvessels. This is known to cause damage to the smaller, more delicate vessels (O'Rourke, 2007). Damage caused by excessive pulsatile energy at the site of the capillaries is thought to contribute to the breakdown of the blood-brain barrier (BBB). Endothelial cell function in the BBB is impaired following exposure to pulsatile flow (Garcia-Polite et al., 2017), and a dysfunctional BBB is associated with the development of cerebral Small Vessel Disease (Schreiber et al., 2013) which contributes to stroke and vascular dementia (Chojdak-Łukasiewicz et al., 2021). It is evident that arterial stiffness is an important factor relating to vessel health in the brain and an accurate local measure is required to improve understanding and assessment of cerebrovascular health and disease.

Pulse wave velocity (PWV) is the current gold-standard method for measuring arterial stiffness and is typically measured systemically between the carotid and femoral arteries. A higher PWV is associated with a greater risk of developing cardiovascular disease (Ji et al., 2018). Carotid-femoral PWV is a robust measure of systemic arterial stiffness, however does not necessarily reflect the condition of the blood vessels in the brain. This has motivated the development of methods to measure PWV in intracranial vessels, allowing for a more specific assessment of cerebrovascular health. A localised measure of arterial stiffness in the cerebral arteries is required to obtain an understanding of flow pulsatility and its propagation along the brain's vascular tree.

There are a number of existing methods to measure blood flow in the brain. Whilst transcranial Doppler ultrasound (TCD) is a relatively accessible and inexpensive method, blood flow is indirectly measured using blood flow velocity. Furthermore, TCD is limited to measuring blood flow velocity in large cerebral arteries and therefore it is not possible to assess pulsatile flow in other downstream vessels. MRI offers a more versatile approach to measuring blood flow, and recent developments have been made to resolve the pulsatile flow waveform for the purpose of

obtaining measures of pulsatility and pulse wave velocity (Bianciardi et al., 2016; Björnfot et al., 2021; Holmgren et al., 2020; Whittaker et al., 2022).

A computational model was developed in this thesis in order to investigate pressure-driven changes in compliant blood vessels, with the aim of modelling pulsatile flow in a network of vessels. Existing models have demonstrated the potential to simulate blood flow across a large network of vessels (Boas et al., 2008; Piechnik et al., 2008). However, these previous models have typically focused on simulating blood flow in steady state and are therefore not suited to investigating dynamic changes in flow in compliant vessels. To model pulsatile flow, it is vital to consider the changes in volume and resistance within a vessel as a response to changes in pressure across time. For this reason, a dynamic vascular network model was developed to simulate blood flow with the intention of understanding how cardiac pulsatile energy is dissipated across the cerebral vasculature, and how this is related to changes in vessel health that are commonly associated with ageing. The model was also developed with the intention of obtaining estimates of arterial stiffness such as vessel compliance and pulse wave velocity in cerebral arteries, using pulsatile flow waveforms resolved from DIMAC MRI data.

9.1 Summary of Main Findings

The model was developed with the aim of simulating blood flow in cerebral vessels. The VAN model by Boas et al. (2008) was used as the basis for this model and was extended by adding compliance to all vessels in the network. To achieve this, the volumes of compliant vessels (and corresponding resistances) were updated at each time step as a response to the changes in pressure at each time point. The development of the model is described in Chapter 4.

Existing models were developed with the aim of modelling blood flow across a large network of vessels (Boas et al., 2008; Piechnik et al., 2008), however the aforementioned models simulate flow in the steady state. To simulate pulsatile flow waveforms, required for estimating important measures of cerebrovascular health, dynamic changes in the vessels following changes in pressure need to be modelled. Compliance was added to the model by updating vessel volumes to investigate dynamic changes in flow across the network. The input network was also designed to allow diameters and compliance values for individual vessels within a level to be set, increasing the flexibility and potential applications of the model.

The Equivalent Single Vessel (ESV) was created so that vessel properties within a level of the network could differ, therefore further increasing the flexibility of the model. The ESV, implemented within the model, reduced the branched network of vessels to a single vessel, allowing calculation of the bulk flow through each of the segments. The flow was then distributed to corresponding segments in proportion to the remaining resistance in the path of blood flow. One example where this is advantageous is modelling flow in pathological conditions such as arteriosclerosis, as vessel parameters can be adjusted in the network to imitate blocked vessels within a branch of the network. The development of the ESV was also required to simulate flow

in the Plausible Vessel Network which split the ICA into the MCA and remaining vessels in the Circle of Willis. Therefore, the model could account for distribution of flow in different paths of this network.

The model was also extended by including the option to choose the number of segments into which each vessel was split. This meant the time taken for the input pressure wave to travel through a vessel could be altered as the model was designed to allow the pressure wave to travel across the network one segment per time step. The number of segments can be set individually for vessels. This is advantageous as changing the number of segments changes the pulse wave velocity of the input pressure wave, increasing the potential uses of the model, allowing stiffness in only parts of the network or at different levels of vessels.

Many existing models involving vascular networks were developed to better understand the origin of the BOLD signal. An early example of this is the Balloon Model by Buxton et al. (1998) which was developed to understand changes in blood flow and blood volume as a consequence of neural activation. The VAN model by Boas et al. (2008) was developed to gain a more detailed understanding of the haemodynamic response, using a network consisting of many more compartments compared to previous models. A more recent computational model developed by Báez-Yáñez et al. (2023) similarly aimed to better understand the haemodynamic changes related to the BOLD signal, using a 3D vascular network to represent the vascular architecture of a single voxel of the cortex. The computational model developed in this thesis was based on the VAN model (Boas et al., 2008) as this provided a simplified approach to modelling blood flow over a large network of vessels, concentrating on pulsatile flow in larger feeding arteries. However, it differs to existing computational models as the aim was to model blood flow to understand how pulsatile energy is dissipated across a network of vessels due to branching and compliance and how this is related to arterial stiffness, thus vascular health in the brain.

Steady state simulations were carried out as a first step validation with the addition of compliance in the model and results from these initial simulations are presented in Chapter 5. The aim of the steady state simulations was firstly to check the model was working as expected, and secondly to characterise the model by investigating how a network of compliant vessels responded to changes in pressure. Furthermore, steady state simulations were required to find suitable values of vessel compliance across the microvessels and to limit the degrees of freedom by setting parameters for future simulations. Results from this set of simulations suggest venule compliance did not influence flow to the same extent as arteriole and capillary compliance. Outputs from the steady state simulations also suggest flow is affected by changes further downstream in the network in addition to local changes, highlighting the importance of considering changes across the whole network when modelling flow in compliant vessels.

A key aim of the model was to simulate blood flow in large arteries to analyse MRI pulsatile flow data collected in the ICA and MCA. Up until this point, the network of blood vessels consisted of arterioles, capillaries and venules, similar to the VAN model (Boas et al., 2008). However, to understand the dampening of pulsatile flow across the network, larger arteries were

modelled. To achieve this, the Plausible Vessel Network was created in Chapter 6 to include arteries and veins as well as the microvessels. Values for vessel diameter and compliance were taken from existing literature where possible and feasible estimates were made for the remaining parameters. The network was also created with the aim of splitting the ICA into the MCA and remaining vessels in the Circle of Willis lumped into a single equivalent vessel. The purpose of this was to simulate flow in the MCA to compare with MCA flow pulsatility measured with the DIMAC sequence (Chapter 8).

Dynamic simulations were run in Chapter 7 to investigate pulsatile flow across the Plausible Vessel Network and to assess how pulsatile energy was dissipated across vessels in the network. A pulsatile pressure wave was inputted into the model and the shape of the simulated flow waveform was compared for a range of compliant networks. Shape changes in flow were expected to occur across a network of compliant vessels as pulsatile flow at the start of the network in the ICA was expected to become steadier at the capillaries. However, flow outputs obtained from this set of simulations unanimously suggest that flow in the capillaries remains pulsatile, which may indicate that the model does not respond to dynamic changes in pressure effectively. This is further highlighted by minimal changes in the shape of the flow profile seen across beats in the ICA, MCA and capillary.

Pulsatile power was calculated using the output time series for pressure and flow and was compared across the ICA, MCA and capillary to further investigate pulsatility across the network. Results suggest that pulsatile power does decrease from the ICA to the capillaries, and therefore pulsatility is dampened across the network despite the shape of the flow waveforms still appearing pulsatile. Whilst blood flow is thought to become steadier once it reaches the capillaries, a study by Hahn et al. (1996) found red blood cell velocity to be pulsatile in capillaries in the skin. This suggests that microvascular flow remains pulsatile to some extent which is in agreement with the outputs from the simulations.

A method for estimating compliance in cerebral vessels, using pulsatile flow waveforms obtained from DIMAC data is outlined in Chapter 8. Input pressure waves were created for three participants using pulsatile waveforms measured in the ICA. Simulated flow waveforms for the MCA were compared to waveforms obtained from DIMAC in the MCA for a range of compliant networks. Some differences between the shape of the input ICA waveform and the simulated MCA waveforms were observed, however DIMAC MCA waveforms were not accurately reproduced by the simulated flow data from the model. Results suggest that there are many parameters that should be set in order to accurately model pulsatile flow in cerebral vessels. Knowledge of suitable compliance values across the whole network, as well as an understanding of how pulse wave velocity changes across levels is required to accurately simulate pulsatile flow.

9.2 Limitations of the Model

One of the main difficulties faced when developing the model was setting appropriate compliance values across the network. While studies have measured arterial compliance in large cerebral arteries (Salvi et al., 2022; Warnert et al., 2016), values for compliance in downstream vessels are not available. Values of arterial compliance also vary across the literature due to the different methods used to obtain them (e.g. TCD or MRI), and as a consequence are biased towards the method. Therefore, it is difficult to ascertain whether the measured values are accurate.

Furthermore, the definition of compliance was found to vary across the literature, making it difficult to find and compare values that are suitable for the model. Compliance can be defined by a power law change due to pressure from a baseline volume, or by a percentage change from an arbitrary starting volume. Translation from one regime to the other is not straightforward. Additionally, the meaning of compliance differs depending on the size of the vessel and the scale at which measurements are taken. This problem is particularly apparent when considering the relative compliance of vessels across sections of the vascular tree. For example, it is unclear how compliant the capillaries should be in relation to other vessels in the network. Single capillaries may not be compliant but, if multiple capillaries are lumped into one compartment, they may have an "apparent compliance" caused by changes in capillary transit time heterogeneity (CTTH), that is, a recruitment of low flow capillaries when pressure increases. Compliance values can vary drastically for a particular level depending on the assumptions used.

Input vessel networks were created to model flow across cerebral vessels. The Plausible Vessel Network was designed to incorporate arteries, microvessels and veins and empirical values from existing literature were used for vessel diameter, blood velocity and compliance when available. However, the network remains a simplification, limiting the accuracy of the outputs from the model. An example of this is only allowing vessels to bifurcate. A recent study by Smith et al. (2019) suggests that capillaries mainly branch into three vessels. In addition, the Plausible Vessel Network was developed to simulate ICA and MCA waveforms with the aim of comparing the outputs from the model with data collected in these vessels using DIMAC. For this reason, the ICA in the first level of the network was split into the MCA and the remaining arteries in the Circle of Willis in the second level. Vessel diameters (and other corresponding parameters) were updated to account for a greater distribution of flow through the vessel representing the Circle of Willis. This is not a realistic representation of the cerebral vascular tree. However, it was the most appropriate method given the aim of the model was to estimate important indicators of vessel health in the brain using the simplest approach possible.

The model could be improved by adding more levels of vessels to the input network. Simulations in Chapters 4 and 5 were carried out using a replication of the network used in the VAN model (Boas et al., 2008) which was created with 14 levels in total. The Plausible Vessel Network was also created with 14 levels in total to represent macrovessels and microvessels. The inclusion of more levels in the input network would make the network more realistic. Results

presented in Chapter 7 show flow is still pulsatile in the capillaries. This could be due to the network not including enough arterial levels to dampen the pulsatile energy before flow reaches the microvessels. However, it should be noted that increasing the number of levels sufficiently in the input vessel network comes at the cost of longer simulation running times and would require suitable computational power. Similarly, the number of segments that each vessel is split into could be increased. The greater the number of segments, the closer the model becomes to a continuous representation. However, increasing the number of segments would require greater computational power to run the model.

Throughout almost all of the simulations carried out for this thesis, compliant vessels were assumed to dilate instantaneously as a response to a change in pressure. This was a simplified approach taken to reflect dynamic changes in the vessel properties in the model. However, this is not realistic as it is likely that different vessels take different lengths of time to react to changes in the system. Implementing this within the model may engender greater differences in flow shape across the ICA, MCA and capillaries.

A key aim of the model was to simulate dynamic pressure-driven changes in flow across a network. To do this, a time parameter needed to be added to the model. Using the VAN model (Boas et al., 2008) as the basis for this model, each vessel was split into smaller segments such that the vessel would be modelled as a string of contiguous vessels. Each segment could be treated independently within the vessel and segment properties could be updated at every time step, leading to a model that could simulate dynamic local changes in flow. As the number of segments reaches infinity, this would in theory result in a continuous model. The model was set up to allow the pressure wave to move across the network one segment per time step. As the pulse wave velocity is determined by the number of segments (i.e. the time it takes to travel across the vessel) the time the pulse wave spends in the vessel depends on the length. This is a limitation as vessels lengths in the current method were calculated to achieve the required pressure drops across each level. Changing the lengths of the segments would change the temporal resolution across the different vessels at different levels and this would affect the calculation of the distribution of flow at each time step and tracking the pulse wave across the network. Future work could be carried out to uncouple the number of segments and the timing parameter, however this would not be easily achieved given how the model has been set up.

9.3 Future Directions

The outputs from the dynamic simulations presented in Chapter 7 show only small changes in the shape of the flow waveform across the ICA, MCA and capillary. This is further highlighted in Chapter 8, as only minimal changes were apparent when comparing the input ICA waveform to the simulated MCA waveform, and therefore the model did not accurately produce the measured MCA waveform. The lack of shape changes observed in the flow waveforms across vessels may have been a result of the constant intracranial pressure (ICP) used in the model. To improve the

model, a time-varying ICP value could be implemented, as this also likely changes in a pulsatile fashion. This idea could be further extended by setting ICP values in individual levels or sections of the network to take into account localised dynamic changes in pressure.

To address the issue of setting accurate compliance values for capillaries, this model could be combined with others that more realistically simulate flow in the microvessels, such as the computational model by Báez-Yáñez et al. (2023). These models use accurate reconstructions of microvessels in small patches of cortex to model flow changes related to neural activity. The capillary levels in our model could be replaced with such a realistic microvascular model and pressure changes throughout could be modelled. Not only would this produce a more accurate description of flow changes, it would give the added benefit of estimating the BOLD signal response to pulsatile flow changes, which could be a sensitive marker of cerebrovascular health in its own right.

The number of segments was varied in levels of the network to explore whether this influenced the shape of the of the flow waveform along the network. In Chapter 7, the number of segments in the Plausible Vessel Network was increased by a factor of 10 as results suggested that the number of segments in a vessel should be greater than the number of time steps across an input flow beat. In Chapter 8, the number of segments was varied across levels of the network. In both cases, results suggest that the number of segments does influence flow across time, thus the pulsatile waveform shape, and therefore is an important factor to consider when simulating flow realistically. The number of segments is related to PWV as the model was designed such that the pressure wave would travel across the network one segment per time step. In a realistic network of vessels incorporating large arteries, veins and microvessels, it is unlikely that the pulse wave velocity would remain the same across the entire network. Therefore, the model could be improved by varying the number of segments across the network. These PWV values could be a free parameter of the model, allowing us to estimate PWV based on shape changes. However, allowing the PWV to vary for each level would lead to overfitting of the data with multiple sets of values yielding the same/similar results. Therefore, it would be important to at least have a good initial idea of the PWV in all levels. However, once set the method for estimating vessel compliance described in Chapter 8 could be used and extended to estimate pulse wave velocity in vessels.

Recent work by Coccarelli et al. (2024) used a mathematical approach to develop a model to study blood flow dynamics across networks of myogenically active arteries in the brain. The authors assessed the model by investigating the haemodynamics following a change in pressure in a vascular network consisting of the MCA and three levels of branched arteries following the vessel. The model offers an alternative approach for simulating flow in an arterial network, using more complex governing equations to describe blood flow dynamics and vessel wall mechanics to account for changes in vascular tone. Future work could aim to incorporate similar equations into this model to gain more physiological realism, however initial results assessing the pressure

and flow dynamics following an increase in upstream pressure are similar to outputs from this model.

9.4 Summary

Throughout this thesis, a comprehensive dynamic model of the cerebrovascular network was developed to observe cardiac-induced pulsatile flow as it traverses the brains vessels. The utility of the model in determining important parameters related to cerebrovascular health has been demonstrated. It is a powerful, flexible model that can incorporate newer empirical information about brain vessel properties as it becomes available in the future, thus improving its accuracy and usefulness in shedding light on the deterioration of cerebrovascular health with age and disease.

References

Abdi, M., Karimi, A., Navidbakhsh, M., Rahmati, M., Hassani, K., and Razmkon, A. (2013). Modeling the Circle of Willis Using Electrical Analogy Method under both Normal and Pathological Circumstances. *Journal of Biomedical Physics & Engineering*, 3(2):45–56.

Afkhami, R., Wong, R., Ramadan, S., Walker, F. R., and Johnson, S. (2021). Indexing Cerebrovascular Health Using Transcranial Doppler Ultrasound. *Ultrasound in Medicine & Biology*, 47(4):919–927.

Alastruey, J., Parker, K. H., Peiró, J., Byrd, S. M., and Sherwin, S. J. (2007). Modelling the circle of Willis to assess the effects of anatomical variations and occlusions on cerebral flows. *Journal of Biomechanics*, 40(8):1794–1805.

Attwell, D., Mishra, A., Hall, C. N., O'Farrell, F. M., and Dalkara, T. (2016). What is a pericyte? *Journal of Cerebral Blood Flow and Metabolism: Official Journal of the International Society of Cerebral Blood Flow and Metabolism*, 36(2):451–455.

Badji, A., Sabra, D., Bherer, L., Cohen-Adad, J., Girouard, H., and Gauthier, C. J. (2019). Arterial stiffness and brain integrity: A review of MRI findings. *Ageing Research Reviews*, 53:100907.

Ballabh, P., Braun, A., and Nedergaard, M. (2004). The blood-brain barrier: an overview: structure, regulation, and clinical implications. *Neurobiology of Disease*, 16(1):1–13.

Bathala, L., Mehndiratta, M. M., and Sharma, V. K. (2013). Transcranial doppler: Technique and common findings (Part 1). *Annals of Indian Academy of Neurology*, 16(2):174–179.

Bianciardi, M., Toschi, N., Polimeni, J. R., Evans, K. C., Bhat, H., Keil, B., Rosen, B. R., Boas, D. A., and Wald, L. L. (2016). The pulsatility volume index: an indicator of cerebrovascular compliance based on fast magnetic resonance imaging of cardiac and respiratory pulsatility. *Philosophical Transactions. Series A, Mathematical, Physical, and Engineering Sciences*, 374(2067):20150184.

Björnfot, C., Garpebring, A., Qvarlander, S., Malm, J., Eklund, A., and Wåhlin, A. (2021). Assessing cerebral arterial pulse wave velocity using 4D flow MRI. *Journal of Cerebral Blood Flow and Metabolism: Official Journal of the International Society of Cerebral Blood Flow and Metabolism*, 41(10):2769–2777.

Boas, D. A., Jones, S. R., Devor, A., Huppert, T. J., and Dale, A. M. (2008). A vascular anatomical network model of the spatio-temporal response to brain activation. *NeuroImage*, 40(3):1116–1129.

Bramwell, J. C. and Hill, A. V. (1997). The velocity of pulse wave in man. *Proceedings of the Royal Society of London. Series B, Containing Papers of a Biological Character*, 93(652):298–306. Publisher: Royal Society.

Buxton, R. B. (2009). *Introduction to Functional Magnetic Resonance Imaging: Principles and Techniques*. Cambridge University Press, Cambridge, 2 edition.

Buxton, R. B., Wong, E. C., and Frank, L. R. (1998). Dynamics of blood flow and oxygenation changes during brain activation: The balloon model. *Magnetic Resonance in Medicine*, 39(6):855–864. _eprint: https://onlinelibrary.wiley.com/doi/pdf/10.1002/mrm.1910390602.

Bydder, G. M. and Young, I. R. (1985). MR imaging: clinical use of the inversion recovery sequence. *Journal of Computer Assisted Tomography*, 9(4):659–675.

Báez-Yáñez, M. G., Siero, J. C. W., and Petridou, N. (2023). A mechanistic computational framework to investigate the hemodynamic fingerprint of the blood oxygenation level-dependent signal. *NMR in Biomedicine*, 36(12):e5026. _eprint: https://onlinelibrary.wiley.com/doi/pdf/10.1002/nbm.5026.

Cecelja, M. and Chowienczyk, P. (2012). Role of arterial stiffness in cardiovascular disease. *JRSM cardiovascular disease*, 1(4):cvd.2012.012016.

Chavhan, G. B., Babyn, P. S., Thomas, B., Shroff, M. M., and Haacke, E. M. (2009). Principles, Techniques, and Applications of T2*-based MR Imaging and Its Special Applications. *Radiographics*, 29(5):1433–1449.

Chojdak-Łukasiewicz, J., Dziadkowiak, E., Zimny, A., and Paradowski, B. (2021). Cerebral small vessel disease: A review. *Advances in Clinical and Experimental Medicine: Official Organ Wroclaw Medical University*, 30(3):349–356.

Cipolla, M. J. (2009). *The Cerebral Circulation*. Integrated Systems Physiology: From Molecule to Function. Morgan & Claypool Life Sciences, San Rafael (CA).

Coccarelli, A., Polydoros, I., Drysdale, A., Harraz, O. F., and Kadapa, C. (2024). A new computational model for quantifying blood flow dynamics across myogenically-active cerebral arterial networks. *ArXiv*, page arXiv:2411.09046v1.

Currie, S., Hoggard, N., Craven, I. J., Hadjivassiliou, M., and Wilkinson, I. D. (2013). Understanding MRI: basic MR physics for physicians. *Postgraduate Medical Journal*, 89(1050):209–223.

Czosnyka, M. (2004). Monitoring and interpretation of intracranial pressure. *Journal of Neurology, Neurosurgery & Psychiatry*, 75(6):813–821.

D'Andrea, A., Conte, M., Cavallaro, M., Scarafile, R., Riegler, L., Cocchia, R., Pezzullo, E., Carbone, A., Natale, F., Santoro, G., Caso, P., Russo, M. G., Bossone, E., and Calabrò, R. (2016). Transcranial Doppler ultrasonography: From methodology to major clinical applications. *World Journal of Cardiology*, 8(7):383–400.

Deshmane, A., Gulani, V., Griswold, M. A., and Seiberlich, N. (2012). Parallel MR imaging. *Journal of Magnetic Resonance Imaging*, 36(1):55–72.

Donahue, M. J., Juttukonda, M. R., and Watchmaker, J. M. (2017). Noise concerns and post-processing procedures in cerebral blood flow (CBF) and cerebral blood volume (CBV) functional magnetic resonance imaging. *NeuroImage*, 154:43–58.

Duffin, J., Sobczyk, O., McKetton, L., Crawley, A., Poublanc, J., Venkatraghavan, L., Sam, K., Mutch, W. A., Mikulis, D., and Fisher, J. A. (2018). Cerebrovascular Resistance: The Basis of Cerebrovascular Reactivity. *Frontiers in Neuroscience*, 12.

Ferreira, H. and Ramalho, J. N. (2014). Basic Principles of Time-of-Flight Magnetic Resonance Angiography (TOF MRA) and MRV. In *Vascular Imaging of the Central Nervous System*, pages 125–136. John Wiley & Sons, Ltd. Section: 7 _eprint: https://onlinelibrary.wiley.com/doi/pdf/10.1002/9781118434550.ch7.

Fu, X., Huang, C., Wong, K. S., Chen, X., and Gao, Q. (2016). A New Method for Cerebral Arterial Stiffness by Measuring Pulse Wave Velocity Using Transcranial Doppler. *Journal of Atherosclerosis and Thrombosis*, 23(8):1004–1010.

Gallagher, T. A., Nemeth, A. J., and Hacein-Bey, L. (2008). An Introduction to the Fourier Transform: Relationship to MRI. *American Journal of Roentgenology*, 190(5):1396–1405.

Garcia-Polite, F., Martorell, J., Del Rey-Puech, P., Melgar-Lesmes, P., O'Brien, C. C., Roquer, J., Ois, A., Principe, A., Edelman, E. R., and Balcells, M. (2017). Pulsatility and high shear stress deteriorate barrier phenotype in brain microvascular endothelium. *Journal of Cerebral Blood Flow & Metabolism*, 37(7):2614–2625. Publisher: SAGE Publications Ltd STM.

Gosling, R. G. and King, D. H. (1974). Arterial Assessment by Doppler-shift Ultrasound. *Proceedings of the Royal Society of Medicine*, 67(6 Pt 1):447–449.

Griswold, M. A., Jakob, P. M., Heidemann, R. M., Nittka, M., Jellus, V., Wang, J., Kiefer, B., and Haase, A. (2002). Generalized autocalibrating partially parallel acquisitions (GRAPPA). *Magnetic Resonance in Medicine*, 47(6):1202–1210. _eprint: https://onlinelibrary.wiley.com/doi/pdf/10.1002/mrm.10171.

Hahn, M., Klyscz, T., and Jünger, M. (1996). Synchronous measurements of blood pressure and red blood cell velocity in capillaries of human skin. *The Journal of Investigative Dermatology*, 106(6):1256–1259.

Hargreaves, B. (2012). Rapid gradient-echo imaging. *Journal of Magnetic Resonance Imaging*, 36(6):1300–1313. _eprint: https://onlinelibrary.wiley.com/doi/pdf/10.1002/jmri.23742.

Harris, S., Reyhan, T., Ramli, Y., Prihartono, J., and Kurniawan, M. (2018). Middle Cerebral Artery Pulsatility Index as Predictor of Cognitive Impairment in Hypertensive Patients. *Frontiers in Neurology*, 9:538.

Hennig, J. (1999). K-space sampling strategies. *European Radiology*, 9(6):1020–1031.

Hindenes, L. B., Håberg, A. K., Johnsen, L. H., Mathiesen, E. B., Robben, D., and Vangberg, T. R. (2020). Variations in the Circle of Willis in a large population sample using 3D TOF angiography: The Tromsø Study. *PLOS ONE*, 15(11):e0241373.

Holmgren, M., Wåhlin, A., Dunås, T., Malm, J., and Eklund, A. (2020). Assessment of Cerebral Blood Flow Pulsatility and Cerebral Arterial Compliance With 4D Flow MRI. *Journal of Magnetic Resonance Imaging*, 51(5):1516–1525. _eprint: https://onlinelibrary.wiley.com/doi/pdf/10.1002/jmri.26978.

Hughes, T. M., Kuller, L. H., Barinas-Mitchell, E. J. M., McDade, E. M., Klunk, W. E., Cohen, A. D., Mathis, C. A., DeKosky, S. T., Price, J. C., and Lopez, O. L. (2014). Arterial Stiffness and β-Amyloid Progression in Nondemented Elderly Adults. *JAMA Neurology*, 71(5):562.

Hussain, B., Fang, C., and Chang, J. (2021). Blood-Brain Barrier Breakdown: An Emerging Biomarker of Cognitive Impairment in Normal Aging and Dementia. *Frontiers in Neuroscience*, 15:688090.

Itoh, T., Matsumoto, M., Handa, N., Maeda, H., Hougaku, H., Hashimoto, H., Etani, H., Tsukamoto, Y., and Kamada, T. (1993). Rate of successful recording of blood flow signals in the middle cerebral artery using transcranial Doppler sonography. *Stroke*, 24(8):1192–1195. Publisher: American Heart Association.

Itoh, Y. and Suzuki, N. (2012). Control of Brain Capillary Blood Flow. *Journal of Cerebral Blood Flow & Metabolism*, 32(7):1167–1176. Publisher: SAGE Publications Ltd STM.

Iulita, M. F., Noriega de la Colina, A., and Girouard, H. (2018). Arterial stiffness, cognitive impairment and dementia: confounding factor or real risk? *Journal of Neurochemistry*, 144(5):527–548. _eprint: https://onlinelibrary.wiley.com/doi/pdf/10.1111/jnc.14235.

Jackson, E. F., Ginsberg, L. E., Schomer, D. F., and Leeds, N. E. (1997). A review of MRI pulse sequences and techniques in neuroimaging. *Surgical Neurology*, 47(2):185–199.

Jefferson, A. L., Cambronero, F. E., Liu, D., Moore, E. E., Neal, J. E., Terry, J. G., Nair, S., Pechman, K. R., Rane, S., Davis, L. T., Gifford, K. A., Hohman, T. J., Bell, S. P., Wang, T. J., Beckman, J. A., and Carr, J. J. (2018). Higher Aortic Stiffness Is Related to Lower Cerebral Blood Flow and Preserved Cerebrovascular Reactivity in Older Adults. *Circulation*, 138(18):1951–1962.

Jezzard, P., Matthews, P. M., Smith, S. M., Jezzard, P., Matthews, P. M., and Smith, S. M., editors (2003). *Functional Magnetic Resonance Imaging: An Introduction to Methods*. Oxford University Press, Oxford, New York.

Ji, H., Xiong, J., Yu, S., Chi, C., Bai, B., Teliewubai, J., Lu, Y., Zhang, Y., and Xu, Y. (2018). Measuring the Carotid to Femoral Pulse Wave Velocity (Cf-PWV) to Evaluate Arterial Stiffness. *Journal of Visualized Experiments : JoVE*, (135):57083.

John K-j Li (2004). *Dynamics Of The Vascular System*. World Scientific Publishing Company, Singapore, SINGAPORE.

Jones, J. D., Castanho, P., Bazira, P., and Sanders, K. (2021). Anatomical variations of the circle of Willis and their prevalence, with a focus on the posterior communicating artery: A literature review and meta-analysis. *Clinical Anatomy*, 34(7):978–990. _eprint: https://onlinelibrary.wiley.com/doi/pdf/10.1002/ca.23662.

Jung, B. A. and Weigel, M. (2013). Spin echo magnetic resonance imaging. *Journal of Magnetic Resonance Imaging*, 37(4):805–817. _eprint: https://onlinelibrary.wiley.com/doi/pdf/10.1002/jmri.24068.

Kelly, B. A. and Chowienczyk, P. (2002). Vascular compliance. In Halliday, A. W., Hunt, B. J., Poston, L., and Schachter, M., editors, *An Introduction to Vascular Biology: From Basic Science to Clinical Practice*, pages 33–48. Cambridge University Press, Cambridge, 2 edition.

Korte, J., Klopp, E. S., and Berg, P. (2024). Multi-Dimensional Modeling of Cerebral Hemodynamics: A Systematic Review. *Bioengineering*, 11(1):72. Number: 1 Publisher: Multidisciplinary Digital Publishing Institute.

Ku, D. N. (1997). Blood Flow in Arteries. *Annual Review of Fluid Mechanics*, 29(1):399–434. _eprint: https://doi.org/10.1146/annurev.fluid.29.1.399.

Larson, A., Lanzino, G., and Brinjikji, W. (2020). Variations of Intracranial Dural Venous Sinus Diameters from Birth to 20 Years of Age: An MRV-Based Study. *AJNR: American Journal of Neuroradiology*, 41(12):2351–2357.

Laurent, S., Katsahian, S., Fassot, C., Tropeano, A.-I., Gautier, I., Laloux, B., and Boutouyrie, P. (2003). Aortic stiffness is an independent predictor of fatal stroke in essential hypertension. *Stroke*, 34(5):1203–1206.

Lee, H.-Y. and Oh, B.-H. (2010). Aging and arterial stiffness. *Circulation Journal: Official Journal of the Japanese Circulation Society*, 74(11):2257–2262.

Levin, R. A., Carnegie, M. H., and Celermajer, D. S. (2020). Pulse Pressure: An Emerging Therapeutic Target for Dementia. *Frontiers in Neuroscience*, 14:669.

Linninger, A. A., Gould, I. G., Marinnan, T., Hsu, C.-Y., Chojecki, M., and Alaraj, A. (2013). Cerebral Microcirculation and Oxygen Tension in the Human Secondary Cortex. *Annals of biomedical engineering*, 41(11):10.1007/s10439–013–0828–0.

Lipowsky, H. H. (2005). Microvascular rheology and hemodynamics. *Microcirculation (New York, N.Y.: 1994)*, 12(1):5–15.

Liu, H., Wang, D., Leng, X., Zheng, D., Chen, F., Wong, L. K. S., Shi, L., and Leung, T. W. H. (2020). State-of-the-Art Computational Models of Circle of Willis With Physiological Applications: A Review. *IEEE Access*, 8:156261–156273. Conference Name: IEEE Access.

Magee, P. (2020). Essential notes on the physics of Doppler ultrasound. *BJA Education*, 20(4):112–113.

Malone, A. F. and Reddan, D. N. (2010). Pulse Pressure. Why is it Important? *Peritoneal Dialysis International*, 30(3):265–268. Publisher: SAGE Publications Ltd STM.

Mandeville, J. B., Marota, J. J. A., Ayata, C., Zaharchuk, G., Moskowitz, M. A., Rosen, B. R., and Weisskoff, R. M. (1999). Evidence of a Cerebrovascular Postarteriole Windkessel with Delayed Compliance. *Journal of Cerebral Blood Flow & Metabolism*, 19(6):679–689. Publisher: SAGE Publications Ltd STM.

Marchais, S. J., Guerin, A. P., Pannier, B., Delavaud, G., and London, G. M. (1993). Arterial compliance and blood pressure. *Drugs*, 46 Suppl 2:82–87.

Marinoni, M., Ginanneschi, A., Forleo, P., and Amaducci, L. (1997). Technical limits in transcranial Doppler recording: Inadquate acoustic windows. *Ultrasound in Medicine & Biology*, 23(8):1275–1277.

Markl, M. and Leupold, J. (2012). Gradient echo imaging. *Journal of Magnetic Resonance Imaging*, 35(6):1274–1289. _eprint: https://onlinelibrary.wiley.com/doi/pdf/10.1002/jmri.23638.

Markus, H. S. (2000). Transcranial Doppler ultrasound. *British Medical Bulletin*, (2).

Martinez-Lemus, L. A. (2012). The Dynamic Structure of Arterioles. *Basic & Clinical Pharmacology & Toxicology*, 110(1):5–11.

Mattace-Raso, F. U. S., van der Cammen, T. J. M., Hofman, A., van Popele, N. M., Bos, M. L., Schalekamp, M. A. D. H., Asmar, R., Reneman, R. S., Hoeks, A. P. G., Breteler, M. M. B., and Witteman, J. C. M. (2006). Arterial stiffness and risk of coronary heart disease and stroke: the Rotterdam Study. *Circulation*, 113(5):657–663.

McGibney, G., Smith, M. R., Nichols, S. T., and Crawley, A. (1993). Quantitative evaluation of several partial fourier reconstruction algorithms used in mri. *Magnetic Resonance in Medicine*, 30(1):51–59. _eprint: https://onlinelibrary.wiley.com/doi/pdf/10.1002/mrm.1910300109.

Mitchell, G. F., van Buchem, M. A., Sigurdsson, S., Gotal, J. D., Jonsdottir, M. K., Kjartansson, , Garcia, M., Aspelund, T., Harris, T. B., Gudnason, V., and Launer, L. J. (2011). Arterial stiffness, pressure and flow pulsatility and brain structure and function: the Age, Gene/Environment Susceptibility – Reykjavik Study. *Brain*, 134(11):3398–3407.

Mitchell, G. F., Vita, J. A., Larson, M. G., Parise, H., Keyes, M. J., Warner, E., Vasan, R. S., Levy, D., and Benjamin, E. J. (2005). Cross-Sectional Relations of Peripheral Microvascular Function, Cardiovascular Disease Risk Factors, and Aortic Stiffness. *Circulation*, 112(24):3722–3728. Publisher: American Heart Association.

Naqvi, J., Yap, K. H., Ahmad, G., and Ghosh, J. (2013). Transcranial Doppler Ultrasound: A Review of the Physical Principles and Major Applications in Critical Care. *International Journal of Vascular Medicine*, 2013:629378.

Nichols, W. W. (2005). Clinical measurement of arterial stiffness obtained from noninvasive pressure waveforms. *American Journal of Hypertension*, 18(1 Pt 2):3S–10S.

Nichols, W. W., Denardo, S. J., Wilkinson, I. B., McEniery, C. M., Cockcroft, J., and O'Rourke, M. F. (2008). Effects of Arterial Stiffness, Pulse Wave Velocity, and Wave Reflections on the Central Aortic Pressure Waveform. *The Journal of Clinical Hypertension*, 10(4):295–303. _eprint: https://onlinelibrary.wiley.com/doi/pdf/10.1111/j.1751-7176.2008.04746.x.

O'Rourke, M. F. (2007). Arterial aging: pathophysiological principles. *Vascular Medicine (London, England)*, 12(4):329–341.

Oswal, A. and Toma, A. K. (2023). Intracranial pressure and cerebral haemodynamics. *Anaesthesia & Intensive Care Medicine*, 24(6):353–357.

O'Rourke, M. F. and Hashimoto, J. (2007). Mechanical Factors in Arterial Aging: A Clinical Perspective. *Journal of the American College of Cardiology*, 50(1):1–13.

Pan, Y., Wan, W., Xiang, M., and Guan, Y. (2022). Transcranial Doppler Ultrasonography as a Diagnostic Tool for Cerebrovascular Disorders. *Frontiers in Human Neuroscience*, 16.

Panerai, R. B. (2009). Transcranial Doppler for evaluation of cerebral autoregulation. *Clinical Autonomic Research*, 19(4):197–211.

Payne, R. A., Wilkinson, I. B., and Webb, D. J. (2010). Arterial Stiffness and Hypertension. *Hypertension*, 55(1):9–14. Publisher: American Heart Association.

Payne, S. (2016). *Cerebral Autoregulation*. SpringerBriefs in Bioengineering. Springer International Publishing, Cham.

Pelc, N. J., Herfkens, R. J., Shimakawa, A., and Enzmann, D. R. (1991). Phase contrast cine magnetic resonance imaging. *Magnetic Resonance Quarterly*, 7(4):229–254.

Piechnik, S. K., Chiarelli, P. A., and Jezzard, P. (2008). Modelling vascular reactivity to investigate the basis of the relationship between cerebral blood volume and flow under CO2 manipulation. *NeuroImage*, 39(1):107–118.

Plewes, D. B. and Kucharczyk, W. (2012). Physics of MRI: A primer. *Journal of Magnetic Resonance Imaging*, 35(5):1038–1054. _eprint: https://onlinelibrary.wiley.com/doi/pdf/10.1002/jmri.23642.

Poels, M. M., Zaccai, K., Verwoert, G. C., Vernooij, M. W., Hofman, A., van der Lugt, A., Witteman, J. C., Breteler, M. M., Mattace-Raso, F. U., and Ikram, M. A. (2012). Arterial Stiffness and Cerebral Small Vessel Disease. *Stroke*, 43(10):2637–2642. Publisher: American Heart Association.

Poustchi-Amin, M., Mirowitz, S. A., Brown, J. J., McKinstry, R. C., and Li, T. (2001). Principles and applications of echo-planar imaging: a review for the general radiologist. *Radiographics: A Review Publication of the Radiological Society of North America, Inc*, 21(3):767–779.

Pries, A. R., Neuhaus, D., and Gaehtgens, P. (1992). Blood viscosity in tube flow: dependence on diameter and hematocrit. *The American Journal of Physiology*, 263(6 Pt 2):H1770–1778.

Purkayastha, S. and Sorond, F. (2012). Transcranial Doppler Ultrasound: Technique and Application. *Seminars in neurology*, 32(4):411–420.

Quick, S., Moss, J., Rajani, R. M., and Williams, A. (2021). A Vessel for Change: Endothelial Dysfunction in Cerebral Small Vessel Disease. *Trends in Neurosciences*, 44(4):289–305.

Rabkin, S. W. (2012). Arterial Stiffness: Detection and Consequences in Cognitive Impairment and Dementia of the Elderly. *Journal of Alzheimer's Disease*, 32(3):541–549.

Ren, Y., Chen, Q., and Li, Z.-Y. (2015). A 3D numerical study of the collateral capacity of the circle of Willis with anatomical variation in the posterior circulation. *BioMedical Engineering OnLine*, 14(1):S11.

Roher, A. E., Garami, Z., Tyas, S. L., Maarouf, C. L., Kokjohn, T. A., Belohlavek, M., Vedders, L. J., Connor, D., Sabbagh, M. N., Beach, T. G., and Emmerling, M. R. (2011). Transcranial Doppler ultrasound blood flow velocity and pulsatility index as systemic indicators for Alzheimer's disease. *Alzheimer's & Dementia*, 7(4):445–455. _eprint: https://onlinelibrary.wiley.com/doi/pdf/10.1016/j.jalz.2010.09.002.

Safar, M. E. (2018). Arterial stiffness as a risk factor for clinical hypertension. *Nature Reviews Cardiology*, 15(2):97–105. Number: 2 Publisher: Nature Publishing Group.

Salvi, P., Valbusa, F., Kearney-Schwartz, A., Labat, C., Grillo, A., Parati, G., and Benetos, A. (2022). Non-Invasive Assessment of Arterial Stiffness: Pulse Wave Velocity, Pulse Wave Analysis and Carotid Cross-Sectional Distensibility: Comparison between Methods. *Journal of Clinical Medicine*, 11(8):2225.

Schmitt, F., Stehling, M. K., and Turner, R. (1998). *Echo-Planar Imaging*. Springer, Berlin, Heidelberg.

Schreiber, S., Bueche, C. Z., Garz, C., and Braun, H. (2013). Blood brain barrier breakdown as the starting point of cerebral small vessel disease? - New insights from a rat model. *Experimental & Translational Stroke Medicine*, 5:4.

Secomb, T. W. (2016). Hemodynamics. *Comprehensive Physiology*, 6(2):975–1003.

Secomb, T. W. (2017). Blood Flow in the Microcirculation. *Annual Review of Fluid Mechanics*, 49(Volume 49, 2017):443–461. Publisher: Annual Reviews.

Shi, Y., Lawford, P., and Hose, R. (2011). Review of Zero-D and 1-D Models of Blood Flow in the Cardiovascular System. *BioMedical Engineering OnLine*, 10(1):33.

Shirwany, N. A. and Zou, M.-h. (2010). Arterial stiffness: a brief review. *Acta Pharmacologica Sinica*, 31(10):1267–1276.

Sleight, E., Stringer, M. S., Marshall, I., Wardlaw, J. M., and Thrippleton, M. J. (2021). Cerebrovascular Reactivity Measurement Using Magnetic Resonance Imaging: A Systematic Review. *Frontiers in Physiology*, 12.

Smith, A. F., Doyeux, V., Berg, M., Peyrounette, M., Haft-Javaherian, M., Larue, A.-E., Slater, J. H., Lauwers, F., Blinder, P., Tsai, P., Kleinfeld, D., Schaffer, C. B., Nishimura, N., Davit, Y., and Lorthois, S. (2019). Brain Capillary Networks Across Species: A few Simple Organizational Requirements Are Sufficient to Reproduce Both Structure and Function. *Frontiers in Physiology*, 10.

Song, N., Adji, A. I., Hungerford, S. L., Namasivayam, M. J., Hayward, C. S., Jabbour, A., and Muller, D. W. M. (2023). Pulsatile energy consumption as a surrogate marker for vascular afterload improves with time post transcatheter aortic valve replacement in patients with aortic stenosis. *Hypertension Research*, 46(3):730–741. Number: 3 Publisher: Nature Publishing Group.

Steiner, L. A. and Andrews, P. J. D. (2006). Monitoring the injured brain: ICP and CBF. *British Journal of Anaesthesia*, 97(1):26–38.

Sun, Z. (2015). Aging, Arterial Stiffness, and Hypertension. *Hypertension*, 65(2):252–256. Publisher: American Heart Association.

Sweeney, M. D., Sagare, A. P., and Zlokovic, B. V. (2018). Blood–brain barrier breakdown in Alzheimer disease and other neurodegenerative disorders. *Nature Reviews Neurology*, 14(3):133–150.

Symms, M. (2004). A review of structural magnetic resonance neuroimaging. *Journal of Neurology, Neurosurgery & Psychiatry*, 75(9):1235–1244.

Tang, M. Y., Chen, T. W., Zhang, X. M., and Huang, X. H. (2014). GRE T2 *-Weighted MRI: Principles and Clinical Applications. *BioMed Research International*, 2014(1):312142. _eprint: https://onlinelibrary.wiley.com/doi/pdf/10.1155/2014/312142.

Tsao, C. W., Seshadri, S., Beiser, A. S., Westwood, A. J., DeCarli, C., Au, R., Himali, J. J., Hamburg, N. M., Vita, J. A., Levy, D., Larson, M. G., Benjamin, E. J., Wolf, P. A., Vasan, R. S., and Mitchell, G. F. (2013). Relations of arterial stiffness and endothelial function to brain aging in the community. *Neurology*, 81(11):984–991.

Turner, R. (2002). How Much Cortex Can a Vein Drain? Downstream Dilution of Activation-Related Cerebral Blood Oxygenation Changes. *NeuroImage*, 16(4):1062–1067.

Verkman, A. S. (2002). Aquaporin water channels and endothelial cell function*. *Journal of Anatomy*, 200(6):617–627. _eprint: https://onlinelibrary.wiley.com/doi/pdf/10.1046/j.1469-7580.2002.00058.x.

Vlachopoulos, C., O'Rourke, M., and Nichols, W. W. (2012). *McDonald's Blood Flow in Arteries: Theoretical, Experimental and Clinical Principles*. CRC Press, London, 6 edition.

Vovenko, E. (1999). Distribution of oxygen tension on the surface of arterioles, capillaries and venules of brain cortex and in tissue in normoxia: an experimental study on rats. *Pflugers Archiv: European Journal of Physiology*, 437(4):617–623.

Wagshul, M. E., Eide, P. K., and Madsen, J. R. (2011). The pulsating brain: A review of experimental and clinical studies of intracranial pulsatility. *Fluids and barriers of the CNS*, 8(1):5.

Warnert, E. A., Hart, E. C., Hall, J. E., Murphy, K., and Wise, R. G. (2016). The major cerebral arteries proximal to the Circle of Willis contribute to cerebrovascular resistance in humans. *Journal of Cerebral Blood Flow & Metabolism*, 36(8):1384–1395. Publisher: SAGE Publications Ltd STM.

Warnert, E. A. H., Murphy, K., Hall, J. E., and Wise, R. G. (2015). Noninvasive assessment of arterial compliance of human cerebral arteries with short inversion time arterial spin labeling. *Journal of Cerebral Blood Flow and Metabolism: Official Journal of the International Society of Cerebral Blood Flow and Metabolism*, 35(3):461–468.

Washburn, E. W. (1921). The Dynamics of Capillary Flow. *Physical Review*, 17(3):273–283. Publisher: American Physical Society.

Weiss, N., Miller, F., Cazaubon, S., and Couraud, P.-O. (2009). The blood-brain barrier in brain homeostasis and neurological diseases. *Biochimica et Biophysica Acta (BBA) - Biomembranes*, 1788(4):842–857.

Westerhof, N., Lankhaar, J.-W., and Westerhof, B. E. (2009). The arterial Windkessel. *Medical & Biological Engineering & Computing*, 47(2):131–141.

Whittaker, J. R., Fasano, F., Venzi, M., Liebig, P., Gallichan, D., Möller, H. E., and Murphy, K. (2022). Measuring Arterial Pulsatility With Dynamic Inflow Magnitude Contrast. *Frontiers in Neuroscience*, 15:795749.

Wymer, D. T., Patel, K. P., Burke, W. F., and Bhatia, V. K. (2020). Phase-Contrast MRI: Physics, Techniques, and Clinical Applications. *Radiographics: A Review Publication of the Radiological Society of North America, Inc*, 40(1):122–140.

Xiao, N., Humphrey, J. D., and Figueroa, C. A. (2013). Multi-Scale Computational Model of Three-Dimensional Hemodynamics within a Deformable Full-Body Arterial Network. *Journal of Computational Physics*, 244:22–40.

Xing, C.-Y., Tarumi, T., Liu, J., Zhang, Y., Turner, M., Riley, J., Tinajero, C. D., Yuan, L.-J., and Zhang, R. (2017). Distribution of cardiac output to the brain across the adult lifespan. *Journal of Cerebral Blood Flow and Metabolism: Official Journal of the International Society of Cerebral Blood Flow and Metabolism*, 37(8):2848–2856.

Yucel, E. K., Anderson, C. M., Edelman, R. R., Grist, T. M., Baum, R. A., Manning, W. J., Culebras, A., and Pearce, W. (1999). Magnetic Resonance Angiography. *Circulation*, 100(22):2284–2301. Publisher: American Heart Association.

Zamboni, P., Tavoni, V., Sisini, F., Pedriali, M., Rimondi, E., Tessari, M., and Menegatti, E. (2018). Venous compliance and clinical implications. *Veins and Lymphatics*, 7(2).

Zarrinkoob, L., Ambarki, K., Wåhlin, A., Birgander, R., Carlberg, B., Eklund, A., and Malm, J. (2016). Aging alters the dampening of pulsatile blood flow in cerebral arteries. *Journal of Cerebral Blood Flow & Metabolism*, 36(9):1519–1527.

Østergaard, L. (2020). Blood flow, capillary transit times, and tissue oxygenation: the centennial of capillary recruitment. *Journal of Applied Physiology*, 129(6):1413–1421. Publisher: American Physiological Society.

Appendix A

Additional Results

A.0.1 Modifying the Input Pressure Wave - Addition of Gaussian noise

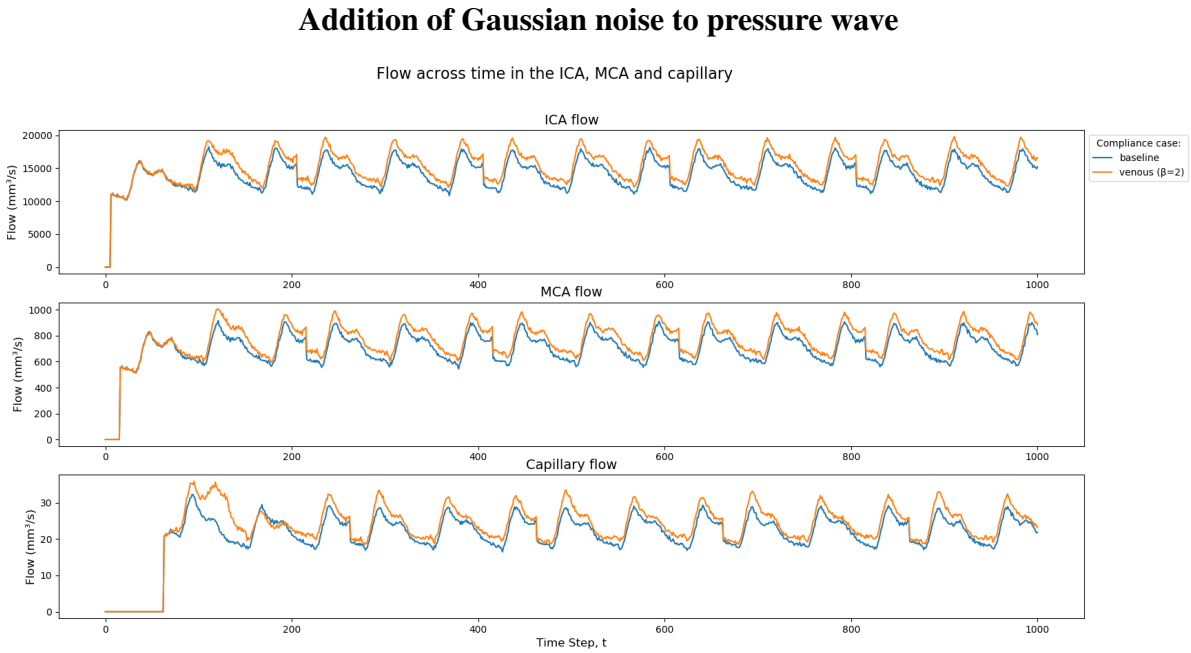

((a)) Flow across time in the ICA, MCA and capillary compared for different compliant network cases.

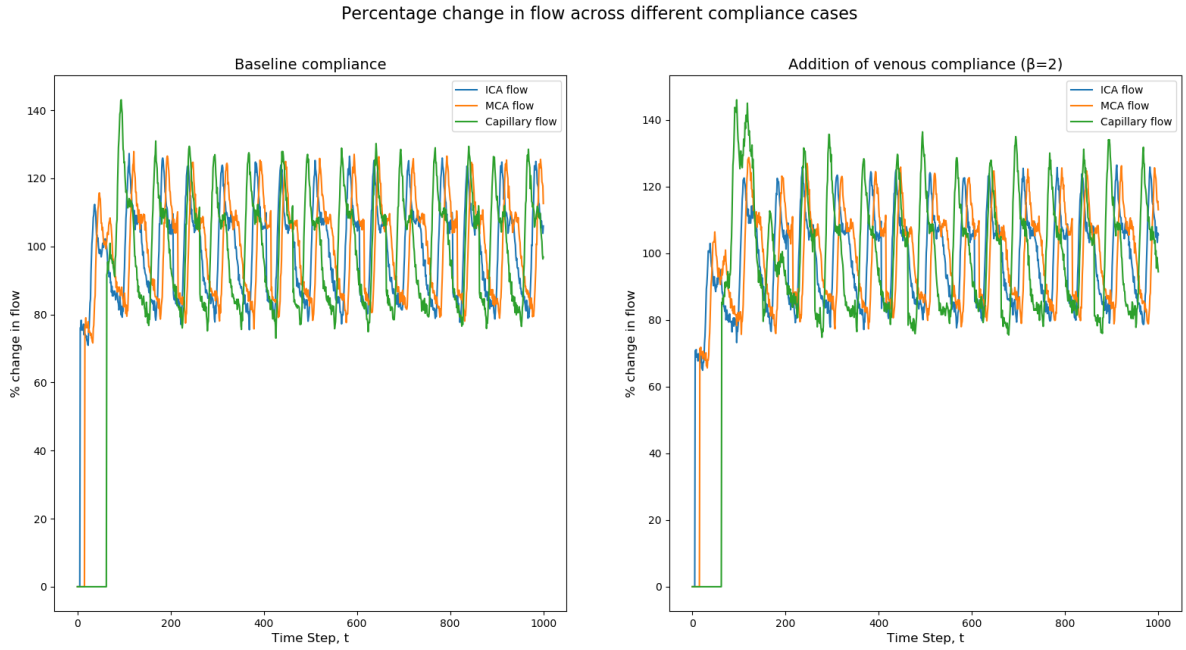

((b)) Percentage difference in flow compared for the ICA, MCA and capillary compared across different compliant network cases.

Fig. A.1 (a) Flow across time and (b) percentage difference in flow in the ICA, MCA and capillary compared for compliant network cases: (0) baseline compliance and (1) venous compliance (β=2) with the addition of Gaussian noise to the input pressure wave.

Appendix B

Using the Model

B.1 Python Files

All python files and relevant documentation can be found here:
https://github.com/kajalsaroay/model_ESV_files.git
Required files include:

- vessels.py - All classes and methods are defined in this file. Vessel classes are used to construct the objects in the input network text files. Baseline pressure (at t=0) and intracranial pressure can be updated in this file.
- model_ESV.py - Reads in input network and pressure wave text files, creates all storage matrices, runs code and saves output pressure, flow, volume and resistance values across time.
- pressure_wave.txt - Example of input pressure wave used in the model. This is loaded into model_ESV.py
- input_network.txt - Example of an input network text file. This is loaded into model_ESV.py
- README.md - Contains up-to-date information on how to run the code and documentation for each file.

Optional files include:

- model_ESV_function.py - Main python file as a function.
- ESV_exec.py - Use when running code with multiple inputs (e.g. multiple pressure waves or multiple input network files). Takes inputs from specified directory and saves outputs (e.g. pressure, flow across time) to a specified directory. Use with model_ESV_function.py to execute the function.

- DIMAC_ESV_exec.py - Specifically for use when running through all nine DIMAC networks. Use with model_ESV_function.py to execute the function.
- plausible_vessel_network_dev.py - Calculates and outputs the diameters, lengths and viscosities for paths A and B in the Plausible Vessel Network. Input parameters can be modified using this file.

An input network file (see section below) is loaded into model_ESV.py and all storage matrices are created to represent the shape of the network (number of levels, number of vessels per level and number of segments per vessel). An input pressure wave is loaded into the file. Simulations are run for the length of the pressure wave. Iterating through time steps, values for pressure, volume, resistance and flow are updated at every time point in all vessel segments. Pressure, volume, resistance and flow values for the vessels are stored and outputted across time steps. Here, pressure refers to input pressure of the vessel, volume and resistance are the total volume and resistance across the segments in a vessel and flow refers to the absolute flow through the first segment. The Equivalent Single Vessel is incorporated into this calculation.

Please see the README file for up-to-date information.

B.2 Input Network

Each network is created in a text file. An example is shown in Fig. B.1. Networks consist of single vessels, diverging branches and converging branches. Each line in the network text file describes a branch in the network. Branches are categorised into their corresponding levels depending on the number of branches per level (i.e. the second line in the text file).

```
[1, 2, 4, 8, 16, 32, 64, 64, 32, 16, 8, 4, 2, 1]     Number of vessels in level
[1, 1, 2, 4, 8, 16, 32, 32, 16, 8, 4, 2, 1, 1]       Number of branches per level

vessels.class(input pressure at baseline, output pressure at baseline, vessel diameter, vessel length, blood viscosity, vessel compliance, no. of segments)
vessels.LongSegment(11., 11., 4000., 426630., 2.5, 151.8, 10)
vessels.DivergingBranchSegment(11., 11., np.array([4013.51, 1920.]), 455072, 2.5, np.array([114.1, 114.1]), 10)
vessels.DivergingBranchSegment(11., 11., np.array([3374.95, 3374.95]), 455072, 2.5, np.array([10, 10]), 10)
vessels.DivergingBranchSegment(11., 11., np.array([1614.52, 1614.52]), 455072, 2.5, np.array([10, 10]), 10)
vessels.DivergingBranchSegment(11., 11., np.array([69.8, 69.8]), 0.0175612, 3.84, np.array([100000, 100000]), 10)
vessels.DivergingBranchSegment(11., 11., np.array([69.8, 69.8]), 0.0175612, 3.84, np.array([100000, 100000]), 10)
vessels.DivergingBranchSegment(11., 11., np.array([30., 30.]), 0.0175612, 2.5, np.array([100000, 100000]), 10)
vessels.DivergingBranchSegment(11., 11., np.array([30., 30.]), 0.0175612, 2.5, np.array([100000, 100000]), 10)
vessels.DivergingBranchSegment(11., 11., np.array([44.8, 44.8]), 0.0199284, 2.98, np.array([100000, 100000]), 10)
vessels.DivergingBranchSegment(11., 11., np.array([44.8, 44.8]), 0.0199284, 2.98, np.array([100000, 100000]), 10)
vessels.DivergingBranchSegment(11., 11., np.array([44.8, 44.8]), 0.0199284, 2.98, np.array([100000, 100000]), 10)
vessels.DivergingBranchSegment(11., 11., np.array([44.8, 44.8]), 0.0199284, 2.98, np.array([100000, 100000]), 10)
vessels.DivergingBranchSegment(11., 11., np.array([20., 20.]), 0.0199284, 2.26, np.array([100000, 100000]), 10)
vessels.DivergingBranchSegment(11., 11., np.array([20., 20.]), 0.0199284, 2.26, np.array([100000, 100000]), 10)
vessels.DivergingBranchSegment(11., 11., np.array([20., 20.]), 0.0199284, 2.26, np.array([100000, 100000]), 10)
vessels.DivergingBranchSegment(11., 11., np.array([20., 20.]), 0.0199284, 2.26, np.array([100000, 100000]), 10)
vessels.DivergingBranchSegment(11., 11., np.array([21.3, 21.3]), 0.00149206, 2.28, np.array([100000, 100000]), 10)
vessels.DivergingBranchSegment(11., 11., np.array([21.3, 21.3]), 0.00149206, 2.28, np.array([100000, 100000]), 10)
vessels.DivergingBranchSegment(11., 11., np.array([21.3, 21.3]), 0.00149206, 2.28, np.array([100000, 100000]), 10)
vessels.DivergingBranchSegment(11., 11., np.array([21.3, 21.3]), 0.00149206, 2.28, np.array([100000, 100000]), 10)
vessels.DivergingBranchSegment(11., 11., np.array([21.3, 21.3]), 0.00149206, 2.28, np.array([100000, 100000]), 10)
vessels.DivergingBranchSegment(11., 11., np.array([21.3, 21.3]), 0.00149206, 2.28, np.array([100000, 100000]), 10)
vessels.DivergingBranchSegment(11., 11., np.array([21.3, 21.3]), 0.00149206, 2.28, np.array([100000, 100000]), 10)
vessels.DivergingBranchSegment(11., 11., np.array([21.3, 21.3]), 0.00149206, 2.28, np.array([100000, 100000]), 10)
```

Fig. B.1 Example of input network text file. The first 26 lines of the Plausible Vessel Network input text file are shown.